Strain Path Effects on Timetal 834 Under Hot Working Conditions

Michael Blackmore

Thesis submitted for the degree of Doctor of Philosophy
University of Sheffield
Department of Engineering Materials

2009

Abstract

Little work has been dedicated to the magnitudes of the strain paths that are imposed on a workpiece during various industrial thermomechanical processing (TMP) routes. Furthermore, previous strain path work has concentrated on linear, sequential and full reversal strain paths due to the ease of performing such tests. No work has been carried out on the complex concurrent strain paths which are imposed during TMP. By combining finite element (FE) modelling and the new Arbitrary Strain Path (ASPII – the second generation of its kind at the University of Sheffield) machine such work is now possible.

The ASPII machine is a test rig capable of imposing independent or concurrent torsion and axial components of deformation under fixed or free end conditions. The machine in equipped with an induction heater capable of testing materials up to $1100°C$ and a water quenching system to capture high temperature deformation microstructures. An induction coil heating system also allows controlled slow air cooling to be carried out to closely reproduce industrial cooling rates. The machine has been calibrated to accurately carry out full reversal in the deformation direction (torsion and tension/compression) over the temperature range of $600-1100°C$ up to a strain rate of $10s^{-1}$ with negligible delay or overshoot.

Model parameter sensitivity analysis, material flow behaviour and model validation have been carried out using axisymmetric FE models for a range of temperatures (950, 990, $1030°C$) and strain rates (0.2, 2, $20s^{-1}$) combined with actual tests carried out within IMMPETUS. The simulations demonstrated that over the tested temperature, strain and strain rate ranges, the models were largely unaffected by most thermal input parameters (e.g. thermal conduction,). The mesh density and friction coefficient have been shown to have the largest influence on FE model output.

FE simulation of a two stage closed die forging of an arbitrary aero engine compressor disc has been carried out. This model has provided 'typical' process parameters to carry out extreme strain path change tests i.e. full reversal tests. Such tests were undertaken to evaluate any effects on the similarly orientated primary alpha grain clusters that are responsible for reductions in fatigue life under dwell loading situations. Such extremes changes in strain path were unsuccessful in breaking up the clusters.

By tracking nodes within the FE model the deformation history has been extracted and subsequent strain paths have been calculated for three points of interest within the forged material. This information has been transferred to the ASPII machine and the deformation has successfully been replayed. Initial tests were followed by a simulated industrial slow air cool. Later work quenched the samples after the forging strain path simulation. It was seen that different strain paths do influence the morphology of the microstructure however in terms of micro and macro texture no significant difference can be found.

Contents

Nomenclature

A	Area
A_m	Material constant
B_o	Material constant
C	Frictional smoothing coefficient
C_s	Material constant
c_p	Specific heat capacity at constant pressure
c_{pa}	Thermal capacity of air
c_v	Specific heat at constant volume
d	Distance, diameter
d_{fmax}	Maximum final diameter
d_{fmin}	Min final diameter
f	Frequency
F	Force
g	Acceleration due to gravity
G	Shear modulus
Gr	Grashof number
h	Convectional heat transfer coefficient
$\bar{h}$	Mean convectional heat transfer coefficient
h_t	Tool heat transfer coefficient
h_a	Environmental heat transfer coefficient
k	Thermal conductivity
k_f	Thermal conductivity of a fluid
k_y	Shear yield strength
l_f	Final sample length
l_o	Initial sample length
L	Characteristic length
m	Friction factor, strain rate hardening coefficient
n	Strain hardening coefficient
$\overline{Nu}_L$	Nusselt number
O_v	Ovality coefficient
P	Mean pressure
Pr	Prandtl number
q	Heat flux
q_{con}	Convectional heat flux
Q_{def}	Activation energy for deformation
q_{rad}	Radiative heat flux
r	Radius
R	True stress at intermediate time

Ra	Rayleigh number
Re	Reynolds Number
r_m	Critical radius
r_x	Distance from cylinders centre
$\bar{t}$	Tangential unit vector
T_1	Experimental temperature
T_2	Corrected temperature
T_a	Ambient temperature
T_f	Final temperature
T_o	Initial temperature
T_t	Tool temperature
T_s	Surface temperature
T_w	Workpiece temperature
T_∞	Temperature of surrounding fluid
$\dfrac{\partial T}{\partial x}$	Temperature gradient
U	Strain energy per unit volume
U_D	Strain energy due to shape change per unit volume
U_T	Total strain energy per unit volume
U_V	Volumetric strain energy
V	Tool velocity
V_{rel}	Relative sliding velocity
α	Material constant
α_D	Thermal diffusivity of a fuid
α_T	Thermal expansion coefficient
β	Thermal expansion coefficient of a fluid
β_{air}	Inverse of the mean temperature
δ	Elastic deflection
δ_d	Depth of penetration
ε	Strain
$\dot{\varepsilon}$	Strain rate
$\varepsilon'_{x,y,z}$	Deviatoric strain component
$\overline{d\varepsilon_{ij}}^{\,p}$	Equivalent plastic strain component
ε_m	Emissivity
γ	Torsional strain
$\dot{\gamma}$	Torsional strain rate
η	Heat conversion factor
μ	Friction coefficient
μ_d	Dynamic viscosity
μ_r	Relative magnetic permeability

θ	Angle displacement
$\dot{\theta}$	Rate of angular displacement
ρ	Density
ρ_{res}	Electrical resistivity
ρ_{Ti}	Electrical resistivity for titanium
$\bar{\sigma}$	Mean stress
σ_{cond}	Electrical conductivity
σ_{SB}	Stefan-Boltzmann constant (5.669×10^{-8} W/m^2.K^4)
$\bar{\sigma}_u$	Equivalent von Mises stress
$\sigma_{x,y,z}$	Stress component
$\sigma'_{x,y,z}$	Deviatoric stress component
σ_{yd}	Yield stress
τ	Peierils-Nabarro stress
τ_{eq}	Equivalent shear stress
τ_f	Frictional shear stress
τ_0	Critical resolved shear stress
τ_{max}	Maximum shear stress
$\tau_{x,y,z}$	Shear stress component
υ	Kinematic viscosity
υ_p	Poissons ratio
ω_c	Frequency of oscillation

Acknowledgments

1. Introduction

1.1. Industrial processing of Timetal®834

Titanium and its alloys demonstrate outstanding corrosion resistance together with excellent room and elevated temperature mechanical properties at approximately half the density of steel alloys. As a result, titanium has been utilised extensively throughout the weight conscious aerospace industry for many applications. For example, the low to intermediate temperatures of the front and centre sections respectively of commercial aero engines are dominated by titanium alloys, due to their high specific properties in these temperature regimes. The low temperature fan blades and first stage compressors are typically manufactured using the well known α/β alloy Ti-6Al-4V. As the air temperature increases throughout the compressor section more advanced alloys are required to fulfil the growing design demands on the material.

Timetal®834 has been developed as a high temperature alloy for use as rotary components in the high-pressure compressor section of turbo-fan engines, replacing the denser nickel based alloys. Its chemistry, process route and microstructure have been tailored to facilitate practical industrial control (e.g. low beta approach curve to allow wider temperature range for a desired α/β phase ratio) and yield a combination of good fatigue and creep resistance along with high temperature strength. Examples of this include α/β forging to maintain creep resistance by the alpha phase pinning the beta grain boundaries, preventing excessive grain growth during processing and the subsequent heat-treatment to produce a Widmanstätten structure in the transformed beta grains yielding a convoluted fatigue crack path and hence good fatigue resistance.

Rotating titanium components are typically manufactured via a hot forging route due to their near net nature, grain alignment to in-service loads and microstructural refinement. However, extensive use of finite element modelling has demonstrated that significant non-homogenous deformations take place during these well established industrial hot working techniques. Closed die forging of complex geometries is no exception to this and generates highly non-linear, heterogeneous strain histories throughout the component, which have been shown to have significant effects on the microstructural evolution.

This study has been conducted with assistance from Firth-Rixson Ltd (Darley Dale division), Timet UK Ltd and the Engineering and Physical Science Research Council (EPSRC) by providing industrial operating parameters, test material and financial support respectively.

1

1.2. Laboratory simulation

The relevance of titanium alloys to aeroengine construction is detailed above and highlights why and how more advanced alloys have been developed. Due to the complex deformation nature of near net closed die forging extensive validation work of all finite element (FE) models was undertaken to prove the accuracy of their output. Parallel work has been conducted on the custom manufactured arbitrary strain path machine, the second generation of such a machine acquired by the IMMEPTUS at University of Sheffield, which is capable of hot deformation testing by both axial and torsional displacements. This project was the first of its kind to utilise not only 'classical' strain path tests (forward-reverse torsion) but also simultaneous multi-axial deformations carried out at high strain rates, and so a large section of this work focuses on the calibration of the ASPII machine to enable accurate reproduction of the strain path deformations calculated by the FE software.

1.3. Project Aim

To investigate the magnitude of strain paths imposed during the hot forging of aero-engine compressors using FE modelling and devise a method for their reproduction in the laboratory and subsequently analyse the microstructural evolution.

1.4. Project Objectives

- Using commercially available FE code develop a model accurately depicting the industrial forging of a complex aero-engine compressor disc and extract strain path histories for several points within the material.
- Utilising the relatively new and un-optimised arbitrary strain path (ASPII) machine the work will devise a method to accurately reproduce the industrial forging route within the laboratory and replay the calculated strain path history. Through this work the machine will under go PID (proportional-integral-derivative) controller tuning to enable such testing to be carried out.
- Using optical metallography and image analysis techniques the microstructure of the thermomechanical processed materials will be analysed in order to determine the effects of strain path changes.

2

1.5. Thesis outline

The following thesis documents the achievement of the said aims using the said objectives and is structured in the following way;

Chapter 2 will introduce the relevant background investigations and theory conducted on the major issues of this work. This includes titanium alloys and their metallurgy, dwell fatigue, electron backscatter diffraction (EBSD) analysis and the issue and definition of strain path. This chapter aims to identifying the state of the relevant science and gain an understanding and appreciation of the field. The research methodologies utilised in this work will be introduced and their use in previous works will be reviewed.

Chapter 3 details the material properties used in all modelling work. Firstly the flow behaviour of Timetal-834 (at temperatures of 950, 990 and 1030 °C and strain rates of 0.2, 2 and 20s^{-1}) is derived and plotted. The flow equations utilized in the FE code are also derived and presented. The thermo-physical properties of alloys similar to Timetal-834 are plotted over a temperature range of 273 – 1600 K.

Chapter 4 describes in detail the experimental techniques used in this work. This chapter will initially introduce the axisymetric FE modelling undertaken to assess various model input parameters to evaluate their effect on model outputs and includes various environmental heat transfer coefficients, friction coefficients and material thermo-physical properties. Utilising results from these earlier models more complex modelling of the strain path specimens and a two stage industrial forging process are then introduced. Following this, the ASPII machine is presented and the methods used to carry out calibrations are explained. Derivation of various mechanical testing parameters is presented based on a von Mises yield criteria together with a system to evaluate equivalent stress/strains in torsional deformations that are independent to strain and strain rate hardening parameters. The 'simple' and 'complex' strain path tests carried out under various different test conditions are shown. This section finishes by elaborating on the methods used to prepare metallographic samples and carry out optical and electron back scatter diffraction analyses.

Chapter 5 details all the results gained during the completion of this thesis. Such results include the validation of the FE models and assessing how sensitive their output is to changes in key process parameters, many of which are difficult to calculate and measure. The simulation of the industrial forging process is also presented in detail, along with the calculated strain path changes for three different points within the forging stock.

3

Following the modelling work, extensive calibration of the ASPII's systems is shown, including calibration of the heating system, actuator displacements and elimination of machine noise. The starting microstructure, texture, chemistry and effects on alpha case formation are presented before the outcome of multiple 'simple' and 'industrial' strain path tests are revealed. These are investigated with optical and EBSD analysis that is presented in orientation image maps (OIM), inverse pole figure (IPF) and pole figure plots.

Chapter 6 presents the conclusions, summaries and key points raised by this work.

Chapter 7 suggests, based on the work completed in Chapters 2-6, further work to be carried out that would be of scientific interest but fell outside the scope and/or time range of this presented thesis.

2. Literature survey

2.1. Introduction

This section will introduce why titanium is so widely used in many industries, especially the aerospace industry. A brief overview of where titanium is found on aircraft is given together with the types of alloys chosen to fulfil particular design criteria. Special attention is given to the high temperature alloys, their microstructural design and thermomechanical processing.

The versatility of titanium and its alloys has led to its exploitation and development in a wide range of industries and applications. Examples include the aerospace, chemical, automotive, architectural, medical, fashion, sports, and marine industries. The most important sector is the aerospace industry, where titanium can be utilised extensively throughout the entire structure of an aircraft due to its low density, large operating temperature window and tailorable mechanical properties. This is especially true for military aircraft, where cost is not such a pressing design issue as it is in civil aircraft. Titanium's low density combined with its high strength plays a critical role in its selection, where weight is a prime design criterion. For example an all titanium aero-engine compressor rotor can save 20% total weight over a hybrid titanium/nickel assembly [1]. Such a replacement would also eliminate additional problems such as thermal expansion and modulus mismatches that can generate considerable stresses, and in extreme cases lead to the failure of a component.

Although alloys such as aluminium and magnesium can be utilised to produce a light structure, their relatively low yield strengths (typically between 120 MPa – 500 MPa) and elastic moduli (45 – 79 GPa) result in somewhat large component sections. For components with volume constraints, such alloys cannot be utilised. An excellent example of this, is the landing gear beams on the Boeing 747 and 757 which are some of the largest β-titanium forgings produced [2] and are shown below.
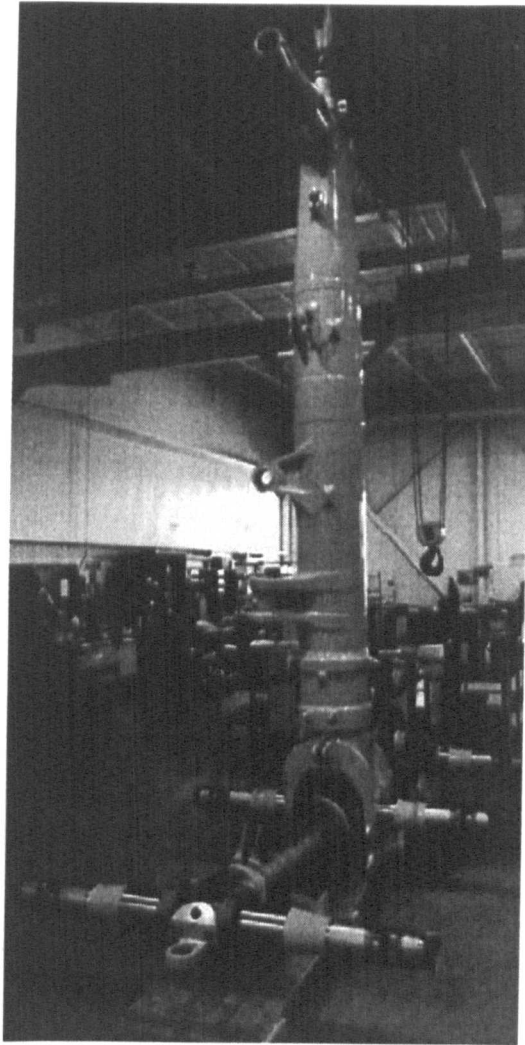
Figure 2.1 Landing gear assembly from a Boeing 747[3]

Corrosion resistance can be a key design feature, and is one where titanium excels. This can be attributed to its highly adherent, non-porous, stable oxide which protects the base metal from a number of aggressive environments up to temperatures as high as ~ 600 °C [4]. Titanium's high corrosion resistance is demonstrated in its use in chemically aggressive environments, for example hydraulic fluid tubes [2] and in salt water conditions. Not only does the oxide protect the metal in a corrosive and oxidising environment, but also when the metal is in direct contact with a material of higher electro-potential, which could generate a galvanic corrosion cell. Thus titanium is able to come into direct contact with carbon fibre composites, which have a tendency to corrode untreated metals such as steel, magnesium, and aluminium. This will become increasingly important in the future of the airspace industry as more polymer matrix composites (PMC) are being utilised throughout aircraft structures. Titanium's low thermal expansion coefficient (α_T) also permits it to be coupled with PMC materials at relatively high temperatures. In such conditions thermal expansion mismatch can cause joint failure due to significant thermal stresses being generated with metals such as

aluminium or magnesium alloys having relatively high α_T of approximately 26 & 24 μm/mK, respectively [5].

Titanium alloys also demonstrate wide operating temperatures ranging from cryogenic temperatures to approximately 600 °C. Titanium does not exhibit any significant decreases in ductility caused by thermal retardation of dislocation movement at low temperatures unlike some steels which can exhibit a ductile to brittle transition temperature. For further increases in low temperature performance alloys of greater purity are available. Such alloys are known as extra low interstitial (ELI) grades which contain highly controlled and very small percentages of interstitial atoms such as nitrogen, hydrogen and oxygen. The effects on the yield strength (σ_y), ultimate tensile (σ_{ut}) strength and fracture toughness can be seen it Table 2.1.

Table 2.1 Affects of interstitial elements on the fracture toughness of two titanium 6Al-4V grades

	σ_y (MPa)	σ_{ut} (MPa)	Elongation (%)	K_{1c} (MPam$^{-3/2}$)
Ti 6Al-4V	830	900	10	70
Ti 6Al-4V ELI	860	860	10	95

In the early days of aviation it was believed that titanium would outperform iron and nickel alloys in high temperature operations because of its low density and high melting point (Ti$_{mp}$-1660 °C, Fe$_{mp}$-1620 °C, Ni$_{mp}$-1453 °C) [4]. However, high temperature titanium alloys have been hampered due to high β-phase diffusion rates and poor oxidation resistance above 600 °C as the base material is able to absorb its own (protective) oxide layer at the surface. With a volume fraction of approximately 40% [6] titanium alloys are one of the three major metals used in the highly demanding environment of aero-engines. Nickel (~40%) and steel (~20%) alloys comprise the remainder of the hotter and highly stressed regions, respectively. The development of more advanced alloys and manufacturing techniques i.e. metal matrix composite (MMC) materials may enable the more widespread use of titanium within the gas turbine. Examples of this include an all titanium final stage compression section and engine shafts [7] replacing nickel and steel respectively. The increase in titanium operating temperature capabilities is shown in Figure 2.2. Here the x-axis has no value as the alloy numbers are not presented by the year in which they are created.

7
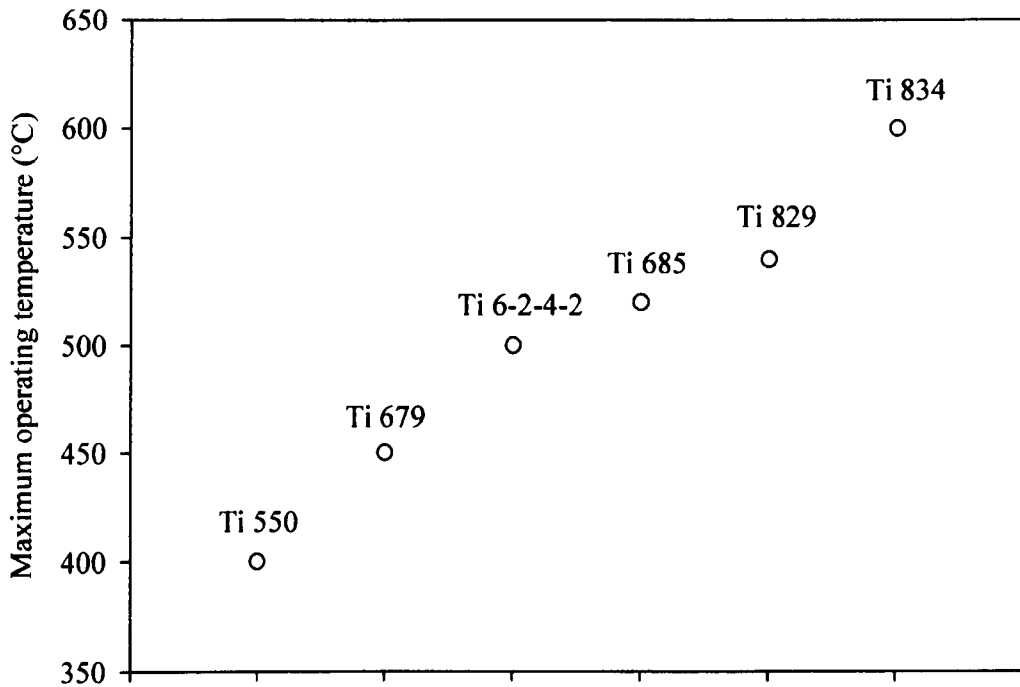
Figure 2.2 Plot showing the increase in maximum operating temperatures for various Timetal alloys. Adapted from D.F. Neal [4]

An ideal aero-engine in its simplest terms is a heat engine so by increasing the burning temperature it is possible to raise the thermal efficiency. This however must be matched by an increase in pressure ratio. Figure 2.3 below shows thermal efficiency evaluated with constant gas properties. The coloured contour line represents the efficiency level that range from 40% (red) to 64% (blue) in 1% divisions. From Figure 2.3 it can been seen that just increasing the turbine burn temperature does not result in an increase in thermal efficiency. Kurzke [8] shows that in general for a perfect gas the achievable thermal efficiency increases with turbine burner temperature. This however must be matched by an increase in the (compressor) pressure ratio as more air is required in the combustion chamber to raise the burn temperature.
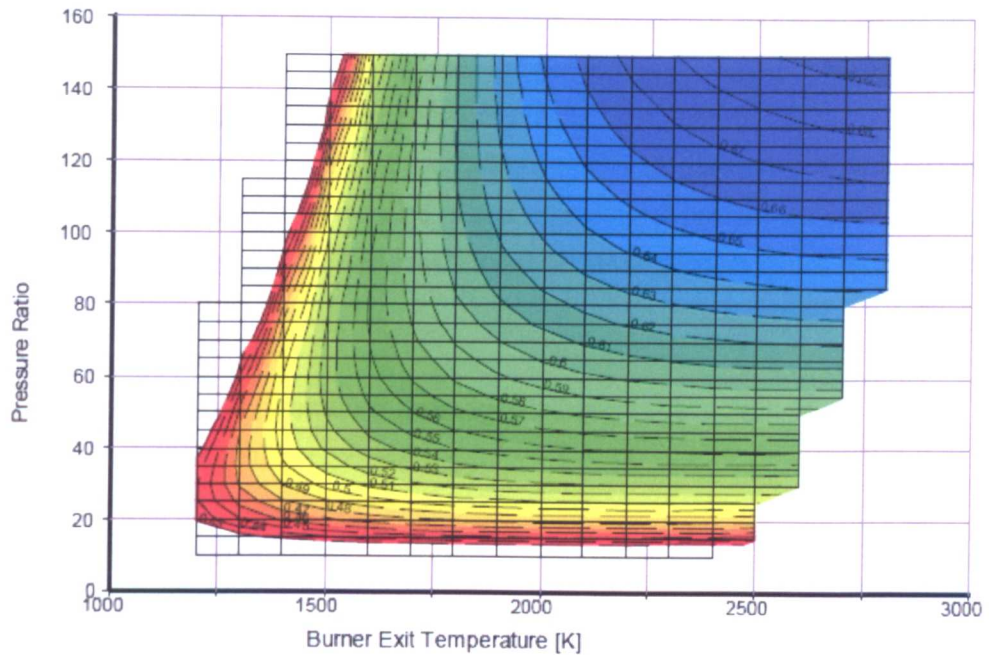
Figure 2.3 Thermal efficiency evaluated with constant gas properties [8]

These high compression ratios produce substantial temperature increases due to adiabatic heating of the compressed air and have increased the final high pressure compressor stage operating temperatures up to approximately 650 °C presenting problems for conventional titanium alloys. As a result there has been stiff competition between advanced titanium and nickel alloys as suitable materials for rotating disc components which are simultaneously subjected to high mechanical loads (including creep, impact and fatigue) and temperatures which vary greatly across the cross section of the disc [9]. The high partial pressure, temperatures and rubbing loads on blades in operation also calls for a suitable material to combine acceptable levels of burn resistance to prevent the possibility of a titanium fire within the engine [2,10,11] which can have catastrophic consequences within seconds [11]. Thus, the allure of titanium's low density has led to extensive research into existing and new alloys, to improve aero-engine performance and reduce overall aircraft structural weight.

2.2. Classification of titanium alloys

Pure titanium is an allotropic metal, with an hexagonal close packed (HCP) crystal structure (α phase) at low temperatures and a high temperature body centred cubic (BCC) phase (β) above 882 °C. The β phase then remains stable up to the melting point at 1670 ± 10 °C [12]. Titanium is a transition metal with an incomplete electron shell which enables it to form extensive solid solutions with most substitution elements having a size factor within ± 20% of itself. It is also a highly reactive element and has a high affinity for small interstitial atoms including oxygen, nitrogen and hydrogen. It

9

does however possess a highly adherent and nonporous oxide scale which forms instantly on exposure to an oxidising atmosphere and is responsible for a high corrosion resistant up to moderately high temperatures.

Alloying elements that affect the phase fields are divided into groups which stabilise the α or β-phase, or are considered to be phase neutral and are shown in Figure 2.4. As a result, different alloys are distinguished by their predominant room temperature phase or phases.

Such alloy groups include:

- o Alpha alloys (including near alpha alloys)
- o Alpha/Beta alloys
- o Beta alloys (including metastable beta)
- o Titanium aluminides

The titanium aluminides will not be discussed in this report as their application is still rather limited due to a lack of ductility, especially at ambient temperatures.
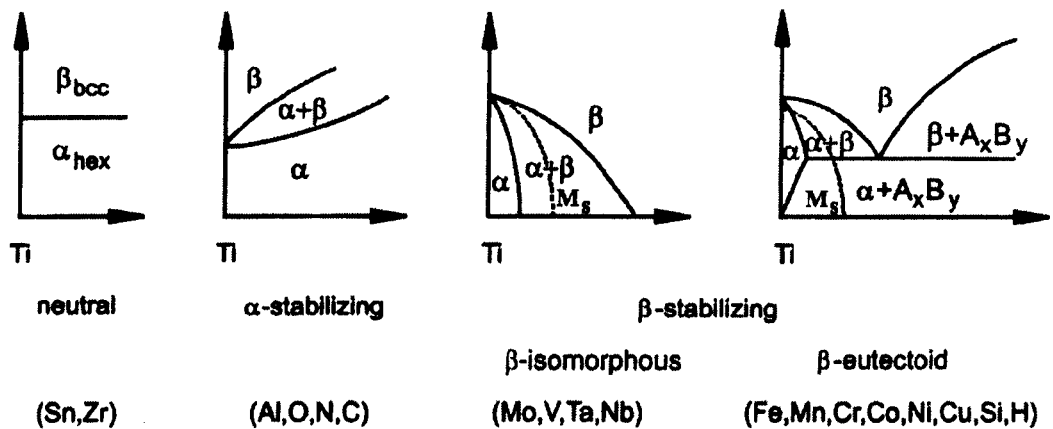
Figure 2.4 Basic types of phase diagrams for alpha and beta stabilising elements [13]

2.2.1. Alpha alloys & Near Alpha alloys

Alpha alloys can be additionally subdivided into three groups; fully alpha alloys such as commercially pure (CP) alloys, near alpha alloys which contain up to 2% beta phase and age hardening alloys. The CP alloys contain closely controlled minor additions of oxygen and nitrogen which are generally in the form of impurities. Such elements provide substantial interstitial hardening, which in turn reduces ductility and toughness. The extent to which these atoms increase the strength of an alloy (especially nitrogen) can be seen below in Equation 2.1. CP alloys display reasonably moderate tensile strength (240-600 MPa) and are comparable to annealed 300 series stainless steel [2]. They demonstrate good formability and ductility when compared with other HCP metals such as magnesium and are generally utilised in low to moderately stressed

components required for high corrosion resistance. An example of this is in aircraft toilet systems.

Fully alpha alloys may also contain additional alpha stabilising elements such as Al, O, N, and C. Both types of alloy exhibit excellent corrosion resistance and are not heat treatable, and thus are readably weldable. Because of mechanical property retention and creep resistance at high temperatures α alloys are employed for elevated temperature operations. Such behaviour can be attributed to the α-phase having a lower diffusion coefficient, especially at higher temperatures as shown below in Table 2.2.

Table 2.2 Coefficients of self-diffusion in titanium (m^2s^{-1}) [13]

$D_\alpha (500 \ ^\circ C)$	$\sim 10^{-19}$
$D_\beta (500 \ ^\circ C)$	$\sim 10^{-18}$
$D_\alpha (1000 \ ^\circ C)$	$\sim 10^{-15}$
$D_\beta (1000 \ ^\circ C)$	$\sim 10^{-13}$

The practical limit of the amount of alpha stabilising elements that can be added to titanium before embrittlement of the alloy occurs is in the order of 9 wt % 'aluminium equivalent' [12]. Equations describing the aluminium and molybdenum equivalent for various stabilising elements are shown below in Equation 2.1 and 2.2.

$$Al_{equiv} = Al + \frac{1}{3} Sn + \frac{1}{6} Zr + 10(O + C + 2N) \qquad (2.1)$$

$$Mo_{equiv} = Mo + \frac{2}{3} V + \frac{11}{25} W + \frac{7}{25} Nb + \frac{1}{5} Ta + 3Fe + \frac{8}{5} Cr - Al \qquad (2.2)$$

After this threshold an ordering reaction occurs and a HCP α_2 phase typical of the composition Ti$_3$X is precipitated. In the Ti-Al system the aging of alloys with 5-6% aluminium can lead to the formation of finely dispersed coherent α_2 [14]. Continual ageing causes coarsening of this phase and work carried out by Williams et al. [14] shows that these precipitates have a significant effect on the slip character of Ti-Al single crystals. In other systems such as Ti-Sn and more complex compositions the α - α_2 misfit is larger and as a result nucleation of α_2 becomes more difficult and tends to be more heterogeneous. This non-uniform distribution has a less detrimental effect on ductility of the material. Within the Ti-Cu system it was noted that the titanium rich region of the alloy system offered potential for an alloy that may respond to age-hardening. The solubility of copper within α-titanium reduces from 2.1% to 0.7% to very low levels for temperatures of 798 °C (eutectoid temperature), 600 °C and room

temperature respectively. Furthermore, such an alloy can be cold worked in the solution treated state and subsequently aged. An alloy of composition Ti-2.5Cu (IMI 230) was developed and solution treated at 805 °C and followed by oil quenching (OQ). A double aging at 400 and 475 °C promotes precipitation of fine metastable Ti_2Cu phase that is coherent with the β matrix, increasing strength but reducing ductility

The final class of alloy, near alpha, has small additions of beta stabilising elements to enhance the processing abilities and to allow manipulation of microstructure and hence the mechanical properties of a particular alloy. Such alloys possess higher room temperature tensile strengths than fully-α alloys and show the greatest creep resistance of all titanium alloys (excluding titanium aluminides) [2]. These near alpha alloys typically contain approximately 2% β phase stabilisers to improve forgeability and facilitate microstructural manipulation.

2.2.1.1. Timetal®834

Timetal®834 (previously know as IMI834) is a near alpha alloy and is currently the most advanced high temperature titanium alloy to date being able to operate for prolonged periods of time at temperatures of 600 °C. The in-service microstructure consists of approximately 15% primary alpha phase (α_P) within a matrix of large grained transformed secondary alpha-phase (α_S) which is transformed from the more readily deformable β-phase when the metal is hot worked in the α/β phase field. The α_S phase displays the classic Widmanstätten structure when air cooled (show in Figure 2.5) where the lath width is dependant upon the cooling rate applied. On oil or water quenching the Widmanstätten structure is replaced by a non-hardening (when compared to the classic steel martensitic transformation) martensitic structure. The resulting microstructure results in a combination of high creep resistance due to low α-phase diffusion rates and high cycle fatigue resistance due to fatigue crack energy absorption deflection at lath boundaries. Such a combination of properties makes Timetal®834 an ideal material for compressor disc applications where high stresses operate towards the centre of the component due to high centrifugal forces generated by high rotation speeds and high temperatures that are generated towards the rim of the disc by hot compressed air passing over the compressor blades [9].

12
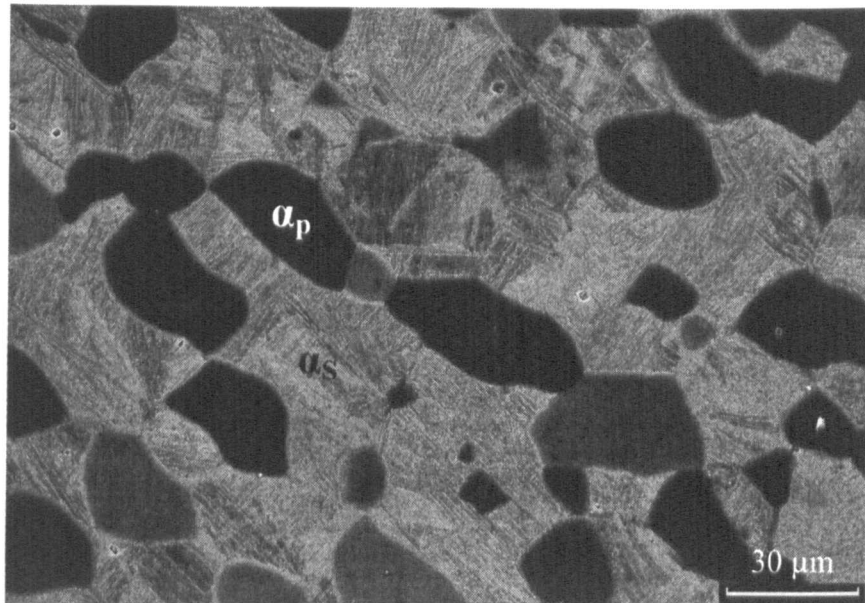
Figure 2.5 Micrograph showing the both the α_S and α_P phases of heat-treated and air cooled Timetal®834

After initial primary ingot break down of the initial vacuum arc remelted (VAR) ingot by the titanium producer to generate a specified microstructure, billet size and cross-section, secondary industrial processing is carried out to shape the material and produce the required microstructure for desired mechanical properties. At Firth-Rixson, Darley Dale the typical forging process for a Timetal®834 billet consists of:

The forming operation; typically hot closed die forging to create a component's geometrical shape*. This may include several forging blows in a variety of different shaped dies and furnace reheats of the workpiece material

⇩

Air cool to room temperature

⇩

Solution treat for 2 hours at 1015 °C and oil quench** to yield ~15 % α_P

⇩

13

Aged at 700 °C (high for titanium alloys) for 2 hours to stress relieve large sections and precipitate fine titanium silicides which improve creep resistance. This is followed by an air cool to room temperature

*This may not be the final components shape as typically more complex geometries are CNC machined into the component in the final manufacturing stages.

**OQ to impose a cooling rate in the region of 100 °C/min again to optimise both creep and fatigue properties [4].

The alloy chemistry of Timetal®834 has been tailored based on earlier alloys such as IMI 679 and IMI685 and is shown below in Table 2.3. The relatively large amount of α-stabilising (aluminium and zirconium) elements has been added together with the phase neutral tin for maximum solid solution hardening. The tin and zirconium provide greater hot strength than just the aluminium [4,12] whilst reducing the tendency for the precipitation of the Ti_3X phase which can lead to reductions in ductility. Using Equation 2.1 the aluminium equivalent of Timetal-843 is seen to be high at 9.53 and contributes to its high temperature strength. The levels of tin are limited by the reduction in weldability and increases in density compared with aluminium additions [4]. Weldability is required for the joining of the compressor blades to the compressor disc.

Table 2.3 Chemical composition of Timetal®834

ELEMENT	WEIGHT%	
	Min.	*Max.*
Aluminium	5.50	6.10
Tin	3.00	5.00
Zirconium	3.00	5.00
Niobium	0.70	1.00
Molybdenum	0.25	0.75
Silicon	0.20	0.60
Carbon	0.04	0.08
Iron	---	0.05
Oxygen	0.075	0.15
Nitrogen	---	0.03
Hydrogen	---	0.006
Residual Elements, each	---	0.05
Residual Elements, total	---	0.20
Titanium	Remainder	

14

Additions of molybdenum and niobium (β-stabiliser) were included as they are effective in improving low and high temperature strength without adversely effecting creep resistance. Once the solubility limit has been reached and β phase begins to form, creep resistance decreases so such additions are small. Molybdenum is less soluble than niobium in alpha titanium and as a result its quantities are less than that of niobium. Both these elements help mitigate against the ordering reaction by occupying some of the lattice sites normally occupied by the ordered aluminium [4] and so allow a more heavily alloyed material. Also, these high valence elements (e.g. Nb^{5+}) substitute the Ti^{4+} ions in the TiO_2 structure and reduce the number of anion vacancies and therefore reduce the oxygen diffusion rate [15] improving high temperature oxidation resistance. Small additions of silicon are added as this provides a major increase in creep resistance and static strength, and is also low in density and non-refractory. Figure 2.6 below shows how additions of silicon increase the creep resistance of titanium alloys, in this case Ti-6462S. The optimum level of 0.1% silicon is presumed to correspond to the limit of supersaturation in this alloy [12]. It has been shown that in Timetal®834 silicon causes precipitation of $(TiZr)_5(SiSn)_3$ (S_2 phase) which segregates at dislocations hindering their climb and likewise subsequent deformation [16].
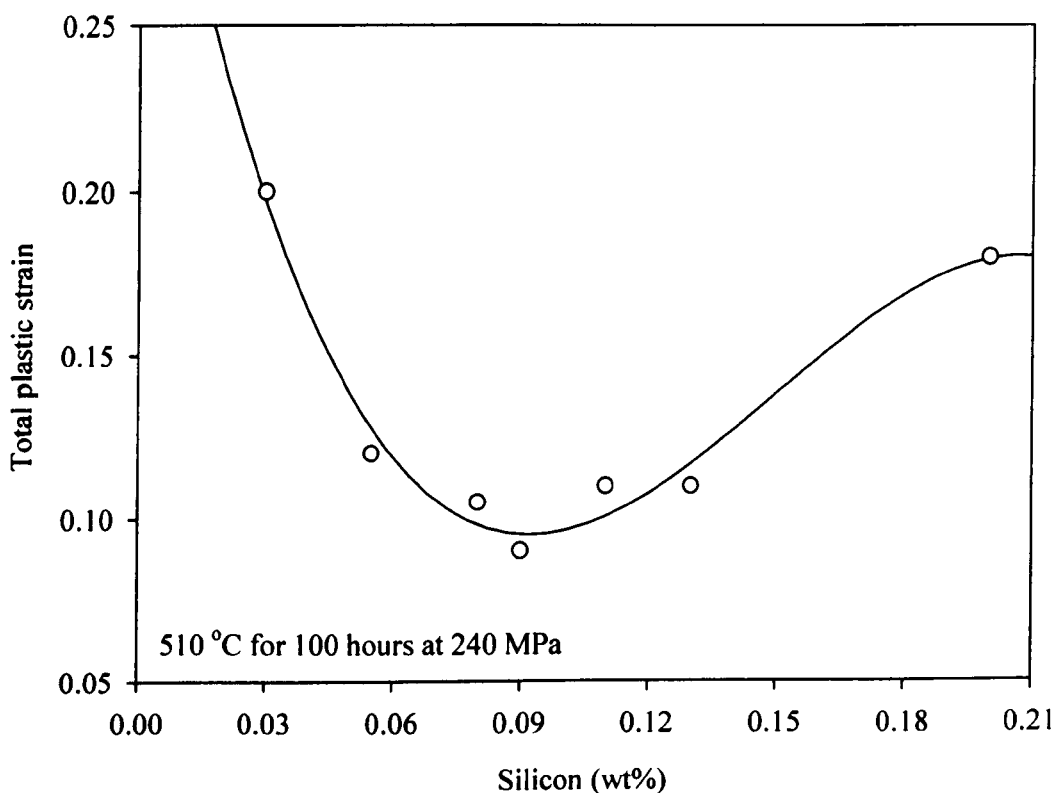
Figure 2.6 Effects of silicon additions on high temperature titanium alloy 6462. Graph reproduced from [12]

15

Carbon additions make Timetal®834 unique among the near alpha alloys as it has the effect of changing the shape of the β-transus approach curve and facilitates heat treatment but is also an α stabiliser and so does not compromise the creep optimised lean β phase composition. Being an α stabiliser carbon also has the added benefit of increasing the β transformation temperature, allowing α/β processing temperatures to be higher and lowers the working loads on tooling and machinery. Again carbon also increases strength significantly and so is important in an engine over speed situation. The effects of the carbon additions on the beta approach curve can be seen below in Figure 2.7 where IMI 829 has almost identical alloy composition compared with Timetal®834 except it has no carbon additions. The resulting effect produces an alloy that can be hot worked with a desired microstructure as the temperature range to produce that microstructure, in this case between 10-20% primary α phase, is in a wide temperature window making it easier to produce in industry.
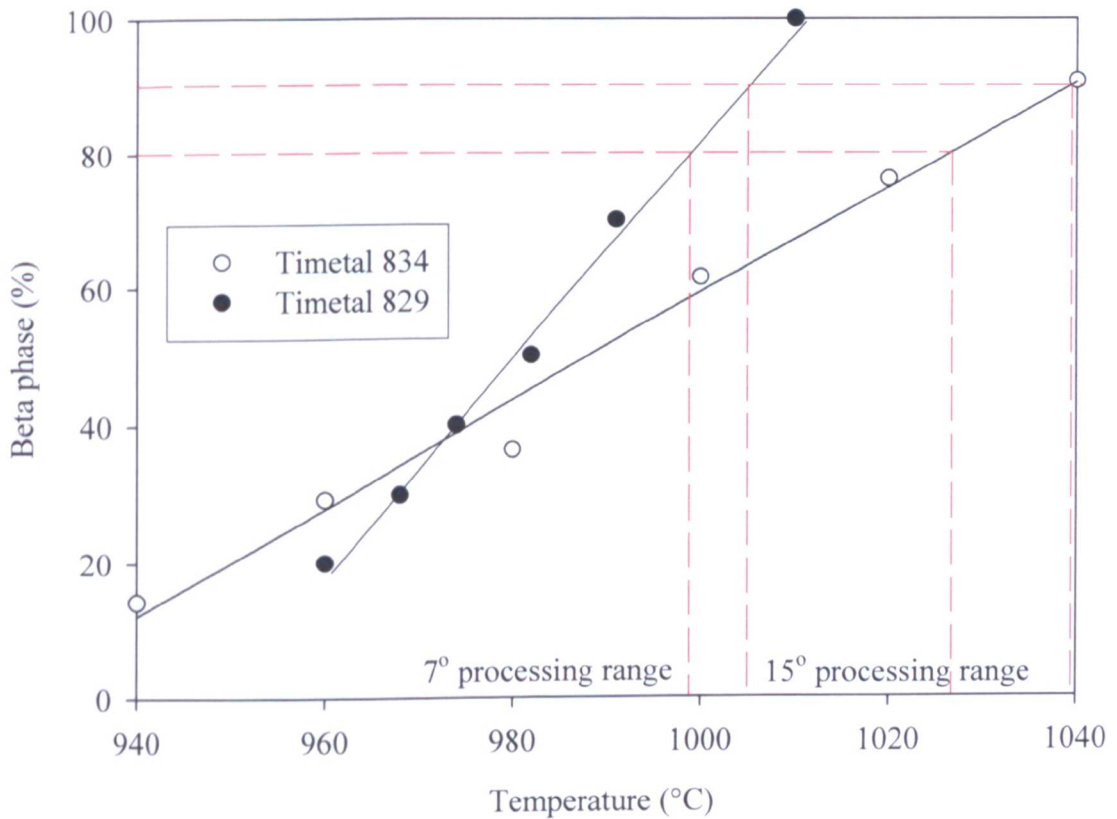
Figure 2.7 Shallow beta approach curve enables practical industrial temperature control. Timetal 829 data taken from Polmear [12]

The remaining elements; Fe, Ni, O and N are generally considered to be detrimental to the alloy and as a result are kept to a minimum. Iron and nickel both degrade creep and stability of titanium alloys. Oxygen & nitrogen are both strong alpha stabilising elements and have considerable solubility in the α & β phases. Although the solid solution strengthening of these elements is quite potent they reduce ductility, offer no improvement in high temperature creep resistance and rapidly lose their strengthening capacity above ~ 200 °C.

Typical forging temperatures are in the region of 980-1030 °C as dictated by the desired optimisation of both fatigue and creep performance. Work by Daeubler *et al.* [1] has shown that these conditions are reached when the volume fraction of the primary alpha phase is between 15-20% as shown schematically in Figure 2.8(b). Although a large grain size is desirable for creep resistant the primary alpha grains help to pin the beta grains during forging and thus prevent excessive grain growth.
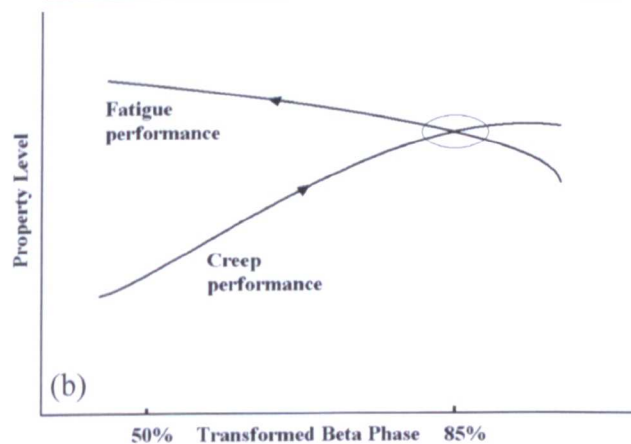
Figure 2.8(a) Hot closed die forging of a titanium alloy (b) Schematic optimal fatigue-creep properties for Timetal®834

The final mechanical properties for heat-treated Timetal®834 as a function of service temperature can be seen below in Figure 2.9.
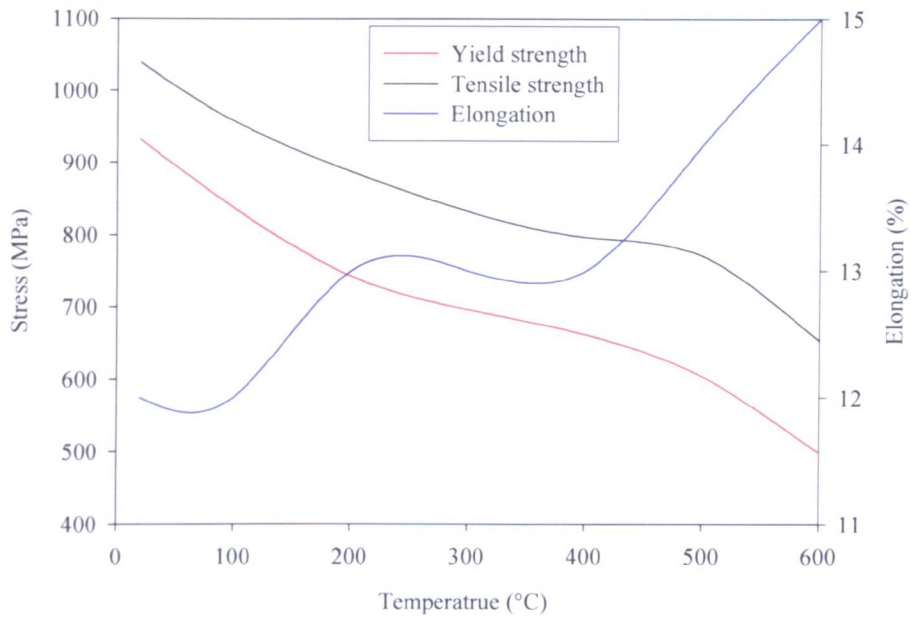
Figure 2.9 Mechanical properties of Timetal®834 as a function of service temperature. Adapted from [17]

2.2.1.1.1. Dwell fatigue

The safety conscious aerospace industry is very conservative when designing components and utilising new materials. One design criteria focuses on component fatigue life prediction techniques. Future developments and improvements in such techniques require knowledge of the underlying science and mechanisms in operation during the lifecycle of a component. In titanium alloys, however, early fatigue crack initiation due to crystallographic effects (e.g. premature cracking along unfavourably orientated crystallographic planes) hampers efficient design and more worryingly significantly reduces low cyclic fatigue (LCF) and can lead to catastrophic component failure [18]. Figure 2.10 shows the effect on fatigue life of a 2 minute dwell (held at overload stress) on Timetal®834 samples machined from 30 diameter bar stock and forged compressor disc material. The fatigue resistance of the disc material is less than that of the bar stock. However, there is a more profound difference between the two materials after the dwell period. There is a very small reduction for the bar stock which could even be within the region of experimental error.
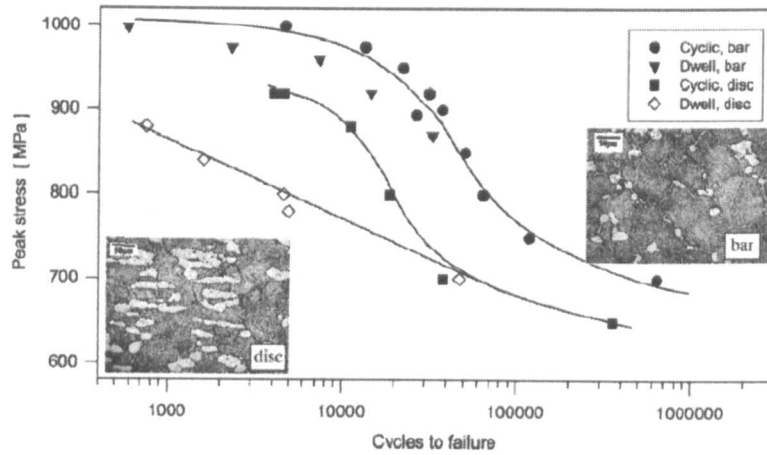
Figure 2.10 Cyclic and dwell fatigue response of Timetal® 834 bar and forged disc stock [19]

However, for the disc material there is a pronounced drop in the fatigue life up to a cyclic stress value of ~700 MPa. It must be noted that from Figure 2.10 there is difference in microstructure of the disc and bar material. It is also not clear where the disc material is machined from within the disc or whether the grains in the rolled bar material are aligned preferentially with respect to the axis of loading for the fatigue testing. Such dwell conditions are experienced during take off and landing of an aircraft when the engines undergo over-speed loading due to the required high acceleration and deceleration of the aircraft. Bache [19] notes that the role of interstitial elements (H, N and O) on the stress-strain response of titanium is quite pronounced and well studied. Although higher concentrations of interstitial atoms increases yield and tensile strengths, ductility is reduced due to brittle hydride formation through time dependant diffusion of hydrogen influenced by a hydrostatic stress field. This has been proposed as a reason for dwell fatigue. However the exact role of hydrides is unknown as precipitating hydrides are very difficult to detect and are only visible through transmission electron microscopy (TEM) analysis as shown in figure 2.11.
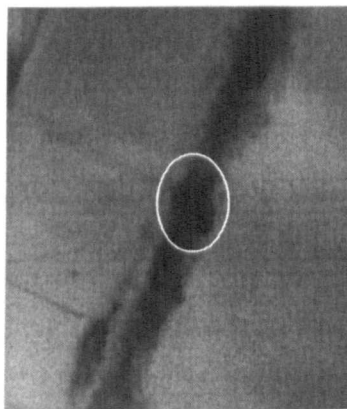
Figure 2.11 Hydride precipitate formed on a prior beta grain lath in ring rolled and heat-treated Timetal®834

19

Work by Bache [19] also shows that high levels of hydrogen do have an adverse effect on the fatigue performance of IMI685 but also shows that the effect is still present in alloys containing hydrogen levels heat-treated to levels below 10ppm. Although evidence seams to show that hydride precipitation does not play a major role in the phenomena of dwell fatigue it appears to play a more subsidiary role in the plastic deformation and dislocation motion.

The anisotropy of the titanium crystal with respect to the crystal axes is well documented and varies from 145 to 100 GPa in the c and a-axis direction respectively [12]. The typical elastic modulus of 120 GPa generally quote for titanium is measured from polycrystalline material with no texture component. However, the probability of two neighbouring grains possessing different elastic moduli is high. Plastic deformation is also an anisotropic mechanism in the titanium HCP crystal and more easily accommodated by slip on the basal plane. This is discussed in more depth in section 2.3.3. The dislocation pile up model proposed by Stroh [20] relates slip within a favourably orientated 'weak' grain with its basal axis inclined to the applied tensile load induces a pile up at the boundary of a neighbouring grain. This in turn induces shear stress in the 'strong' grain and instigates the formation of a slip band which forms the nucleus for a fatigue crack under the cyclic loading [19]. This is represented in Figure 2.12(a) below. Bache [19] also proposes and alternative 'two element' model to describe the affects of this microscopic anisotropy on the deformation of titanium alloys. This is shown schematically in Figure 2.12(b).
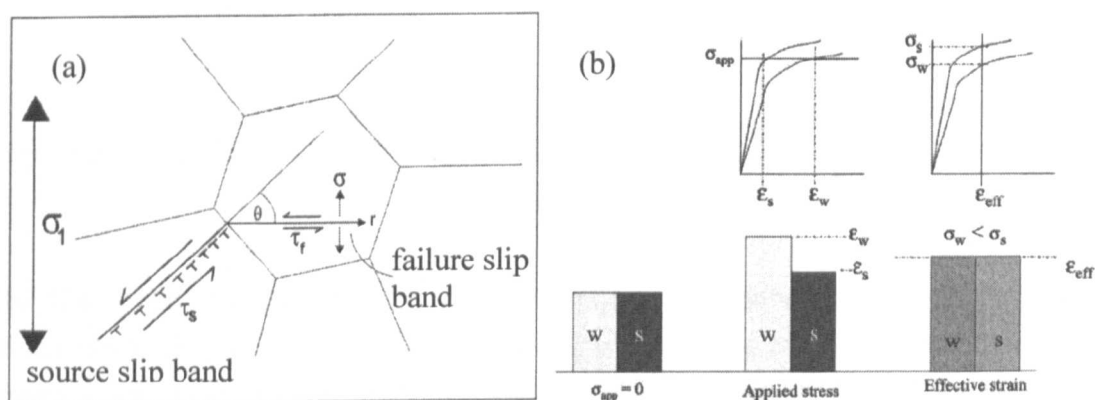
Figure 2.12 (a) Schematic of slip band model to describe quasi cleavage facets formed on basal planes in titanium alloys [21] and, (b) schematic two element model describing stress redistribution between grains [19]

Initially, a weak grain (for example where the basal plane is angled at 45° to the tensile axis) sits beside a strong grain. W and S designate weak and strong respectively. One assumption is that of fixed applied stress where the difference in elastic moduli of each grain causes the grains to elongate to different values of strain ε_w and ε_s. In reality grains are constrained by the material and will achieve the same value of effective

strain ε_{eff}. Consequently, despite the global fixed stress applied a fixed strain condition is imposed on the individual grains and hence the stronger grain accommodates a larger value of stress. Thus, the weaker grain transfers stress onto the stronger grain which eventually fails through cyclic loading.

Bache also shows [21] the similarity between the α/β processed Timetal®834 and it's predecessors, the β processed Timetal 685 and 829 alloys. Figure 2.13 below shows the room temperature LCF behaviour of Timetal 685, 829, 834 and Ti 6246 together with the effects of a 2 minute dwell period. A normalised stress criterion (applied stress divided by the ultimate tensile strength) is used to account for the differences in strengths between the alloys. This plot also shows the effects of morphology and specimen geometry on the LCF performance of Timetal 685.
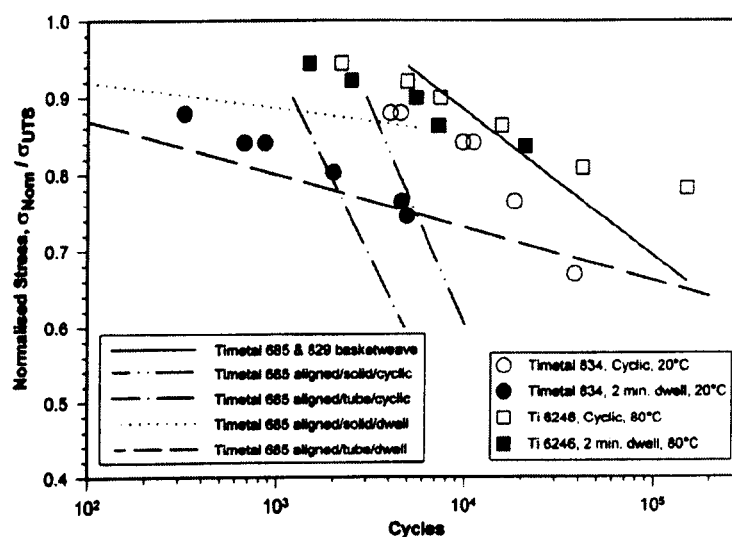
Figure 2.13 Combined LCF data for the alloys Timetal 685, 829 and 834 together with Ti 6426 [21]

The Ti 6246 alloy demonstrates superior performance compared to the cyclic behaviour of the other alloys. This is achieved through processing above the beta transus to ensure a random orientated, relatively fine grained structure with a small percentage of retained primary α grains i.e. the microstructure is almost fully transformed and contains the BCC β phase which minimises the local grain to grain anisotropy.

In addition to this localised stress transfer effect the LCF performance problem is magnified by Timetal®834 billet material containing regions (also referred to as clusters) of similarly orientated primary alpha grains as reported by several different authors [22-25]. Figure 2.14 taken from Germain *et al.* [22] shows how large these clusters can be with the red colour representing basal planes orientated parallel to the viewing direction. Here long fibres of similarly orientated grains can be seen throughout the whole 6mm of the horizontal scan direction. The exact size and morphology of such clusters is dependant on the direction in which they are viewed

21

with respect to the billet axis and the thermomechanical processing carried out on the billet.
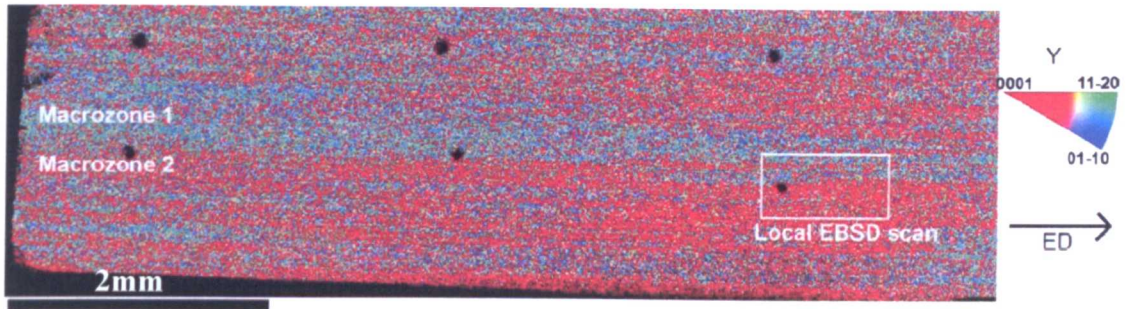
Figure 2.14 Low magnification IPF map of the reference sample revealing sharp texture heterogeneities [22]

Dwell fatigue work carried out by Bache *et al.* [26] utilised EBSD to measure the orientation of fracture facets within IMI685 and IMI834 (Timetal®834). It was seen that fatigue failure is initiated sub-surface and at the origin of these sites facets occur in both alloys. Figure 2.15(a) shows these facets at the initiation site in Timetal®834 and Figure 2.15(b) is the corresponding inverse pole figure for EBSD measurements taken on the facets.
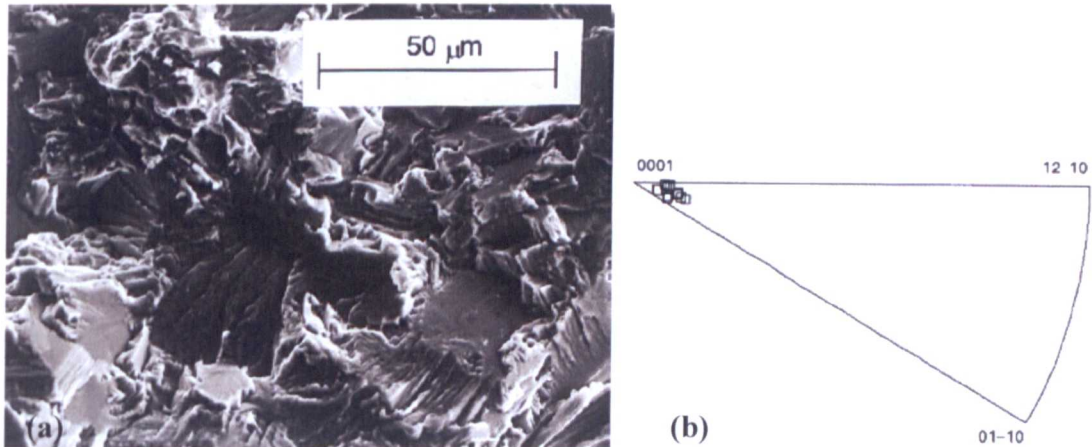
Figure 2.15(a) Facets at the initiation site in Timetal®834 and (b), inverse pole figure for EBSD measurements taken of the fracture site facets [26]

This pole figure clearly shows the basal orientation of the facets. This highlights that if the basal plane is where accumulative fatigue damage is occurring, combined with the large clusters of similarly orientated primary alpha grains, then titanium components potentially contain large 'critical flaws' (on the millimetre scale) that will only manifest themselves in service and so will be very difficult to identify through non-destructive testing (NDT). Thus, for Timetal®834 to be successfully utilised to its full potential a

thermomechanical process route is required that will minimise local grain damage due to anisotropy effects and break up the clusters of primary alpha grains which are believed to be inherited from the large columnar grains generated by the VAR process.

2.2.2. Alpha/Beta alloys

The strength of α alloys is limited by the formation of ordered intermetallic precipitates at high solute content, which in turn lead to the embrittlement of the alloy, especially when used operated at high temperature for substantial periods of time. This led to the development of α/β alloys which possess higher strengths and greater formability without the severe embrittlement observed in α alloys rich in alloying elements. Most α/β alloys contain both α and β stabilising elements with sufficient amounts of β stabilisers to allow substantial amounts of β to be retained at room temperature.

Today alloys such as Titanium-6Al-4V (IMI 318) dominate the aerospace market, accounting for over 50% of titanium sales [12]. The β-phase (BCC) as well as the higher β-phase field processing temperature allows greater formability of these alloys when compared with fully α-alloys. In addition to this, alloy strength and fracture toughness can be tailored accordingly by subsequent tempering or ageing to produce a desired microstructure, and thus mechanical properties. Where, in general a fine scale microstructure:

- Increases the strength and ductility by reducing effective slip length within a grain.
- Retards crack growth by providing an undulating crack growth path, absorbing energy.
- Allows superplastic forming, which in some cases can reduce manufacturing costs by 20-50%.

a coarse microstructure increases:

- Resistance to creep, since creep strain is inversely proportional to the square of the grain size.
- Resistance to fatigue crack initiation, resulting in improved LCF properties.

As the strength (and other mechanical properties) can be influenced by heat treatment, problems can arise in thick sections where titanium's low thermal conductivity can aggravate through-section temperatures and cooling rates, which greatly affects the resultant microstructure and final mechanical properties [12]. Solution treating and aged provides the greatest strengthening for Ti-6Al-4V alloys, however full hardenability is limited to approximately 25mm due to the afore mentioned thermal effects [2]. It must be stressed that the microstructure (and so resulting mechanical properties) depends highly on prior processing, and so close process control is required to ensure high-quality product control and consistency.

2.2.3.   Beta alloys

Such alloys are defined as those which contain enough β-stabilisers to ensure that a fully β-microstructure is retained at room temperature when the alloy is quenched from above the β-transus [12]. Alloys with sufficient β-stabilisers to lie between the martensite start-line and the β-transus line are referred to as metastable β-alloys (see Figure 2.16). Such alloys will precipitate a second phase (generally α) on ageing.
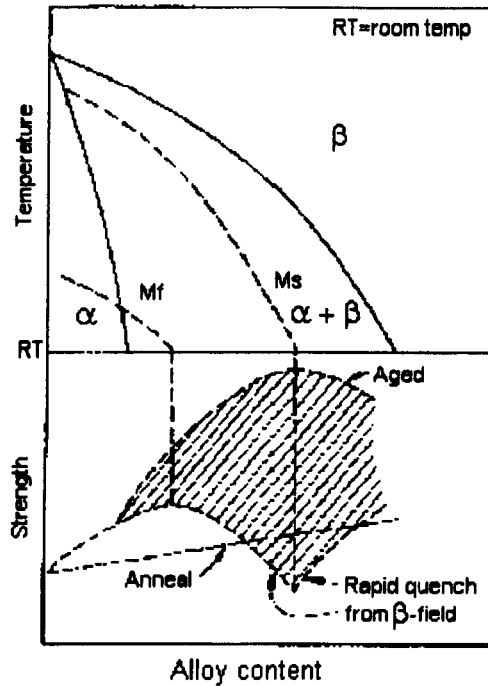
Figure 2.16 Heat treatment of β-isomorphous titanium alloys [12]

More highly alloyed compositions (to the right of the β-transus line) are known as stable β-alloys as these will not precipitate on ageing and are so non-hardenable.

The attraction of such alloys is their formability (which is higher over alpha titanium due to their BCC crystal structure) high strength, tailorable properties and high resistance to stress corrosion cracking. Various alloys can be cold rolled in a relatively soft condition and then strengthened by heat treatment. Some alloys can also be forged at lower temperatures, thus reducing operational and die costs [12]. High solute content increases the hardenability and may facilitate through-section hardening of large thicknesses. In addition to their favourable properties, the prior processing to produce a required microstructure is not as critical for such alloys as it is for mixed phase alloys. This can be attributed to the solution treatment usually being carried out above the β-transus temperature.

2.3. High temperature deformation and the strain path phenomenon

The principles of the hot working of metals have been known and utilised for many thousands of years. Annealing and hot working of hammer formed gold and silver has been traced back at least as far as 500 B.C, however, the scientific field of physical metallurgy is only a little over a century old [27]. Yet the knowledge gained of the mechanisms underpinning these complex processes has yielded significant improvements in the design of better materials and processing.

This section will introduce the important aspects of metallurgy and plastic deformation which are necessary to describe and analyse the strain path phenomenon. Plastic deformation of metals is reflected in the microstructure and texture, which in turn determines the mechanical behaviour. The plastic flow behaviour of metals is strongly dependant on temperature and strain rate and displays complex variations with strain, strain rate and temperature [28]. To understand the mechanisms operating during the (dual phase) hot working of titanium alloys the deformation mechanisms of both crystal structures are reported. Metals with a HCP crystal structure can exhibit pronounced anisotropic crystal plasticity. To add complexity the deformation mode in operation is also highly temperature dependant with more modes (e.g. dislocation climb) becoming active with increasing thermal energy.

The issue of strain path adds ever increasing intricacy to the field of plastic deformation. The final section of this chapter introduces the principle of strain path, the definition of the strain path angle, previous work conducted, typical strain path effects observed and attempts to model the effect of strain paths on microstructural evolution.

2.3.1. Deformation of metallic crystals

During pioneering work conducted by Von Laue in 1912 on the diffraction of x-rays by metallic crystals it was realised that metals were fundamentally composed of atoms arranged in specific geometric lattices [29]. Plasticity work by Ewing and Rosenhain [30,31] demonstrated that these lattices deform by sliding over one another along defined crystallographic planes called slip planes. The extent to which a single crystal slips under the influence of external loads is dependent on the geometry of the crystal and the orientation of the active slip planes with respect to the shearing stresses. Slip begins when the shear stress on the plane reaches a value of critical resolved shear stress, τ_0. The magnitude of the critical resolved shear stress of a crystal is determined by the interaction of its population of dislocations with each other and with other defects such as vacancies, interstitials and impurity atoms.
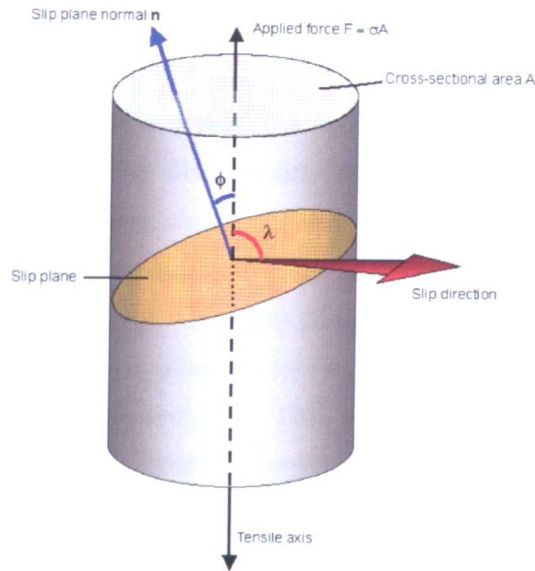
Figure 2.17 Resolved shear stress on a slip plane in a single crystal under applied tensile load (F)

By considering a cylindrical single crystal as shown in Figure 2.17 and defining the angle between the normal to the slip plane and the tensile axis as ϕ, and the angle which the slip direction makes with the tensile axis as λ. The area of the inclined slip plane will be $A/\cos\phi$ and the component of axial load acting in the slip plane is $P/\cos\lambda$. Therefore, the critical resolved shear stress is given by:

$$\tau_0 = \frac{P\cos\lambda}{A/\cos\phi} = \frac{P}{A}\cos\phi\cos\lambda \qquad (2.3)$$

Equation 2.3 gives the shear stress resolved on the slip plane in the slip direction. This shear stress is a maximum when both ϕ and λ are equal to 45°. If the tensile axis is normal or parallel to the slip plane (i.e. either λ or ϕ are equal to 90°) then the resolved shear stress will be zero and there will be no slip on these orientations. This behaviour, known as Schmid's law, is best demonstrated with HCP metals where the limited number of slip systems allows large differences in the orientation between the slip plane and tensile axis. The ratio of the critical resolved shear stress to the axial stress is known as the *Schmid factor m*. Crystals close to orientations where the resolved shear stress on the slip planes is close to zero tend to fracture rather than slip [32]. Such an effect could be a contributing factor to the dwell fatigue mechanisms operating in near alpha titanium alloys as discussed in Section 2.2.1.1.1.

26

2.3.2. Dislocations

The concept of dislocations in a crystalline solid was introduced by Polanyi, Orowan and Tayler in 1934 [33]. The dislocation represents a line defect or discontinuity between part of a crystal that has sheared and a part that has not, so deformation occurs by passage of such dislocations along the slip plane, and not by the unified shear over the whole crystal simultaneously. The slip plane can be divided into two regions, one where slip has occurred and the other which remains unslipped. Separating these two regions the structure will be dislocated. This boundary is referred to as a dislocation line or dislocation [34]. Three apparent simple properties of a dislocation are:

1. It is a line discontinuity
2. It forms a closed loop in the interior of the crystal or emerges at the surface
3. The difference in the amount of slip across the dislocation line is constant

The last property is the most important as a dislocation is characterised by the direction and magnitude of slip associated with it. This is called the Burgers vector *b*.

Some sections of the dislocation line can lie perpendicular to *b*, others parallel while the remainder are at an angle to *b*. Those dislocation lines that lie normal to the slip direction are known as edge dislocations. When the line is parallel to the slip direction the dislocation line is known as a screw dislocation. In reality dislocation lines are rarely pure edge or screw dislocations lines, but it is convenient to use these ideal dislocations as any dislocation can be resolved into edge and screw components [33].

During slip a dislocation moves through the crystal structure. The Peierls-Nabarro stress is required to move the dislocation from an equilibrium location to another. The shear stress to move the dislocation is given by equation 2.4:

$$\tau = c \exp(-kd / b) \tag{2.4}$$

The shear stress required to move the dislocation is τ, d is the interplanar spacing between adjacent slip planes, **b** is the Burgers vector and c and k are both material constants. Under applied stress a dislocation will move in a slip system that requires the least expenditure of energy. Equation 2.4 shows us that the stress required to move a dislocation increases exponentially with the length of the Burgers vector and so the likely slip direction will have a small repeat distance or high linear density. Additionally the stress decreases exponentially with the interplaner spacing of the slip planes. Thus, slip occurs most easily between planes of 'smooth' atomic planes where the 'hills' and 'valleys' of the atomic surface are smallest. The close-packed directions in metals satisfy these criteria [5].

2.3.2.1.   Burgers vector

During plastic deformation dislocation motion can be described using the Burgers vector which defines the magnitude and direction of the slip within a Burgers circuit. A sequence of lattice vectors is taken to form a closed circuit around the dislocation. The same sequence of dislocations is then imposed on a perfect lattice where it can be shown it fails to close. The vector required to close the loop is defined as the Burgers vector **b**. The Burgers vector defines the atomic displacement produced as the dislocation moves across the slip plane.

2.3.3.   Slip in HCP metals

Considering the atoms within the HCP crystal to be hard spheres and the stacking sequence of ABAB is followed the ideal c/a ratio would be 1.633 or $\sqrt{8/3}$, but this is not found in any pure metal [35]. Table 2.4 shows the c/a ratios for commonly used HCP metals.

Table 2.4 c/a ratios of technological interesting materials in descending order [35]

Element	c/a ratio
Cadmium	1.886
Zinc	1.856
IDEAL	1.633
Cobalt	1.623
Magnesium	1.623
Rhenium	1.615
Zirconium	1.589
Titanium	1.587
Hafnium	1.565
Beryllium	1.565

In general metals with a high c/a ratio deform by slip on the basal plane however alloying additions can activate additional slip systems e.g. lithium in magnesium reduces the axial ratio and allows slip on the $\{10\bar{1}0\}$ planes at room temperature giving a marked improvement in ductility. As reported by many authors [28,35,36] the directions for easy crystallographic slip in HCP single crystals are the three $\langle 11\bar{2}0 \rangle$ or $\langle a \rangle$ closed packed directions. The three dominant sets of planes which contain this slip direction are (i) the three $\{0001\}$ basal planes, (ii) the three $\{10\bar{1}0\}$ prismatic planes and

28

(iii) the six $\{10\bar{1}1\}$ pyramidal planes as shown together with 1st and 2nd order $\langle c+a \rangle$ pyramidal slip systems in Figure 2.18.

Basal-< a >	Prismatic-< a >	Pyramidal-< a >	Pyramidal-< c + a >	Pyramidal-< c + a >
(0001) < 11$\bar{2}$0 >, 3	{10$\bar{1}$0} < 11$\bar{2}$0 >, 3	{10$\bar{1}$1} < 11$\bar{2}$0 >, 6	{10$\bar{1}$1} < 11$\bar{2}$3 >, 12	{11$\bar{2}$2} < 11$\bar{2}$3 >, 6
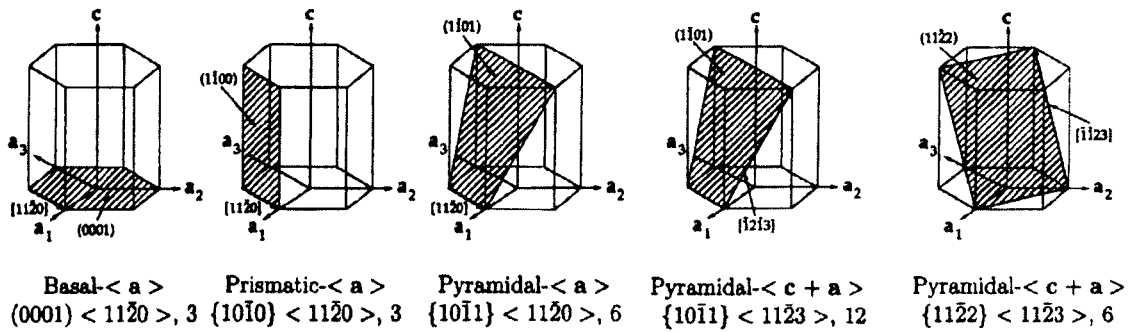
Figure 2.18 The type, direction and number of slip systems in the HCP crystal. From left to right; basal $\langle a \rangle$, prismatic $\langle a \rangle$, pyramidal $\langle a \rangle$ slip systems, together with first and second order pyramidal $\langle c + a \rangle$ slip systems in HCP metals [37]

Crystallographic slip in HCP single crystals is commonly observed to occur on the prismatic $\langle a \rangle$ or basal $\langle a \rangle$ systems. The activation of the pyramidal $\langle a \rangle$ slip systems in titanium polycrystal aggregates occurs primarily due to the large stresses generated in the grain boundary regions because of the misorientation between neighbouring grains [37].

All of the easy $\langle 11\bar{2}0 \rangle$ slip directions are perpendicular to the c-axis and therefore do not produce any elongation or shortening parallel to c-axis. The von Mises criterion states that a polycrystal aggregate requires five independent slip systems to undergo homogenous strain without changes in volume [38]. It has been suggested by may authors [37,39-41] since only $\langle 11\bar{2}0 \rangle$ type slip directions have been reported in magnesium and titanium the von Mises criterion cannot be satisfied. Nevertheless, these metals do exhibit reasonable ductility, especially in the case of pure titanium where elongation to failure can be in the region of ~35%. It was suggested in early HCP deformation work that grain boundary sliding [42] and twining shear [43] must contribute to the overall strain to satisfy von Mises criterion. However, this contribution was considered too small to successfully explain the observed ductility within these materials. For example, the maximum elongation that can be produce by complete twinning of a suitably orientated magnesium crystal is approximately 7% [44]. Since the grains in a non-textured polycrystal are randomly orientated and also do not demonstrate complete twinning, the total amount of strain generated by twinning will be very small. Therefore, it is evident that additional slip mechanisms are in operation within the HCP structure. Work conducted by Balasubramanian [37] on CP titanium suggests that in order to accommodate straining in the c-direction, slip or twin systems with $\langle c + a \rangle$ slip/twin directions must be operative. Williams *et al.* [14] concurs with

this explanation and states that in the absence of twinning $\langle c + a \rangle$ slip is the only mode which permits a shape change in the c-axis. Yoo *et al.* [40] proposes a possible source mechanism for $\langle c + a \rangle$ cross-slip which is shown below in Figure 2.19.
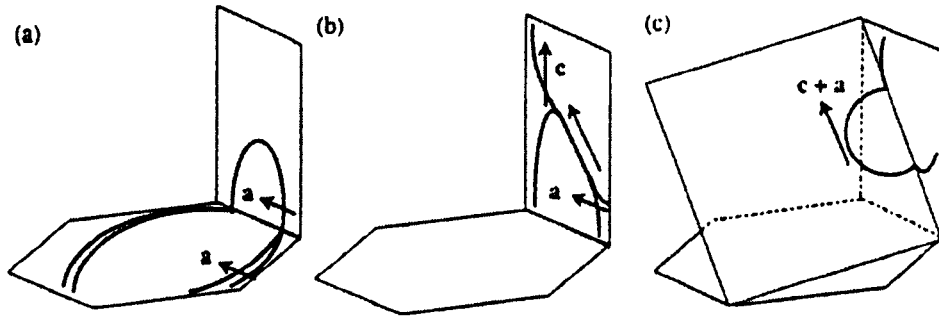
Figure 2.19 Evolution of a dislocation source for a $\langle c + a \rangle$ pyramidal slip system. (a) cross-slip of the dislocation, (b) formation of $\langle c + a \rangle$ dislocation junction and (c) cross slip of $\langle c + a \rangle$ dislocation [40]

Figure 2.19(a) shows a schematic cross-slip of a $\langle a \rangle$ dislocation from the basal plane to a $(1\bar{1}00)$ prism plane. Figure 2.19(b) depicts a $\langle c + a \rangle$ dislocation junction along its near-screw orientation, formed when an active prismatic slip dislocation interacts with a sessile $\langle c \rangle$ dislocation. Here Yoo *et al.* [40] assumes $\langle c \rangle$ dislocations exist in the grain as part of the initial microstructure. Figure 2.19(c) then illustrates the subsequent cross-slip of the $\langle c + a \rangle$ screw dislocation from the $(1\bar{1}00)$ prism plane to the $(1\bar{1}22)$ pyramidal plane. At low homologous temperatures twinning is the dominant deformation mechanism that allows inelastic shape change in the c-direction. At high homologous temperatures slip in the $\langle 11\bar{2}3 \rangle$ directions becomes possible and the slip planes containing this slip direction are the first order pyramidal $\{10\bar{1}1\}$ and second order pyramidal $\{11\bar{2}2\}$ planes [37]: see Figure 2.18. This same conclusion is also made by many other authors [14,40,45-47] for single crystal and polycrystal aggregates in both CP and α-alloys. Work conducted by Numakura *et al.* [45] suggests that stress concentrations at grain boundaries act as sources for the $\langle c + a \rangle$ dislocations. Here it is recognised that it is difficult to envisage that a $\langle c + a \rangle$ dislocation glides on the $\{10\bar{1}1\}$ planes as a perfect dislocation due to the large Burgers vector and the small interplanar spacing. These dislocations were found to dissociate into two partial dislocations on the glide planes.

During compression deformation work on unalloyed titanium (630 wt.ppm O) single crystals Naka and Lasalmone [48] demonstrate that the slip lines in crystals deformed at cryogenic temperatures (77 K) are fine and straight. At a temperature of 472 K the slip lines were extremely wavey revealing the importance of cross-slip at elevated temperatures. This evidence is confirmed by Yoo *et al.* [40] who also state that cross-

slip becomes more energetically favourable above 300 °C. Figure 2.20 shows dislocations in a cross slip plane. Screw dislocations lying in the $(10\overline{1}0)$ planes are seen and a cross slipped area is visible in area A. The cross slip plane was found to be $(10\overline{1}1)$ (the first order pyramidal plane) and is not surprising as it is considered to be one of the easiest secondary slip planes in titanium [39].
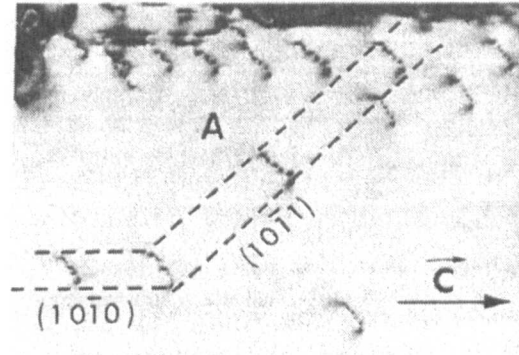
Figure 2.20 Dislocations in a cross-slip plane (1st order pyramidal) [40]

Churchman [36] conducting work on pure titanium (of 0.1wt% oxygen and nitrogen) confirmed that the three slip systems mentioned above (*basal, prismatic and, pyramidal*) dominate the deformation of the HCP crystal but these slip systems are affected by interstitial content. It was shown that in higher purity metal containing 0.01wt% oxygen and nitrogen, slip was confined to $(10\overline{1}0)$ prismatic planes although occasionally basal slip was observed as a secondary slip system. Thus, the critically resolved shear stress for slips systems on the three planes are different and vary in their sensitivity to the oxygen and nitrogen content. Similarly the compositional effects of aluminium additions on the predominant slip modes have been conducted by Blackburn/Williams [49] and Williams *et al.* [14]. Blackburn/Williams [49] carried out room temperature, low strain rate tensile tests on titanium-aluminium alloys of varying aluminium content from 0-16 wt%. Changes in the dislocation substructures were shown to be related to the content of aluminium in the alloy. For CP alloys many dislocation loops and dipoles are formed creating a cell structure within individual grains. The addition of 3% aluminium results in a more homogeneous distribution of dislocations with neither a well defined cell structure nor planar arrays of dislocations. Planar arrays are observed in alloys containing >6% aluminium. Dislocations tangles are observed in such alloys at higher strains and the strain required to produce such tangles increases with the aluminium content. TEM trace analysis demonstrated $\langle 11\overline{2}0 \rangle$ slip in all the Ti-Al alloys. In alloys with higher aluminium content slip on the $\{10\overline{1}0\}$ planes tends to predominate at yield but slip on the $\{10\overline{1}1\}$ and to a lesser extent on $\{0001\}$ is found at higher strains. In alloys with increased aluminium content the $\{10\overline{1}0\}$ planes tend to predominate at yield but slip on the $\{10\overline{1}1\}$ and to a lesser extent (0001) is found at higher strains. Increasing aluminium content tends to produce

narrower slip bands. In the 6% aluminium alloy dislocations are seen to cross slip on to the basal plane. The frequency of this observation decreases as aluminium content increases and is rarely seen if alloys contain high volume fraction of the α_2 phase. Additional $\langle 11\bar{2}3 \rangle$ type slip was found in all the compositions (including the CP titanium) up to 10% aluminium as no such slip was observed in the 16% aluminium alloy. This type of slip appears to decrease with increasing aluminium content.

In later work Williams *et al.* [14] tested titanium-aluminium alloys in compression over a temperature of 77-1000 K with varying aluminium content of 6.6, 5, 2.9, and 1.4 %. For crystals orientated for basal slip the presence of oxygen and/or aluminium is effective in suppressing twinning and so in the absence of twinning $\langle c+a \rangle$ slip is required to enable grains in a polycrystalline metal to undergo arbitrary shape change during plastic deformation. In an alloy of 6.6% aluminium content the crystals deformed by the basal $(0001)[11\bar{2}0]$ slip system over the entire temperature range of 77-1000 K (-196 – 727 °C). As the temperature increased the slip character changes from fine planar slip to coarse planar slip. For alloys with aluminium concentrations of 5% or less the predominant slip system in operation is highly dependant on temperature. At low temperatures (77-190 K) the dominant deformation mechanism is twinning on the $\{11\bar{2}1\}$ planes. Above 300 K there is a marked change in deformation mode which changes to that of basal slip on the (0001) planes, although some twinning does persist. As the aluminium concentration and temperature decreases the dominance of basal slip as the primary deformation mechanism diminishes. Below 300 and 500 K twinning on the $\{11\bar{2}1\}$ planes is the dominant mechanism for 5 and 2.9% aluminium content alloys respectively. Above these temperatures basal slip becomes predominant although $\{11\bar{2}1\}$ twinning is still evident. This work shows that both aluminium content and deformation temperature have a pronounced effect on both resolved stress for slip and on the deformation character. Most significantly, the relative changes in τ_0 with aluminium content are such that basal slip will become increasingly important with increasing aluminium content. Figure 2.21 shows the resolved shear stress for basal and prism slip plotted against aluminium content for temperatures of 300 and 1000 K.
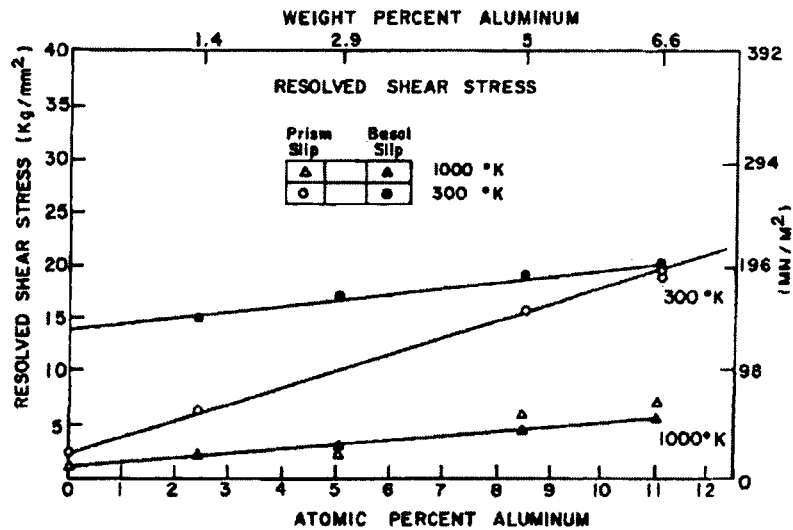
Figure 2.21 Resolved shear stress for prism and basal slip as a function of aluminium concentration for crystals deformed at 300 K and 1000 K [14]

Data for the effect on aluminium content on slip system for 300 and 1000 K shows that solution hardening occurs for both prism and basal slip but the hardening is more rapid for prism slip that basal slip at 300 K. This suggests prism slip is the dominant polycrystal deformation mechanism in dilute alloys. Prism and basal slip should both be equally important when the aluminium content reaches the region of 5-6 wt%. The tests at 1000 K show the hardening rate for both prism and basal slip is the same over the entire composition range and so both slip systems should be equally favoured [14].

2.3.4. Twinning

Another important mechanism operating within metals during deformation is twinning. A twin results when a portion of a crystal adopts a mirror image orientation of the parent crystal lattice in a defined symmetrical way. The plane of symmetry is known as the *twinning plane*. It is recorded by several authors [32-34,49] that in the case of alpha titanium the twin plane is typically $(10\bar{1}2)$ in the $[\bar{1}011]$ direction. Churchman [36] observed that after considerable deformation twins of the $(11\bar{2}2)$ type were present in pure titanium loaded in uniaxial tension. For metals with the c/a ratio > 1.633 (the ideal value), as in zinc and cadmium twinning only occurs on one system but if c/a < 1.633, as for titanium and zirconium, more than one system may operate [51]. Twinning differs from slip in several specific respects. In slip, the orientation of the crystal above and below the slip plane is the same after deformation, while twinning results in an orientation difference across the twin plane. Slip is usually considered to occur in discrete multiples of the spacing, while in twinning the atom movements are much less than an atomic distance. Slip occurs on relatively widely spaced planes, but

33

in the twinned region of a crystal every atomic plane is involved in the deformation. There is evidence suggesting slip is essential prior to twining as arrays of dislocations must be formed to create stress concentrations to nucleate twin formation [32]. Single crystal experiments show that twinning occurs at substantially higher critical resolved shear stress (CRSS) than deformation on the basal plane where a shear stress of 100-700 gmm^{-2} and 20-30 gmm^{-2} is required to cause twinning and slip respectively in cadmium. Consequently, twinning will only take place if the basal plane is unfavourably orientated (within 5-10°) of the tensile axis [33].

Two types of twins can be produced and are known as *mechanical* or *annealing twins*. Mechanical twins are produced in HCP and BCC metals at lower temperatures and high strain rates [28], often requiring shock loading (e.g. explosive forming) to be induced. This can be attributed to the fact twins can be formed within a few microseconds where there is a delay of milliseconds before a slip band is formed. Twinning is not the dominant deformation mechanism in metals with multiple slip systems and generally occurs when the slip systems are restricted or when something increases the critically resolved shear stress so that the twinning stress is lower than that of slip. During plastic deformation the gross amount of deformation accommodated by twinning is small as the lattice strains needed to produce a twin is also small. However the important role of twinning in plastic deformation comes not from the strain produced by twinning but from the fact the lattice orientation changes and may place a new slip system in a favourable orientation with respect to the stress axis so that additional slip may occur. Thus, twinning is an important deformation mechanism in metals with limited slip systems such as HCP metals.

2.3.5. Texture

The majority of materials, both manmade and naturally occurring, comprise of a collective of crystals which form on solidification. These crystals are known commonly known as grains. Generally, in a single phase material each grain will have the same chemical compression and crystal structure. The two main differences between grains are; the shape of the grain (which will be a function of the solidification and thermomechanical processing received by the metal) and secondly, the orientation of the constituent crystal lattice measured to some fixed direction e.g. the rolling direction [52].

The crystallographic orientation in any given material is generally non-random [53,54]. Such non-random orientations are referred to as 'texture'. The preferred orientation formed is modified during plastic deformation, recrystallisation or phase transformation. In textured polycrystalline materials many macroscopic properties such as Young's

modulus, ductility, thermal expansion coefficient, etc are dependant on the direction in which they are measured, i.e. there may be pronounced anisotropy within the material. Texture may be subdivided into macro-texture and micro-texture. Macro-texture regards grains as a statistical population. Humphreys reports [55] that experimental results suggest that the number of orientations required to produce statistically meaningful data needs to be in the region of 500 – 1500 respectively. Micro-texture relates the grain-orientation data directly to the grain location in the sample [56].

Deformation textures have their origins in the crystallographic nature of the familiar deformation processes of slip and twinning. When large strains are applied, slip is usually the major factor, however twinning can be significant because of the substantial reorientations involved [57]. Due to the result of slip combined with the geometrical constraint of the surrounding material the crystal lattice of a deformed grain rotates. The limited number of slip systems available produces rotations towards a limited number of end points and deformation texture is produced. Thus, the resulting texture will be a function of the imposed stress (or strain) system, the extent of deformation, and the deformation modes in operation which in turn are temperature dependant and defined by the crystal structure and atomic bonding.

Transformation textures have their origin in the orientation relationships between the parent and product phases of the transformation. In the case of two titanium allotropes, the α and β phases, the transformation follows the Burgers relationship:

$$(0001)_\alpha \| (110)_\beta \qquad\qquad [11\bar{2}0]_\alpha \| [1\bar{1}1]_\beta$$

This explicit relationship ensures that where a texture existed originally, the titanium phase transformation will necessarily create a new and different texture in the produce structure however there will always exist a parent-child relationship between both crystal structures.

2.3.5.1. Representation

In cases where certain orientations are of interest due to crystallographic anisotropy (e.g. c-axis in HCP materials), unit vectors, axes and crystal planes can all be described within a coordinate frame. One of the coordinate frames of importance when describing single crystal orientations is linked to the crystal structure. In cubic crystals it is the norm to choose a Cartesian frame x, y, z aligned with the unit cell base vectors $\mathbf{a}$, $\mathbf{b}$ and $\mathbf{c}$. Within this crystal frame, it is common to describe lattice directions and planes by integer indices. For example, a direction r in a Cartesian frame is described by the vector sum

$$\mathbf{r} = u\mathbf{a} + v\mathbf{b} + w\mathbf{c} \qquad (2.4)$$

and more concisely denoted by the symbol $[uvw]$. A set of parallel lattice planes is described according to the equation

$$h\,x/a + k\,y/b + l\,z/c = 1 \qquad (2.5)$$

where x, y, z are the coordinates of any point on one specific plane of the set and a, b, c are the lengths of the base vectors of the unit cell [54]. From Equation 2.5, the Miller indices (hkl) denote the reciprocal multiples of the axis intercepts reduced to the smallest integer. A list of the most common texture notation is given below:

- $[uvw]$ is a direction (in real space)
- $<uvw>$ describes a class of directions (symmetry related)
- (hkl) gives the direction of plane normals (Miller indices)
- $\{hkl\}$ refers to class of (symmetry related) plane normals

For crystals of the hexagonal systems, a non-orthogonal coordinate system of four axes is often used: one along the 6-fold (or 3-fold) rotation axis $\mathbf{c}$ and three perpendicular to it in the hexagonal basal plane, $\mathbf{a}_1$, $\mathbf{a}_2$, $\mathbf{a}_3$ at $120°$ to each other (Figure 2.17). In the 4-axis $\mathbf{a}_3$ is redundant since $\mathbf{a}_3 = -(\mathbf{a}_1 + \mathbf{a}_2)$. In this system a direction $\mathbf{r}$ will have 4 indices such that [39]:

$$\mathbf{r} = u\mathbf{a}_1 + v\mathbf{a}_2 + t\mathbf{a}_3 + w\mathbf{c} \qquad (2.6)$$

In the hexagonal frame planes can still be described by their reciprocal intercepts on all four axes leading to the 'Miller-Bravais' indices $(hkil)$ where;

$$h + k + i = 0 \qquad (2.7)$$

A vector in three dimensions cannot be unambiguously decomposed into four components, however, it can be unambiguously projected onto the four axes and. In the case of a hexagonal basis, the projections are proportional to vectors components so long as the sum of the three redundant indices is set to zero.

2.3.5.1.1.   Description of orientation

In quantitative texture analysis the coordinate system of the sample must be related to that of the crystal. This requires three quantities, for example the classical Euler angles that relate two orthogonal right handed coordinate systems through three rotations or an angle axis pair of coordinate systems that bring the two systems to coincidence through

a single rotation about a specific axis [53]. The sample coordinate system for metals is usually defined by the forming process for example, rolling direction (RD), transverse direction (TD) and normal direction (ND) [53,57]. The sequence relating the crystal coordinates to the sample/system coordinates is shown schematically in Figure 2.22 where the principle axes of the crystal is e_i^c and the sample is e_i^s.
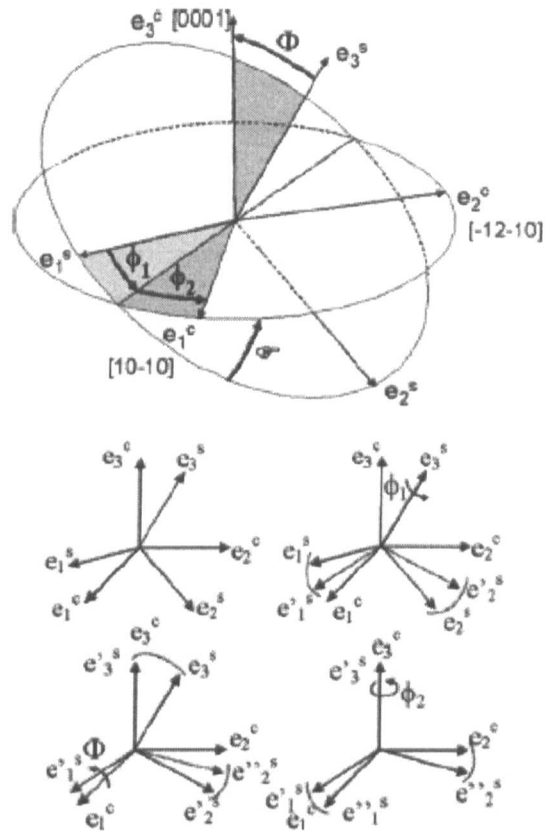
Figure 2.22 Illustration of the successive rotations that specify an orientation through the Euler angles ϕ_1, Φ and ϕ_2 [58]

These three rotations correspond to the Euler angles ϕ_1, Φ, ϕ_2. Using the Bunge convention ϕ_1 is a rotation about e_3^s axis followed by a rotation Φ about the e_1^s axis then finally a rotation ϕ_2 about e_3^s again. ϕ_1 and ϕ_2 vary from 0 to 2π and Φ from 0 to π.

2.3.5.1.2.   *Description of textures*

Preferred crystal orientations are usually described by the means of pole figures. These simple stereographic projections show the distribution of particular crystallographic directions in the assembly of grains under analysis. For the pole figure to have any meaning it must also contain some reference directions and again these are usually

chosen to correspond to easily defined directions in the sample. Figure 2.23(a) shows how the sample (labelled sheet in this case) is positioned at the centre of the stereographic sphere with orthogonal reference axes (Figure 2.23(a)). The orientation of a single grain in the sample can be represented by plotting its three {100} poles at the appropriate angular positions relative to the reference directions. In practice all the poles concerned are projected onto the equatorial plane to produce a stereographic projection (Figure 2.23(b)).
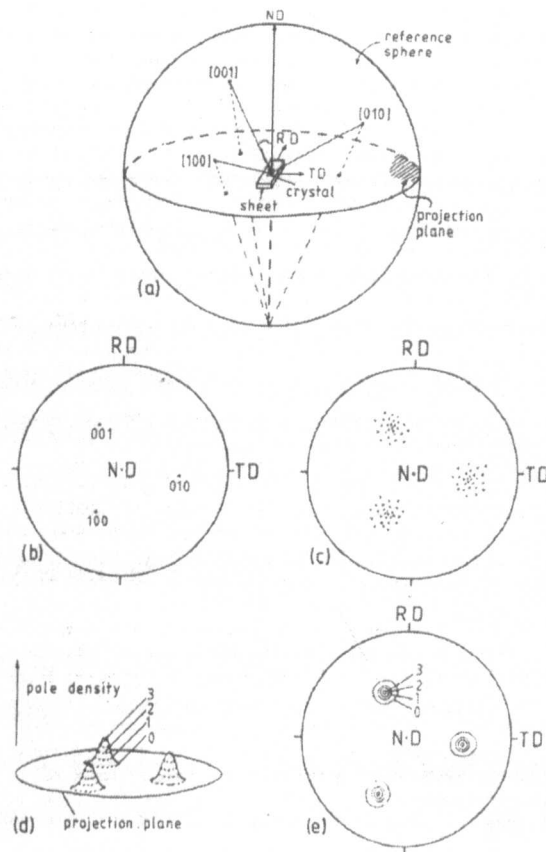
Figure 2.23 (a) projection sphere and reference directions, (b) projection poles for a single grain, (c) projection of poles from textured grains, (d) pole density distribution, and (e) contour map of pole density [57]

For a polycrystalline sample all the grains are considered and the three {100} poles must be plotted for each to give the pole figure. If the resulting poles are distributed uniformly then the specimen is said to have random texture. In real materials this is very rare and the poles tend to cluster together in certain areas of the pole figure to produce a texture shown in Figure 2.23(c). The large number of grains typically analysed makes the determination of individual poles impossible [57]. To over come this data is collected from many grains simultaneously and presented in the form of density contours on the pole figure. Figures 2.23(d) and Figures 2.23(e) show how the

38

pole density may be visualised and presented as contour line on the stereographic projection. The density values are expressed relative to that which be expected for a sample displaying random texture.

2.3.5.2. Misorientation and disorientation

When the high angle boundary between two adjacent grains is detected the angular relationship between the two crystals can be calculated as each orientation is known [55]. This relationship may be expressed in terms of the *rotation matrix* [59,60], the *Rodrigues vector* [61] or as the *angle axis pair*. Data represented in this report uses the latter definition which defines the angle by which one of the crystals must rotate about an inclined axis in order to bring it into register with the other crystal. In the cubic system there are 24 possible solutions (variants) and in the HCP system 12. It is convectional to describe the relationship between grains using the smallest rotation variant which is often deemed the *disorientation*. Thus, this report will use the term *misorientation* when describing micro-texture however it is noted here that strictly speaking it is the disorientation that is being used to describe the rotation.

2.3.5.3. Electron back scatter diffraction

The electron back scatter diffraction technique is becoming increasingly popular and is relatively new in the materials science research domain when compare with TEM, X-ray and neutron diffraction techniques. Although the EBSD technique lacks the very high resolution of transmission electron microscopy it is not restricted to thin areas along a hole in a small sample (~3mm), but is capable of analysing crystal orientations and dislocation substructures over a large sample area.

Electron back scatter patterns are generated by the elastic interaction of a primary electron beam with a steeply tilted specimen, typically 70°. This minimises the amount of the signal absorbed and maximises the diffracted proportion of the beam energy. Surface preparation is a paramount step in obtaining EBSD patterns. This is due to the small interaction depth of the beam and specimen being in the region of 10 nm. This layer must also be relatively strain free for clear patterns to be obtained [56]. Sample preparation must therefore not induce any more plastic deformation in previously deformed materials.

When a stationary scanning electron microscope (SEM) beam is focused on a specimen the incident beam is scattered elastically through large angles within the specimen at a point source just below the specimen surface and impinges on crystal planes in all directions [56]. The back scattered signal increases with atomic number (z) and thus the

quality of the diffraction pattern can be expected to increase with z accordingly [55]. When viewed using electron photosensitive film or a phosphorous screen the scattering forms '*Kikuchi*' lines when the Bragg condition is satisfied. These patterns are measured by sensitive CCD cameras where the Kikuchi patterns are read by computer software and indexed. Figure 2.24 shows a schematic representation of a modern EBSD setup.

Figure 2.24 EBSD detection equipment arrangement [62]

Two forms of scanning can be utilised to obtain texture data using the EBSD technique. The first is beam scanning where the normal scan mode of the SEM is disabled and the electron spot is controlled by the acquisition software. This method is rapid as the time to reposition the spot is negligible. It is however limited by inaccuracies in angular resolution and beam defocus brought about by the beam moving off the optic axis [56]. The accuracy in determining absolute orientations using this method is approximately 1° [63]. The stage scanning mode moves the sample and the electron beam is stationary. The sample stage is controlled by the EBSD software and this eliminates the problem of defocus and inaccuracies in orientation measurement. It is however considerably slower as the time for each step can take ~1 second. In addition, the position accuracy of the SEM stage is not high and so the usable step size is limited to ~ 1µm [55].

For the highest possible spatial resolution a field emission gun scanning electron microscope (FEGSEM) is required. Such equipment has lead to the technique being used as a quantative method for metallurgical analysis of materials with substructure as small as 0.2 µm [55]. Figure 2.25(a) shows the effect of beam current on both a

tungsten filament SEM and FEGSEM. The resolution of the W-filament is highly dependant on the probe current [55,64]. For small probe currents the software has difficulties separating overlapping patterns, where large probe currents suffer from beam spread in the sample due to the large beam size. Thus an optimum is achieved somewhere between to two extremes. A FEGSEM system is much less sensitive to the probe current than the W-filament.
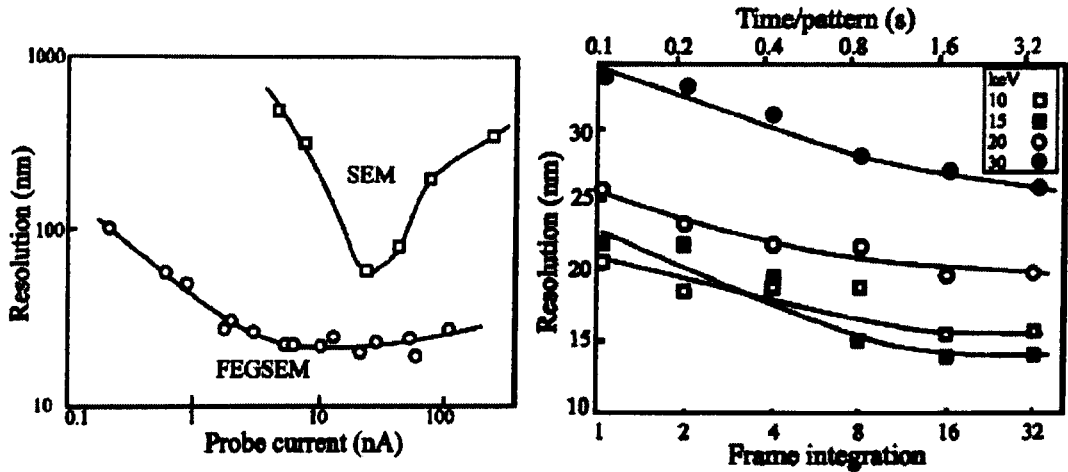
Figure 2.25 (a) the effect of probe current on the effective spatial resolution in aluminium at 20 keV for a W-filament SEM and a FEGSEM and (b) the effect of accelerating voltage and frame integration on the effective spatial resolution for aluminium at a beam current of ~15 A [55]

Other factors affecting EBSD performance include accelerating voltage and pattern averaging times. In Figure 2.25(b) it can be seen that reducing accelerating voltage improves spatial resolution as the spread of the beam deduces accordingly. However, below 15 keV the resolution deteriorates as the efficiency of the phosphor screen reduces at the lower voltages. It can also be seen that as the length of pattern averaging times is increased so does the quality of the pattern and thus the overall resolution.

2.3.6. Strain path phenomenon

Simple tensile and compression tests have been used for many decades to measure the strength and plastic behaviour of metals at room and elevated temperature. During such tests simplistic assumptions are made on how the material flows in order to calculate mechanical properties. An example would be the assumption that the strain across the samples cross-section is equal and so as the material plastically deforms all the material flows in one direction. Even in such a simple example this is not the case (as seen by the folding over of a samples side surfaces in an axisymmetric compression test in Section 5.1.2) and the vector (or strain direction) in which any given element of material

flows is not linear. For operations such as rolling and forging the direction in which a material element is deformed varies greatly through the whole process and the material stock. In the case of rolling, the relative velocity of the sheet and the rolls changes throughout the operation and imposes significant strain path changes just below the surface of the material. Consider a roll with constant angular velocity whose roll surface is travelling at a constant speed relative to the slow moving roll stock that is entering the roll gap. Figure 2.25(a) below shows a FE model of such an operation, the nonuniform strain (b) and strain path distribution (c) through the cross-section.
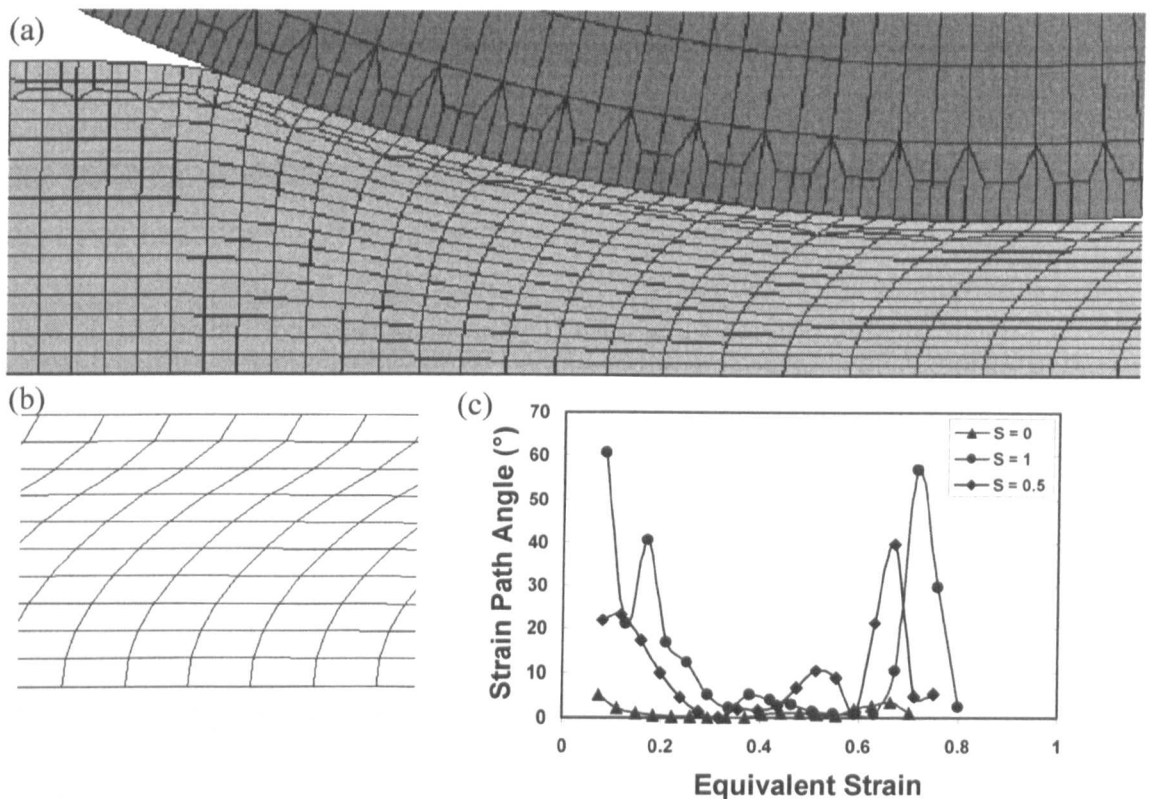
Figure 2.25 (a) FE modelling of experimental rolling of an aluminium – 1% magnesium slab of 20 mm initial thickness by 50% at an ingoing temperature of 400 °C, including (b) the distortion of each element and (c) the dependence of strain path angle on strain during a rolling pass for elements at different positions between the centre-line, S = 0, and the surface, S = 1 [65]

As the material makes contact with the faster moving roll then friction drags the material into the roll gap and causes a forward shearing (with respect to the rotation direction of the roll) of the layer of material. As no dilation of the material can occur and the thickness of stock is reduced then the material within the roll gap accelerates. The velocity of the material is now greater than that of the work roll and an additional shear is imposed on the subsurface material as the surface of the stock is constrained by friction at the slower moving roll. This additional shear strain results in an increase in equivalent strain from the expected homogeneous strain at the centre-line towards the

surface. In addition to these changes in deformation conditions, there are also differences in strain path for material travelling in defined streamlines. The most dramatic change shown in Figure 2.25(c), where the centre-line undergoes almost monotonic plane strain compression, whereas the near surface material is subjected to the mentioned additional shear strain [65]. The effects of shearing effects are discussed later in this section.

Consider Figure 2.26, where the axes are the normal and shear stresses and there are two points A and B. The space within this graph can be described as the strain space, where there are an infinite number of ways to travel between A and B, i.e. the strain paths. To induce a strain state from A to B, it can be seen that accumulative strains will be the same; however the strain paths taken by the material to reach these points can be completely different and will change deformation mechanisms are activated (e.g. which slip planes are active) and can have significant effects on the material behaviour.
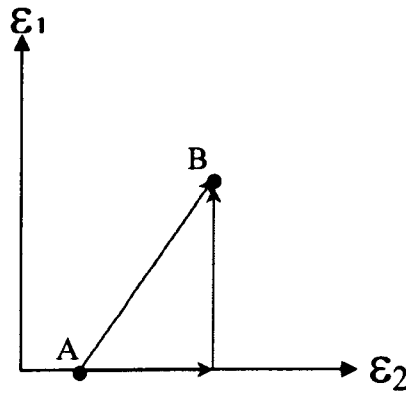
Figure 2.26 Strain space showing two different strain paths

Schmitt et al. proposed a scalar parameter to measure the change in strain path. The strain path angle change in strain space (with respect to a macroscale) can be defined as [66]:

$$\theta = d\varepsilon_p \cdot d\varepsilon \qquad (2.8)$$

θ is the scalar product of $d\varepsilon_p$ and $d\varepsilon$, the strain tensors in strain space which correspond to the prestrain and subsequent strain respectively. θ also corresponds to the cosine of the angle between the vectors which represent the successive strain tensors. By including this information and applying the dot product, Equation 2.8 can be rewritten as:

$$\cos \alpha = \frac{d\varepsilon_p \cdot d\varepsilon}{|d\varepsilon_p||d\varepsilon|} \qquad (2.9)$$

This scalar parameter characterises the sequence of loadings from a microstructural perspective [67], and assumes that plastic strain is the same in each grain as it is macroscopically imposed. The norms of each strain increment may be defined as [67]:

$$\left| d\varepsilon_p \right| = \sqrt{\left(d\varepsilon_{ij} d\varepsilon_{ij} \right)} \tag{2.10}$$

As a result of combining Equation 2.9 and 2.10, the strain path angle (α) can be described as:

$$\cos \alpha = \frac{d\varepsilon_A \cdot d\varepsilon_B}{\sqrt{d\varepsilon_A \cdot d\varepsilon_A} \cdot \sqrt{d\varepsilon_B \cdot d\varepsilon_B}} \tag{2.11}$$

thus for the non-plane strain forging operating ;

$$\cos \alpha = \left(\frac{\{[\varepsilon_{11}]_A \cdot [\varepsilon_{11}]_B\} + \{[\varepsilon_{22}]_A \cdot [\varepsilon_{22}]_B\} + \{[\varepsilon_{12}]_A \cdot [\varepsilon_{12}]_B\} + \{[\varepsilon_{33}]_A \cdot [\varepsilon_{33}]_B\}}{\left(\sqrt{\varepsilon_{11}^2 + \varepsilon_{22}^2 + \varepsilon_{12}^2 + \varepsilon_{33}^2}\right)_A \cdot \left(\sqrt{\varepsilon_{11}^2 + \varepsilon_{22}^2 + \varepsilon_{12}^2 + \varepsilon_{33}^2}\right)_B} \right) \tag{2.12}$$

If the successive strains are unidirectional and performed at constant strain rates, then Equation 2.12 can be written as [68]:

$$\cos \alpha = \frac{\dot{\varepsilon}_A \cdot \dot{\varepsilon}_B}{\sqrt{\dot{\varepsilon}_A \cdot \dot{\varepsilon}_A} \cdot \sqrt{\dot{\varepsilon}_B \cdot \dot{\varepsilon}_B}} \tag{2.13}$$

where $\dot{\varepsilon}_A$ and $\dot{\varepsilon}_B$ are the strain rate tensors of the prestrain and subsequent strain respectively.

Davenport et al. [69] provide a concise way of graphically mapping the strain path. In general strains relative to fixed axes it is possible to define three normal components and six shear components of strain. For plastic deformation the normal components are not independent because there is no dilation, therefore;

$$\varepsilon_{11} + \varepsilon_{22} + \varepsilon_{33} = 0 \tag{2.14}$$

Also the shear components are symmetric, therefore;

$$\varepsilon_{12} = \varepsilon_{21} \qquad \varepsilon_{13} = \varepsilon_{31} \qquad \varepsilon_{23} = \varepsilon_{32} \tag{2.15}$$

Thus, there are only five independent components of strain. For simple graphical mapping certain constraints must be applied. By presenting only the three normal

components, then, from Equation 2.14, a two dimensional map with three axis at 120° to each other [70] can be used as shown in Figure 2.27.
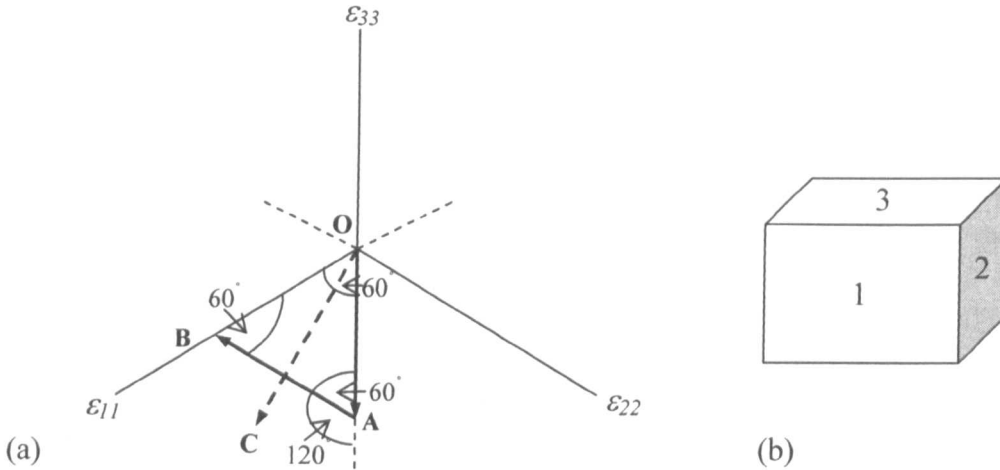
Figure 2.27(a) Graphical representation of strain paths using axes at 120° for the normal strain components and (b) a cube showing the faces on which sequential strains are applied to produce the vectors in (a) [69]

A uniaxial compression, ε_{33}, on face 3 (Figure 2.27(a)) produces the strain vector OA in Figure 2.27(a) because from Equation 2.14;

$$\varepsilon_{11} + \varepsilon_{22} = -\varepsilon_{33}\Big/2 \tag{2.16}$$

and $\cos 60 = \dfrac{1}{2}$

If the specimen is then given an equal uniaxial compression on face 2 the strain path is AB and the strain path undergoes a 120° rotation. In the mapping, the gross train OA + AB = 2OB, but the net, defined by the initial and final positions in strain space is $\overline{OA} + \overline{AB} = \overline{OB}$, where OB is equivalent to a single uniaxial tension applied to face 1. In contrast, if plane strain compression is applied to face 3 in a channel die with $\varepsilon_{22} = 0$, then the strain path is **OC**. Applying a second plane strain compression on face 1, again with $\varepsilon_{22} = 0$, then reverses the path along **CO** and the strain path undergoes a 180° reversal which is comparable to a full reversal in direction during a torsional deformation. In real industrial forming processes, strain path changes are far less severe than a complete reversal (180° change in strain path) and are more likely to be less than 120°. Additionally, in many of these operations additional shear strains are imposed along with the normal strains and so the orientation of the principle axes change. In this case a further orientation diagram is needed to describe the change in strain path, which makes interpretation of the observed microstructures difficult.

The microscopic effects of strain path changes can manifest themselves macroscopically via changes in flow stresses and recrystallisation kinetics. These strain

path effects can be broken down into two broad categories [52]: those concerning strain reversal (i.e. θ=180°), also known as Bauschinger effects. The second incorporates combinations of axial and shear deformation, which Davenport and Higginson [52] refer to as normal-shear strain path effects. For the strain path tests presented in this work full reversal strain paths are referred to as 'simple' strain path tests where Davenport's normal-shear strain paths are referred to as 'industrial' strain path tests. Figure 2.28 shows the Bauschinger effects within an aluminium alloy. It can be seen that the torsion load is stopped at a strain of 3.8, and then is applied in the opposite direction.
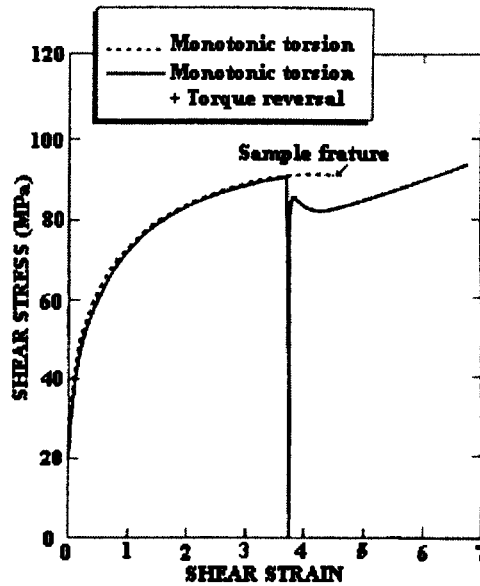
Figure 2.28 Bauschinger effect in an Al-Mn alloy [70]

It is clear to see the increased work hardening rate followed by flow softening and then a subsequent lower flow stress, before the flow stress climbs back to its original monotonic flow stress. In this example the material also demonstrates enhanced elongation to failure during the reversed shearing. Stout and Rollett [71] have proposed an equation to quantify the Bauschinger affect, as a quantity known as δ_B, or the normalised Bauschinger stress. The yield stress after stress reversal is denoted as δ_R. The final (largest) flow stress in the forward direction is σ_F and σ_o is the 'virginal' flow stress.

$$\delta_B = \frac{\sigma_F - |\sigma_R|}{\sigma_F - \sigma_o}$$

(2.17)

A high value of δ_B corresponds to more significant Bauschinger effect, and vice versa. The Bauschinger effect is more of an observation rather than a single mechanism, which can be seen in many different cases, and is not always the same for different materials.

46

TEM studies have revealed that the dislocation structure developed during two stage strain paths is responsible for the macroscopic observations in changes in flow curves and recrystallisation kinetics [72-77]. The initial increase in work hardening is thought to be brought about by the greater resistance to the mobile dislocations. This is caused by the dislocation sub-boundaries which have formed during the first stage of deformation to minimise the stored energy within the system. The following reductions in work hardening rates are believed to be associated with the partial dissolution of these dislocation substructures generated by the prestrain annihilating oppositely polarised dislocations [72,75-79]. The typical dislocation substructures found in a reverse strain test on a material that undergoes dynamic recovery can be seen in Figure 2.29. The dislocation sub-grain cell walls are labelled by A-D, and a uniform distribution of mobile dislocations can also be seen within these boundaries.
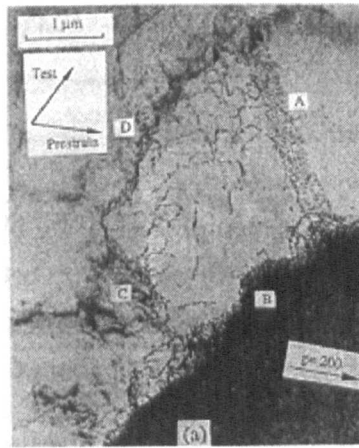
Figure 2.29 Dislocation substructure in aluminium [7]

Like the flow softening mechanisms (recovery and recrystallisation) the dislocation substructure will be a function of the stacking fault energy (SFE) of the material, and thus the mobility of the materials dislocations. However, the changes in the work hardening rates will also be affected by numerous material variables such as grain structure, texture, second phase particles, twins, localised shear, etc. The resultant dislocation structure and thus stored energy within the metals' lattice will ultimately affect the recrystallisation kinetics. Such effects have been studied by Higginson and Sellars [79], where they demonstrated strain path effects were concentrated towards the surface of hot rolled steel and reduced recrystallisation kinetics on annealing. They propose that the stored energy, and hence the driving force for recrystallisation is given by [79]:

$$E \approx \frac{\mu b^2}{10} \left[\rho_i \left(1 - \left(\ln 10 b \rho_i^{0.5} \right) \right) + \frac{2\theta}{b\delta} \left(1 - \ln \frac{\theta}{\theta_c} \right) \right] \tag{2.18}$$

47

Where μ is the shear modulus, b is the Burgers vector, ρ_i is the internal dislocation density, θ is the sub-grain misorientation, θ_c is the critical sub-grain misorientation (typically 15°), and δ is the sub-boundary separation. Thus the energy stored, and the driving force for recrystallisation in a material is governed by the dislocation density, sub-grain orientation, and the sub-boundary separation. It is therefore proposed that strain path reversal towards the surface of the rolled sheet reduces the dislocation density and reduces the driving force for recrystallisation and hence the recrystallisation rates.

Work by McLaren and Sellars [80] shows that by comparing tension-tension and tension-compression strain path tests on 316L stainless steel at 930°C to a strain of 0.15, retards the kinetics of static recrystallisation. It is noted that this is important when attempting to predict the development of microstructure in rolling where reversal of strains occur (as demonstrated in Figure 2.25). Figure 2.30 from earlier McLaren and Sellars work [81] below shows the predicted and measured percentage recrystallised microstructure in rolled 316L stainless steel. At approximately 0.8 from the centre of the sample centre it is predicted that there should be a large proportion of recrystallised material due to a higher strain distribution in this region. However, the measured results show that there is significantly less recrystallised material, with the model demonstrating approximately 25-35% (recrystallised material) compared to that of the actual value. It is noted that this discrepancy is not derived from the work hardening or boundary constraints applied in the model but from the use of equivalent strains which do not take into account the redundant shear strain (strain path) changes which are present below the surface (~0.8 from the centre) of a rolled product.
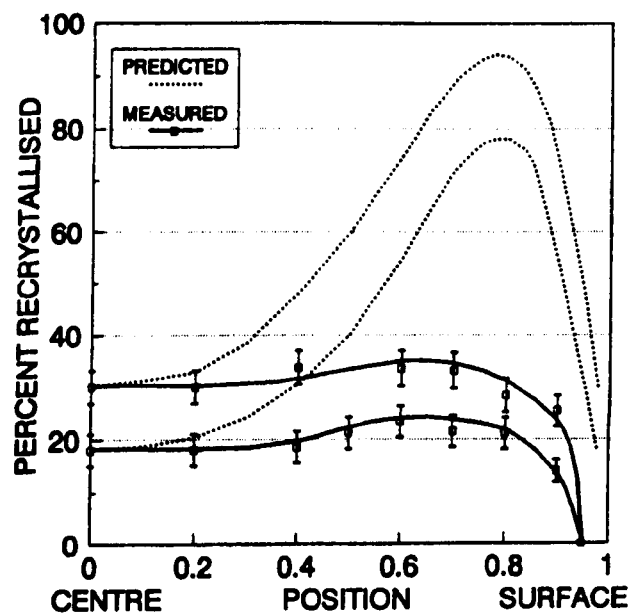
Figure 2.30 Predicted and measured distribution of microstructure through thickness of slab after annealing at 1000 °C for 86 (lower) and 142 (upper) seconds [81]

48

Work by Black *et al.* [82] physically demonstrated this reversal in shear strain by rolling an Al-Mn alloy with a pin inserted thought the thickness of the roll stock. Different pin shapes during forward-forward and forward-reverse two pass rolling highlights the difference in local shear and the change in shear direction in the sub-surface region as mentioned above. Although such a technique offers excellent insight into the local shear within the material the results don't provide any quantitative strain path data. The response of the material to industrial deformation (or normal-shear as [52] define it) will depend on the response of the dislocations and the substructures formed. In addition to this, the effects of different slip systems activated by shear, tensile and compressive deformation modes will also play a factor. This is intrinsically related to the crystallographic orientation, i.e. texture, of the grains. In the case of titanium, a HCP metal, such effects will be complicated by the large plastic anisotropy within the crystal structure as discussed in Section 2.3.3. It is evident from strain path related literature that the level of strain path knowledge is not sufficient for its effects to be successfully incorporated into material models. Some attempts have been made to model the effects of strain path through the dislocation density and their subsequent substructures [74,83], however these do not include the effects of the texture. A series of publications by Peeters *et al.* [72-74] simulates microstructural changes inside each crystal and successfully couples the full anisotropy due to crystallographic slip, the texture and the dislocation structure. The model operates at low homologous temperatures for BCC polycrystals that recover and form distinct cell block structures, in this case interstitial free (IF) steel. This cell block structure is represented by three dislocation densities; of immobile dislocations in the cell boundary (CB), immobile dislocations stored in the cell block boundary (CBB) and the directionally moveable dislocation density associated with CBB density which possess polarity.
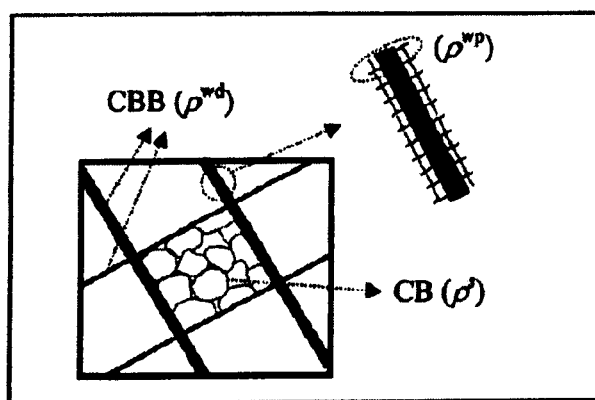
Figure 2.31 Schematical representation of the internal variables characterising the intensity of the microstructural features proposed by Peeters et al. [72]; cell boundary dislocation density (CB (ρ^s)), cell block boundary dislocation density (CBB (ρ^{wd})) and the directionally moveable dislocation density associated with the CBB (ρ^{wd}))

A schematic of which is given in Figure 2.31. Material parameters for the model are calibrated from the stress-strain response of the material under five defined tests and measured intensities of dislocation polarity of CBB for various crystal orientations are correlated to equivalent strain. Results show good agreement between measured and calculated stress strain response. TEM work reveals than during a two stage strain path the dislocation ensemble, which develops in the grains during plastic deformation, is responsible for the specific features in the macroscopic stress-strain curves. However in this work it is recognised that additional effort is required as the model does not completely incorporate the texture evolution, or precisely capture the increase in work hardening rates on reversal or the saturation back to the 'normal' flow stress after a given amount of strain. This model relies highly on multiple material parameters and substructure response to be known from given mechanical tests. The simulation of these mechanical tests are good however modelling on a non-calibration test is not presented nor is the model tested on a concurrently changing strain path deformation and so it is unclear whether it is capable of accurately simulating complex 'real' forming operations. Strangely, in addition it this no experimental conditions such as strain rate and temperature are stated in all three papers.

The utilisation of FE modelling in metal forming operations relies on the exploitation of an accurate constitutive equation that describes the metals flow behaviour over a given range of process variables. As mentioned earlier this equation is derived from the test data produced by carrying out simple mechanical tests at various temperatures and strain rates. Thus, this method is not entirely accurate as it cannot incorporate the effects of strain path changes on the behaviour of the metal. Work by Figueiredo *et al.* [84] recognises that FE analysis depends on the availability of accurate stress-strain curves of the material being processed including the effects of temperature, strain rate and strain path changes. Figure 2.32 demonstrates the procedure followed in this work to model the effects of the strain path change on the bulk material. FE simulation of a two stage equal channel angular pressing (ECAP) processing of copper showed that the strain distribution along the axis of the sample was uniform except for the ends which were removed before the second ECAP pass. The strain distribution along the cross section of the specimen is computed during the first ECAP simulation. For the second ECAP pass simulation each column of elements (with respect to the longitudinal axis of the specimen) are then assigned calculated strain values from the first pass as initial conditions. In addition to this a forward-reverse torsion test is carried out. The forward torsion applies the same strain calculated in the first ECAP pass. The strain is then reversed and the resultant stress strain curve is used to define the material flow behaviour in the second ECAP simulation.
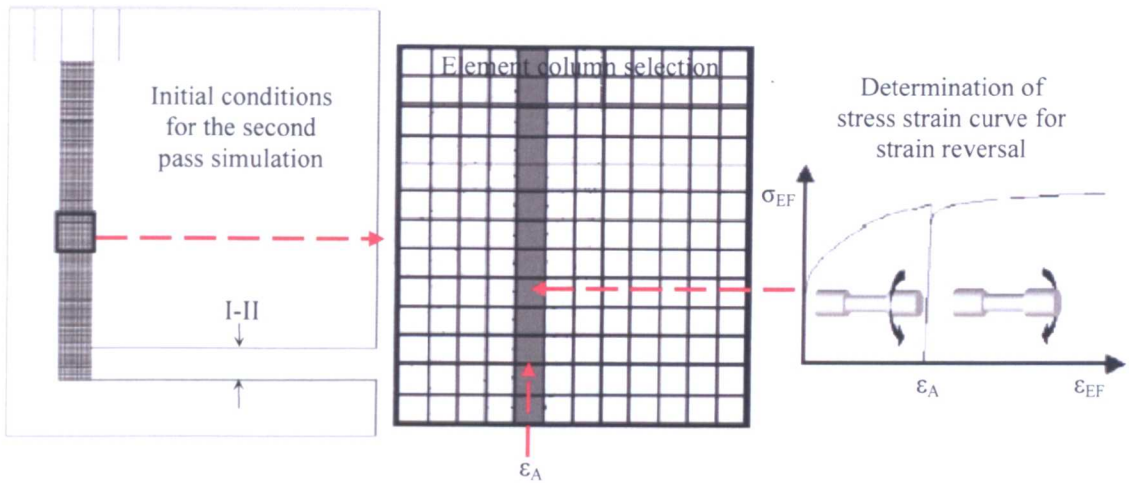
Figure 2.32 Procedure followed by Figueiredo et al. [84] for the determination and insertion of the adequate stress strain curves in the element columns for the FEM simulation of the second ECAP pass. Sample is placed into the dies so that the deformed sample top and bottom surfaces now become the right and left faces of the under extruded second pass sample

Results from the forward-reverse torsion tests also show a transient decrease in work hardening rate on strain reversal followed by a permanent decrease in flow stress and is again attributed to dislocation dissolution. The results of the same model, one considering the change in flow direction and the other not (monotonic flow stress) are plotted below in Figure 2.33 showing the strain distribution and the resultant tool force.
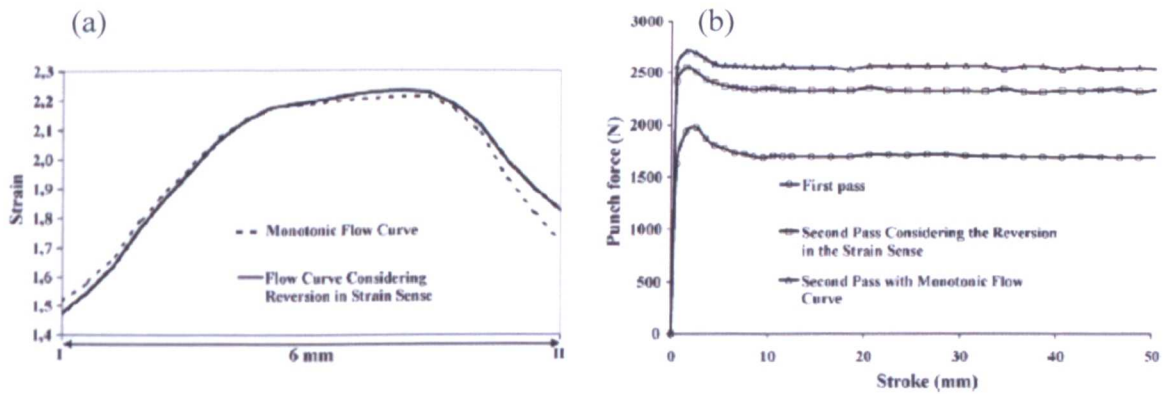
Figure 2.33 (a) Effective strain distribution along the sample cross-section (line I-II in figure 2.32) after two ECAP passes to impose a 180° strain path change between passes and (b) the punch force for each process [84]

With regard to strain distribution the inclusion of the strain reversal in the flow curves only causes a minor change which is greatest at the top and bottom of the lower die channel and have a maximum deviation of 0.1 from the monotonic flow curve strain calculation. This is attributed to the negative strain hardening gradients observed in the stress strain curves after strain reversal, together with the lower flow stress of the

material after reversal. The effects of the considered strain reversal on the punch force for the process shows that a lower punch force of approximately 250N is required to generate a constant strain rate.

2.4. Conclusions

Of all the possible variations in strain path tests, full reversal deformations ($\theta=180^{\circ}$) are the most commonly utilised [71,75,76,85] due to their relative simplicity to perform and significant effects on dislocation substructure. This is due to the work hardening of a material being governed by the interactions of dislocations and the microstructural features generating them. As a result, the reverse torsion approach allows one to analyse and compare such interactions. However, smaller, more complex, and more industrial relevant strain paths have not received so much attention. In addition to this, simple alloys including mild steel, pure aluminium, aluminium alloys, copper, and brass have been examined for their relatively low flow stresses and the simplicity of their microstructure. Such metals have face centred cubic (FCC) or BCC crystal structures, and the absence of phase transformations, for metals tested at higher temperatures [75]. Very little work has been carried out [74,76,83,86] on industrially relevant engineering metals such as heat-treatable aluminium alloys, high strength steels, and titanium alloys. The majority of work has been done using sequential deformation at room temperature [74,76,77,85,87-89]. Although this work is of scientific interest, it does not address the issue of strain path changes from an industrial manufacturing point of view. As many metals are frequently hot worked on a large scale, and with time (and financial) constraints, the deformation mechanisms and operating parameters will be significantly different. In addition to this, the sequential deformations cannot accurately represent the real strain path changes imposed upon a hot worked metal. This is due to the intimate relationship between strain path and texture [52], and thus the different slip systems that are activated by different shear and tensile deformation modes. In other words, sequential testing will not be able to evaluate the effects these different textures and deformation modes have on simultaneous deformation responses. In addition to this, sequential testing at high temperatures may also induce additional effects, brought about by thermally activated mechanisms (e.g. creep, dislocation climb or dynamic recovery) that may impose themselves upon the test results.

3. Material properties

3.1 Introduction

To formulate meaningful FE models of hot working operations fundamental material properties must be defined and often as a function of temperature, strain and strain rate. Accurate data, however, is not easy to acquire due to the inherent difficult nature of laboratory-based testing at elevated temperatures. This issue is also broadened when working on less commonly investigated materials such as titanium. It, therefore, can become necessary to extrapolate available data or utilise information from similarly behaving materials. Based on this information it is easy to see where errors can be introduced in to FE predictions so it is essential that all results are validated and that any uncertainties are well known.

This section initially introduces the material in its as received state and the flow behaviour over a range of temperatures (990, 1010, 1030 °C) and strain rates (0.2, 2, 20 s^{-1}). It will then concentrate on the material properties which are required to generate a coupled thermo-mechanical FE model. Most of these properties are dependant upon temperature and where possible are displayed as such. It will become clear that such data must be used with caution due to a large amount of scatter and the scarcity of available literature. The effects of these errors will be investigated in a later chapter.

3.2 Flow behaviour

The derivation of material flow curves from hot axisymmetric/plane strain compression tests forms the basis of the FE technique by providing essential material deformation behaviour and additional information to aid with the calibration and evaluation of FE models. The derivation of material flow curves relies on the assumption of uniform deformation (in this case) of a cylinder as depicted in Figure 3.1, The implies there is no barrelling during the compression and thus the instantaneous area of the test piece can be calculated as a result. However, for valid flow curves this assumption must be reasonable and as a result several test piece deformation parameters must be surpassed. These are highlighted is section 3.3.1 and 3.3.2. The raw data for the calculation of the following flow behaviour has been kindly supplied by Thomas [90].
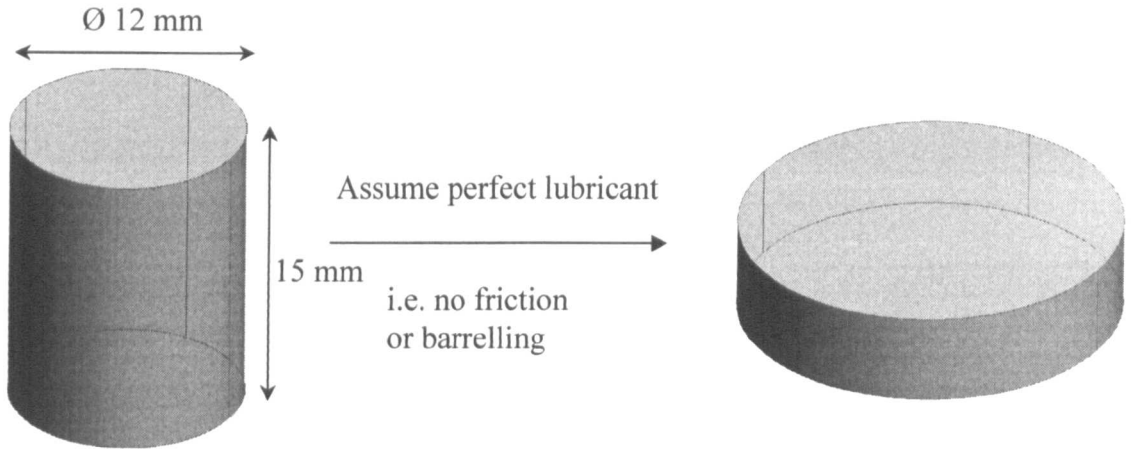
Figure 3.1 Assumed shape change of the test sample during hot compression tests

Assuming no barrelling and a constant volume of the material, the instantaneous area of the deforming cylinder is related to the instantaneous height of the cylinder (measured by the thermomechanical compression machine (TMC)) as shown below, where the volume of the axisymmetric sample is 1.696×10^{-6} m^3.

$$A_2 = \frac{1.696 \times 10^{-6}}{h_2} \tag{3.1}$$

The stress and strain used in the calculation are true stress/strain not engineering stress/strain. Thus:

$$\sigma = \frac{F}{A_2} \tag{3.2}$$

And

$$\varepsilon = \ln\left(\frac{h}{h_o}\right) \tag{3.3}$$

An equation or applying corrections for friction during axisymmetric compression tests is given by Dieter [32], but a value of friction coefficient (μ) is needed, for example;

$$P = R\left[\frac{h}{\mu d}\right]^2 \left[\exp\left[\frac{\mu d}{h}\right] - \frac{\mu d}{h} - 1\right] \tag{3.4}$$

Where P is the mean pressure, R is the true stress at intermediate time and h is the sample height at intermediate time. For low values of μ, a valid assumption for lubricated tests, this can be simplified by expanding the exponential term [91];

54

$$P = R\left[\frac{1 + \mu d}{3h}\right]$$

(3.5)

Where;

$$P = \frac{4F}{\pi d^2}$$

(3.6)

And;

$$R = \frac{F}{A}$$

(3.7)

By combining this information with that recorded by the TMC machine during the compression test, it is possible to derive the hot flow curves for the test material. The data logged by the TMC machine also allows it's control system to be check against the ideal test conditions required for a constant strain rate to be imposed.

If there is no sudden change in microstructure (e.g. precipitation or recrystallisation) within the temperature range being analysed then the sensitivity of the flow stress to strain rate and temperature can be expressed by the following equation [92]:

$$\sigma_\varepsilon = B_{(\varepsilon)} f\left(\dot{\varepsilon} \exp\left(\frac{Q_{def}}{RT}\right)\right) = B_{(\varepsilon)} f(Z)$$

(3.8)

Where

$\sigma_{(\varepsilon)}$ = flow stress at strain ε

$B_{(\varepsilon)}$ = material constant at strain ε

Q_{def} = activation energy of deformation

Z = Zener Hollomon parameter

f = an unknown functional relationship

$$Z = \dot{\varepsilon} \exp\left(\frac{Q_{def}}{RT}\right)$$

(3.9)

Rewriting Equation 3.8 to take the 'fixed strain value' to be the steady state strain value taken at the peak stress of the flow curve where s indicates the steady state value,

$$\sigma_s = B_s f\left(\dot{\varepsilon} \exp\left(\frac{Q_{def}}{RT}\right)\right)$$

(3.10)

Rearranging equation 3.10 so that;

55

$$\dot{\varepsilon} = C_s \exp\left(\frac{-Q_{def}}{RT}\right) \tag{3.11}$$

By taking the natural log of Equation 3.11 a linear plot of strain rate verses inverse temperature will yield the Q_{def} of the material, thus;

$$\log\dot{\varepsilon} = \frac{1}{\ln 10}\left(\frac{-Q_{def}}{RT}\right) + C \tag{3.12}$$

As the $\log_{10}$ function is simpler to plot the $1/\ln 10$ function is introduced to Equation 3.12, as $1/\ln 10 \equiv \log e$. However, firstly $\log\dot{\varepsilon}$ verses σ_s must be plotted to give data for a constant value of flow stress at different temperatures and corresponding strain rates. Figure 3.2 shows such a plot for Timetal®834.
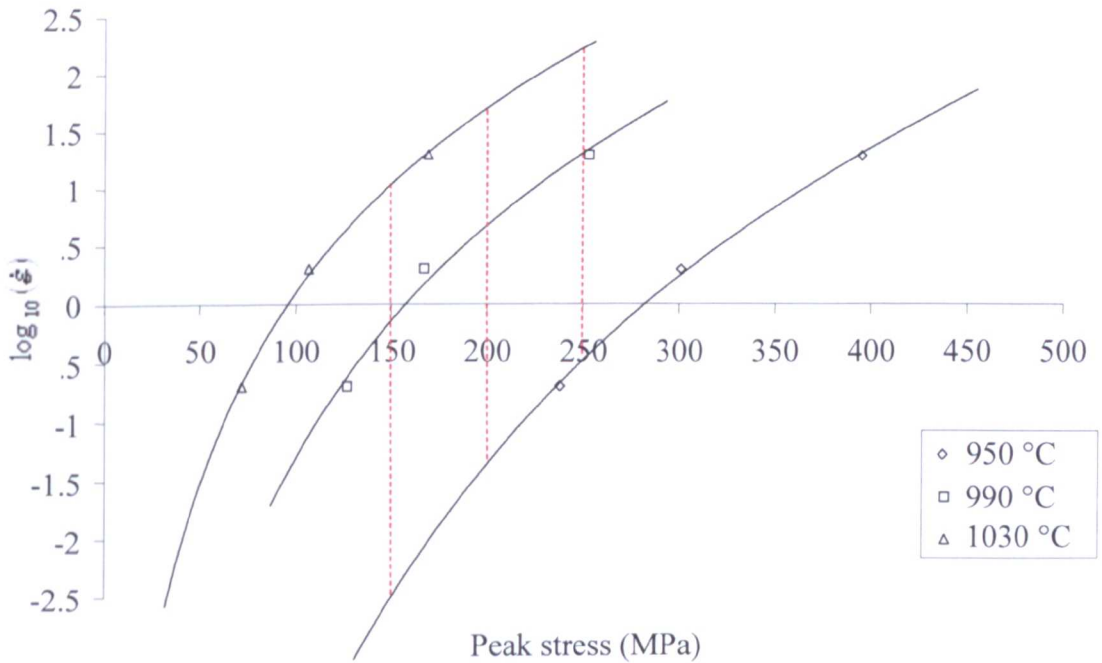
Figure 3.2 $\log\dot{\varepsilon}$ vs. peak stress for Timetal®834 at three different temperatures
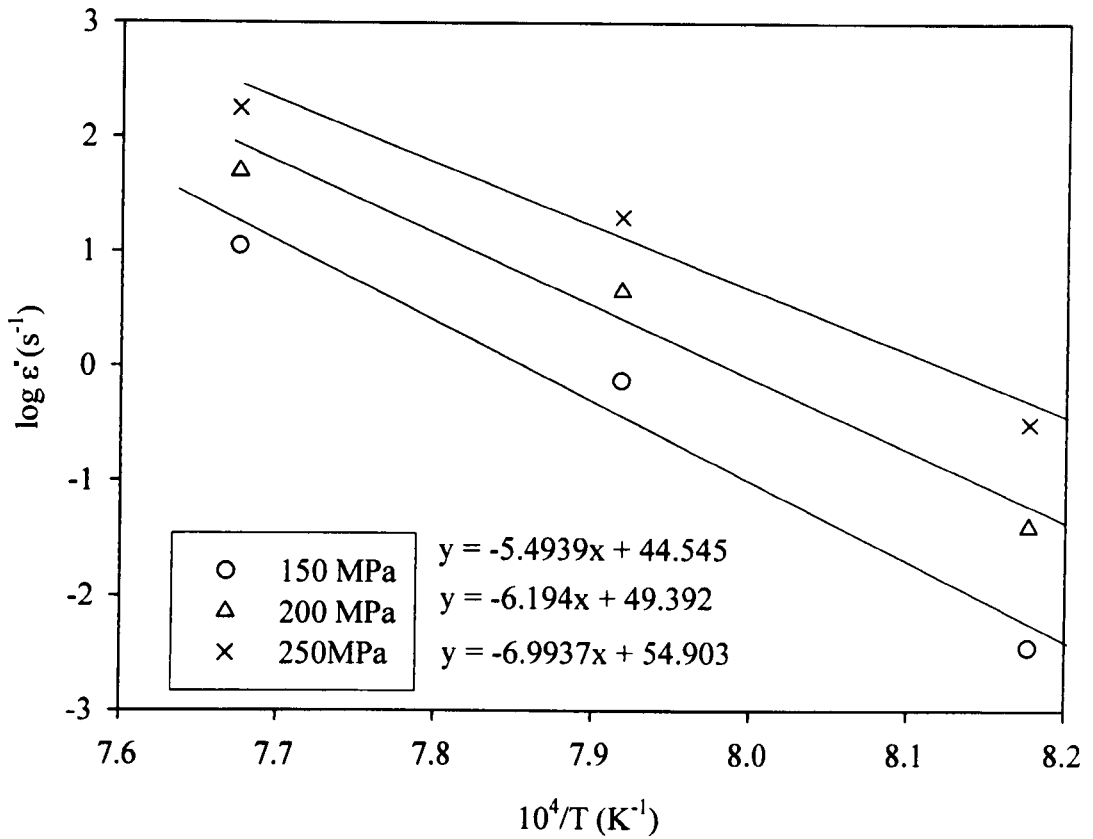
Figure 3.3 Plot of $\frac{1}{T}$ *vs.* $\log \dot{\varepsilon}$ *from which* Q_{def} *can be calculated from the gradient*

Thus, by determining $\dot{\varepsilon}$ to give the same flow stress at different temperatures (red lines in figure 3.2) this enables $\log \dot{\varepsilon}$ *to be* plotted against $\frac{1}{T}$ and Q_{def} can be determined as shown in figure 3.3. For a material where Q_{def} is constant over the deformation range all three curves will be parallel. However, the plot shows there is some discrepancy and may be attributed to the change in volume fraction of the two phases as the temperature of the test is changed and thus there is a significant change in the micro-mechanisms of deformation. However, using the value of the 200 MPa curve the Q_{def} is estimated at 1185 kJmol^{-1}.

When testing high strength materials large temperature variations can be exhibited due to deformation heating and heat transfer between tools and the test piece. Such temperature changes will effect the bulk temperature distribution within a test piece and may impose itself on the flow behaviour masking the true stress-strain behaviour. At high stresses the dependence of Z on the flow stress can be described by equation 3.13;

$$Z = A_2 \exp(\beta\sigma) \tag{3.13}$$

Where A_2 and β are material constants.

The value of the constant β can be found by plotting $\ln(Z)$ against σ and taking the gradient of the best fit line. Equation 3.14 can be derived from the exponential law (equation 3.13) to temperature correct every data point [93].

$$\sigma_2 = \sigma_1 + \frac{Q_{def}}{\beta R}\left(\frac{1}{T_2} - \frac{1}{T_1}\right) \tag{3.14}$$

Where σ_1 and T_1 are the experimental values of stress and temperature respectively, σ_2 and T_2 are the corrected isothermal values. R represents the universal gas constant that is taken to be 8.31 JK^{-1}mol^{-1}. The following graphs show the corrected (temperature and friction) and uncorrected flow behaviour for Timetal®834 at 950, 990 and 1030 °C and strain rates of 0.2, 2 and 20 s^{-1}.
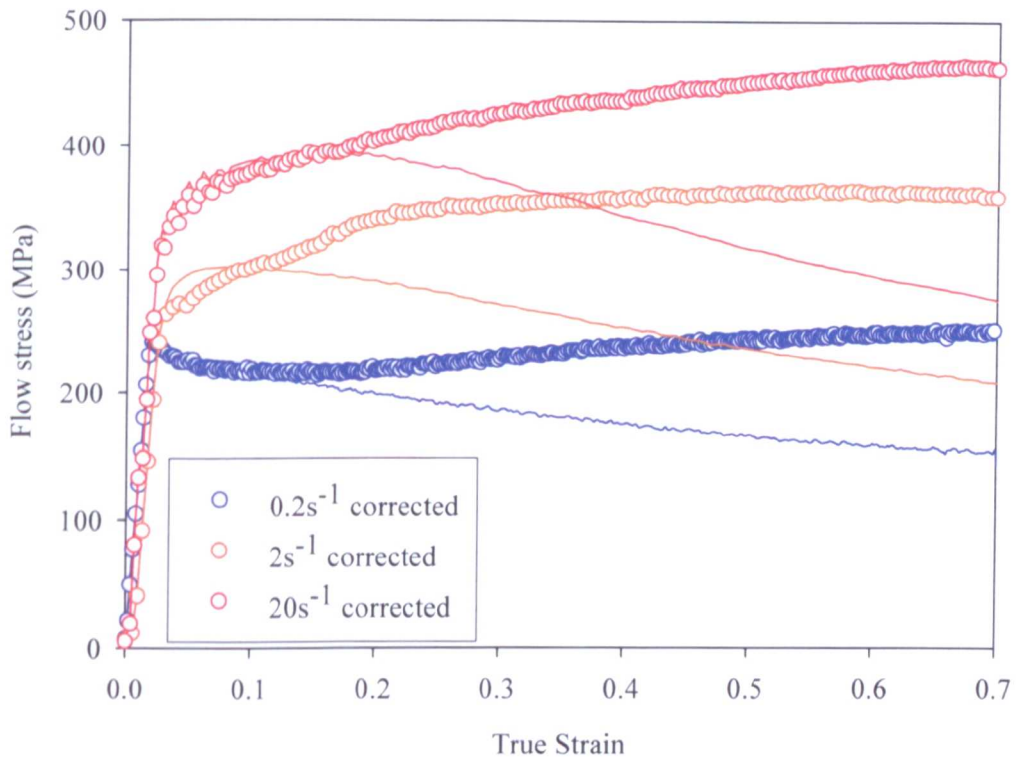
Figure 3.4 Calculated and corrected (deformation heating and friction) flow curves for Timetal®834 at 950 °C and $\dot{\varepsilon} = 0.2, 2, 20s^{-1}$. Solid lines represent uncorrected data

58
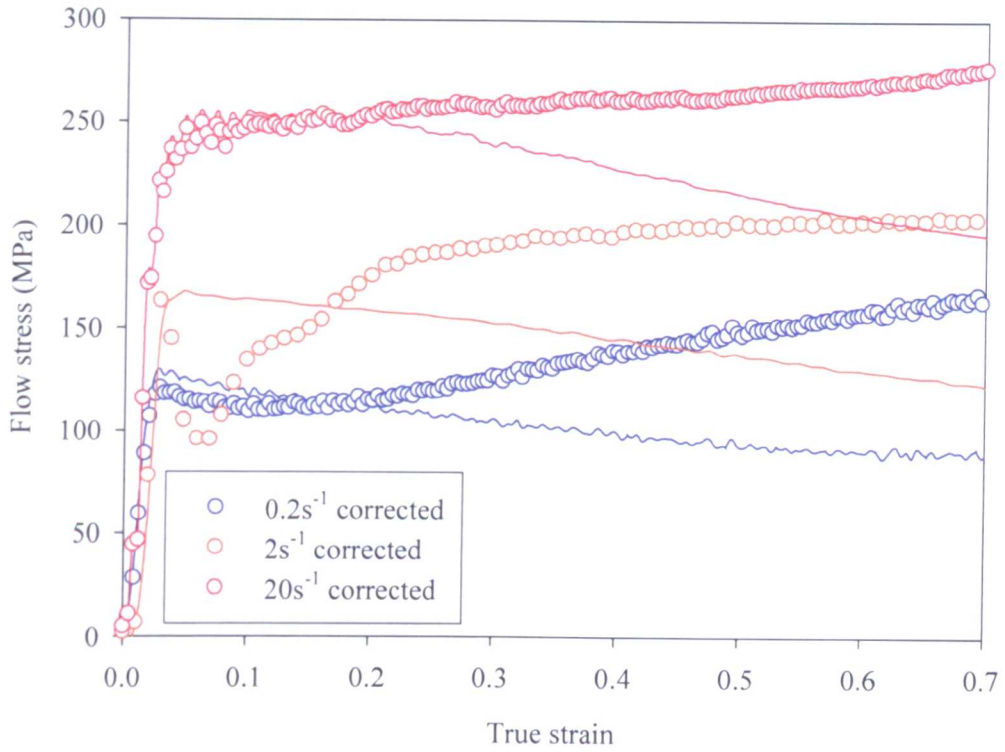
Figure 3.5 Calculated and corrected (deformation heating and friction) flow curves for Timetal®834 at 990 °C and $\dot{\varepsilon} = 0.2,2,20s^{-1}$
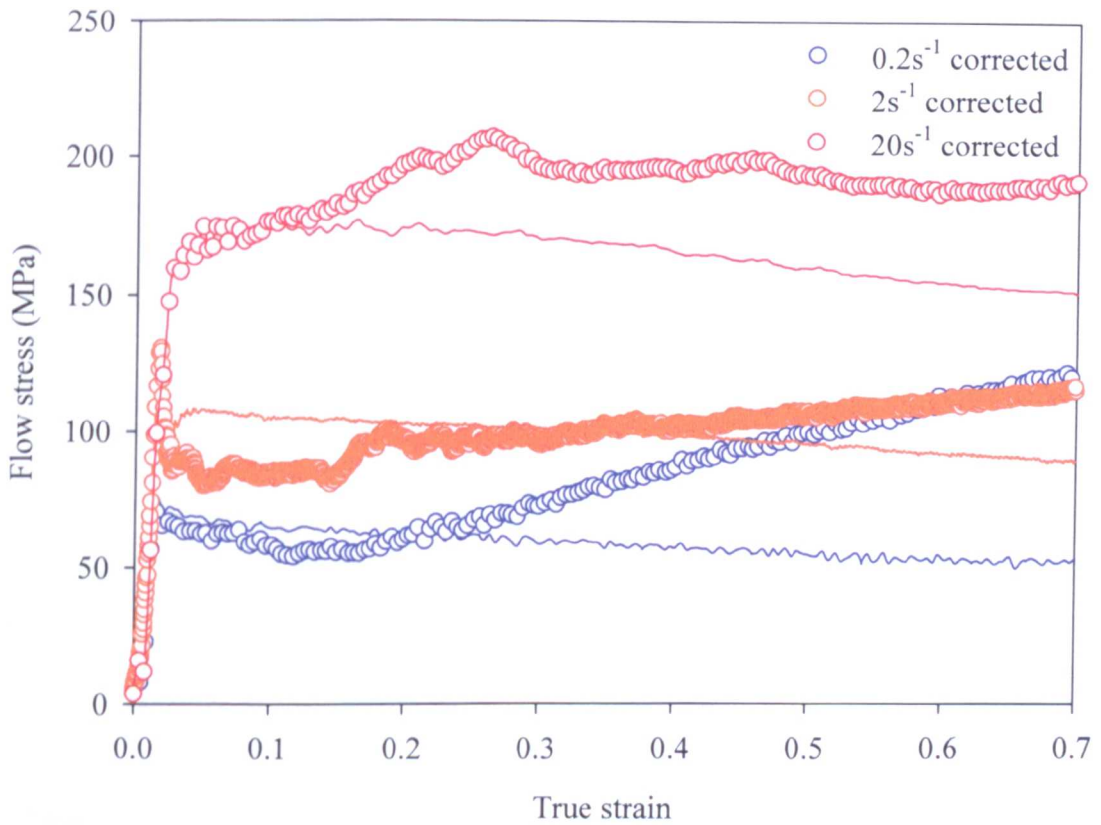
Figure 3.6 Calculated and corrected (deformation heating and friction) flow curves for Timetal®834 at 1030 °C and $\dot{\varepsilon} = 0.2,2,20s^{-1}$

The drop in figure 3.5 and 3.6 of the $\dot{\varepsilon} = 2s^{-1}$ curve is due to brief thermocouple separation and loss of intimate contact with the material as the thermocouple hole is squashed in the deformation which has also been observed by Jupp [94].

The flow behaviour of Timetal®834 has been modelled by Wanjara *et al.* [95] where the flow behaviour can be expressed using equation 3.8;

$$\dot{\varepsilon} = A_m \sinh(\alpha\sigma)^n \exp\left(\frac{-Q_{def}}{RT}\right)$$

(3.8)

For the α & β region (915 °C-1045 °C) the material constants (A and α), stress exponent and activation energy respectively are:

$A_m - 1.188 \times 10^{28}$

$\alpha - 0.018$

$n - 3.66$

$Q_{def} - 703,000$ J/mol

For the β region (above 1045 °C):

$A_m - 0.86 \times 10^6$

$\alpha - 0.018$

$n - 3.64$

$Q_{def} - 153,000$ J/mol

The above information can be used to describe the yield surface of the material with MSC Superform FE software using the so called 'Kumar model' but requires flow stress to be defined as;

$$\sigma = B_o \sinh^{-1}\left[\left(\frac{\dot{\varepsilon}}{A_m}\right)^{1/n} \cdot \exp\left(\frac{Q_{def}}{RT}\right)\right]$$

(3.9)

Rearranging Equation 3.8

$$\frac{\dot{\varepsilon}}{A_m} \exp\left(\frac{Q_{def}}{RT}\right) = \sinh(\alpha\sigma)^n$$

(3.10)

Thus

$$\sigma = \frac{1}{\alpha} \sinh^{-1}\left[\left(\frac{\dot{\varepsilon}}{A_m}\right)^{1/n} \cdot \exp\left(\frac{Q_{def}}{RT}\right)\right] \qquad (3.11)$$

Where B_0 is equal to α^{-1} (55.56).

By analysing the activation energies in the literature it is clear to see that Wanjara's 703 kJmol⁻¹ is low and tested a bimodal initial microstructure with approximately 20% α_p the same as that of heat treated in-service material. Thomas and Bate [90, 96] have reported activation energies of 985 and 803 kJmol⁻¹ (over a temperature range of 950-1020 °C) respectively. The starting microstructures for Thomas and Bate contained 40% and 70% α_p respectively. Such scatter in these results would suggest the content of the 'harder' α_p phase will play a major role in the deformation mechanisms. The full thermomechanical history of the material will also play a role and so the different starting microstructures and process routes of the various authors materials produces scatter in the observed values of calculated Q_{def}.

To model the material behaviour with the commercial FE code MSC Superform the parameters calculated by Wanjara *et al.* [95] will be used. However the activation energy will be modified as this work does not take into account the significant amount of deformation heating that is generated when hot working titanium alloys. Thus, Wanjara's material model describes a material that has a lower flow stress than in reality and so Q_{def} in this work is taken to be 775 kJmol⁻¹ and equation 3.11 becomes;

$$\sigma = 55.56 \sinh^{-1}\left[\left(\frac{\dot{\varepsilon}}{1.188 \cdot 10^{28}}\right)^{1/3.66} \cdot \exp\left(\frac{775000}{8.31 \cdot T}\right)\right] \qquad (3.12)$$

The validity of this equation is discussed in section 5.1.1.

3.2.1 Aspect ratio

The test sample starting dimensions were; h_1 – 15mm and $\varnothing_1$ – 12mm. These samples had small troughs machined into their top and bottom surfaces to retain the glass lubricant during testing. Their aspect ratio was 1.25 in accordance with the good practice guide lines where any value between 1-2 maybe utilised [91].

Another important aspect affecting the validity of a test is final shape of the test piece. This can be affected by a magnitude of different factors, all of which must be assessed to validate the test. For example if the there is significant barrelling then frictional effects will impose themselves on the test data and result in large uncertainties in the measured flow stress. Following the good practice guide [91] the barrelling coefficient is defined as;

$$B = \frac{h_f d_f^2}{h_o d_o^2}$$

(3.12)

The ovality coefficient is defined as the ratio of the maximum to the minimum diameters of the deformed test piece.

$$O_v = \frac{d_{f\,max}}{d_{f\,min}}$$

(3.13)

Ovality can occur though microstructural and texture effects on the deformation behaviour of the test piece and can be particularly relevant for hexagonal close packed materials.

The height coefficient relates the ratio of the standard deviation of four measurements of the deformed height to the average height of the deformed test piece.

$$H = \frac{Sh_f}{h_f}$$

(3.14)

If H is equal or greater than 0.04 then the test is deemed invalid.

3.3 Young's modulus

Young's modulus is defined as the slope of the stress-strain curve in the elastic region and represents the resistant of the material to deform elastically. Information on the temperature dependence of Young's modulus for titanium alloys is hard to come by. As the elastic deformation is small compared with the plastic any temperature effects are ignored and the Young's modulus is taken to be that of the room temperature value for this alloy (120 GPa).

3.4 Poisson's ratio

Poisson's ratio is defined as the ratio of lateral strain to axial strain in an axially loaded specimen. In the elastic region Poisson's ratio, ν, is given by:

$$\nu = \frac{E}{2G} - 1 \qquad\qquad (3.15)$$

where E is the Young's modulus and G is the elastic shear modulus. Although data is very limited on the temperature dependence of Poisson's ratio it is safe to assume that it would be affected by temperature. However under hot working conditions elastic strains are typically small and ignored during analysis. The room temperature value for Poisson's ratio of Ti-6Al-4V is taken to be 0.34 for all analyses.

3.5 Specific heat capacity

The specific heat capacity of a material defined as the amount of heat energy required to raise the temperature of a unit mass of the material by one Kelvin and those SI units are $J^{-1}kg^{-1}K^{-1}$. To convert from units of $cal^{-1}g^{-1}K^{-1}$ to an SI value a multiple of 4187 can be used. For the purpose of this text the specific heat capacity is defined as c_p, the specific heat capacity at constant pressure as the majority of material processing is typically conducted at constant pressure, i.e. atmospheric pressure. The effect of temperature on the specific heat capacity of thirteen commercially pure (CP) and two Ti-6Al-4V alloys is taken from Touloukian [97] and shown in Figure 3.7. This graph suggests the aluminium and vanadium additions do not have much of an influence on c_p as there is little scattering of the results. The c_p gently increases with temperature up to the beta transus (~1150 K) where there is a sudden increase due to increased energy absorption as the crystal structure rearranges from a hexagonal close packed to a body centred structure.
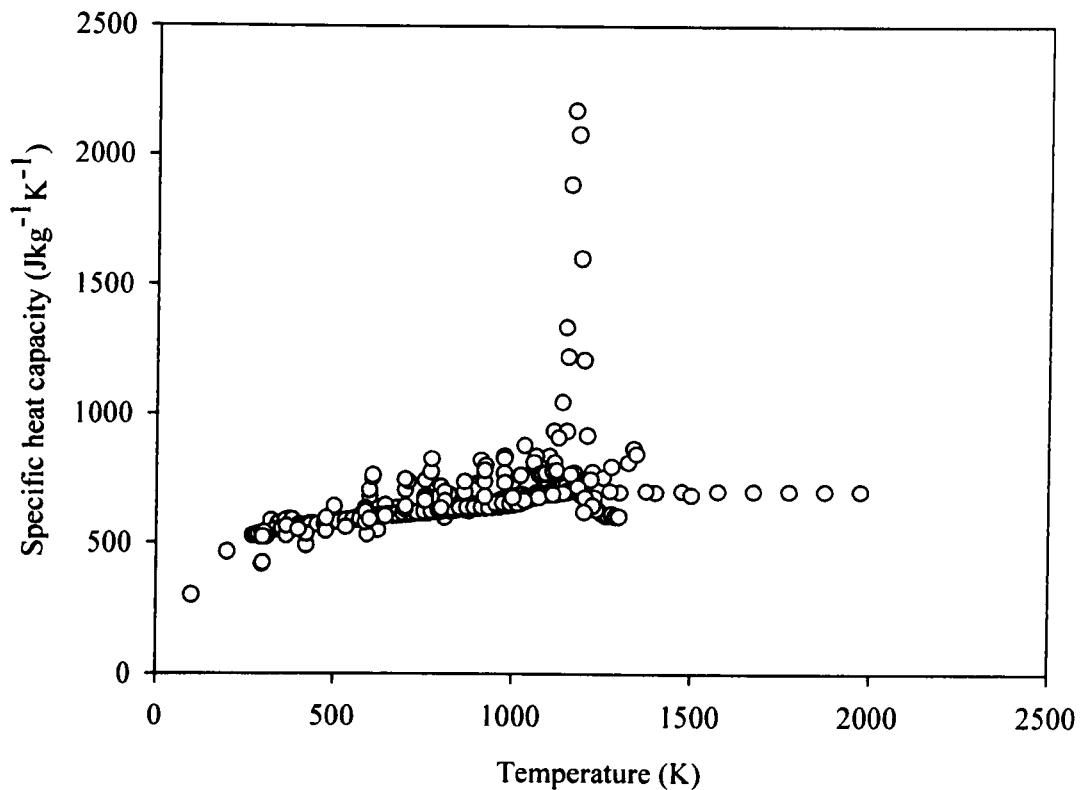
Figure 3.7 Plot showing fifteen different data sets of the specific heat capacity for CP titanium and titanium 6-4, adapted from [97]

After the crystal structure has changed the specific heat capacity then begins to slowly rise similar to that of the alpha phase. For the purpose of FE modelling the spike in c_p at he beta transus will be ignored and the specific heat capacity will be assumed to be an average value 690 $Jkg^{-1}K^{-1}$.

3.6 Thermal conductivity

Thermal conductivity is defined as the quantity of heat that passes in a unit of time through a unit of area of a plate, whose thickness is unity, when its opposite faces differ in temperature by one degree. Practically speaking it is a measure of a material's ability to transfer heat with titanium being classed as a poor thermal conductor. The thermal conductivity of selected CP and titanium alloys [97] over the temperature range of 200-1600 K is shown in Figure 3.8.
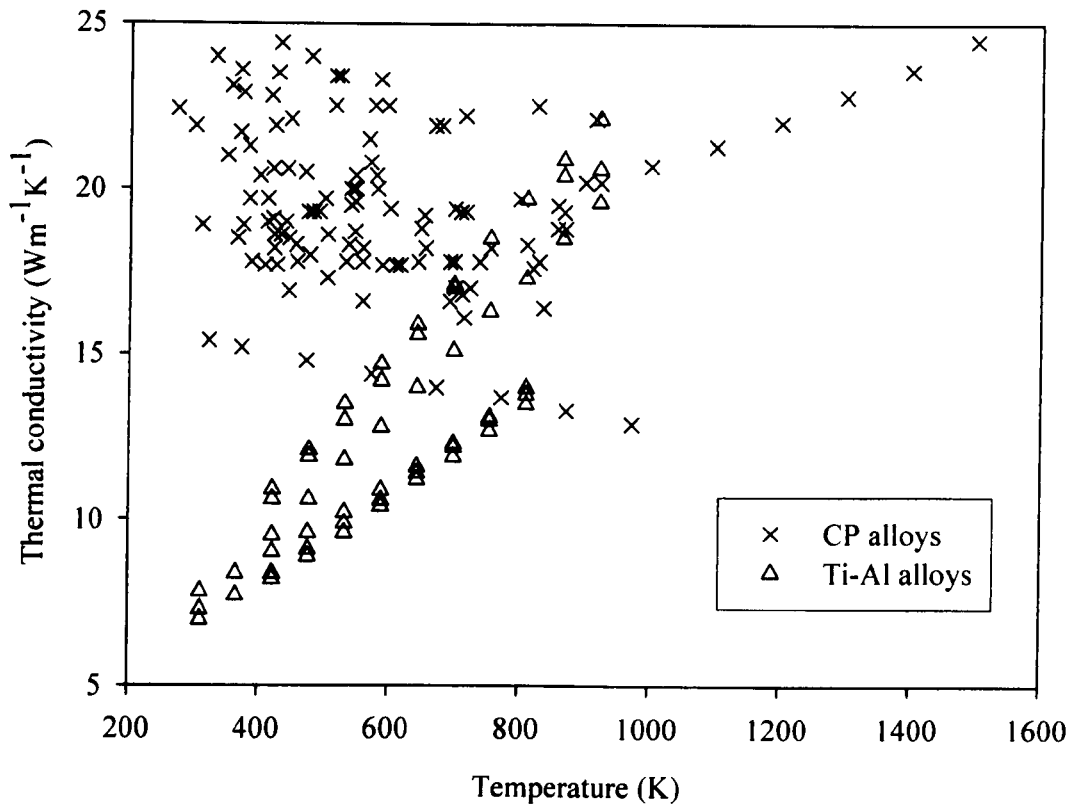
Figure 3.8 Thermal conductivity for various CP titanium and α/β-alloys adapted from [97]

When the temperature of a metal increases the two opposing factors effect where the thermal conductivity increases or decreases. The higher temperature is expected to increase the energy of the valence electrons and thus creating more 'carriers'. However, the greater lattice vibrations scatter the mobile electrons and reduce the thermal conductivity. This combined effect leads to very different behaviour for different metals and alloys and creates large amounts of scatter in results. Figure 3.8 shows the thermal conductivity has a reasonably constant value over a large temperature range for CP titanium where as for the titanium alloys thermal conductivity increases linearly with temperature. For modelling purposes k is assumed to be a constant 13 $Wm^{-1}K^{-1}$.

3.7 Thermal expansion coefficient

Thermal expansion coefficient is defined as the change in dimension of a material per unit length for one degree change in temperature. The variation of the average thermal expansion coefficient for selected CP titanium alloys is given in Figure 3.9. These values are considered to be ± 3 °C and ± 5 °C accurate in the alpha and beta phase regions respectively [97].
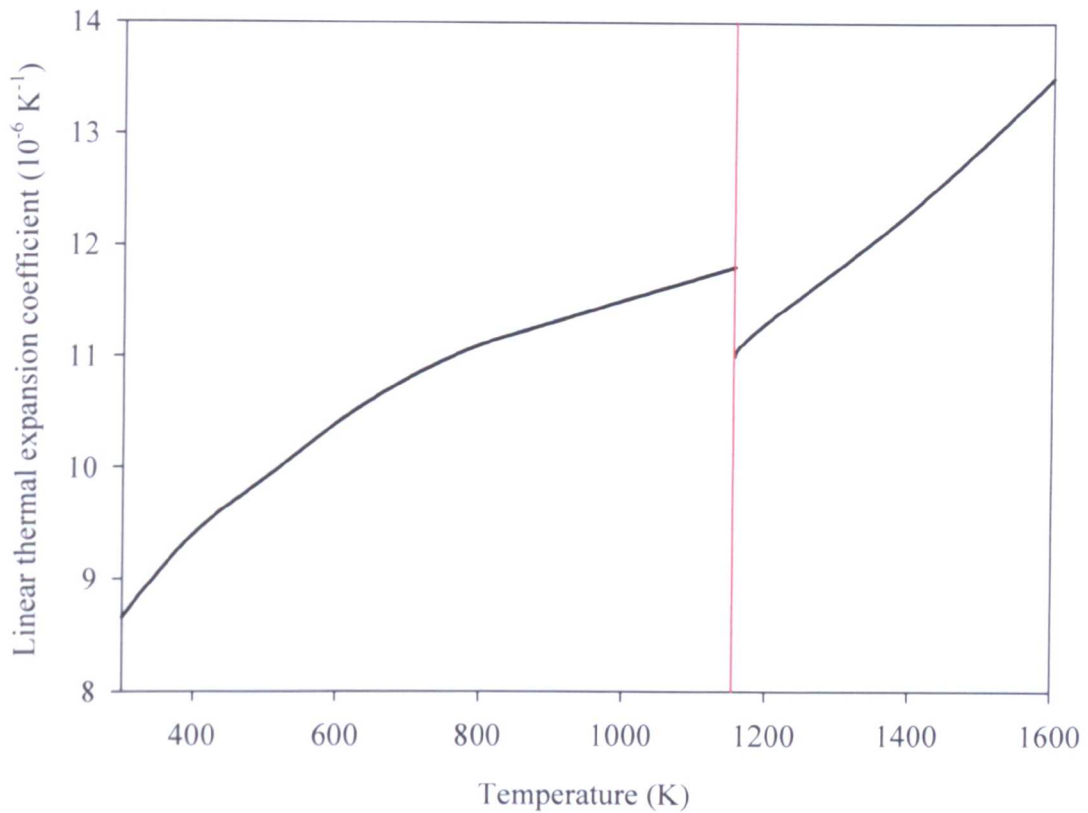
Figure 3.9 Thermal expansion coefficient for CP titanium alloy adapted from [97]. The beta transus is shown by the red line

The coefficient of thermal expansion is related to the strength of the atomic bonds. As a result materials with higher melting points tend to have smaller thermal expansion coefficients. The expansion characteristics of a material are also dependant on sample orientation due to crystal anisotropy and phase changes. The expansion coefficient is also affect by the phase change at the α/β or β transus where the material becomes isotropic in the β phase. The effects of the abrupt change from α to β phase can be seen in Figure 3.9. For alloys which possess an α/β transus the change varies linearly until the β thermal expansion (α_T) is reached. The values for α_T with respect to the a or c crystal axis for the α phase do not vary greatly and are ignored in this text.

Alloy additions have little effect on α_T. Table 3.1 shows the values for three different titanium alloys at 1100 K.

Table 3.1 Thermal expansion coefficients for three types of titanium alloys which are considered to be accurate within ± 7 °C over the temperature range [97]

Alloy	α_T (1100K)
Ti + 5Al + 5Sn + 5Zr + Σ X_i	10.4×10^{-6}
Ti + 6Al + 4V+ Σ X_i	11.6×10^{-6}
Ti + 4Al + 3Mo+ Σ X_i	11.8×10^{-6}

For FE analysis α_T is assumed not to vary over the narrow hot working temperature range and has the value of 10.4.

3.8 Emissivity

Real surfaces are not perfect emitters and absorbers of radiation energy. The emissivity of a material is defined as the ratio of energy radiated by that material compared to the energy radiated by a black body at the same temperature where a true black body is a perfect emitter and has an emissivity of 1. In a practical sense it is a measure of a material's ability to absorb and radiate energy. Figure 3.10 shows the emissivity for three different CP and two α/β titanium alloys measured by a variety of methods and authors.
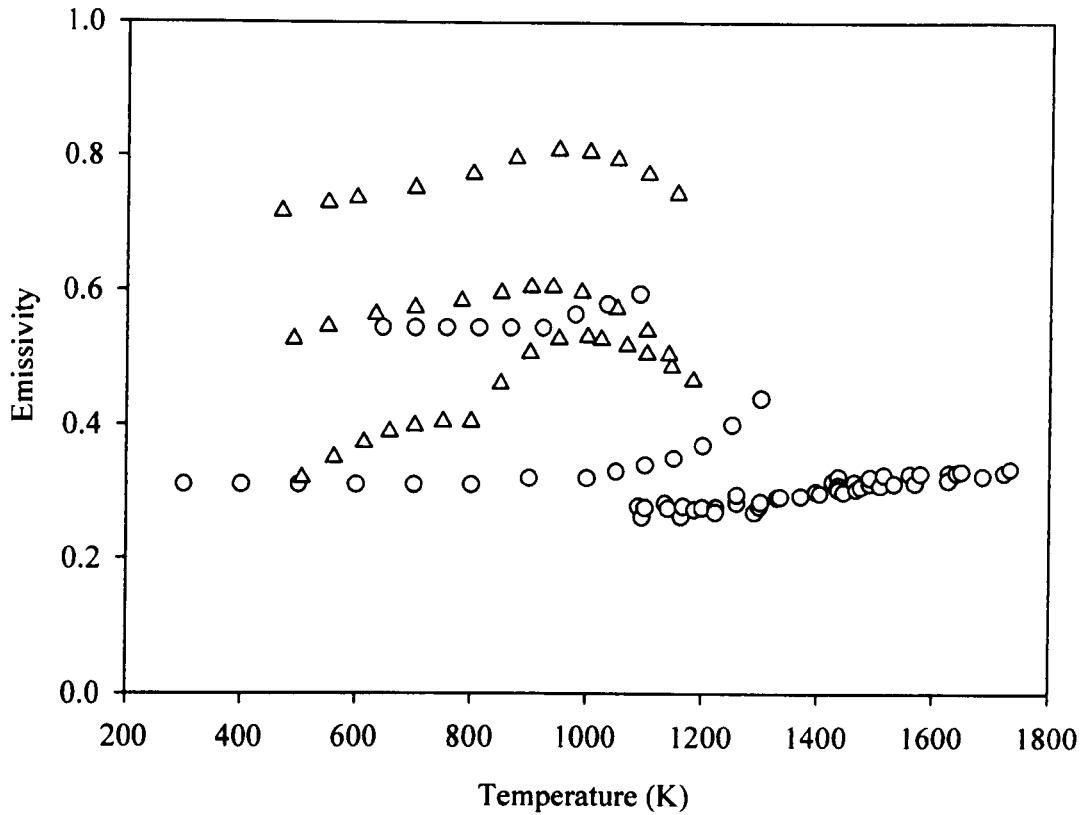
Figure 3.10 Compilation of total hemispherical emissivity for CP (triangle) and titanium + Al + Σ X$_i$ alloys (circle) plotted against temperature adapted from [97]

Values for emissivity however demonstrate great scatter as it is a function of wavelength, direction, temperature and surface finish. The surface finish is often not a constant during a test as samples begin to oxide at elevated temperatures. The average emissivity is taken for this analysis and so is averaged with respect to the wavelength and directional emissivity. It will also be assumed that the oxide formed during hot working will not affect the value. A value of 0.45 is estimated at the upper level of the titanium + Al + Σ X$_i$ alloys and the lower level of the CP titanium. This is used in Section 4.2.1.5.2 to predict a value for the combined convectional-radiation heat loss coefficient.

3.9 Conclusions

The fundamental material properties necessary for this work have been defined and, where possible, described as functions of temperature. The data shows that many of the parameters to be used in FE modelling due not need to be defined as a function of temperature as variations are small over the processing temperature range. Many of the properties titanium are not well established in the literature and so the information has been extrapolated based either upon available data or theoretical considerations. Examples of this are the specific heat capacity, which shows large amounts of scatter in the data, and the emissivity which is always difficult to predict. When extrapolations have been employed, the reasoning has been explained. Overall, the necessary information for modelling has been described. However, a model is only a reflection of reality and is only as good as the information provided to it. As a result any input parameter demonstrating uncertainty in its exact value will be evaluated with FE modelling; this will include effects of k and c_p.

The flow curves of Timetal®834 have been calculated and show the typical behaviour of the material under various strain rates and temperatures. For the purpose of FE modelling a mathematical empirical model has been developed based on the activation energy and method applied by Wanjara *et al.* [95]. This model takes into account the initial model has significant error due to the lack of isothermal correction. A modified value of Q_{def} is therefore used which, with a degree of experimental error, is similar to that measured by this report and additional authors [90,96].

4. Experimental Procedure

4.1. Introduction

This section of the thesis introduces the FE modelling undertaken, the ASPII machine and how data generated by the FE models is replayed upon the ASPII machine. Details of sample preparation after testing are also presented. The initial FE modelling was carried out in conjunction with axisymmetric compression data from tests carried out within the research group. This information was used to determine the flow behaviour of Timetal®834 and also as validation of the models. When particular material parameters were hard to come by in the literature or there was significant scatter in the results then parameter sensitivity analysis was carried out to evaluate the magnitude of their effects on the model results. The more advanced forging models are based on the information generated by the axisymmetric models.

Initial strain path work concentrated on good practice guidelines and the calibration on the machine. This included thermal and mechanical calibration, and how to load a sample for accurate and reproducible test results. Without such work no tests derived form FE strain path data could be deemed valid as the ASPII machine would not replay them accurately. This was followed by 'extreme' strain path change testing to investigate the potential break down of clustering of similarly orientated primary alpha grains. Later strain path work is derived directly from the deformation calculated in industrial forging models.

4.2. FE modelling

The finite element method by it's very nature produces large amounts data. As a result the majority of modelling is only carried out upon a particular section of the component being analysed as there is often a symmetry plane within a component. The flow behaviour for Timetal®834 was obtained from data provided by Thomas [90] who carried out axisymmetric compression tests over a temperature range of 950-1030 °C and a strain rate range of 0.2-20 s^{-1}. From this raw data isothermal and frictional corrected flow curves where derived. These can be found in Section 3.2 along with the methodology to derive them. Due to issues with the FE software accepting the calculated flow curves were not used to define the flow behaviour and so the flow curves are only used to gauge the material flow behaviour under different temperatures and strain rates. Instead a modified version of the stress-strain relationship derived by Wanjara et al. [95] has been utilised, details of which can be found in Section 3.2. Nine elastic-plastic axisymmetric models consisting of 4-node heat conducting quadrilateral axisymmetric elements were conducted at 950, 990, 1030 °C and strain rates of 0.2, 2,

20 s^{-1} using the commercially available MARC Superform FE code. All other axisymmetric compression FE models used to investigate modelling parameters are based upon this first model. Table 4.1 shows the material and model parameters used in the analysis together with their SI units.

Table 4.1 FE model parameters for various models

Parameter	Symbol	Value			Units (SI)
Bulk thermal properties					
Density	ρ		4500		kgm^{-3}
Specific heat capacity	c		686		Jkg^{-1}m^{-3}
Thermal conductivity	k		13		Wm^{-1}K
Heat conversion efficiency	η		0.9		-
Heat transfer parameters		*Cold*	*Warm*	*Hot*	
Tool-workpiece coefficient	h_t	20	25	30	kWm^{-2}K
Environment coefficient	h_a	170	200	350	Wm^{-2}K
Temperatures					
Tools	T_t		300		°C
Ambient	T_a		15		°C
Workpiece	T		variable		°C

Due to axisymmetric rotational symmetry a quarter model of the axisymmetric compression samples was used. These cylindrical samples had a diameter of Ø12mm and a height of 15mm.
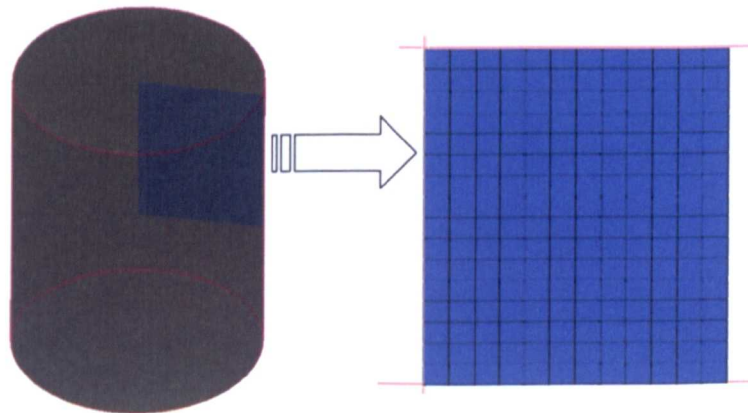
Figure 4.1 (a) Axisymmetric compression sample and (b) equivalent FE model (quad element mesh)

For the FE model the tool velocities need to be specified to ensure a constant strain rate is applied during the compression test and subsequent model. This is calculated in full

in Section 4.4.3. It can be shown that the tool velocity for an axisymmetric compression test conducted at a strain rate of 0.2 s^{-1} will be governed by Equation 4.1 where l is the instantaneous sample length, l_o the initial length, $\dot{\varepsilon}$ the strain rate and t-time. Thus, using the sample dimensions the instantaneous length of the compression sample compressed at a strain rate of 0.2 s^{-1} is;

$$l = 15 \left(\exp(-0.2 \ t) \right) \tag{4.1}$$

To compress the 15mm sample to a strain of -0.7 this strain rate is imposed for 3.5 sec and can be seen in half second increments in Table 4.2 below. For the FE models these velocities are halved as the model only represents one quarter of the sample.

Table 4.2 Calculated tool velocity and instantaneous sample height during a compression test carried out at 0.2s^{-1}

Time (s)	Sample length (mm)	Velocity (mms^{-1})
0	15	3
0.5	13.57	2.71
1	12.28	2.46
1.5	11.11	2.22
2	10.05	2.01
2.5	9.10	1.82
3	8.23	1.65
3.5	7.45	1.49

4.2.1. Parameter sensitivity analysis

The ability for an FE model to produce an accurate solution depends strongly on many input factors such as the materials flow curves, boundary conditions and the mesh used. As a result different parameters were varied in the models used to investigate the magnitude of their effects on important test parameters such as strain, strain rate and temperature.

4.2.1.1. Mesh sensitivity

To determine the point when the model becomes insensitive to the mesh density the axisymmetric model was run with an increasing number of elements at a temperature of 825 °C, $\dot{\varepsilon} = 1s^{-1}$ and with the auto-remesher active. The remesher deviation angle was set to 40° and the outside remesh refinement level to 2. The x and y direction symmetry

was fixed and the friction was modelled as coulomb friction with a relative sliding velocity of 0.01 and a friction coefficient of 0.3. All heat transfer coefficients were set to zero to neglect heat induced effects.

4.2.1.2. Remesh effects

The automatic remesher within the MSC software was utilised to minimise errors brought about by large element distortion and to allow the modelling of the complex forging die dimensions and prevent tool penetration into the workpiece. The remesh criterion has two predominant parameters which may affect its performance. These included the outside element refinement levels and the derivation angle [98]. The outside refinement governs how many layers of elements on the outside of the workpiece are to be refined when significantly distorted. Figure 4.2 illustrates this but it must be noted that in an actual model all the node connections will ensure connectivity is maintained unlike the simplified representation below.
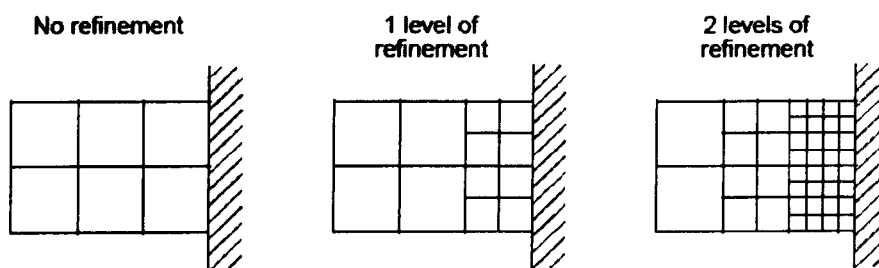
Figure 4.2 Levels of outside element refinement when workpiece is distorted by a solid object [98]

The element distortion deviation angle remeshes the identified body when the distortion in an element becomes large, or it is anticipated that it will become large. This criterion is based upon examining the angles of the elements at the end of the increment and an estimate of the change in angle in the next increment. For example, for a square element mesh with a remesh deviation angle of 10° would remesh when one of the corner angles within the square element is distorted greater than 80° or 100°.

Theses two models use the same initial condition and boundary conditions as Section 4.2.1.1. The first set of models had the deviation angle changed from 5° to 40°. The second set of models where run with a deviation angle of 40° and the outside refinement level ranged from 2 to 5. Tool penetration is ignored as there are no curved tool surfaces, however this will be important in later models.

4.2.1.3. Thermal conductivity

In Chapter 3 it has been shown there is always a significant amount of uncertainty in thermo-physical properties of a material. The following section investigates whether such values have a significant effect on the outcome of a model.

By comparing alloys with similar chemical compositions as Timetal®834 it was assumed that the thermal conductivity varied from 18 $Wm^{-1}K^{-1}$ at room temperature to 13 $Wm^{-1}K^{-1}$ at 1400 K. To investigate the effects of using different thermal conductivities models were run with thermal conductivities of 13, 18, 100 and 200 $Wm^{-1}K^{-1}$. The larger values of 100 and 200 $Wm^{-1}K^{-1}$ are typical values for an aluminium and copper alloy and would exaggerate any possible effects more than the subtle change from 13 to 18 $Wm^{-1}K^{-1}$. The workpiece was at a temperature of 975 °C, deformed at $10s^{-1}$, m = 0.3, and the tool heat transfer coefficient was set to 20 $kWm^{-2}K^{-1}$.

4.2.1.4. Frictional effects

In metal forming friction plays a crucial role in determining the life of the tools, the flow of the material and the quality of the final component. Industrial forging processes are too complex to analyse analytically without the aid of sophisticated modelling techniques due to inherent complexity of the interaction between the metal flow and the undulating die geometry. Many operations are carried out without lubrication and as a result simple sliding friction conditions between to tool and the workpiece no longer apply [92]. Furthermore, the friction is also dependant on temperature, tool velocity, lubricant, and strain rate, all of which are not constant over the workpiece [99,100]. In practical hot working conditions (and in this work) an average μ is defined for convenience. Values for the coefficient of friction are difficult to come by in the relevant literature. Hu *et al.* [101] using a shear stress based friction model suggest friction factors in the region of 0.1 - 0.3 for a lubricated Ti-6/4 alloy. Liu [102] forged IMI 685 with no lubricant and found there was no slip and modelled the friction as rough friction. Similarly Brookes [103], Srinivasan *et al.* [104] and Zhan [105] all used a friction factor of 0.2 for the forging of Ti-Al, glass lubricated Ti-685 and Ti 6Al-4V respectively. The industrial forging process modelled in this study uses a graphite lubricant. The sliding between the tool and the specimen surfaces has been modelled using a shear based model of friction such that;

$$\tau = -mk_Y \frac{2}{\pi} \arctan\left(\frac{v_{rel}}{C}\right)\bar{t} \qquad (4.2)$$

In forging operations were there are high deformation speeds (and thus v_{rel} is high) the coulomb friction criterion can not be used as it will often yield friction stresses that are greater than that of the materials tensile strength. In Equation 4.2 τ is the shear/frictional stress; m is the friction factor, k_Y is the shear yield stress; and $\bar{t}$ is the tangent unit vector in the direction of the relative sliding velocity; C is a constant taken to be about 1% of a typical relative velocity v_{rel}, which smoothes the discontinuity in the value of the shear stress when stick/slip transfer occurs between the surfaces in a contact. A very large value of C results in a reduced effective value of friction where a small value results in poor convergence. A value of between 1 and 10% of the relative sliding velocity is typically used.
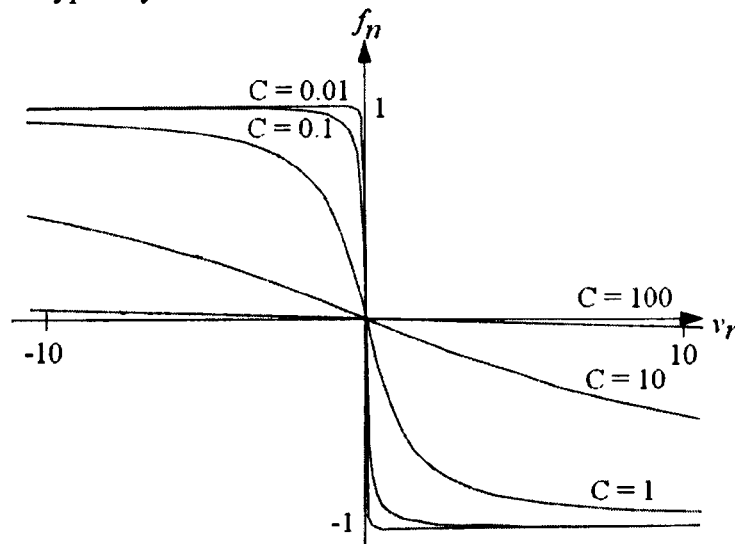
Figure 4.3 Effect of c on the stick-slip step function [97]

An isothermal version of the axisymmetric model (to neglect any thermal effects) was run at 990 °C and a strain rate of 2s⁻¹. The friction coefficient was varied from 0.2 to 0.6 in 0.1 intervals and the effects on strain distribution within the sample are plotted in Section 5.1.2.

4.2.1.5. Heat transfer coefficients

Heat transfer coefficients are notoriously difficult to measure and estimate as they are dependant on many different factors and often vary with time, temperature, pressure, etc. The MSC Superform software has preset heat transfer coefficients for the environmental heat sink and tool transfer coefficients. These include three values of cold, warm and hot forming coefficients as shown in Table 4.1. These were used to evaluate the extent of their effects on the models and to give rough ball-park numbers by which to work with. The workpiece temperature was 825 °C, $m = 0.3$ with a remesh deviational angle of 40° and refinement of 2. For the first set of models the tool transfer

coefficient was set to zero and the environmental transfer coefficient was varied. For the second set of models the inverse was applied.

4.2.1.5.1. *Convectional heat loss*

Convection is essentially heat conduction through a fluid; however the flow of the fluid modifies the conductive heat transfer. The heat is conducted into the layer of fluid in contact with the object, and this layer is then swept away down stream and transferred to the surrounding fluid. Convectional heat transfer can be classified in accordance with the nature of the fluid flow by which an object is surrounded. If the fluid is being driven by an external means, for example by a fan or a pump, then it is said to be forced convection. However, convection may also arise from temperature (and thus density) distributions caused by the presence of an object at elevated temperatures, higher than that of the mean surrounding temperature. Such a mechanism is known as free or natural convection. The convectional heat transfer coefficient depends on many factors which include specific heat, viscosity, thermal conduction, density, temperature difference, and the state of the fluid in contact with the solid. As a result analytical determination of h_a is extremely difficult and so is often determined empirically [101]. Although forced convection is being imposed on the upper loading cell of the ASPII machine (to cool it; see Figure 4.9), it will be assumed that this has no effect on the convection experienced by the ASP specimen. Only natural convection will be assumed at the ASP specimen. The surrounding air is also assumed to be quiescent. Generally natural convection will produce laminar flow over the heated object due to the low airspeeds. However, due the undulating geometry of the ASP sample and the geometry of the ASPII machine, it is difficult to gauge whether the airflow will be turbulent or laminar. As mentioned by Incropera [106] the transition from laminar to turbulent flow has a strong effect on heat transfer. The calculations below show the significance of the airflow changing form laminar to turbulent.

The rate of heat transfer by free convection is given by Newton's law of cooling and is a function of surface area (A), surface temperature (T_s) and surrounding fluid temperature (T_∞):

$$q = \bar{h} A (T_s - T_\infty) \tag{4.3}$$

where $\bar{h}$ is obtained with knowledge of the Rayleigh number [107].

$$Ra_L = \frac{g\beta(T_s - T_\infty)L^3}{\alpha_D \nu} \tag{4.4}$$

Where g is gravity's acceleration, β is thermal expansion coefficient, L is the characteristic length, α_D is thermal diffusivity and ν is kinematic viscosity. Calculating Ra_L for a test temperature of 915 $\dot{}$C, and using values of α_D and ν from the table in the appendix [107]:

$$Ra_L = \frac{9.81 \times (1/1188)(915 - 25) \times 0.2^3}{(224 \times 10^{-6})(162.9 \times 10^{-6})} = 1.61 \times 10^6$$

The critical value for Ra_L is 10^9 and so this flow is laminar. Thus Equation 4.5 is used to calculate the Nusselt number ($\overline{Nu}_L$), and where Pr is the Prandtl number:

$$\overline{Nu}_L = 0.68 + \frac{0.67 Ra_L^{\,1/4}}{\left[1 + \left(0.492/Pr\right)^{9/16}\right]^{4/9}} \tag{4.5}$$

$$\overline{Nu}_L = 0.68 + \frac{0.67(1.61 \times 10^6)^{1/4}}{\left[1 + \left(0.492/0.728\right)^{9/16}\right]^{4/9}} = 19.05$$

Hence as $\overline{Nu}_L$ is related to thermal conductivity of the fluid (k_f) via;

$$\overline{Nu}_L = \frac{\overline{h}L}{k_f} \tag{4.6}$$

$$\overline{h} = \frac{19.05(76.3 \times 10^{-3})}{0.2} = 7.27 \text{ Wm}^{-2}\text{K}^{-1}$$

If this is repeated for the upper temperature bounds (1318 K) of the proposed tests, it can be seen that $\overline{h}$ =7.96 Wm⁻²K⁻¹. Thus, there is very little variation in the free convection heat coefficient over the test temperature range for laminar flow.

However, the calculation above is only valid for a simple vertical cylinder and does not take into account the undulating contours of the ASP sample. Thus the above calculation is to be checked for turbulent flow to determine the effect on the heat transfer coefficient. Assuming turbulent flow, Ra_L is $\cong 1 \times 10^9$ and the test temperature is 1188 K:

$$\overline{Nu}_L = \left\{0.825 + \frac{0.387(Ra_L)^{1/6}}{\left[1 + \left(0.492/Pr\right)^{9/16}\right]^{8/27}}\right\}^2 \tag{4.7}$$

$$\overline{Nu}_L = \left\{ 0.825 + \frac{0.387\left(1 \times 10^9\right)^{1/6}}{\left[1 + \left(\frac{0.492}{0.728}\right)^{9/16}\right]^{8/27}} \right\}^2 = 123.28$$

$$\overline{h} = \frac{123.28(76.3 \times 10^{-3})}{0.2} = 47.03 \ \text{Wm}^{-2}\text{K}^{-1}$$

It is clear to see that turbulent flow will significantly increase $\overline{h}$, and thus modify the overall heat transfer. Turbulent fluid flow will increase h as the air streams mix more readily, taking the heat energy with them. In order to determine the correct h_a value, it is essential to determine what type of airflow is moving over the test sample. As noted by Hand et al. [108] the value of h will be relatively high compared with the values of a horizontal test piece due to chimney effects arising form the geometry of the test sample in the induction coil. Thus the air flow is likely to become turbulent at some point on the specimen. From this information a convectional heat transfer coefficient will then be estimated at 20 Wm^{-2}K^{-1}.

4.2.1.5.2. Radiational heat loss

One of the boundary conditions applied to a coupled thermal-mechanical model is the heat loss to the surrounding environment, as well as to the tools. MSC Superform is capable of processing time/temperature dependant convective boundary conditions and models based on Equation 4.8.

$$q_{conv} = h_{conv}\left(T_s - T_\infty\right) \tag{4.8}$$

The radiative boundary condition can be expressed as;

$$q_r = \sigma_{SB}\varepsilon_m\left(T_s^4 - T_\infty^4\right) \tag{4.9}$$

By expanding Equation 4.9 the radiative boundary condition can be shown to be equivalent to a nonlinear convection heat loss mechanism, where the radiational heat transfer coefficient (h_r) is shown in equation 4.12;

$$q_r = \sigma_{SB}\varepsilon_m\left(T_s^2 + T_\infty^2\right)\left(T_s^2 - T_\infty^2\right) \tag{4.10}$$

$$q_r = \sigma_{SB}\varepsilon_m\left(T_s^2 + T_\infty^2\right)\left(T_s + T_\infty\right)\left(T_s - T_\infty\right) \tag{4.11}$$

$$q_r = h_r\left(T_s - T_\infty\right) \tag{4.12}$$

Where;

$$h_r = \sigma_{SB}\varepsilon_m \left(T_s^2 + T_\infty^2\right)\left(T_s + T_\infty\right) \qquad (4.13)$$

Thus, the total heat loss to the surrounding environment from the surface of the exposed workpiece (i.e. not considering the surfaces conducting heat into the tools) can be expressed as a function of both radiational and convectional heat transfer coefficients;

$$q_{total} = h_r\left(T_s - T_\infty\right) + h_{conv}\left(T_s - T_\infty\right) \qquad (4.14)$$

$$q_{total} = \left(h_r + h_{conv}\right)\left(T_s - T_\infty\right) \qquad (4.15)$$

Over a wide temperature range this value of heat flux will vary greatly as h_r and ε are also a function of temperature. Such effects are shown by inputting the relevant values into Equation 4.15 and plotting (Figure 4.4). It is accepted that some degree of error will be introduced here as the emissivity (ε) is also highly dependant upon surface finish, temperature, oxide scale, etc. A figure showing the values of emissivity for titanium-aluminium alloys used in this calculation can be found in Section 3.8.
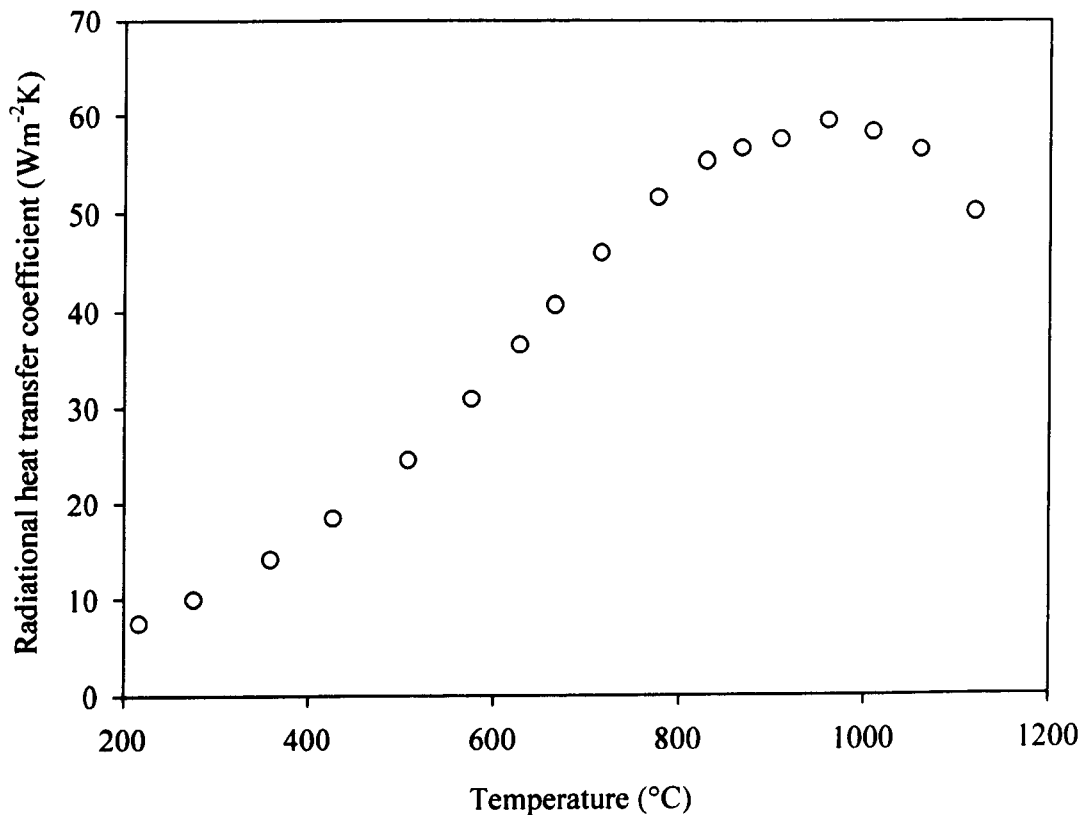
Figure 4.4 Radiative heat transfer coefficient as a function of temperature for Timetal®834

Figure 4.4 shows that over the typical forging temperature range for Timetal®834 (950-1050 °C) the actual nonlinear radiation heat transfer coefficient is approximately equal to 60 $Wm^{-2}K^{-1}$. Such a result permits a simpler model, and does away with the need for a temperature dependant environmental film coefficient user defined subroutine. Thus, by combining the two radiative and convectional components the overall heat transfer coefficient can be estimated at 80 $Wm^{-2}K^{-1}$.

4.2.1.5.3. Conductional heat loss

The heated billet is in contact with a hydraulic manipulator arm as it is removed from the furnace and transferred to the forging dies. Heat loss to the manipulator is deemed to be negligible and so ignored. Determining a heat transfer coefficient for the forging dies is difficult due to the wide range of values found in the literature and the fact these vary with many different process parameters. Malinowski et al. [109] reveals h_t varies from 50 to 20000 $WK^{-1}m^2$ for contact between two stainless steel dies depending on the contact pressure. It is also noted that h_t is not constant along the arc of contact and is also affected by the pressure distribution, oxide layer, surface roughness, lubrication, surface chemistry and temperature. Burte et al. [110] carrying out ring tests on 2024-O aluminium and also confirms that h_t increases with pressure but above a threshold value it becomes insensitive to the pressure increase. This threshold value is slightly lower for a lubricated sample compared to a dry sample. This work also notes that under low pressures the value of h_t is a magnitude lower than at high pressures. This is also confirmed by Hu et al. [101], working with Ti 6Al-4V, who have measured h_t to be 234 and 2474 $WK^{-1}m^2$ at low and high pressure respectively. Authors also disagree as to whether lubrication increases or decreases h_t. Burte et al. [110] shows that lubricating a sample increases the value of h_t. A possible explanation of this could be that the lubricant fills in the asperities of the two mating surfaces creating more intimate contact and increasing contact area. This is contradicted by Hu et al. [101] who says a glaze on the sample reduces h_t. This value increases during the deformation as the glaze spreads and so reduces the thickness of additional material which the heat must flow through.

An extreme axisymmetric model was run to exaggerate any possible effects of rapid heat loss to the tools. This was based on same model as in Section 4.2. and the tool temperature was set at room temperature (15 °C) to generate a large temperature gradient between the sample and the tools.

4.2.2. ASP sample cooling/heating

To quantify the combined convectional and radiational heat losses from an ASP sample a specimen was clamped in the machine and cooled from 900 °C. This data was then utilised to evaluate/tune FE models. This test was carried out under load control to

prevent sample distortion and thus any (possibly negligible) effects from a change in shape brought about by thermal expansion. For simplicity the ASP sample has been modelled by ignoring the slits cuts at both ends for the jaws for clamping, and so it is assumed that these will have no significant effect on the model as they remain relatively cool and conductional heat loss to the machine tools will be very small compared with radiational and convectional heat losses. The mesh is comprised of 20952 8-node isoparametric heat conducting brick elements. The temperature profile in a sample held at 900 °C was measured by placing thermocouples intermittently along the length of the sample. The different temperature regions within an FE model were specified below in Figure 4.5.
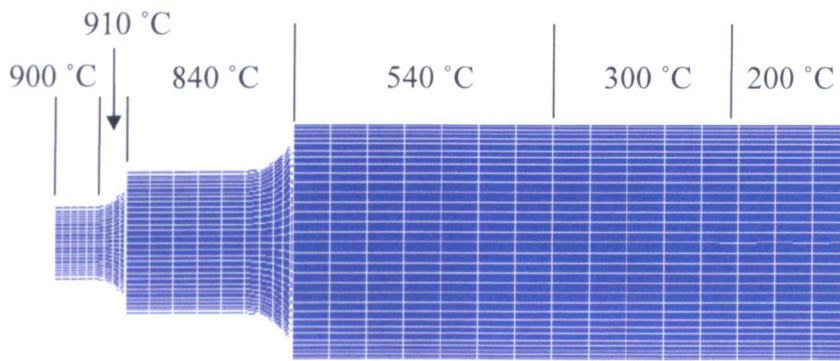
Figure 4.5 Regions of different temperatures in FE model using data measured buy thermocouples (half symmetry 3D model)

4.2.3. Industrial closed die forging

A three stage closed die forging operation with two extrusion channels was selected for analysis as it would produce complex material deformation and flow patterns. This would in turn generate a large range of different strain path angles from 'simpler' shapes such as the first die forge to more complex and undulating strain paths which will be produced by the second die's extrusion channels. Due to time and strain constraints only the first two stages of the operation are modelled. The two dies used can be seen below in Figure 4.6 and the full process can be seen in Figure 4.7.

A 50 kg billet of material of high aspect ratio is heated in a gas fired furnace for 3 – 5 hours at a temperature of 990 °C to homogenise microstructure and temperature. The high aspect ratio ensures a large amount of work is put into the material during the first, upsetting forging stage which breaks up the coarse billet microstructure. The billet is transferred from the furnace to a flying wheel (energy) driven forging press by a hydraulic manipulator arm. This process takes approximately 20 seconds and results in some cooling of the workpiece. It is assumed that only air cooling takes place and the manipulator arm conducts no heat from the material. It is also assumed that the movement of the billet through the air as it is transferred has no affect in increasing the

convectional heat transfer coefficient. The dies are preheated to 300 °C to prevent excessive die chill and forming a relatively harder material or 'skin' at the tool-workpiece interface. These dies are lubricated between each blow with a graphite-water suspension which is blown on with a hose nozzle by the forging press operator. Damp sawdust is thrown onto the workpiece before each blow as this generates steam at each forging blow which in turn pushes the work piece out of the die and prevents sticking. This is not modelled as it is assumed to have no effect on the process and is only a simple solution to a processing problem.

(a)   (b)
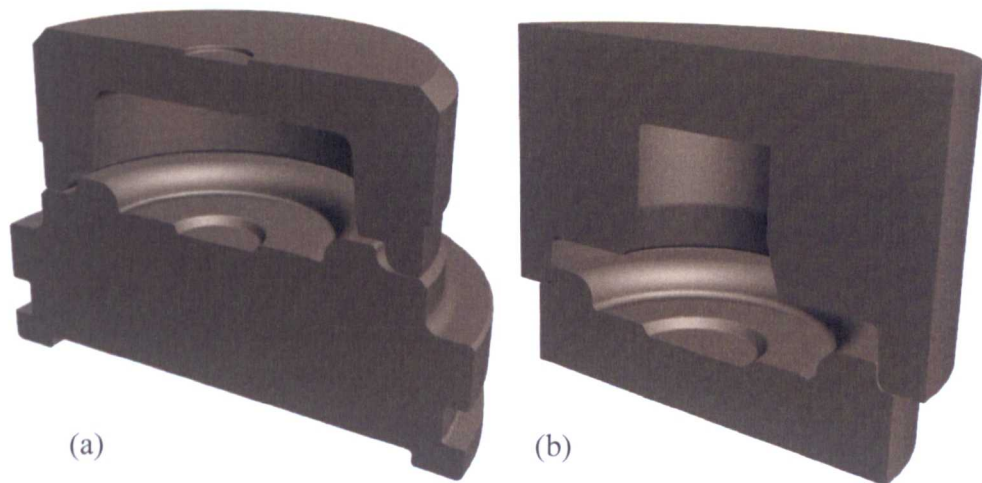
Figure 4.6 (a) 1ˢᵗ and (b) 2ⁿᵈ forging dies used in FE model of the closed die operation

After a blow is delivered 8 seconds pass as the top tool is raised and the next subsequent blow hits the workpiece. The first forging operation is to impose a lot of deformation in the material and try to break up the billet microstructure. The second set of dies deliver four blows forming the disc's rim and extrudes material into the channel on the top of the forging. The actual forming process this work is based on has an additional forging process performed. After the second forging stage the workpiece is allowed to cool and the flash skirt is machined off and a third die set extrudes a second channel on the opposite side of the component, however due to time constraints together with a limited amount of total plastic strain that can be applied to a sample before failure, the third forging operation is ignored. It is however used for the industrial forging cool in Section 4.2.4 as this is when the material will receive a solution treatment at 1015 °C (15% α_p) for 2 hours followed by an oil quench and an aging/stress relieving heat treatment at 700 °C which is then subsequently air cooled. This is the only time when the forged component will have a uniform temperature distribution and so is considerably easier to model to calculate cooling rates. Figure 4.7 shows the workpiece from the billet stage and after each subsequent forging stage.

The forging process was modelled using an axisymmetric half symmetry model where time-velocity curves were used to drive the top tools for both operations. Table 4.3 shows the start velocities of the top die at the beginning of each blow and the duration

of the deformation. Each blow is modelled by reducing the velocity of the top die linearly from the initial velocity to zero over the blows duration. After each blow the top tool was backed off approximately 1mm over 8 seconds to release contact with the workpiece and to allow convectional-radiational cooling. This would simulate time delay caused by the tool moving up after each blow. 4-node isoparametric quadrilateral axisymmetric elements were used for the mesh. An initial mesh comprising of 10 by 40 square elements was used as these would be used to form the flow lines as this shows how the material flowed in the dies. A remesher with an outside refining parameter of 2 and remesh criteria of tool penetration or element distortion of 20° was used. The environmental and tool heat transfer coefficients were 350 $Wm^{-2}K$ and 30 $kWm^{-2}K$ respectively. The friction coefficient is 0.3 and uses the same methodology as mentioned in Section 4.2.1.4.

(a)

990 °C

5 blows

(b)

(a)

990 °C

4 blows

(c)

990 °C

3 blows

(d)

Flash skirt is machined off prior
to final forging stage

After final forge the flash is again
removed and a centre hole is bored
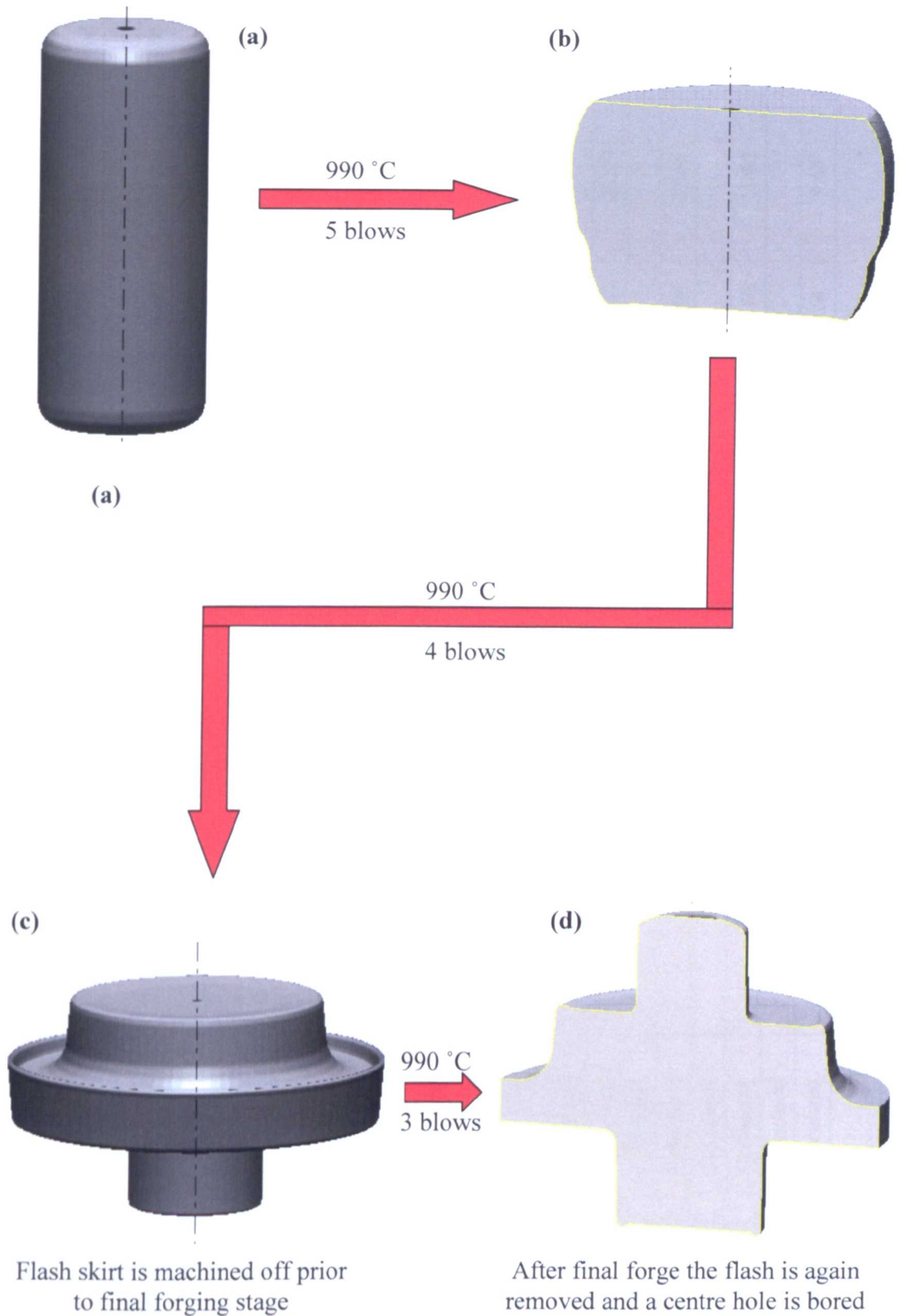
Figure 4.7 Schematic of the workpiece during the 3 stage forging process

Table 4.3 Time, velocity and temperature data for FE input to represent a flywheel driven forging press. Information courtesy of Firth-Rixson

OPERATION/BLOW		Temperature (°C)	Initial tool velocity (mms⁻¹)	Action time (s)	Total time (s)	Distance (mm)			
						Start	Finish	Moved in blow	Total
OP1_BL1	Approach	990	-	20	20				
	Blow 1	Calculated	360	0.36	20.36	252.1	178.45	73.65	73.65
	Cool	Calculated	-	8	28.36				
OP1_BL2	Blow 2	Calculated	360	0.3	28.66	178.45	118.02	60.43	134.08
	Cool	Calculated	-	8	36.66				
OP1_BL3	Blow 3	Calculated	360	0.26	36.92	118.02	67.24	50.78	184.86
	Cool	Calculated	-	8	44.92				
OP1_BL4	Blow 4	Calculated	360	0.21	45.13	67.24	24.39	42.85	227.71
	Cool	Calculated	-	8	53.13				
OP1_BL5	Blow 5	Calculated	310	0.14	53.27	24.39	0.79	23.6	251.31
	Cool	Calculated	-	8	61.27				
	Reheat	990		3600	3661.27				
OP2	Approach	Calculated	-	20	3681.27				
OP2_BL1	Blow 1	Calculated	310	0.13	3681.4	63	42.27	20.73	20.73
	Cool	Calculated	-	8	3689.4				
OP2_BL2	Blow 2	Calculated	310	0.1	3689.5	42.27	26.64	15.63	36.36
	Cool	Calculated	-	8	3697.5				
OP2_BL3	Blow 3	Calculated	300	0.07	3697.57	26.64	15.58	11.06	47.42
	Cool	Calculated	-	8	3705.57				
OP2_BL4	Blow 4	Calculated	550	0.04	3705.61	15.58	6.54	9.04	56.46

4.2.4. Industrial forging cooling rates

In order to directly compare the cooling rate of a 50 kg forging to that of an ASP sample the cooling temperature for the model was set to 990 °C not 700 °C at which the material is actually aged/stress relieved and air cooled as mentioned in Section 4.2.3. The six tracking points for the temperature (and later strain) are shown below in Figure 4.8 and are the same points after deformation as those shown in the billet in Figure 4.18. The 3D model consisted of 13350 iso-parametric heat conducting axisymmetric elements. The same environmental heat transfer coefficient from the tuned ASP sample cooling work shown in Section 5.3.1 was used to define the heat loss. A tool with zero heat transfer was defined to be touching the bottom of the forging to represent a concrete floor which would not absorb much of the billets heat when compared with that of the surrounding atmosphere.
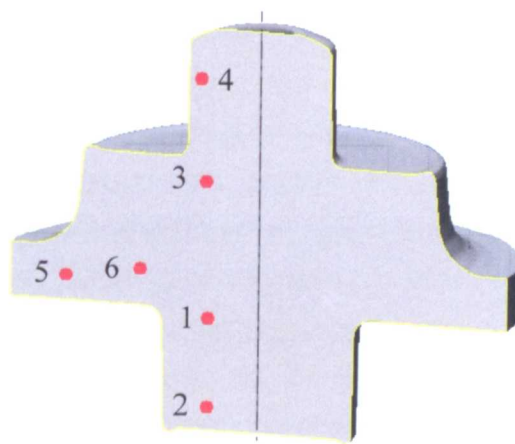
Figure 4.8 Cross section of forging after the final 3rd stage showing geometry of cooling rate model. Numbers represent the points where cooling points are calculated

4.3. ASPII machine

The ASPII machine was designed specifically to investigate nonlinear forming operations by imposing combined axial and torsional deformation to test samples. It is a servo-hydraulic machine controlled via PID controllers embedded in purpose made software allowing the operator to tune machine response and carry out complex deformations via a simple flow chart interface. Figure 4.9 shows a photograph of the ASPII machine with all major components highlighted. These components are as follows:

1. Load cell and lower clamping assembly
2. Actuator and upper clamping assembly
3. Crosshead

4. Accumulators
5. Induction coil
6. Quenching system
7. Cooling fins

The load cell (1) is encased within the lower clamping assembly measuring instantaneous axial load and torque. This is water cooled to protect the electronics. If the temperature rises above 80 °C the machine cuts out to ensure the electronics are protected and ensure accurate load/torque readings. With the induction coil (5) being in such close proximity to the load cell experiments conducted under load control proved difficult due to the strong electromagnetic field from the induction coil interfering with the load cell's measurements. How this problem was overcome is discussed in Section 5.2.1.1. Samples are deformed by the actuator (top clamping assembly - 2) rotating or moving up/down axially to impose torsion, tension or compression strain respectively. The actuator is cooled with forced convection over the cooling fins (7). Deformation can be concurrent or sequentially at fixed or variable strain rates to designated strains. The computer controlled machine is also capable of replaying input files, e.g. from FE models, to recreate complex multidirectional strain paths. After deformation samples can be water quenched (6), naturally air cooled or controlled air cooled by the induction coil to a specified rate. The actuator and pressure accumulators (4) are mounted to the cross head (3) which are able to move up and down on the two large stanchions and facilitates sample loading. The maximum capabilities of the machine are as follows:

- Maximum torque - 500 Nm
- 500 rpm continuous rotation and 1000 rpm single rotation
- Maximum axial load +/- 100 kN
- Axial stroke +/- 30 mm
- Maximum controllable strain rate (see Section 5.2.2 and 5.2.3) – 10 s^{-1}
- Temperature - up to 1300 °C
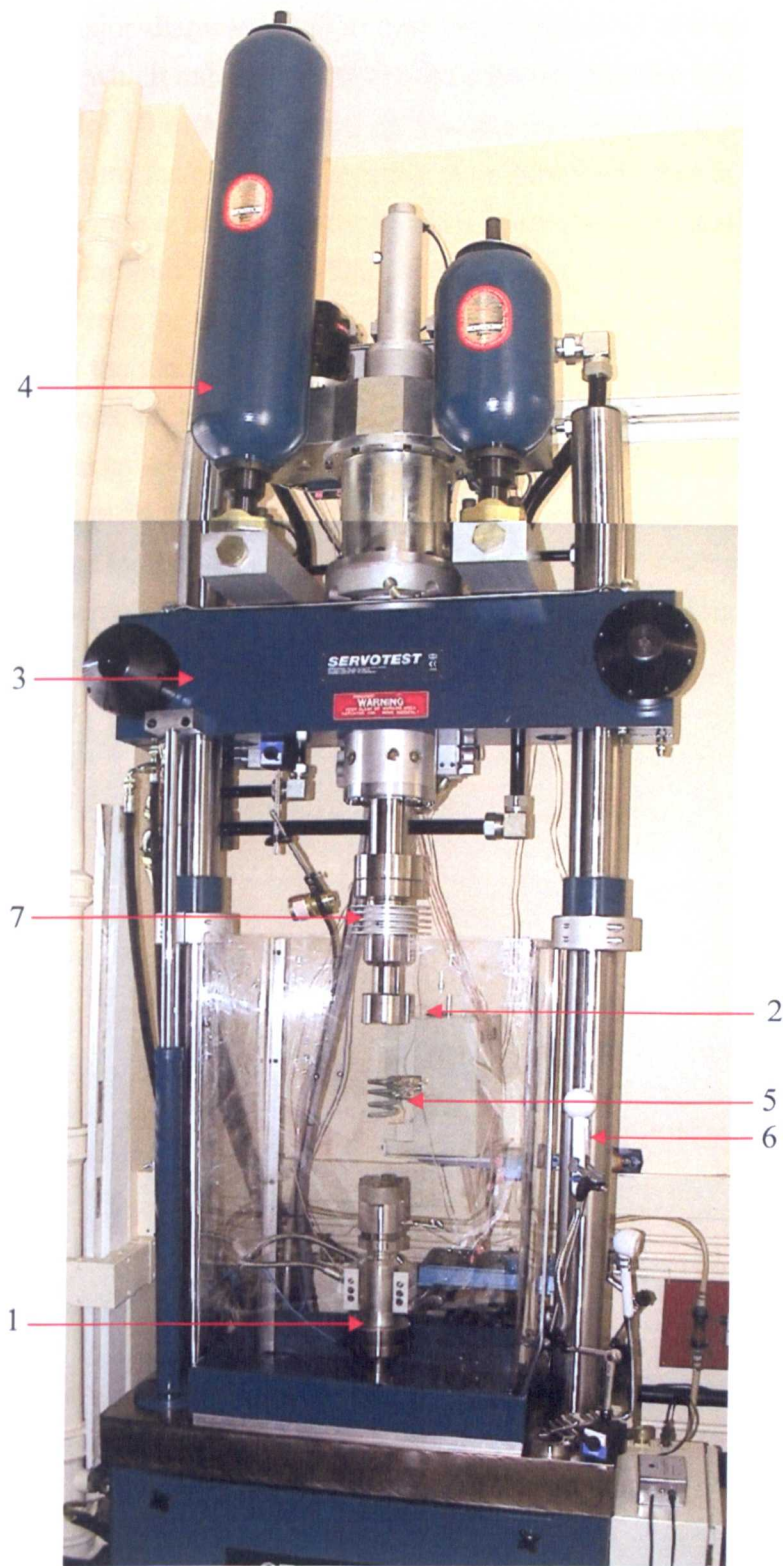
Figure 4.9 ASPII machine with major components shown by numbers 1-7

4.3.1. ASP samples

A technical drawing for the samples can be found in Figure 4.10. Test samples were machined with a major diameter of Ø30 mm and a length of 200 mm. The samples contained two radii which reduced the test volume of the material to Ø10 mm diameter and a gauge length of 10 mm. As noted by Barraclough *et al.* [111] this 2:1 length to radius ratio is optimum for obtaining accurate flow behaviour data at high strain rates. The samples incorporate a 2mm chamfer on their bottom and precisely machined ends to aid sample insertion into the clamping assembly of the machine. The high tolerance machining at both ends of the sample ensure it sits snugly into the top and bottom recesses situated in the clamping assembly and ensure the sample is perfectly aligned with the rotation axis of the machine. Unless stated on the technical drawing all tolerances can be taken to be ± 0.5mm. Only the gauge length and very ends of each sample are required to be machined to high tolerances. One thermocouple is situated at the base of the gauge length so as not to interfere with any deformation. This is also on the bottom of the sample so it remains fixed during any deformation and as a result is more likely to survive the test.

SIDE VIEW
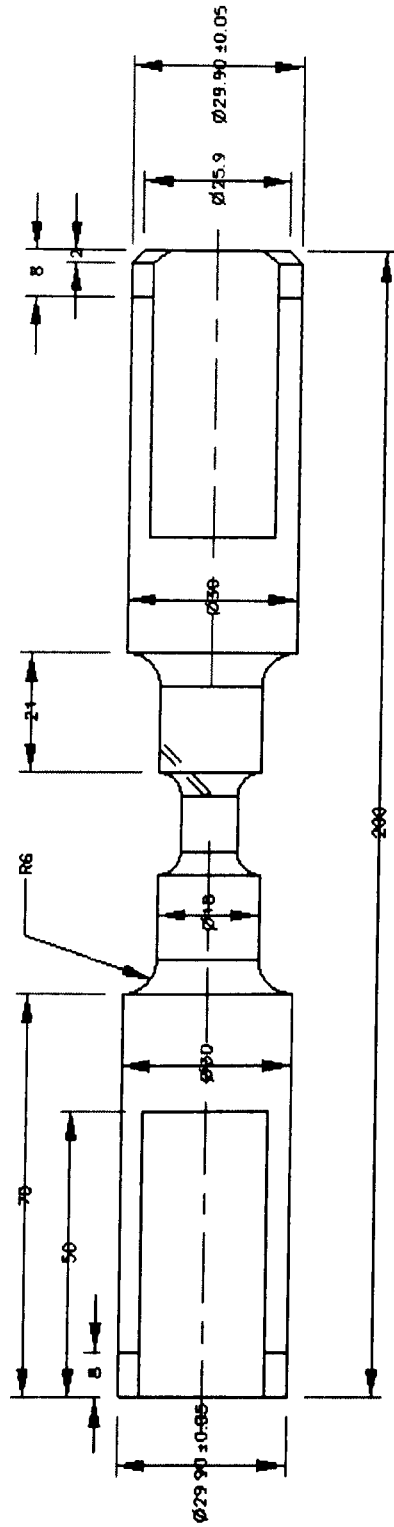
END VIEW
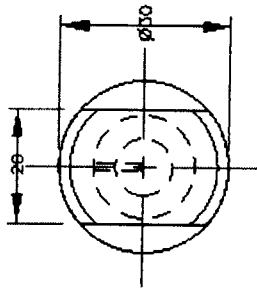
CENTRE SECTION

Notes:

Dimensions:–mm

Drawings not to scale.

The thermocouple hole goes in at 45 degrees, 5mm back from the R4 mm shoulder

All drawings by Mike Blackmore
Contact: 2225459 / 07765150065
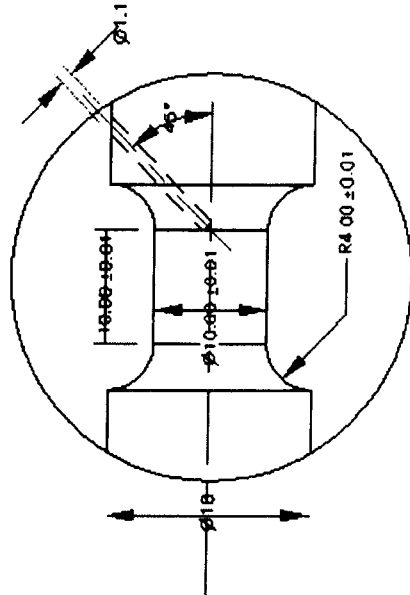
Figure 4.10 Technical drawing of an ASPII sample

90

4.3.2. Correct loading of an ASP sample

Previous work with the ASPII machine has been conducted on soft materials such as non-heat treatable aluminium alloys and annealed stainless steels. Many problems have been encountered when attempting to load titanium samples into the ASPII machine as this higher strength material does not allow the jaws to bite into the material and generate enough grip to hold the mounting assembly together for convenient bolting to the upper load cell assembly. The arrangement of the clamping mechanism for the machine is shown below in Figure 4.11.
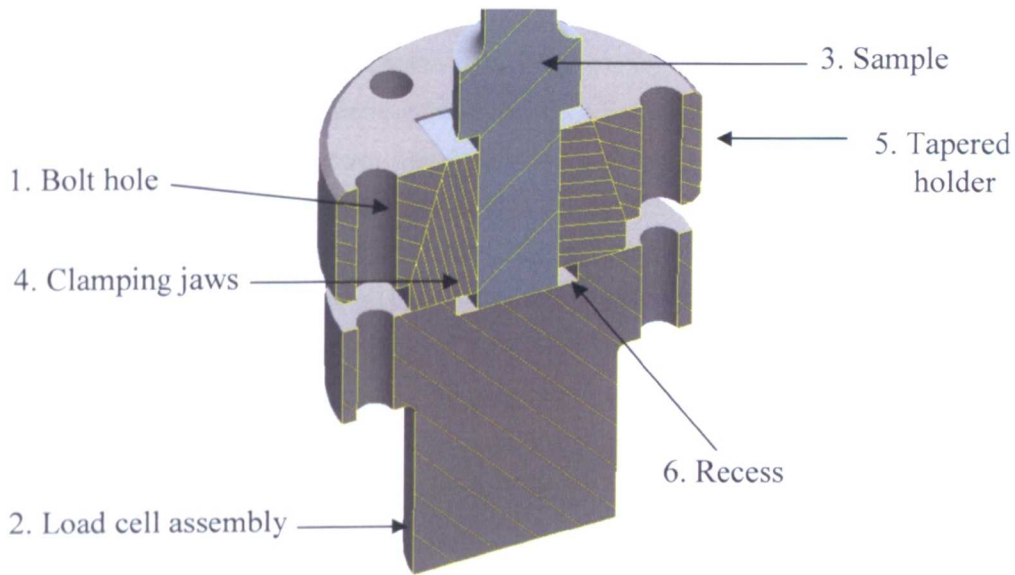
Figure 4.11 Cross sectional view of the clamping assembly with a sample loaded

This assembly operates by tightening six bolts through the holes (1) in the tapered holder (5) to the load cell assembly (2) which drives down the tapered holder (5), in turn forcing the clamping jaws (4) to bite onto the sample (3). When the sample is attached to the upper load cell the whole crosshead can be lowered to allow the sample to go through the induction coil. The crosshead is stopped when there are several millimetres between the sample and the lower load cell. At this point the sample must now be lowered though the lower clamping jaws assembly and into the lower load cell by the actuator control as this provides better control and smaller displacement steps. The sample should be advanced in intervals of 0.1mm, whilst all the time monitoring the load cell for any significant change in load which would suggest the sample has made contact with the load cell. If the sample does make contact then the actuator should be backed off and small adjustments of the sample's orientation should be made. The addition of a 2mm chamfer on the bottom of the sample helps it enter the circular recess (6) more easily. Once the sample is in the hole then it may be advanced with care until the sample reaches the bottom and load is detected. The whole top and bottom load cell

assemblies can then be tightened to hold the sample rigidly and perfectly inline with the rotation axis of the machine. By having the precisely machined ends on the sample off axis rotations can be avoided by the recesses (6) in both clamping assembles aligning the sample with the rotational axis of the actuator.

4.3.3. *Thermal calibration*

The temperature of an ASP specimen during testing is controlled from a single thermocouple at the base of the gauge length, point X, as shown in Figure 4.12. This thermocouple provides the input signal for the heating proportional-integral-differential (PID) control which holds the specimen at the desired test temperature. However before a full scale ASP test can be carried out the PID must be calibrated for the particular material and the temperature gradient measured as different materials and slightly different sample geometries will respond differently to the electromagnetic field produced by the induction coil. The initial testing is to calibrate the PID controller to reach and hold desired temperatures accurately. This was done by setting desired heating rates and hold temperatures. If the induction coil did not heat at the desired rate or reach the desired temperature then the PID values were altered accordingly. To derive a relationship between the centre of the gauge length temperature and that of the control thermocouple five thermocouples were imbedded along the central longitudinal axis. Figure 4.12 shows the arrangement of the thermocouples in the calibrating specimen with three placed along the gauge length and two at either end.
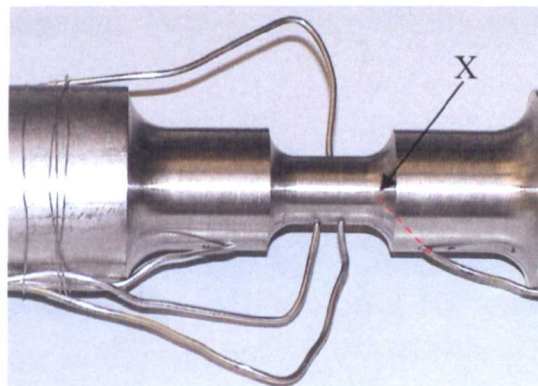
Figure 4.12 ASP specimen with calibration thermocouples. Dashed red line shows the end thermocouples embedded at the base of the gauge length

It should be noted that the test material for calibration is Ti 6Al-4V as this has very similar thermo-physical properties when compared with Timetal®834, but is more easily obtainable and considerably cheaper. The results from this calibration can be

seen in Section 5.2.1. This test was carried out in load control, i.e. the axial load was held at zero and the actuator was allowed to move to compensate for thermal expansion.

4.3.4. Torsional calibration

Torsion calibration tests were carried out using forward-reverse torsion ($\varepsilon = \pm 0.35$) at a strain rate of 10 s^{-1} and at 1000 °C. These conditions were derived from the FE models and identified as typical strain and strain rates being imposed on the material during the forging process. Such an extreme and fast strain path change will calibrate the ASPII machine for any worse case scenario and as a result it will be capable of performing any deformation sequence required. The equations governing the definition of an ASP test can be found in Section 4.4. By scoring a line vertically along the length of the sample's gauge length it will be possible to determine (using this line as a datum) whether the ASPII machine is accurately reproducing the test conditions specified. If this line is straight after forward-reverse torsion then the machine has successfully strained the sample to the correct values and there has been no localised deformation. This methodology was later applied to tension-compression test but with the lines scored circumferentially.

The first mechanical calibration was carried out in displacement control (fixed end) due to control issues, and as a result there will have been an axial component of stress applied due thermal expansion. This of no importance in such a test as the microstructure is not being investigated. The second mechanical calibration test was carried out in load control (free end), i.e. axial displacements allowed to compensate for axial expansion (or contraction). Such a condition will be required for later tests.

4.3.4.1. PID control

A forward-reverse torsion deformation at high strain rates is very difficult process to optimise as it involves several fast accelerations and decelerations. The actuator is quickly accelerated to the required angular velocity to impose the desired strain rate in the forward torsion. It then has to decelerate in the smallest possible time to stop at a fixed rotation to impose the correct strain. Then the direction must be reversed with the minimal delay. This requires a highly tuned PID controller to start and stop the actuator with the smallest setting time and with minimal overshoot. Excessive overshoot of the actuator will impose many small strain forward-reverse strain path deformations which will deem a test invalid. To carry out PID tuning a sample doe not need to be loaded into the machine and so calibration is effectively done 'off line' and samples are not destroyed. PID values were varied ('off line') to produce the optimum response from the actuator. Details of the PID controller tuning can be found in Section 5.2.2.

4.3.5. Tension-compression calibration

A similar procedure to the torsion calibration was used for axial calibration. The deformation was then reversed and brought back to a net strain of zero. The PID values were varied to decrease settling time, overshoot and steady state error. Once this was achieved a sample was deformed at a constant strain rate of $10s^{-1}$ to a compressive strain of 0.5.

4.3.6. Reproducibility

After the tuning of the PID at high strain rates two Ti 6Al-4V samples were subjected to $180°$ torsion at a strain rate of $2s^{-1}$ in order to check the reproducibility of a test. A lower strain rate was utilised in order to check how a highly responsive (possibly 'twitchy') PID controller would operate satisfactory under lower strain rates. The two flow curves for each sample are show in Section 5.2.4 and are calculated by the method outlined in Section 4.4.

4.4. Strain path testing

A change in strain path angle during deformation is a complex deformation to quantify. This section will derive the mathematics used to define tension/compression and torsion tests from first principles and to quantify the strain path angle changes during a deformation.

4.4.1. Yield criterion

The most widely used theory for strain hardening assumes the yield locus increases in size during continuous plastic deformation without change in shape [112]. The yield locus is therefore defined only by the final plastic state of stress and is the same no matter what strain path is imposed to reach that plastic state [113]. In other words the material remains isotropic throughout the deformation and any Bauschinger effect is ignored. The state of hardening at any stage is therefore specified by the current uniaxial yield stress $\overline{\sigma_u}$. Using the von Mises criterion this stress is shown to be Equation 4.16;

$$\overline{\sigma_u} = \frac{1}{\sqrt{2}}\left[\left(\sigma_x - \sigma_y\right)^2 + \left(\sigma_y - \sigma_z\right)^2 + \left(\sigma_z - \sigma_x\right)^2 + 6\left(\tau_{xy}^2 + \tau_{yz}^2 + \tau_{xz}^2\right)\right]^{\frac{1}{2}} \quad (4.16)$$

The von Mises yield criterion is derived in fulfil Section 9.1. The quantity $\overline{\sigma_u}$ is also known as the equivalent stress, which increases with increasing plastic strain. To complete the hardening rule, it is necessary to relate $\overline{\sigma_u}$ to an appropriate measure of plastic deformation. A hypothesis often used in the literature [112] assumes $\overline{\sigma_u}$ to be a function of a suitable measure of the total plastic strain during the deformation. To derive such a relationship we introduce a scalar parameter $\overline{d\varepsilon}^p$, known as the equivalent plastic strain [112];

$$\overline{d\varepsilon}^p = \sqrt{\frac{2}{3}}\left(d\varepsilon_{ij}^p d\varepsilon_{ij}^p\right)^{1/2} \tag{4.17}$$

$$\overline{d\varepsilon}^p = \sqrt{\frac{2}{3}}\left\{\left(d\varepsilon_{xx}^p\right)^2 + \left(d\varepsilon_{yy}^p\right)^2 + \left(d\varepsilon_{zz}^p\right)^2 + 2\left(d\varepsilon_{xy}^p\right)^2 + 2\left(d\varepsilon_{yz}^p\right)^2 + 2\left(d\varepsilon_{zx}^p\right)^2\right\}^{1/2} \tag{4.18}$$

The superscript p in the equivalent strain denotes a plastic fraction of strain. At high temperatures, the elastic deformation is negligible compared to that of the imposed plastic strain and is subsequently ignored. Equation 4.18 implies that in the case of uniaxial tension, $\overline{d\varepsilon}^p$ is equal to the longitudinal plastic strain increment, provided the yield function is regular. Mathematically this strain hardening hypothesis may be written;

$$\overline{\sigma_u} = F\left\{\int \overline{\varepsilon^p}\right\} \tag{4.19}$$

Where the integral is taken along the strain path of a given element. Thus, the amount of hardening depends only on the sum total of all the strain increments.

4.4.2. Pure tension/compression

During a tensile test the longitudinal strain is accommodated by compressive lateral strains, as shown in Figure 4.13. Therefore the strains are defined as ε_x in the longitudinal direction and ε_y, ε_z for the lateral strains, where $\varepsilon_y = \varepsilon_z$ and $\varepsilon_x \neq \varepsilon_y$.
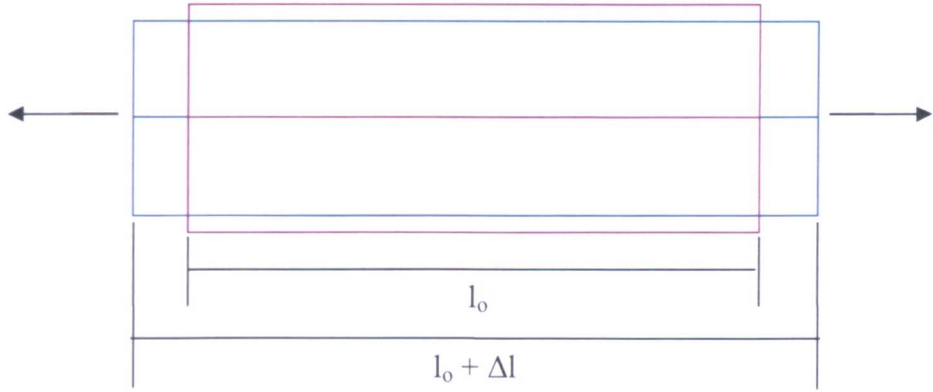
Figure 4.13 Simple tension test

As the sum of the plastic strains gives; $\varepsilon_x + \varepsilon_y + \varepsilon_z = 0$, then;

$$d\varepsilon_x = -2d\varepsilon_y = -2d\varepsilon_z \tag{4.20}$$

Using these values, and the von Mises criterion from Equation 4.18 the value of equivalent tensile plastic strain for the pure tension can be shown to be;

$$\overline{d\varepsilon}^P = \sqrt{\frac{2}{3}\left\{ \left(d\varepsilon_{xx}^P\right)^2 + \left(d\varepsilon_{yy}^P\right)^2 + \left(d\varepsilon_{zz}^P\right)^2 \right\}^{1/2}} \tag{4.21}$$

$$\overline{d\varepsilon}^P = \sqrt{\frac{2}{3}\left\{ \left(d\varepsilon_x^P\right)^2 + \left(\frac{d\varepsilon_x^P}{2}\right)^2 + \left(\frac{d\varepsilon_x^P}{2}\right)^2 \right\}^{1/2}} \tag{4.22}$$

$$\overline{d\varepsilon}^P = \sqrt{\frac{2}{3}\left\{ \frac{6}{4}\left(d\varepsilon_x^P\right)^2 \right\}^{1/2}} = \sqrt{\frac{2}{3}\left\{ \frac{3}{2}\left(d\varepsilon_x^P\right)^2 \right\}^{1/2}} \tag{4.23}$$

And thus;

$$\overline{d\varepsilon}^P = d\varepsilon_x^P \tag{4.24}$$

96

4.4.3. Constant strain rate

To carry out a meaningful tension or compression test a constant strain rate must be applied through the whole of the test. This principle can be derived by considering an infinitely small strain;

$$de = \frac{dl}{l} \tag{4.25}$$

Thus integrating from l to l_o gives;

$$\varepsilon = \ln\left(\frac{l}{l_0}\right) \tag{4.26}$$

Differentiating Equation 4.26 with respect to time gives;

$$\frac{d\varepsilon}{dt} = \frac{1}{l}\frac{dl}{dt} = \dot{\varepsilon} \tag{4.27}$$

Where l is the sample length and $\left(\frac{dl}{dt}\right)$ is the cross head velocity (V), thus.

$$\dot{\varepsilon} = \frac{V}{l} \tag{4.28}$$

To keep a constant strain rate we must vary V as l is constantly changing.

$$\varepsilon = \ln\left(\frac{l}{l_0}\right) \tag{4.29}$$

$$\exp\varepsilon = \frac{l}{l_0} \tag{4.30}$$

$$l = l_o \exp\varepsilon \tag{4.31}$$

For a constant strain rate the equivalent strain must be;

$$\varepsilon = \dot{\varepsilon}\, t \tag{4.32}$$

Therefore;

$$l = l_o \exp\left(t\dot{\varepsilon}\right) \tag{4.33}$$

4.4.4. Simple torsion

To define a relationship between the measurable quantity of engineering shear strain and the pure shear strain imposed on a microscopic scale, consider an infinitesimal shear strain imposed on an equally small 2D element as shown below;
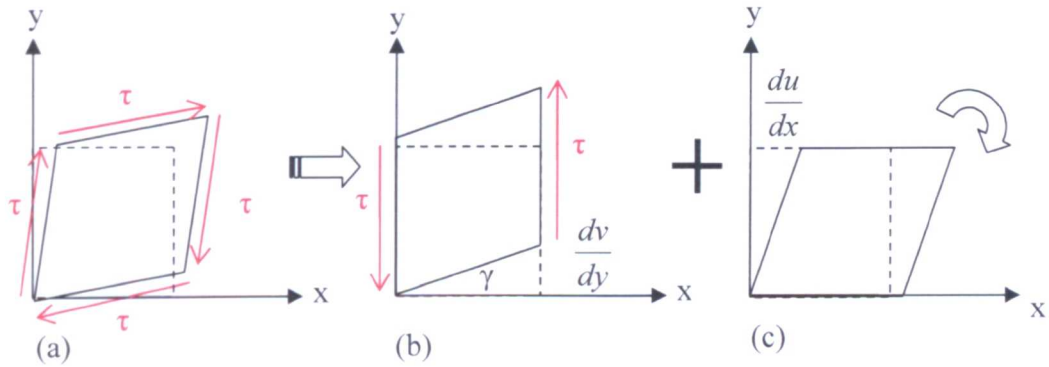
Figure 4.14 The 2D shear strain imposed on an element of material is equivalent to a shear and a rotation of a material element

A pure torsional loading condition would produce an engineering shear strain of γ (Figure 4.14(b)). However, on an elemental level this is not the case as the material element requires an equal and opposite set of shear stresses to oppose the 'y-direction' shear stresses and prevent the element purely revolving in space. The resultant condition is shown in Figure 4.14(a). This deformation is equivalent to the first pure torsional deformation (Figure 4.14(b)) plus a small rotation about the origin (Figure 4.14(c)). Thus the equivalent pure shear strain can be written as the sum of half the small strain increments in the x and y-directions;

$$\varepsilon_{xy} = \frac{1}{2}\left(\frac{du}{dx}\right) + \frac{1}{2}\left(\frac{dv}{dy}\right) = \frac{1}{2}\left(\frac{du}{dx} + \frac{dv}{dy}\right) \tag{4.34}$$

By considering the engineering strain in Figure 4.14(b);

$$\gamma = \frac{dv}{dy} \tag{4.35}$$

Thus by considering a pure torsional deflection, the x-direction strain is neglected and Equations 4.34 and 4.35 become;

$$\varepsilon_{xy} = \frac{1}{2}\left(\frac{dv}{dy}\right) = \frac{\gamma}{2} \tag{4.36}$$

Such a relationship is used by a number of authors in the literature [114-116] to define the relationships between the two strain components.
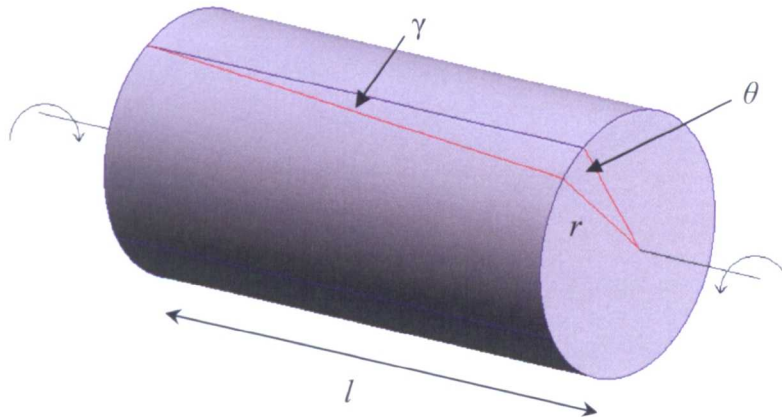
Figure 4.15 Torsion deflection of a solid cylinder

Compared with torsion of a thin walled cylinder the solid cylinder is more complex due to the fact the shear stresses (and $\dot\gamma$) are varying over the cross-section of the cylinder. Considering the twisting of a uniform cylinder as shown in Figure 4.15 of length l and radius r to an engineering shear strain of γ, then a twist angle of θ is produced. When equal and opposite torques are applied at each end along the longitudinal axis it is assumed;

1. There are only small angles of twist.

2. The radii remain straight during the twisting.

3. Cross sections remain parallel during the twist.

4. Twist is uniform along the shaft, i.e. all normal cross sections the same distance apart experience the same relative rotation.

From Figure 4.15 and assuming small angles of twist the relative twist angle of the two ends of the cylinder can be shown to produce two infinitely small triangles as shown in Figure 4.16. Although not shown in Figure 4.15, p will represent the opposite length from the twist angles of the triangles formed by the deformation. This can also be envisaged as an infinitely small cord on the edge of the circular cross-section.
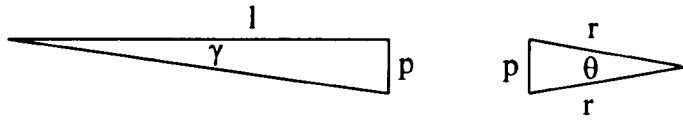
Figure 4.16 The two infinitely small triangles formed as a result of the torsional deflection

Thus;

$$\tan \gamma = \frac{p}{l} \tag{4.37}$$

And for the equilateral triangle on the cross section;

$$\frac{p}{\sin \theta} = \frac{r}{\sin\left(90 - \frac{\theta}{2}\right)} \tag{4.38}$$

Applying the small angle assumption $\left(\sin \theta = \theta, \tan \theta = 0, \frac{\theta}{2} = 0\right)$ then both equation reduce down, respectively, to;

$$\gamma = \frac{p}{l} \text{, and } p = r\theta$$

Thus;

$$\gamma = \frac{r\theta}{l} \tag{4.39}$$

and;

$$\varepsilon_{xy} = \frac{\gamma_{xy}}{2} = \frac{r\theta}{2l} \tag{4.40}$$

4.4.5. Constant torsional strain rate

From Equation 4.40 the shear strain rate $\left(\dot{\gamma} = \frac{\gamma}{t}\right)$ can be seen to be;

$$\dot{\varepsilon}_{xy} = \frac{\dot{\gamma}_{xy}}{2} = \frac{r\dot{\theta}}{2l} \tag{4.41}$$

The ASPII requires an angle input in degrees so this can be rewritten as;

$$\dot{\varepsilon}_{xy} = \frac{\dot{\gamma}_{xy}}{2} = \frac{r\dot{\theta}}{2l}\frac{2\pi}{360} = \frac{\pi r\dot{\theta}}{360l} \tag{4.42}$$

Similarly the instantaneous angle $\left(\theta = t\dot{\theta}\right)$ is given by;

100

$$\theta = \frac{360 l \dot{\varepsilon}_{xy} t}{r \pi}$$

(4.43)

4.4.6. Critical radius

As mentioned above, the shear strain imposed on a cylindrical specimen varies along the radius of that cylinder. Although the surface shear and stress state can be determined from the torque measured during a torsion test it is not possible to relate this information with any microstructural mechanisms. An approach to overcome this problem has been proposed by Barraclough et al. [111] where it is assumed the shear stress at any given radius is related to the shear strain and the shear strain rate at that radius as:

$$\tau = K \dot{\gamma}^n \gamma^m$$

(4.44)

where K, m and n are constants, γ is defined in Equation 4.39 and;

$$\dot{\gamma} = \frac{r\dot{\theta}}{l}$$

(4.45)

at an angle of twist θ and a twist speed $\dot{\theta}$ for a specimen of gauge length l the torque is:

$$T = 2\pi \int_{r_1}^{r_2} r^2 \tau dr = 2\pi \int_{r_1}^{r_2} \left(\frac{r\dot{\theta}}{l}\right)^n \left(\frac{r\theta}{l}\right)^m dr$$

(4.46)

$$T = \frac{2\pi K (\dot{\theta}/l)^n (\theta/l)^m}{3+m+n} \left[r_2^{(3+m+n)} - r_1^{(3+m+n)}\right]$$

(4.47)

$$T = \frac{2\pi}{3+m+n} \left[r_2^3 \tau_2 - r_1^3 \tau_1\right]$$

(4.48)

where τ_1 and τ_2 are the shear stresses at the inner surface and outer surface respectively. Rewriting Equation 4.47 in terms of shear stress τ_x at a given radius r_x gives:

$$T = \frac{2\pi \tau_x}{(3+m+n) r_x^{(m+n)}} \left[r_2^{(3+m+n)} - r_1^{(3+m+n)}\right]$$

(4.49)

To overcome problems arising from m and n varying with strain rate and strain respectively, an effective radius can be defined. Consider that a constant value of shear

stress (τ^*) exists throughout the cross section so that $m = n = 0$, thus from Equation 4.48:

$$T = \frac{2\pi\tau^*}{3}\left[r_2^{\ 3} - r_1^{\ 3}\right]$$

(4.50)

Combining Equations 4.49 and 4.50 yields:

$$\frac{\tau^*}{\tau_x} = \frac{3}{3+m+n}\frac{\left[r_2^{\ (3+m+n)} - r_1^{\ (3+m+n)}\right]}{\left(r_2^{\ 3} - r_1^{\ 3}\right)r_x^{\ (m+n)}}$$

(4.51)

The 'effective radius' r_m is defined as the radius at which $\tau^*/\tau_x = 1$, so that:

$$r_m = \left(\frac{3}{3+m+n}\frac{r_2^{\ (3+m+n)} - r_1^{\ (3+m+n)}}{\left(r_2^{\ 3} - r_1^{\ 3}\right)}\right)^{1/(m+n)}$$

(4.52)

the ratio of τ^*/τ_x calculated from Equation 4.51 for different values of $(m+n)$ as a function of radius was carried out by [111] who demonstrated that for solid cylindrical samples (i.e. $r_1 = 0$) r_m is independent of $(m+n)$ at a ratio of $r_m/r_2 = 0.724$.

The insensitively of the 'effective radius' to the value of $(m+n)$ and hence the structural gradient within the specimen makes it sensible to calculate the deformation parameters at this radius rather than the sample's surface. Thus, the shear stress is calculated as:

$$\tau = \frac{3T}{2\pi r_m^{\ 3}} \quad \text{and similarly} \quad \gamma = \frac{r_m\theta}{l}, \ \dot{\gamma} = \frac{r_m\dot{\theta}}{l}$$

(4.53)

Such a mathematical definition now allows the definition of the materials flow behaviour in torsion and also yields an ample surface to carry out microstructural analysis. Figure 4.17 below shows the gauge length cut from an ASP sample and has been ground and polished back to the critical radius (r_m) of 4mm. This yields an area of 10 x 6 mm for analysis.
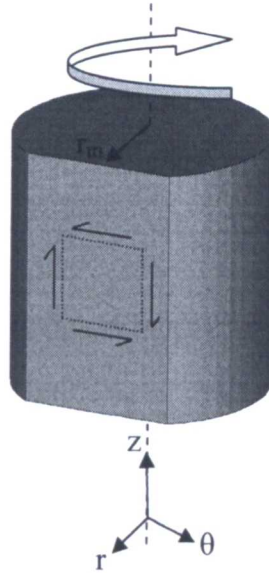
Figure 4.17 Gauge length of an ASPII sample showing the analysed face at the critical radius (r_m), and shearing directions and the sample orientation axis

4.4.7. 'Simple' strain paths

'Simple' strain path tests imply that only one component of strain is imposed; i.e. only torsional shear strain. Table 4.4 below shows the tests carried out under purely torsion deformation and under free end conditions where the axial load is kept to zero and the actuator moves to compensate for any axial stresses caused by thermal or textural influences. The optimised PID values generated by the calibration of the machine are used for all tests.

Test parameters (strain, strain rate and temperatures) have been derived from the FE models of the forging process and typical values have been selected as the test parameters for simple strain path experiments. For the 1st forging operation the strain rate ranges from 0.25 – 3 s^{-1} with a typical value of ~ 2 s^{-1}. For the 2nd operation the range increases to 3 – 25 s^{-1} with an average value of ~ 10 s^{-1} which is used as an upper limit to tune the ASPII machine response with. The very high strain rates (of up to 25 s^{-1}) however are only generated over a short time period and so generate small strains which will be ignored. Table 4.4. presents simple strain path tests utilising such parameters. All such tests are conducted at a strain rate of 2 s^{-1}, the reasons for which are explained in Section 5.3.3.

Table 4.4 Test matrix for 'simple' strain path

Test	Temp (°C)	θ	θ̇	ε_{eq}	ε̇_{eq}	γ	γ̇
1	990	180/-180°	2480	0.73/-0.73	10	6.3	17.3
2	990	180/-180°	992	0.73/-0.73	4	2.52	6.92
3	990	180/-180°	496	0.73/-0.73	2	1.26/-1.26	3.46
4	990	360°	496	1.45	2	2.51	3.46

4.4.8. Complex strain paths

The 'complex' strain path tests utilises data generated by FE modelling and involves possible concurrent axial and torsion imposed strain components. Six arbitrary points which are shown below in Figure 4.18(a) have been tracked throughout the entire deformation and their deformation history recorded. Three points, 1, 5 and 6 have been analysed in detail as points 2, 3 and 4 sit with the large dead zones caused by frictional constraints. For each track point the $\varepsilon_{xx}, \varepsilon_{xy}, \varepsilon_{yy}$ and ε_{zz} component of strain is recorded as a function of time together with temperature, strain rate and total equivalent plastic strain. The data for points 1, 5 and 6 can be found in graphical and tabular form in Sections 5.3.4 & 5.4.4. It is not possible to directly replay each strain component on the ASPII machine as the strains involved in the forging operation are too large and thus samples would fracture. Instead it is assumed the change in strain path change is instantaneous with each blow so that the strain path angle is calculated with respect to the strain imposed by the previous forging blow. The strain path angle α is calculated using equation 2.6. Large strain components are accommodated with torsional deformation and so the corresponding axis defined for the forging and ASPII are not the same as shown in Figure 4.18(b). When there is no change in strain path a linear torsional deformation is carried out to the specified strain under free end conditions not to impose axial stress. To simulate a strain path change on the ASPII machine an axial deformation (ε_{zz}) is carried to simultaneously with a torsional strain.
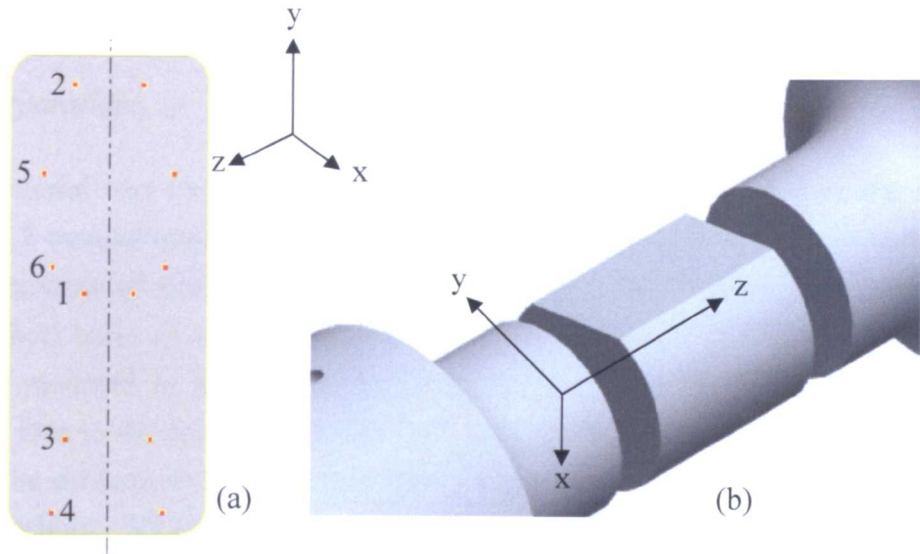
*Figure 4.18(a) Track points within the central plane of the billet material together with
reference axis and (b) the reference axis for a ASP sample*

The magnitude of this axial strain is determined by a ratio of (ASP reference axis)
$\varepsilon_{xy}/\varepsilon_{zz}$ which gives achievable strains for an ASP sample to accommodate and is
calculated using equation 2.12 and 4.16. This procedure reduces the equations to give
only two unknowns and assumes that the material is isotropic (a reasonable assumption
for a material with no distinct texture) and so;

$$\varepsilon_{xx} + \varepsilon_{yy} + \varepsilon_{zz} = 0 \tag{4.54}$$

and thus;

$$\varepsilon_{xx} = \varepsilon_{yy} = -\frac{\varepsilon_{zz}}{2} \tag{4.55}$$

Tables 5.11-5.13 in Section 5.3.4 show the FE predicted strain components, the
calculated strain path angles together with the corresponding ASPII axial and torsion
deformations.

4.5. Microscopy

4.5.1. Preparation

Sample material was sectioned using either the Accutom cutting disc or the Buehler Abrasimet 2 manual cutting wheel, depending on the specimen's size. In both cases, copious amounts of coolant were used as titanium's low thermal conductivity can aggravate heat build up and lead to local heat affected zones in the metal. All samples were then mounted in non-conducting bakelite, ready for mechanical grinding and polishing. Due to the dual-phase nature of Timetal®834, mechanical polishing by hand proved to be difficult as the primary alpha phase pulled out of the matrix and caused severe scratching. All grinding and polishing was carried out upon the Struers Abramin automatic polishing machine, which allowed a constant even force of 150N to be applied during grinding and polishing. Grinding was carried out using a Struers MD Piano 220 resin bonded diamond disc with a segmented surface (Figure 4.19(a)), designed to minimise build up of abraded material, allowing consistently high material removal rates and optimum flatness. This is carried out for approximately 2 minutes until a flat plane is produced on all of the samples and is equivalent to a 220 silicon carbide grit finish. Fine grinding was then carried out using a Struers MD Largo pad (Figure 4.19(b)) with 9μm diamond suspension, until a satisfactory finish was produced. Polishing was finalised by a mechanical/chemical polish with colloidal silica (0.05 μm silco) on a porous neoprene polishing pad (Figure 4.19(c)). The silco was gradually applied in a continuous drip using a syringe to prevent crystals being introduced and scratching the specimens. Care must be taken at this final stage to prevent silco drying on the sample, spoiling its surface finish. If this is to be avoided, then the silco must be washed off instantly with water after polishing.

Figure 4.19 (a) MD Piano diamond grinding disc, (b) MD Largo fine grinding disc, (c) porous neoprene polishing disc

4.5.2. Etching

Once a perfectly flat and scratch free surface had been produced, etching was carried out to emphasize the microstructure of the metal. Due to titanium's high affinity for oxygen, it forms a very stable and adherent oxide instantly on exposure to oxygen. This oxide layer yields titanium's excellent corrosion resistance however it also presents difficulties in its etching. As a result highly corrosive etchants are required which include Krolls reagent or 2% Ammonium Hydrogen Di-Fluoride. The chemical composition of the etchants can be seen in Table 4.6.

Table 4.6 Composition of two etchants used

Etchant	
Krolls reagent	**Ammonium Hydrogen Di-Fluoride**
2ml Hydrogen Fluoride	2g Ammonium Hydrogen Di-Fluoride
4ml Nitric acid	100ml De-ionised water
100ml Water	-

The etchants used here are extremely corrosive and toxic, and as a result great care must be taken in handing them. All etching was carried out within a fume cupboard whilst wearing a full body apron, full-face visor, lab coat and 3/4 length gauntlet gloves. Each specimen was submerged in the etchant for 6-8 seconds before being transferred to lime solution to neutralise the acid and then washed in water. It was discovered that the krolls reagent produced the best results for optical analysis, as the 2% Ammonium Hydrogen Di-Fluoride produced an etch which was too severe. This is however dependant on the age and cleanliness of the chemicals being used. In later work the ammonium hydrogen di-fluoride was found to give better results by removing the sample from the etchant as soon as bubbles begin to form on the surface of the metal.

4.5.3. Optical

This technique enables a quick and simple method of microstructural investigation. It can reveal the morphology and scale of the microstructure. In addition to this, the Polyvar microscope combined with KSRun software allow digital pictures to be obtained and from this calculate volume fractions of second phase particles to be calculated, and in the case of Timetal®834, the volume fraction of primary alpha.

4.5.4. Scanning electron microscopy

In order to carry out more detailed investigations of specimen's morphology, the JEOL 6400 SEM was used. This microscope is capable of high resolution secondary and backscatter imaging, as well as energy dispersive spectroscopy (EDS) and electron back scatter diffraction imaging. To prevent electron charging in the sample's surface during SEM operation silver dag was applied to the sample to create an electron sink from the sample's surface. Initial images were taken using secondary electrons. Imaging was carried out using a spot size of 5 with an accelerating voltage of 20kV at a working distance of 25mm.

4.5.5. Electron back scatter diffraction

EBSD analysis was carried using the Sirion microscope and HKL Channel 5 software. Samples where prepared the same as the optical/SEM samples up to the final silco polish. Here samples where polished with a colloidal silco and 10% hydrogen peroxide mix to prevent etching from the silco. This polishing was carried out for 6 minutes using a porous neoprene polish pad on a Struers Abramin automatic polishing machine. Immediately before, or the day before a scan it is advantageous to give the sample a final silco-hydrogen peroxide polish by hand to minimise an oxide layer that may have formed.

Microstructure and texture analysis was done in the Z-θ plane at r_m using EBSD. EBSD data was acquired using an FEI Sirion FEGSEM, equipped with a fully automatic HKL Technology EBSD attachment, operated at 15 kV. All EBSD data was filtered using in-house modified Kuwahara filtering software for edge retaining orientation averaging. Table 4.7 shows the microscope operating parameters used.

Table 4.7 FEI Sirion FEGSEM microscope EBSD operations parameters

Parameter	Value
Magnification	200
Beam spot size	3
Beam accelerating voltage	15kV
Number of background frames	64
Number of average frames	4-8
Timing per frame	100-120 µs
Step size (high res./texture)	0.25/2µm
Mapping rate	0.6-1.2s-1
Camera binning	4 x 4

4.6. Conclusions

Three experimental methods have been successfully applied in this project: FE modelling, mechanical testing and electron microscopy. The FE modelling can be subdivided into axisymmetric validation experiments and industrial (forging) processing of titanium. Extensive modelling and parameter sensitivity analysis is carried out to ensure the validity of the complex forging models. These will include checking the deformation behaviour, frictional affects and the heat loss from the workpiece and results compared with that measured during mechanical testing. FE modelling of the forging will yield the range of strain paths imposed during an industrial process with complex material flow. The method of their extraction from the model and their conversion to a laboratory test is also shown.

The mechanical testing can also be subdivided into 'simple' strain path testing to investigate whether extreme changes in strain path (180°; forward-reverse torsion) could be exploited to break up the clustering of similarly oriented primary alpha grains. The second 'complex' strain paths focused on replaying the of strain path angle changes that are induced in forging complex components. Initial work with the ASPII machine has aimed to produce parameters that enable precise control at high strain rates and temperatures together reproducibility. The mathematic derivation behind all test definitions and material flow behaviour are also presented in this chapter.

The preparation of optical and EBSD samples has been shown to be very rapid and reproducible when using automatic grinding and polishing machines. With respect to the best etchant, although the Krolls reagent produced superior contrast between the two different morphologies it is very dependant on chemical cleanliness and age and the working conditions. Etching times may vary widely when using ammonium hydrogen di-fluoride but as soon as bubbles are seen on the samples surface then the material is etched sufficiently.

5. Results and discussion

The following chapter is subdivided into two sections of FE and ASPII machine validation together with the results produced by both simulation and real machine tests. In the first section the complex FE models that have been formulated are validated against test data, and the magnitude of change in model input parameters is evaluated. The tuning and calibration of the relatively new ASPII machine is discussed in detail in order to facilitate the reproduction of such complex deformation sequences.

The second section of this chapter is concerned with the data produced by modelling of the ASPII tests and the simulation of the forging process. From this data strain path changes are derived and their resultant behaviour on the ASPII machine is shown together with the effects on the microstructural evolution of the material.

5.1. FE validation

This first section of FE modelling concentrates on axisymmetric compression to evaluate the abilities of the constitutive behaviour equations derived in Chapter 3. Such models are compared and validated against real test data conducted by Thomas [90]. The effects of model input parameters that are difficult to measure (e.g. friction, heat transfer, etc) are also assessed.

Due to the complex nature of the planned ASP tests the ASPII machine required extensive calibration in order to successfully carry out such demands. This chapter also presents the results of the various machine calibrations, including thermal and PID calibration to ensure the correct temperatures and plastic deformations were induced.

5.1.1. Deformation heating and strain reproduction

The fundamental input parameter for a thermomechanical plasticity FE model is the constitutive equation used to describe the material behaviour under various strains, strain rates and temperatures. The validation of such an equation for Timetal®834 was carried out using data from axisymmetric compression tests. The first check for model validity was in the shape and strain distribution within the deformed material. The model accurately reproduces these compared with the real compression tests as seen below in Figure 5.1. Figure 5.1(a) shows the predicted total equivalent plastic strain (TEPS) distribution in a quarter of the axisymmetric FE model, the shape of which very closely matches that of the real axisymmetirc test as shown in Figure 5.1(b). This model also highlights the strain concentration on the very top right corner of the sample that has folded over in the micrograph. Although the model correctly predicts the large

strain concentration at this point it does not contain any information regarding the hardening of the hot exterior surfaces due to interstitial absorption and the formation of a stronger (than base alloy) alpha case, seen as a lighter region on the top and right hand sides of the sample (Figure 5.1(b)).
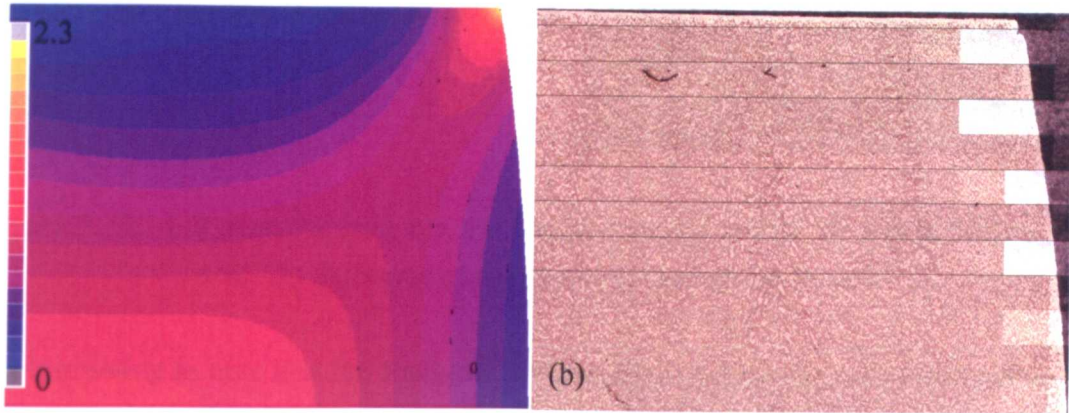
Figure 5.1 Quarter sample (a) FE model and (b) axisymmetric compression test at 1010 °C and a $\dot{\varepsilon} = 2s^{-1}$ to a strain of 0.7[90]

Additional results for a typical axisymmetric compression test can be seen below in Figure 5.2 with lower temperatures and strain rates. This model demonstrates the highly nonlinear deformation that exists in (the majority of) material deformation techniques, even the seemingly simple tests such as axisymmetric compression. Shearing at approximately 45° accommodates the majority of the deformation within the sample. This produces two dead zones of material; one produced by frictional constraints at the tool-work piece interface, the other by being simply pushed out by the deforming slip line field. Such a result highlights the necessity of FE modelling in thermomechanical processing, allowing the quantification of the microstructure to given testing parameters by matching these parameters to regions under going the same conditions.
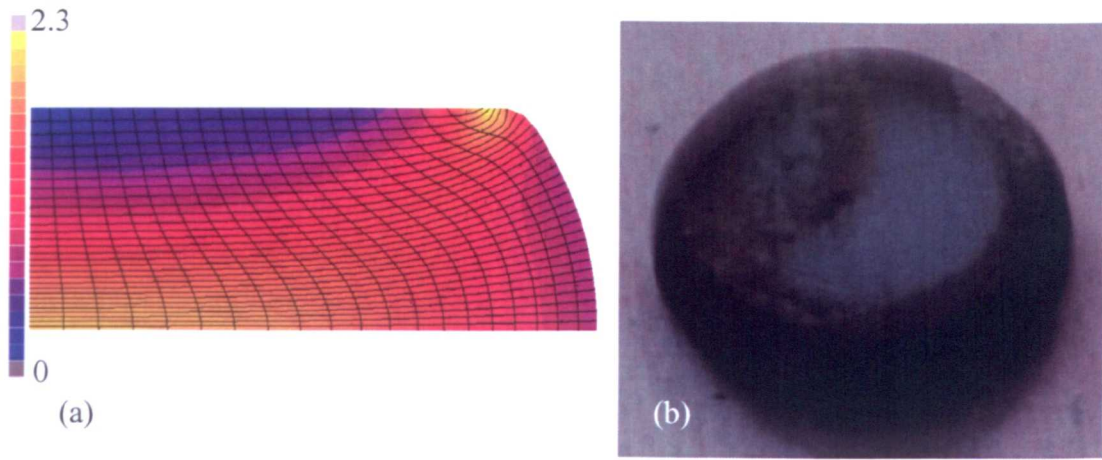
Figure 5.2(a) axisymmetric compression (quarter model) at 825 °C, $\dot{\varepsilon} = 1s^{-1}$ to a strain of 0.7(b) deformed axisymmetric compression sample

It is interesting to note that the frictional force is high enough to cause the constraining of the material at the tool interface as the tool moves down. This results in the sides of the cylindrical sample (in this case the right-hand side) folding over and becoming the top surface, and as a result produces the high strain concentration on the right hand edge of the top surface. Figure 5.2(b) shows light areas demonstrating where the lubricant has bonded to the top surface of the sample by the heat and pressure and thus shows roughly the original top surface. The rest of the deformed top surface is bare metal as the sides of the sample folded over to become the top surface. The corresponding FE model highlights the stress concentration in Figure 5.2(a). A similar phenomenon is reported in work on steel alloys during the determination of friction coefficients via the ring test Jupp [94].

The model is capable of reproducing the same shape observed in an axisymmetic tested sample and highlights subtle localised conditions that may led to defects in a test, e.g. the folding over of a samples corner due to high stress concentrations and frictional constraint. However, the correct values for the amount of plastic strain imposed are of upmost important to any microstructure analysis. The deformation heating is a very useful means to check this as it is directly related to the plastic deformation imposed. Assuming adiabatic conditions, i.e. no heat transfer in or out of the control system, then the heat generated by plastic deformation can be obtained from the stress strain curve as shown in Equation 5.1 Burton [117]. This relates the energy of deformation per unit volume (area under stress-train curve) to the specific heat capacity of the material. Such a model is embedded into the FE code when calculating thermomechanical deformations and uses the assumption that 90% of the work put into the material is converted to heat. The remaining 10% is used to generate defects such as dislocations.

$$\delta T = \left(\frac{\sigma}{\rho c_p}\right)\delta \varepsilon \qquad (5.1)$$

Assuming ideal plasticity i.e. a material deformed at constant stress (a reasonable approximation for hot working as restoration mechanisms preventing excessive work hardening), the temperature increase is obtained by integrating Equation 5.1.

$$\Delta T = T - T_{initial} = \left(\frac{\sigma}{\rho c_p}\right)\varepsilon \qquad (5.2)$$

rearranging yields:

$$T = \left(\frac{\sigma}{\rho c_p}\right)\varepsilon + T_{initial} \qquad (5.3)$$

Substituting the thermo-physical values for Timetal®834 (ρ-4550 kg/m^3, c_p-525 J/kg°C), and using a mean stress in MPa, the actual temperature for hot worked Timetal®834 can be calculated by:

$$T = \left(\frac{\sigma}{2.4}\right)\varepsilon + T_{initial} \qquad (5.4)$$

Where $T_{initial}$ is the starting temperature, σ is the mean flow stress at the deformation conditions and ε is the total equivalent plastic strain imposed on the material. For example, deforming at 1030 °C and with a $\dot{\varepsilon}$ - 0.2 s^{-1}, gives a mean stress of approximately 70 MPa.

$$\Delta T = \left(\frac{70}{2.4}\right)0.7 = 20\ °C$$
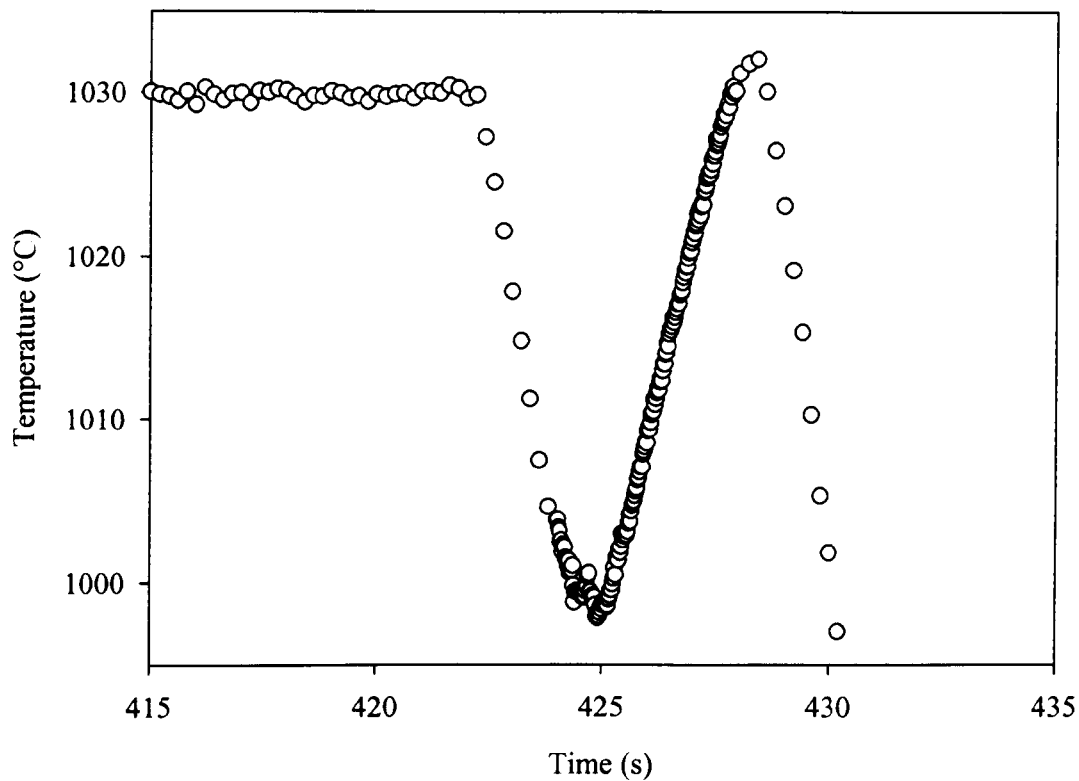
Figure 5.3 Deformation heating measured during an axisymmetric compression test at 1030 °C, $\dot{\varepsilon}$ - 0.2 s^{-1} adapted from [90]

From Figure 5.3, during this test the temperature drops from 1030 °C to ~998 °C as the sample is moved from the induction coil into the deformation furnace. The resultant deformation heating is ~33 °C, 13 °C higher than predicted above. The calculation is close to that of the measured value, however, error is introduced as the actual test temperature is lower than the desired temperature and as a result the material has a slightly higher flow stress and so more deformation heating is measured. Figure 5.4 shows the FE predicted deformation heating for various temperatures and strain rates plotted against the measured deformation heating. This graph suggests there is a clear agreement between the FE calculated deformation heating and that measured during testing. There is more deviation from the desired trend line of all the high strain rate tests (20 s^{-1}) and one of the 2 s^{-1} tests. All these points follow the same gradient of ~45° as the other accurately placed points but the FE prediction gives values that are ~20 °C higher than the measured values. This is likely a combination of the temperature drop on entering the deformation furnace and by considering that the deformation times for strain rates of 0.2, 2, and 20 s^{-1} are 3.5, 0.35, and 0.035 s respectively. Together with titanium's low thermal conductivity the thermocouples may not have sufficient time for the heat to flow through the sample and for them to measure the exact temperature

within the sample. Such a "thermocouple lag" phenomenon is also reported elsewhere by Jupp [94] in the rolling of steel plate.
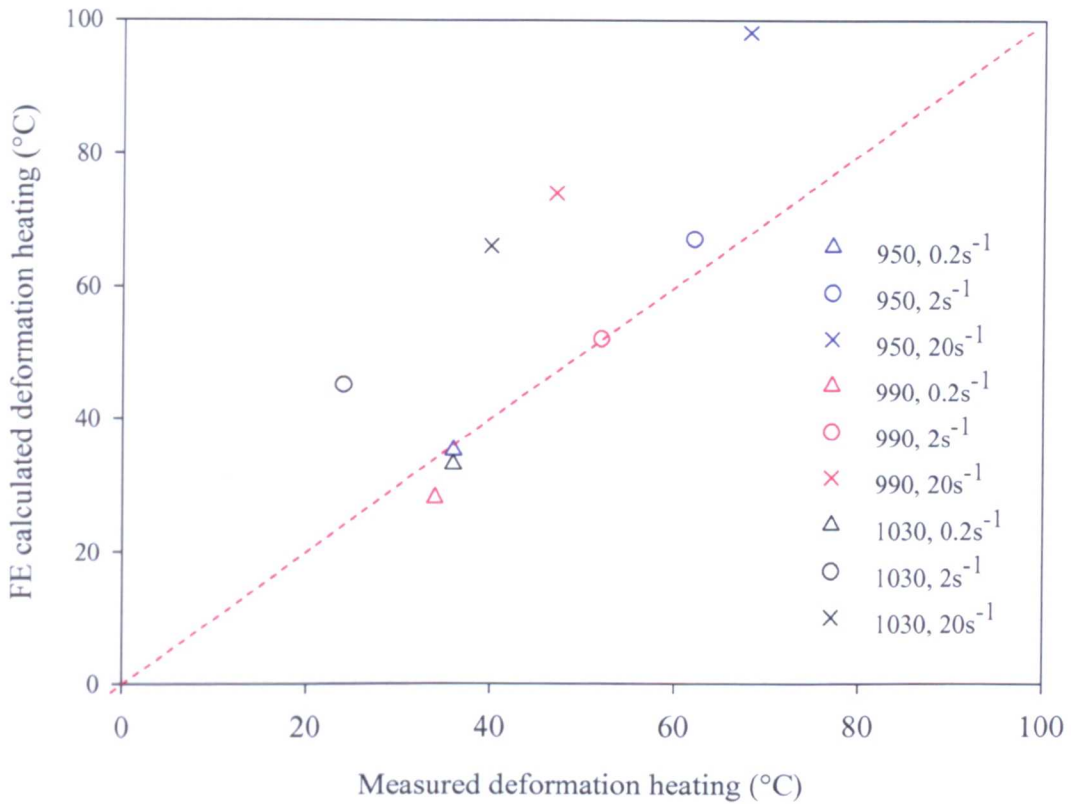
Figure 5.4 Deformation heating measured from axisymmetric compression tests plotted against deformation heating calculated by FE models. The key shows the temperature and strain rate for each point

In combination to checking the values of FE calculated strain to that of the experimentally measured (in the form of deformation heating) the flow stress was evaluated by measurement of the tool force during compression at various strain rates. Figure 5.5 plots the FE calculated tool force together with the corresponding measured tool force for three axisymmetric tests conducted at a strain rate of $20s^{-1}$ at 950, 990 and 1030 °C to a strain of 0.7. For all three temperatures the yield stress is accurately predicted by the constitutive equation however this predicted value is fractionally higher than that measured. The slow rate of work hardening is also captured by the constitutive equation although at all temperatures this is over estimated all the end of deformation. More additional work could be conducted to greater improve the performance of the constitutive equation and fine tune the FE model to more accurately predict flow stress however for the purpose of this work the current response is adequate.
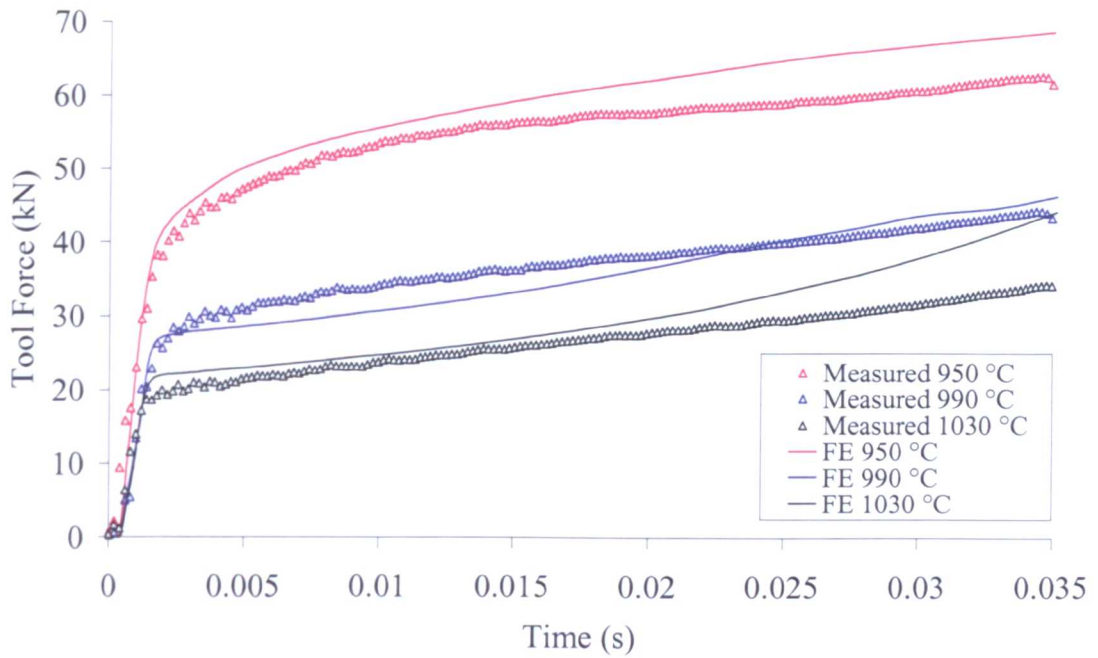
Figure 5.5 Measured and FE predicted axisymmetric compression tool force for Timetal®834 deformed at 20 s⁻¹ and 950, 990 an 1030 °C to a strain of 0.7

5.1.2. Parameter sensitivity analysis

The effect of the remesh distortion angle over the range of 5° to 40° is shown below in Figure 5.6. The top plane label on the graph refers to the surface which is in contact with the top tool (dashed lines) and the mid-plane is through the centre of the sample (solid lines). The total equivalent plastic strain is plotted against the distance from the very centre of the sample to the outer edge.
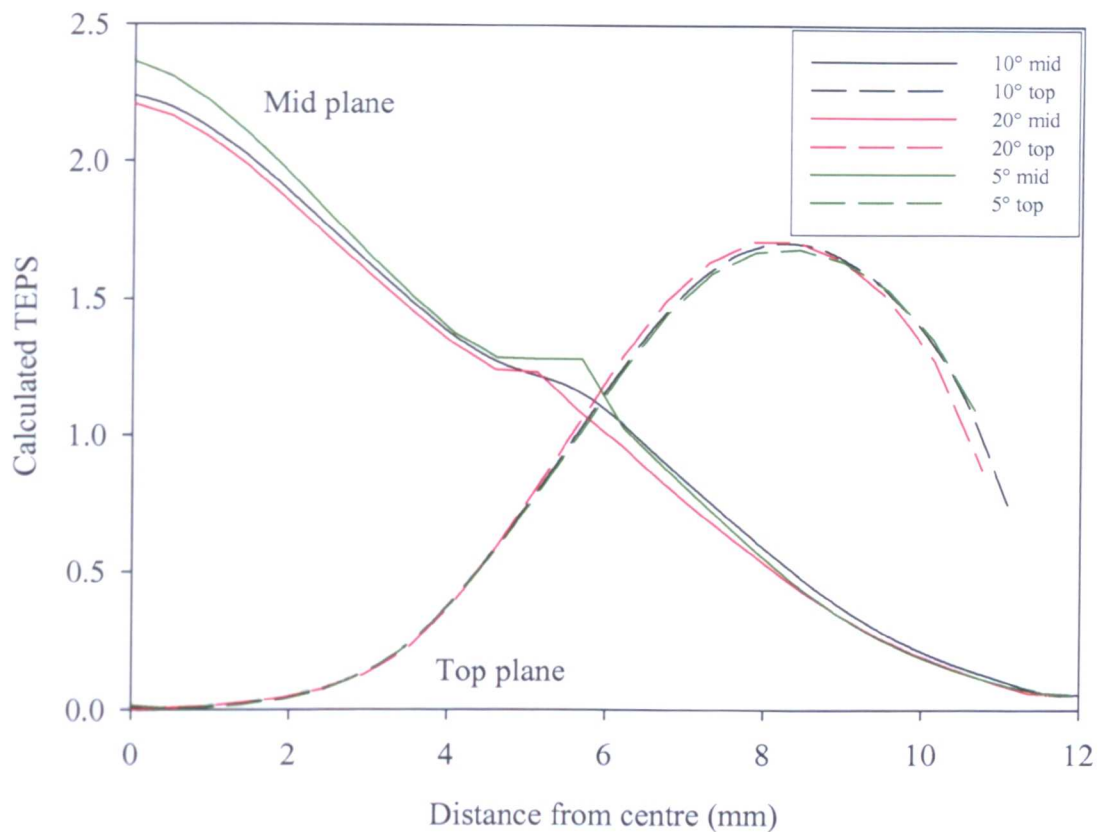
Figure 5.6 Graph showing the effects of remesh deviation angle on the TEPS for the mid plane and top surface of an axisymmetric sample at the end of deformation (20=30=40 ° and are therefore not plotted)

This figure shows that changes in remesh deviation angle from 5° to 40° have very little effect on the TEPS distribution within an axisymetric compression test sample in the two planes selected. On the top surface of the compression sample where the most severe deformation and thus element distortion is, as discussed previously, the affect of deviation angle is insignificant as elements here rapidly become distorted to evoke a remesh. The largest discrepancy between 5° and 40° is a strain of approximately 0.05, which is too small a strain to produce any noticeable or even measurable microstructural effects.

Through the mid plane of the sample the effects are more prominent compared to the top surface, however these are still small at a strain difference of ~0.1. As to be expected, the smaller deviation angle the more detailed is revealed. Deviation angles of 40, 30 and 20° produce exactly the same strain distribution in both the top and mid plane of the sample and as a result 30° and 40° are plotted. Only when the angle drops to as low as 5 and 10° does it reveal more detail in the strain distribution. A deviation angle of 5° also produces a slightly higher strain at the centre of the sample and picks up a plateau of strain approximately 5mm away from the centre. However, these effects

are small and would not have a major effect on the overall output. A deviation angle of 5° will be used for future models to ensure maximum element mesh angles are guaranteed and calculated stress/strain values are accurate.

A valid FE model must be mesh insensitive, as a coarse mesh would introduce errors into the model due to issues with excessive element distortion and possible tool penetration into the workpiece. Conversely, a very finely meshed model would be very heavy on the processor resulting in very long calculation periods and is thus impractical to use. Figure 5.7 below shows the effects of changing the mesh density in order to find a suitable balance between the two extremes. Here the TEPS is plotted against the distance from the centre of an axisymetric sample (again for both top and mid planes) with the numbers of elements in the x and y directions. The sample is deformed to a strain of 0.7 at $2s^{-1}$ and 990°C.
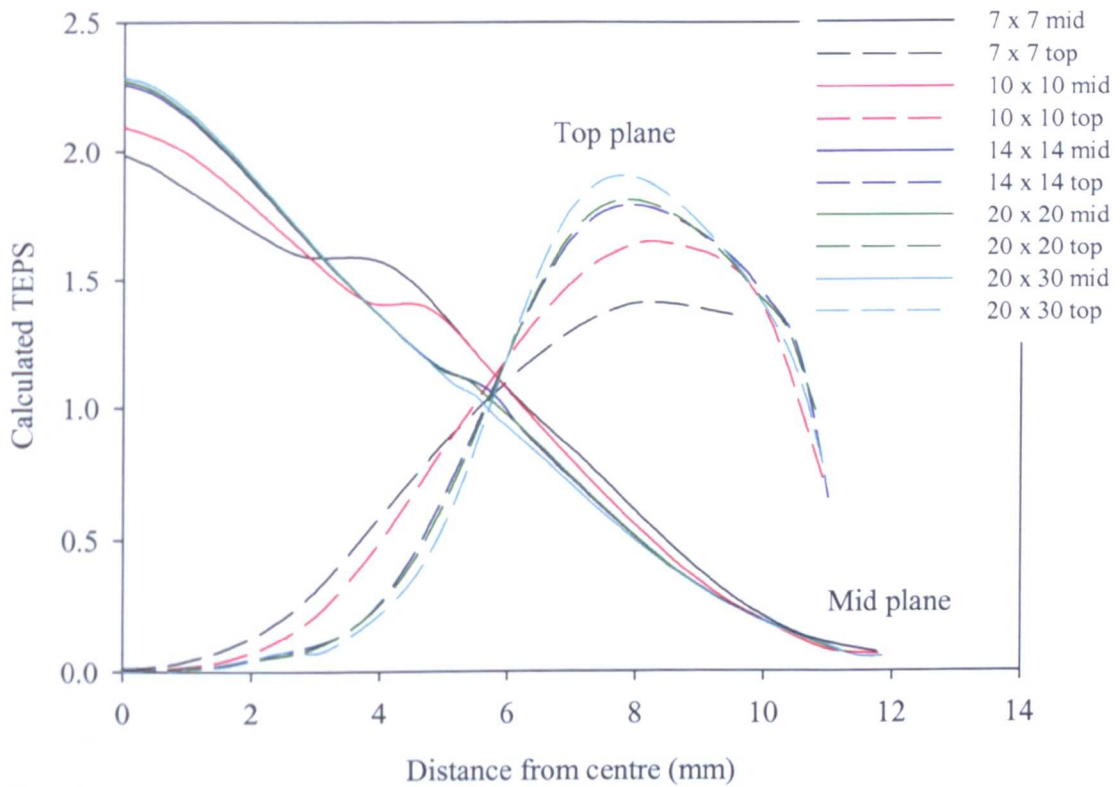
Figure 5.7 Effects of remesh density on the TEPS for the mid plane and top surface of an axisymmetric sample at the end of deformation

Although all the plots follow the same trend the differences in calculated strain values is quite significant. The largest discrepancy in the coarsest and finest mesh is 0.25 in the mid plane and 0.5 in the top plane. The high discrepancy in the on the top plane highlights the issue of excessive element distortion at the corner of the sample as material folds over from the side of the sample. As the element numbers approach 200 (14 x 14) the differences between calculated strain values becomes very small for the

top plane of the sample. The same effect is also seen in the mid plane where only a very small difference in calculated strain for higher mesh densities can be seen. This result is also confirmed in Figure 5.8 where the maximum calculated TEPS is plotted against the number of elements in the mesh. The value for the calculate strain rapidly rises to a value of 2.30. Above 200 elements (as demonstrated above) and up to 1200 elements the strain value slowly increases from 2.25 to 2.33.
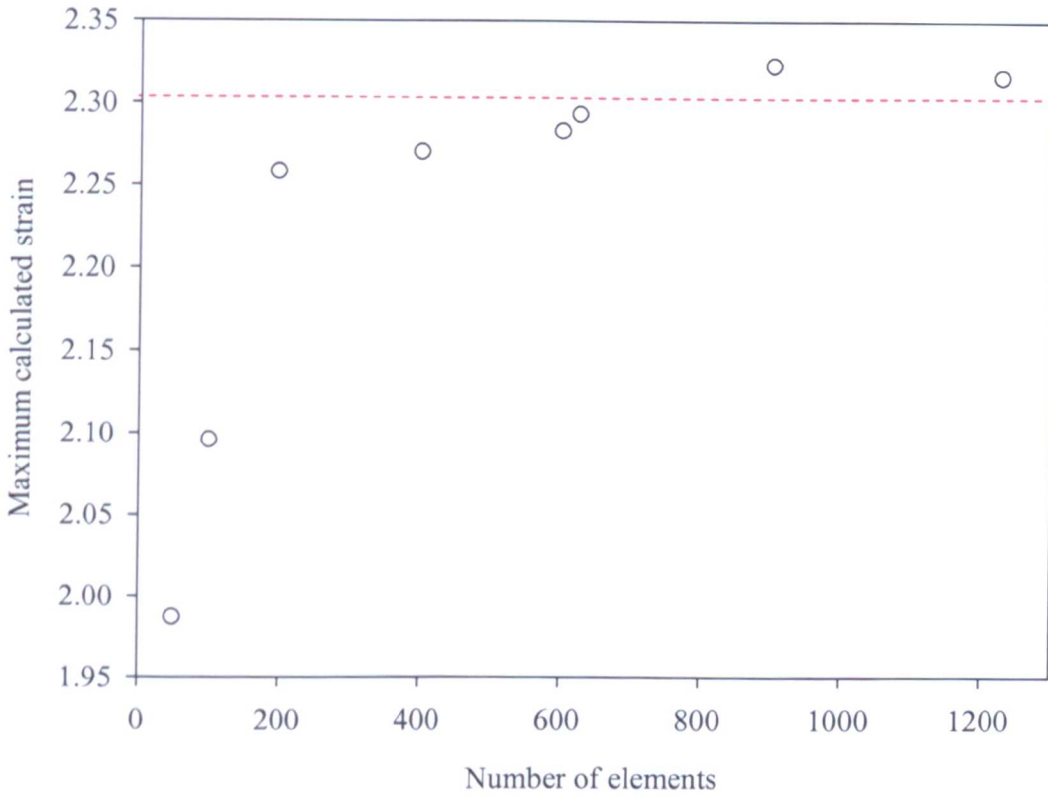
Figure 5.8 Maximum calculated strains in FE models of varying mesh density

By combining the data from both these two graphs it can be seen that a mesh density of approximately 4.4 elements/mm^2 (196 elements/(6 x 7.5mm)) will yield sufficiently accurate strain calculations and that increasing the number of elements will just result in unnecessary increased computation times. Although the presented work maybe seemingly simple it is very important as the FE method is very good at generating data, however this must validated against measurable parameters (e.g. temperature) and the significance of individual model parameters need to be evaluated. By considering Figure 5.7 for example, all the data plots follow the same trend even though the calculated values of TEPS differ quite considerably. Only when there are several different iterations of the model run with increasing mesh densities is it possible to hone in on the correct calculated value. This affect is also highlighted in Figure 5.8.

The above work has investigated the effects of the FE mesh parameters on the outcome of the axisymmetric compression model. This next portion of work demonstrates the

effects of the materials physical properties on the outcome of the models. In Section 3.6 it was shown that Ti-Al alloys thermal conductivity varies from 7 $Wm^{-1}K^{-1}$ at room temperature and rises linearly to 18 $Wm^{-1}K^{-1}$ at hot working temperatures and Timetal®834 also exhibits a thermal conductivity of 7 $Wm^{-1}K^{-1}$ at room temperature [17]. Figure 5.9 shows the effects that different thermal conductivities have on the temperature (dashed lines) and TEPS distribution (solid lines) within an axisymetric sample deformed at 925 °C, a strain rate of $10s^{-1}$, to a strain of 0.7.
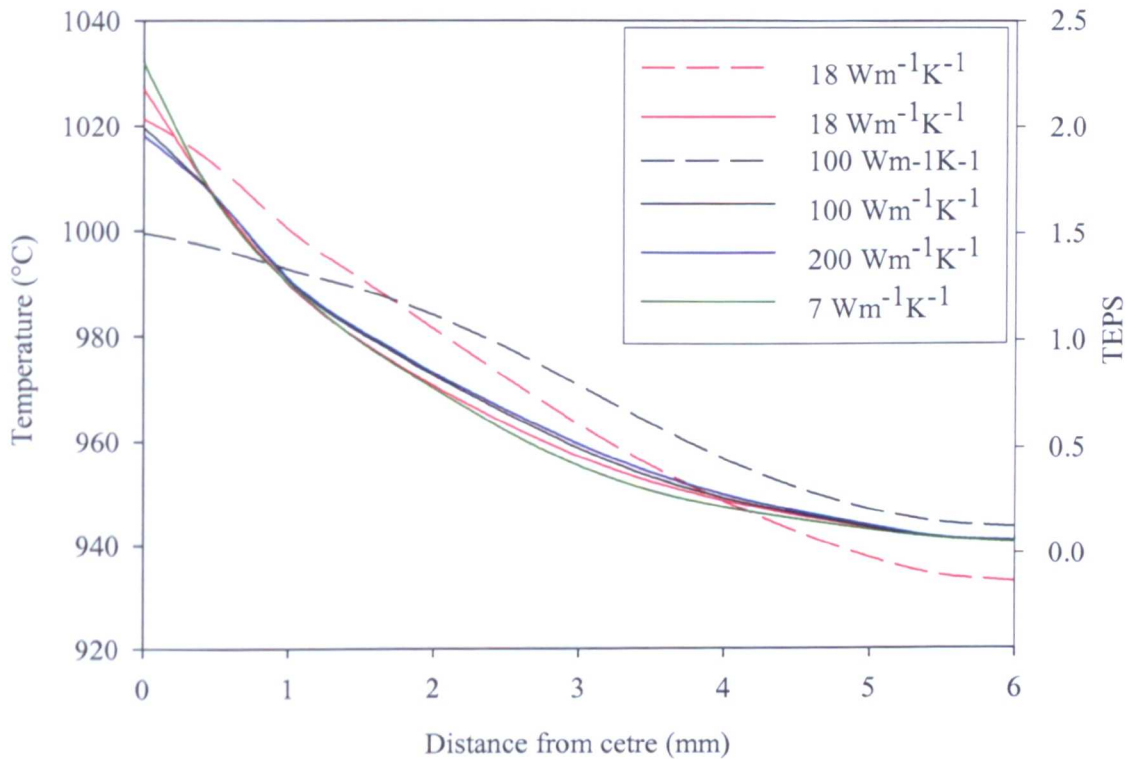
Figure 5.9 Effects of thermal conductivity on the temperature (dashed line) and TEPS for the mid plane of an axisymmetric sample at the end of deformation

This figure not only shows the effect the variation in Timetal®834's thermal conductively has on the TEPS over a particular temperature range, but also for a very large change in k as if the material exhibited thermal conductivities similar to that of aluminium and copper alloys (100 and 200 $Wm^{-1}K^{-1}$ respectively). Comparing the temperature distribution of the 18 and 100 $Wm^{-1}K^{-1}$ plots there is a noticeable difference in temperature of 20 °C and 10 °C at the centre and edges of the sample respectively. However the difference in TEPS for both these variables is very minor and they both yield almost the same value across the same. Only at the centre is there a more noticeable difference between the two with the 18 $Wm^{-1}K^{-1}$ plot giving a 0.2 increase in calculated strain. The same trend can be seen with a k of 7 $Wm^{-1}K^{-1}$ where there is an increase in TEPS at the centre of 0.3 compared to the 100 $Wm^{-1}K^{-1}$ plot. Thus, the

lower thermal conductivity results in a higher temperature in the centre of the sample and a lower temperature at the surface when compared with the higher conductivity giving a material with lower flow stress at the centre and increasing the amount of strain experienced here. This would seem quite obvious, as the high conductively would allow the heat to flow throughout the sample more readily creating a more even distribution of temperature and a slightly less sharp increase in the TEPS at the very centre of a sample. This result emphasizes that when combined with titanium's relatively high flow stress and deformation heating, a low thermal conductivity can begin to cause localised plastic flow/adiabatic deformation.

Overall this result shows that over a large range of thermal conductivities (7-200 $Wm^{-1}K^{-1}$) the affect on the TEPS distribution is small. A higher conductivity will produce a more even temperature distribution in a sample and a slightly lower strain in the centre. A lower conductivity will generate a larger range in temperature at the side surface and in the centre of a sample compared to a high thermal conductivity as heat flow through the material is less efficient. This results in higher strains at the very centre of a sample but is less pronounced after further than 0.5mm where the effect of thermal conductivity on the TEPS is negligible.

The effects of three different tool heat transfer coefficients on TEPS and temperature distribution at the end of deformation are shown in Figure 5.10 where the TEPS is plotted in solid lines for the mid and top plane of the sample and the temperature is plotted with a broken line. The three values are predetermined values in the MSC software for 'cold', 'warm' and 'hot' deformation as shown in Table 4.1. The three different values generate three different temperature distributions throughout the sample, all following the same trend. The higher the tool transfer coefficient, the lower the temperature on the mid plane of the sample. At the centre this effect is most noticeable where the 20 and 30 $kWm^{-2}K$ coefficients produce a 5 and 3 °C difference from the 25 $kWm^{-2}K$ 858 °C. This small difference can be attributed to titanium's low thermal conductively confining the chilling effect of the cold tools to the very surface of the work piece.
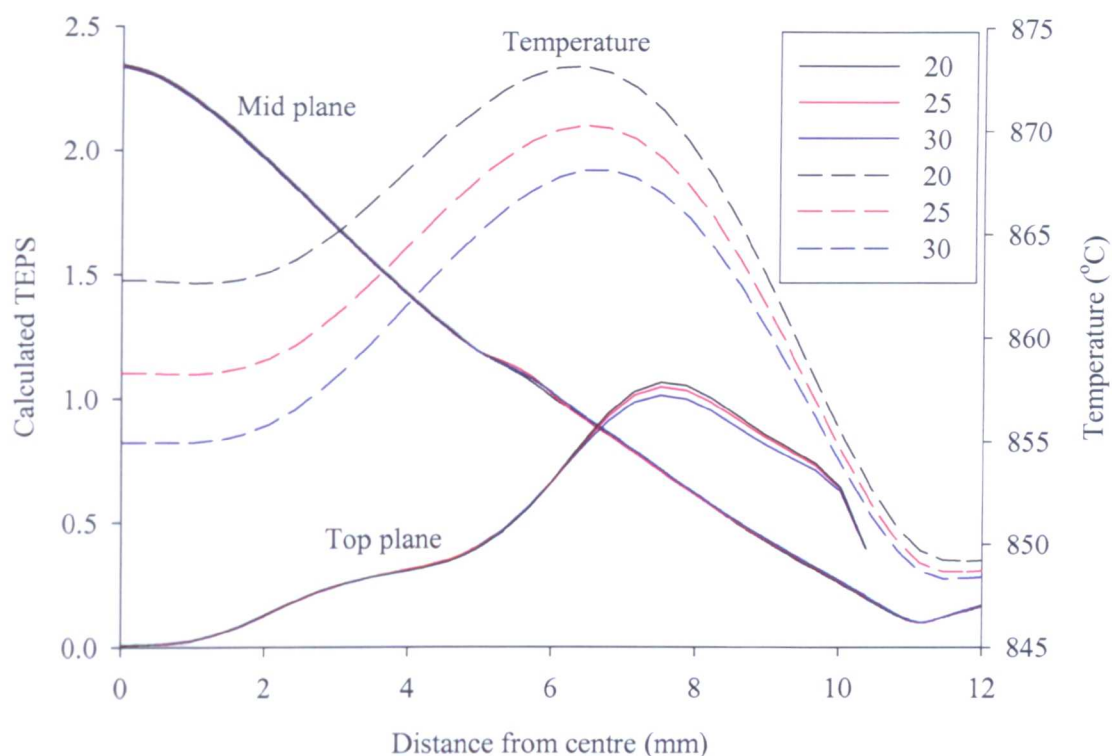
Figure 5.10 Effects of tool heat transfer coefficient on the TEPS for the mid plane and top surface of an axisymmetric sample at the end of non-isothermal deformation (tool temperature, 15 °C) at 10s⁻¹ and 925 °C

This is shown in the two strain distributions for the top and mid plane plots. On the mid plane where there is only a maximum temperature difference between the three curves of 8 °C there is no appreciable difference in TEPS distribution. On the top plane where considerably more heat is conducted out of the workpiece into the tools there is a small decrease in calculated strain for a higher heat transfer coefficient. However, over this range the difference is very small at ~0.1. Although the literature [101,109,110,118,119] quite rightly points out that it is very difficult to measure tool heat transfer coefficients, all of which vary greatly with temperature, pressure, etc. Here it is show that for values covering the range to be utilised in this work have a very small affect on the calculated strain and any error in this value will be introduced on the surface of the workpiece.

The effects of the 'cold'-20 kWm²K and 'hot'-30 kWm²K coefficients on the tool force for the model is shown above in Figure 5.11 to demonstrate the effect of the two 'extremes' preset in the software. Here the tool temperature is set to 300 °C which is used in the industrial forging of Timetal®834 to prevent excessive die chilling and cracking of the workpiece.
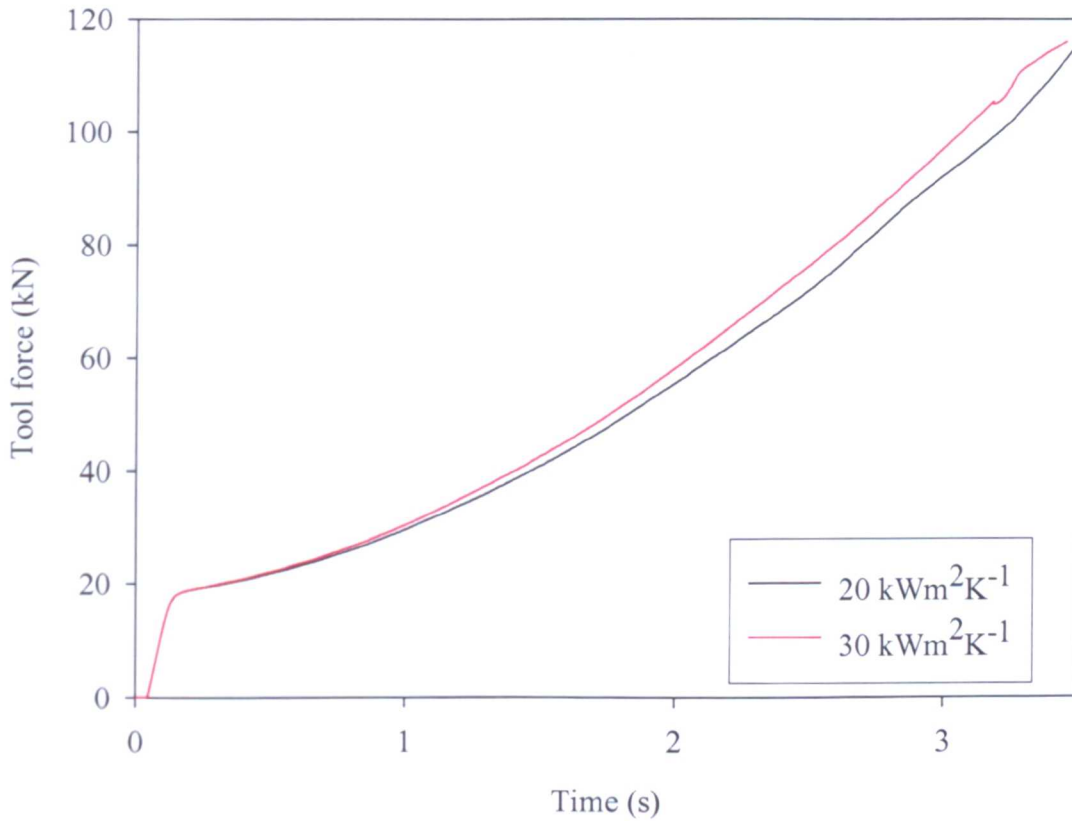
Figure 5.11 Effects of tool heat transfer coefficient on the tool force during an axisymmetric test at 990 °C and $\dot{\varepsilon} = 0.2s^{-1}$ with a tool temperature of 300 °C

The plot shows a small amount of time before the tool comes into contact with the sample and is then followed by a small region of elastic deformation before yield occurs. Both curves display the same trend of increasing tool force as the deformation continues. From Figure 3.4 the material does not exhibit a high strain-hardening coefficient under these conditions so the increase in tool force can be attributed to the increase in sample area as it is spread out during the deformation. After approximately 1 second the higher heat transfer coefficient begins to increase the tool force more as the material is chilled more rapidly giving a higher flow stress. At the end of the deformation this results in a maximum difference of 5kN force. Provided that the correct magnitude of heat transfer coefficient is utilised, relatively small deviations from such a value has minor effects on the tool force and temperature distribution of the workpiece. As shown previously the value of calculated TEPS is essentially unaffected. The next group of plots in Figure 5.12 show the effects of the environmental heat transfer coefficients (combined convectional and radiation heat loss as discussed in Section 4.2.1.5.2) and the results are very similar to those observed in Figure 5.10. The three coefficient values again come directly from suggested values in the software for

'cold', 'warm' and 'hot' working conditions and are higher in magnitude than those calculated in Section 4.2.1.5..
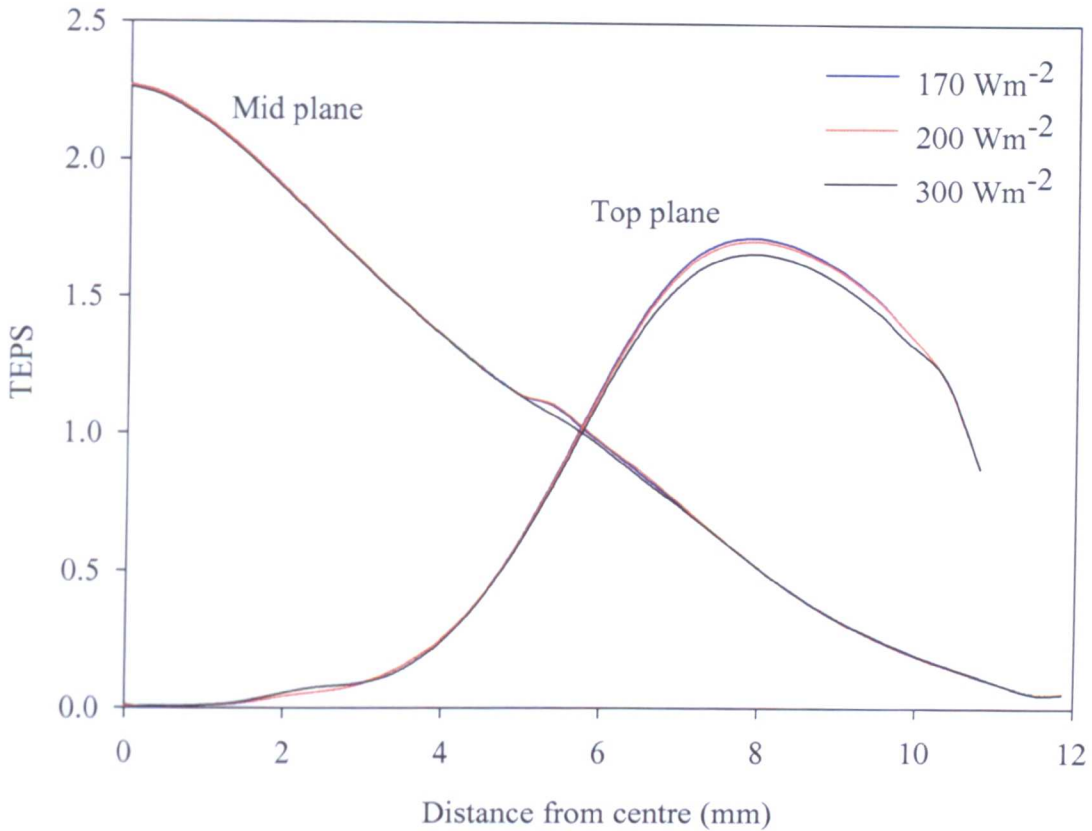
Figure 5.12 Effects of environmental heat transfer coefficients within the MSC software on TEPS distribution in an axisymetric sample deformed at 925 °C, $\dot{\varepsilon} = 0.2s^{-1}$

As in Figure 5.10 the higher the heat transfer coefficient the more heat is removed so a small maximum strain difference of 0.08 is produced between the 170 and 300 Wm^{-2} coefficients at a distance of 7.9mm from the sample centre. This is only noticeable at such a distance of 7.9mm as the material that was the side of the sample is folded over to become the top surface that is in contact with the colder tool. Here the small effects of the different environmental coefficients have on removing heat through the side surfaces on the sample is exaggerated by the more rapid heat lost to the top tools. Again as for the results shown in Figure 5.10 the heat transfer effects on strain distribution are isolated to the surface of the samples by the lower thermal conductively and no effect is visible on the mid plane of the sample.

Like the tool heat transfer coefficients, friction coefficients are very dependant on a multitude of deformation parameters as stated by many other authors [92, 99,100,120]. This work does not utilise a complex or varying friction model, only the one described in Section 4.2.1.4 with a fixed value of μ. Although μ can be derived for various compression tests, authors [101-105] working under similar conditions and with similar

alloys still produce a range of friction coefficients. Friction conditions on different surfaces also arise during 'real' testing, for example, axisymetric compression samples can display non-uniform deformation as the lubricant used during testing can be lost easily from the bottom surface of the sample compared to the top surface where it is typically unaffected by gravity. This results in a sample which has been frictional constrained more at the bottom tool interface compared to the top. Thus, it is critical that the effects of different friction coefficients on the TEPS distribution in a workpiece are understood.
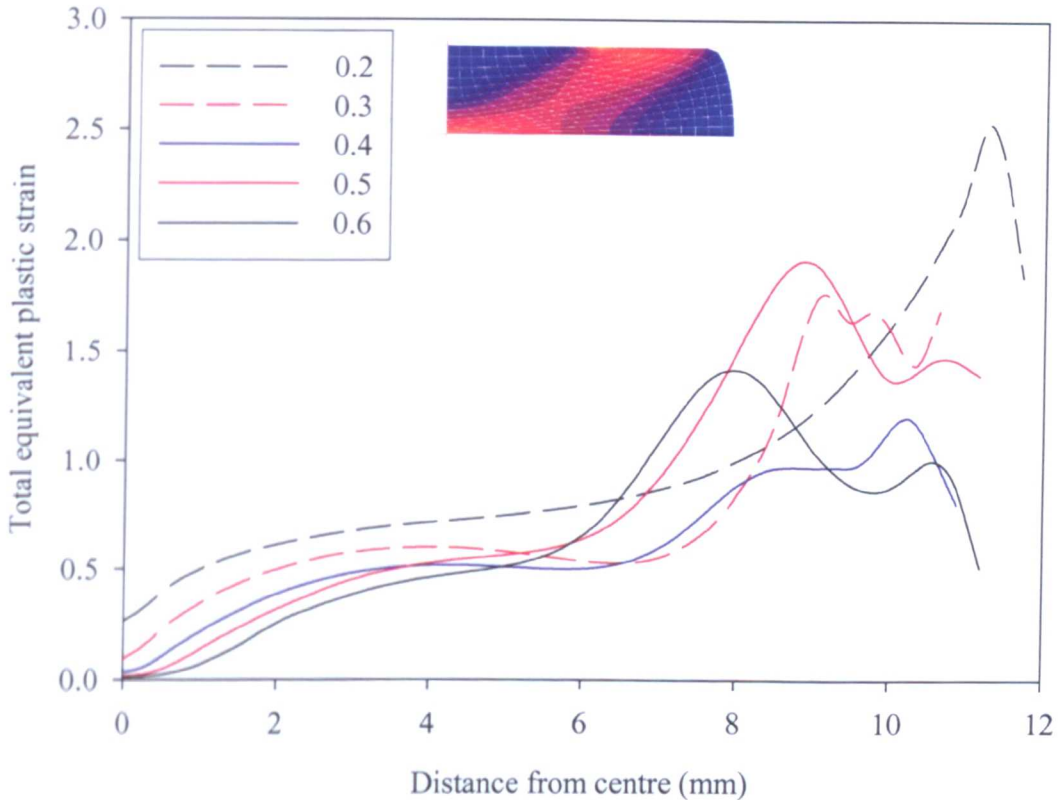
Figure 5.13 Effects of friction coefficient on TEPS on top plane of an axisymetric sample deformed at 990 °C, $\dot{\varepsilon} = 0.2s^{-1}$

Figure 5.13 above shows an axisymetric model that has been deformed at 990 °C, $0.2s^{-1}$ with various friction coefficients. This figure also includes an image of the typical strain distribution produced in an axisymetric compression test, however it does not depict the distribution for that particular test test. The distribution in TEPS for Figure 5.13 is along the top plane of the sample. All the curves display the same trend with a quick increase in plastic deformation, followed by a plateau. This is then succeeded by a rapid rise in plastic deformation followed by a rapid drop. Some curves have one or two oscillations in this final decrease. There is no gradual change in the deformation gradients from one coefficient to the other. The friction algorithm in the software decides whether the local conditions at each individual node are sufficient to cause that node to stick or stick relative to the tool as the material moves over it causes this effect.

125

Thus, as each model is deformed and re-meshs slightly differently to each other then there isn't a gradual change through each friction coefficient as all the meshes keep changing during deformation and so the nodes and elements in contact with the tool are not the same for all the five models.
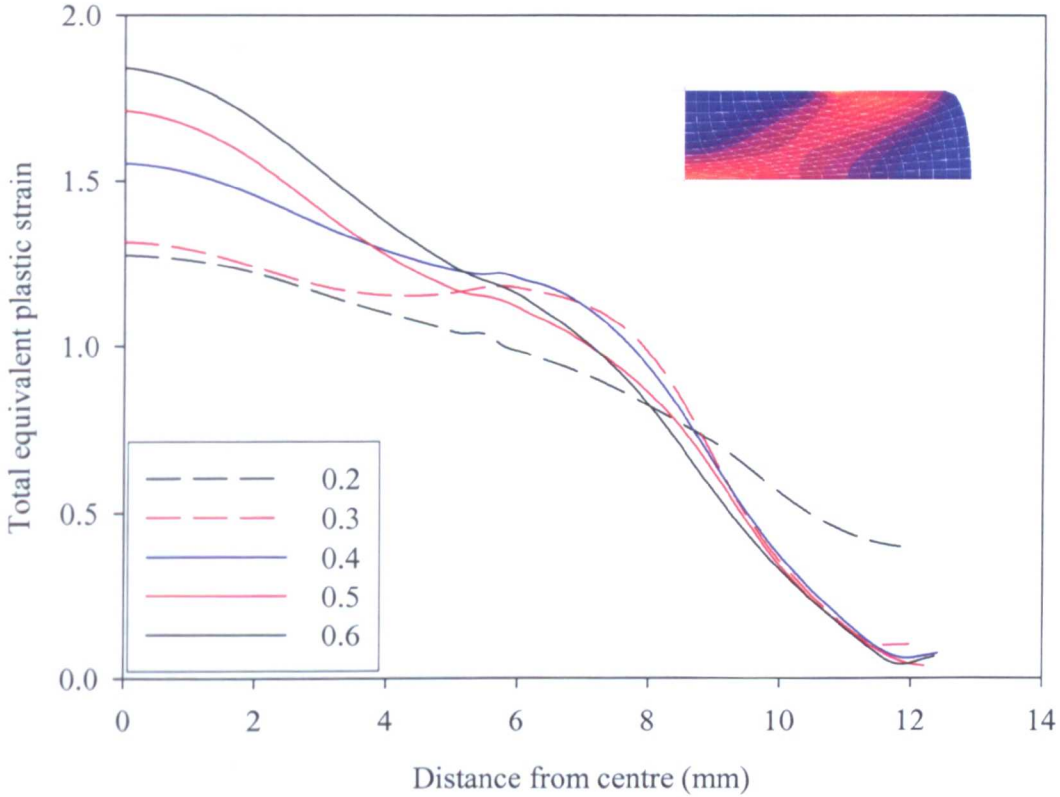
Figure 5.14 Effects of friction coefficient on TEPS on mid plane of an axisymetric sample deformed at 990 °C, $\dot{\varepsilon} = 0.2s^{-1}$

Here at the top surface it is difficult to come to any strong conclusions however some information can be used for this graph. For a μ of 0.2 and 0.3 the whole sample slides relative to the tool as the strain at the very centre of the sample is 0.25 and 0.1 respectively. For a μ of 0.4, 0.5 and 0.6 the strain begins at zero in the centre of the sample so here material has been fully constrained by the higher friction value, with the higher the friction coefficient the high the constrain and size of deadzone.

Figure 5.14 shows the same model displayed above in Figure 5.13 for the mid planes of the sample, here all the plots follow a similar trend of a large deformation in the centre that reduces almost to zero (except for a μ of 0.2) in an approximate linear fashion. This rate of decrease is slowed momentarily at ~5.5mm before it begins to fall again. For a μ of 0.2 the decrease does exhibit the same behaviour and shape as the other friction coefficients, including a very slight decrease in the rate of strain reduction at ~5.5mm, however it is much slower in doing so and does not fall to a value of zero strain at the edge of the sample. This is due to no frictional constraint of the material anywhere on the tool surface allowing a more uniform strain to be generated in the

material. For a μ of 0.3 or greater the deformation distribution changes as the centre of the top surface of the sample is constrained and the majority of the deformation is accommodated by shearing at 45° from the centre, creating a second dead zone towards the middle of the outside of the sample. After ~5.5mm from the centre of the sample the strain becomes very insensitive to the friction coefficient (except and very low friction) and effectively after 9mm the model becomes insensitive to friction coefficient as this marks the edge of the second 'dead zone'. Before this region, the higher the μ value the higher the strain value in the centre of a sample. From the literature [101-105] typical friction coefficients for lubricated titanium is reported to be in the region of 0.2-0.4. At the centre where the difference in the calculated strains is the largest there is 0.3 variation in strain over this range in μ and so it can be assumed there is can be an error of ±0.15 in the calculated strain in the highly deformed centre of a sample.

A similar study in two papers by Snape *et al.* [121,122] on FE model parameter sensitivity of open, closed and backward extrusion forging confirms some of the results presented here. In these papers, percentage deviations in output are measured for changes in model input parameters. Such parameters include heat transfer coefficient, friction factor, strain rate sensitivity index, temperature term, strain hardening index and material constant. Within Snape's constitutive equation the material constant and temperature sensitivity term have a greater influence on the results compared to the very small effect the strain rate sensitivity and strain hardening terms have. Although the work presented here does not evaluate the effect on model output for each individual term it can concur that the activation energy (equivalent to Snape's temperature term) does have a large effect on the material flow curve and did require tuning to accurately represent the real flow behaviour of Timetal®834. For the case of closed die forging, at the die-workpiece interface friction is more important that the cooling effect of the die although in general none of the parameter variations examined had a significant effect on the shape or strain predictions. This is backed up by the above work that has shown minimal effects on TEPS for various inputs parameters, the largest of which is friction that can give an error of ± 0.15 in TEPS.

5.2. ASPII machine validation

This section evaluates the ASPII machine performance and demonstrates how it is calibrated and tuned to enable it to replay the calculated strain paths for the FE models presented in Section 5.3.4. This includes the temperature distribution and measurement within an ASP sample and also the tuning of the PID controller for all directions of deformation to ensure high strain rates are achieved and that desired strains and changes in direction are accurately produced and proven to be reproducible.

5.2.1. *Thermal calibration and sample temperature distribution*

Figure 5.15 below shows the positions for the thermocouples position in the gauge length during thermal calibration at various temperatures to measure the temperature gradient across the entire volume or material under test. These thermocouples sit at positions of 0, ±2.5, ±5mm relative to the centre of the gauge length. The data provided by these test provided the temperature distribution across the gauge length, a relationship between the control thermocouple (No. 3) and the centre gauge length temperature (test temperature) and the reproducibility of the desired temperature.
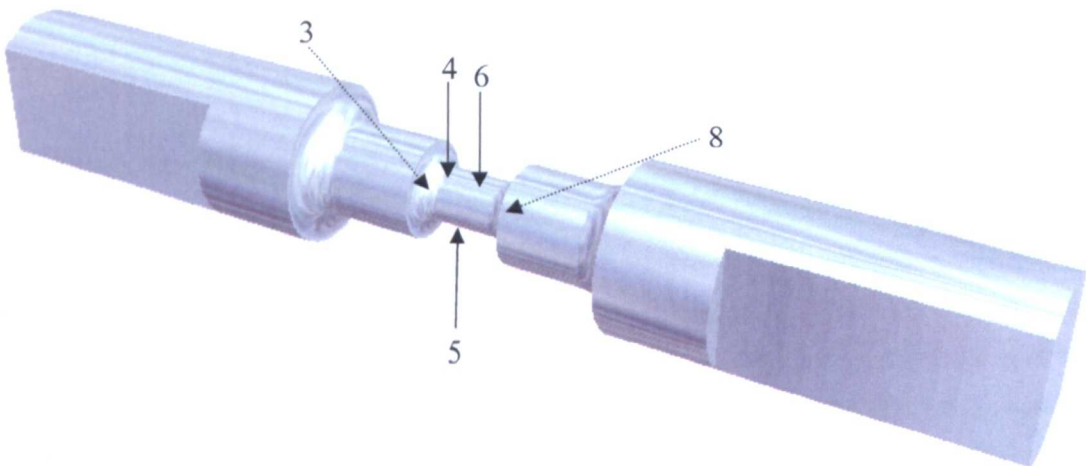
Figure 5.15 Thermocouple positions and numbers in the thermal calibration

The ASPII's induction coil is controlled via a PID controller and is capable of heating rate and temperature control as will be demonstrated later. Figure 5.16 below shows three plots of various thermal calibration tests heated at rates of 1, 4 and 6 °Cs⁻¹. The gradient of these graphs show that the heater control is capable of heating titanium samples to the desired heating rate up to 6 °Cs⁻¹ (higher rates have not been tested) within an accuracy of ±0.4 °Cs⁻¹. The smooth, consistent gradient of the curves shows that the control is operating well within its capabilities and suggests that it will perform

well in holding temperatures for tests and not over shoot or oscillate around a set temperature, as this would be very undesirable in a material that undergoes a temperature induced transformation.
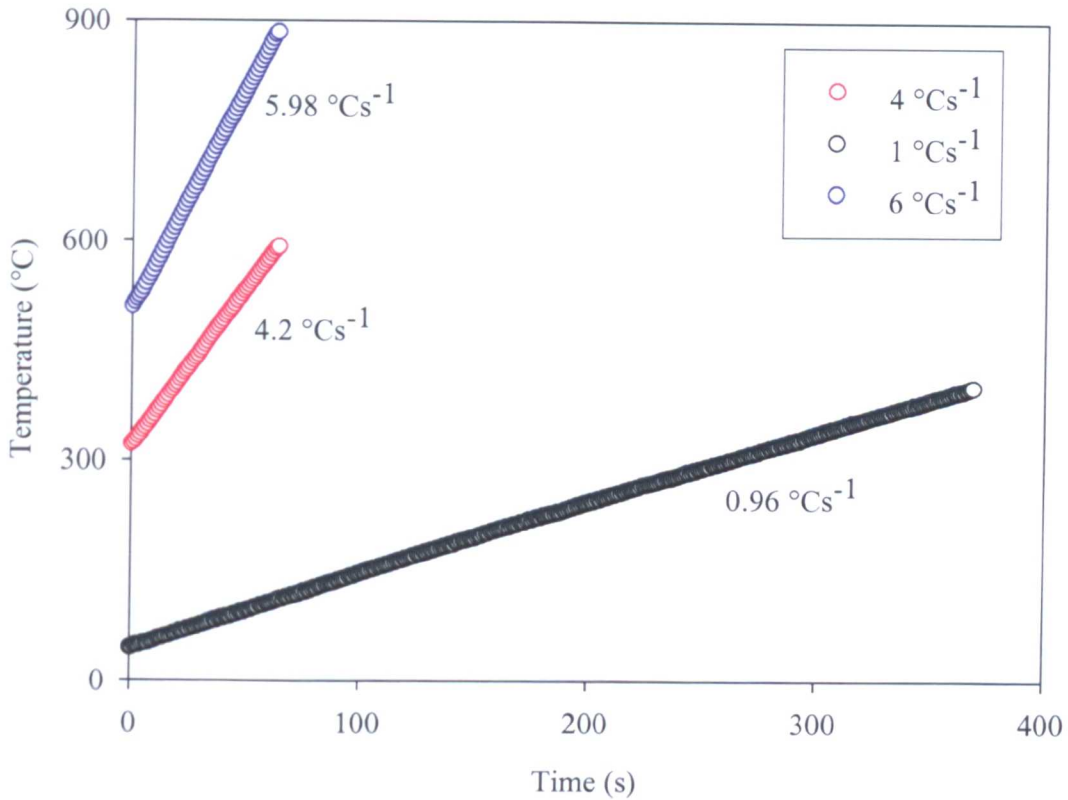
Figure 5.16 Various heating rates controlled using PID on the ASPII machine

The temperature profile generated along the gauge length of an ASP sample heated to 900 °C can be seen below in Figure 5.17. The control thermocouple is positioned at the bottom of the test volume and is used to predict and control the centre temperature of the sample during testing. Thermocouples 8 & 3 and 4 & 6 at both at the same temperature of 899 and 890 °C respectively and the centre temperature is half way between the two at 894.5 °C. This demonstrates that a very symmetrical (about the centre of the sample) temperature distribution is produced along the gauge length, which starts higher at the very ends of the gauge, falls by 9 °C and then rises by 4.5 °C at the centre. A temperature variation over the tested gauge length is not ideal as it may present problems with differences in flow behaviour and possibly cause adiabatic shearing as reported [123-126] as a problem when processing titanium alloys. This temperature difference is not considerable and produces a temperature gradient from the centre to the edge of the test volume of approximately 1 °Cmm^{-1}. The difference in temperature within the gauge length is cause by the complex interaction of the electron magnetic field generated by the induction coil. As the samples profile changes within the coil the energy density of the field with respect to the volume of material it is

generating eddy currents in (and so heating) are not even, thus temperature is not entirely even.

The thermocouple readings, especially number 4 and number 5, show a common oscillation within them suggesting this is a machine affect and not the resolution/accuracy of the thermocouples. This is due to the heat control PID controller attempting to reach specified targets, thus showing how quickly it is responding to reach and hold the specified temperatures.
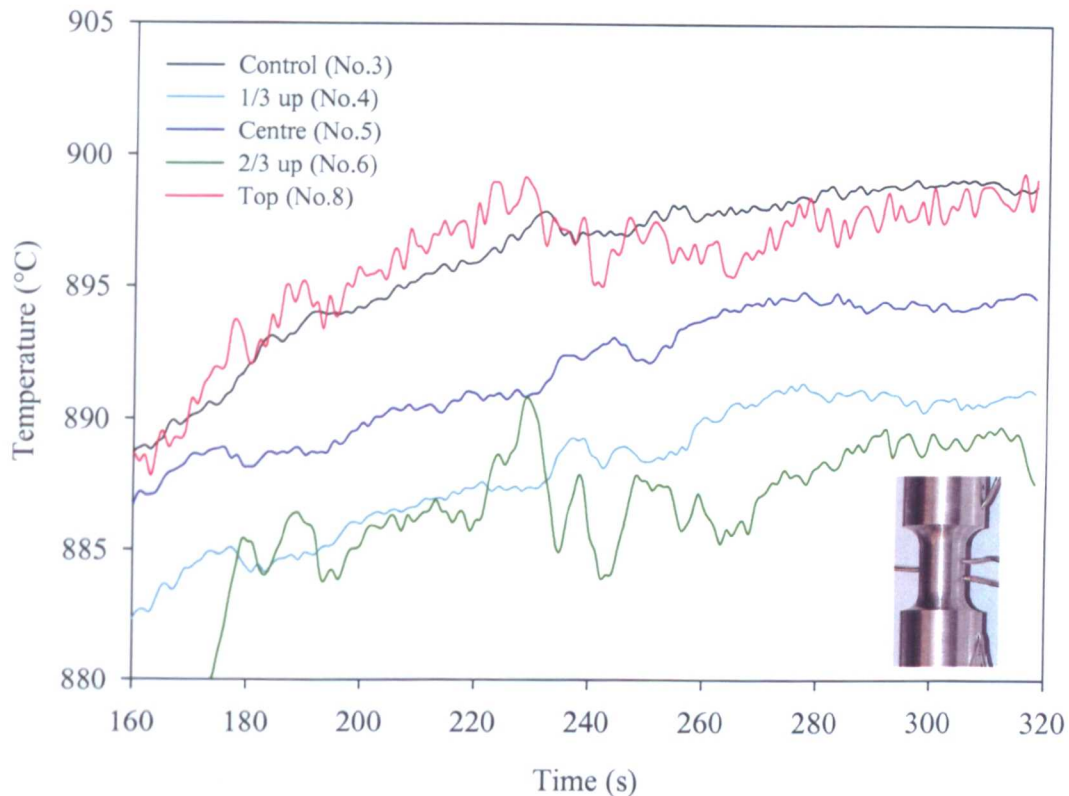
Figure 5.17 Temperatures from the five thermocouples in a sample being heated up to and held at 900 °C

Due to the high temperatures that titanium alloys are processed at the temperature profile can be seen with the naked eye. Occasionally it was observed that when a sample was at testing temperature that a non-uniform temperature profile was being generated, i.e. the induction coil was not placed directly over the centre of the sample and so the top or bottom half of the sample was hotter that the other. Due to various issues the induction coil required alignment with the sample by eye and so possible human error was being introduced. To check the reproducibility a sample was heated and cooled four times. Each time the coil was randomly misaligned and then realigned by eye. Figure 5.18 below shows the temperatures of a thermocouple at the top and centre of a sample. After 240 seconds the temperature has stabilised and there is a variation in temperature of ±2 °C at the top of the gauge and ±1 °C at the centre both of which are within experimental error.
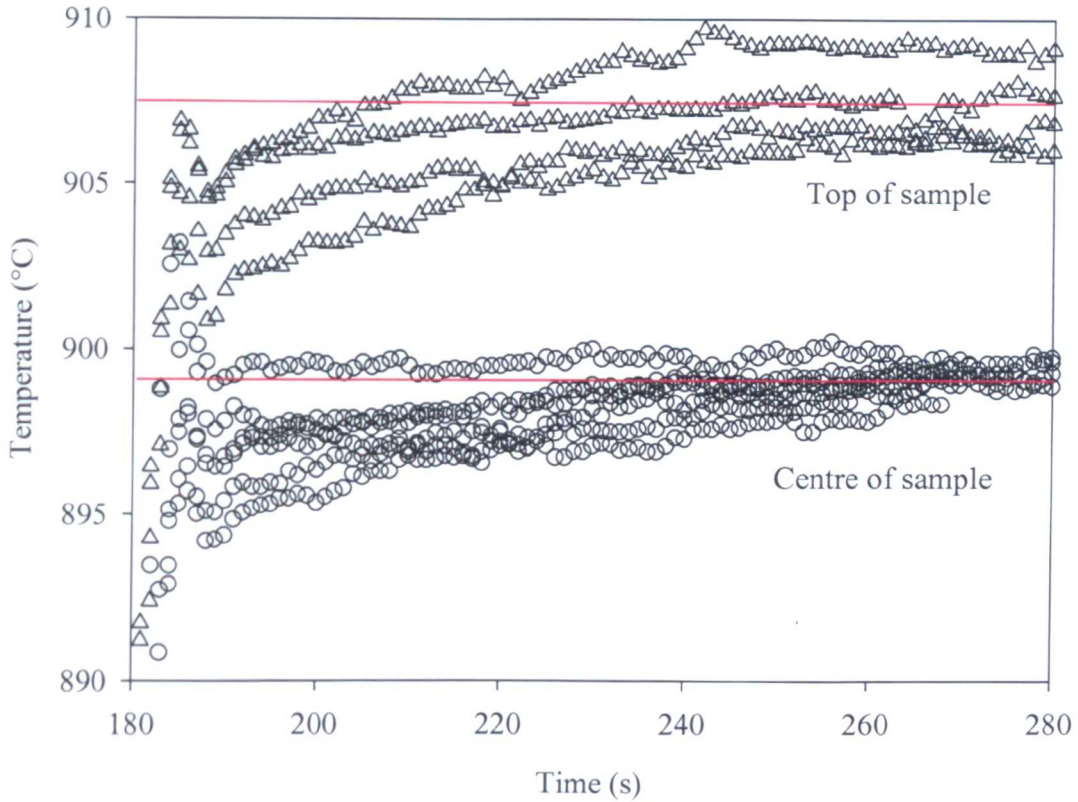
Figure 5.18 Top and centre temperatures of an ASP sample showing the effects of aligning the induction coil by eye to generate an even heating profile along the length of a sample

Thus, even if the induction coil is not correctly positioned this is easily detectable by eye due to the uneven radiant colours generated in the sample shoulders and can be rectified before deformation. A 'red hot' sample can be seen imposed in Figure 5.19. Unfortunately this technique would not work for lower temperature tests or alloys such as aluminium and magnesium as the radiant heat loss is insufficient if it to be seen by the human eye.

It must be noted that the temperature difference between the two positions in the samples is different to those generated in Figure 5.16 as the top thermocouple in the reproducibility experiment was not fully inserted into its hole and so both are not measuring exactly the same temperature as their positions are several millimetres apart.

By carrying out thermal calibrations at various temperatures the temperature of the centre test volume can be calculated by plotting the centre temperature against that of the control temperature. Thus any test can be controlled by one control thermocouple that doesn't impinge on the test material in the gauge length. A polynomial line, whose equation is shown in Figure 5.19, demonstrated the best fit to the data. By simply entering the desired test temperature into the equation, the ASPII machine is able to produce a desired temperature within the centre of the sample's test volume over a wide temperature range.
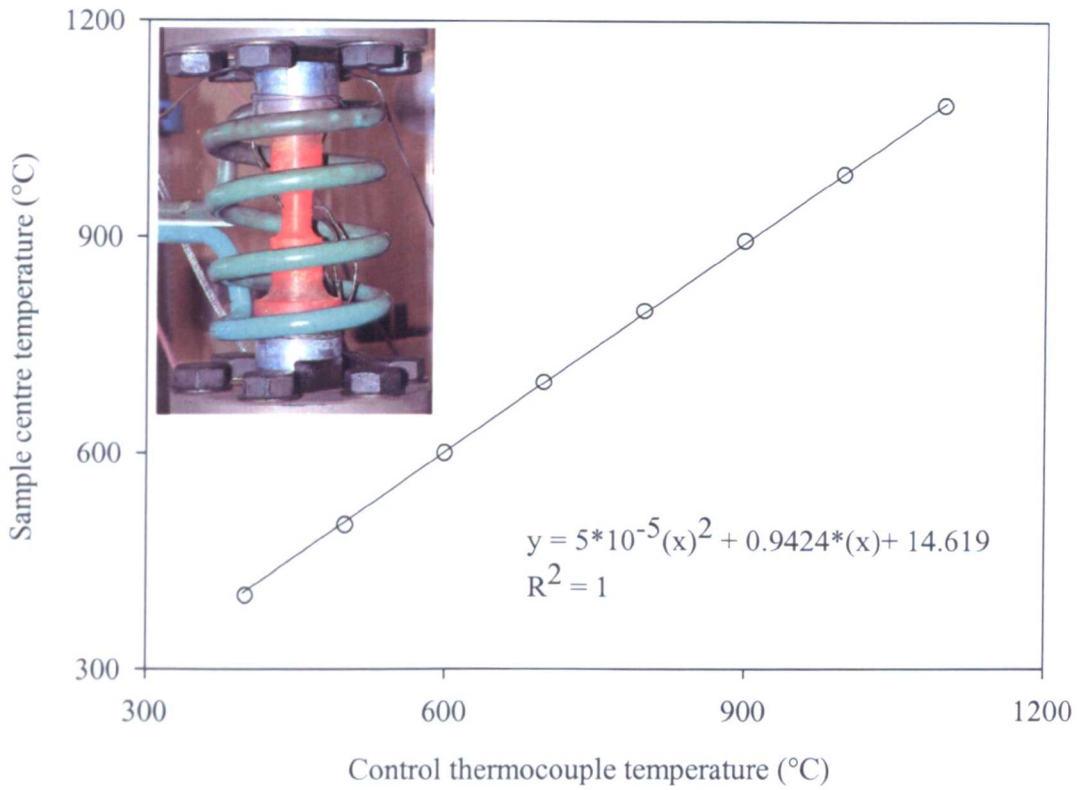
Figure 5.19 Thermal calibration curve for various temperatures together with polynomial trend line photo of a hot ASP sample

The graph shows the axis label "Sample centre temperature (°C)" with values 300, 600, 900, 1200, and "Control thermocouple temperature (°C)" with values 300, 600, 900, 1200. The equation displayed is:

$$y = 5*10^{-5}(x)^2 + 0.9424*(x) + 14.619$$
$$R^2 = 1$$

Figure 5.20 below shows the temperature from a torsional calibration test carried out at 990 °C. The heater control successfully holds the test temperature, however 0.75 seconds before the forward torsion begins the induction heat is switched off and the temperature of the test material falls by 8 °C. The forward and reverse torsional deformations generate a small amount of heat however at the end of the test which has taken just over 2 seconds the temperature of the test material has fallen by almost 20 °C. By referring to Timetal®834's beta approach curve (Figure 2.7), this equates to a difference of 15% in primary alpha content if the transformation kinetics were quick enough.
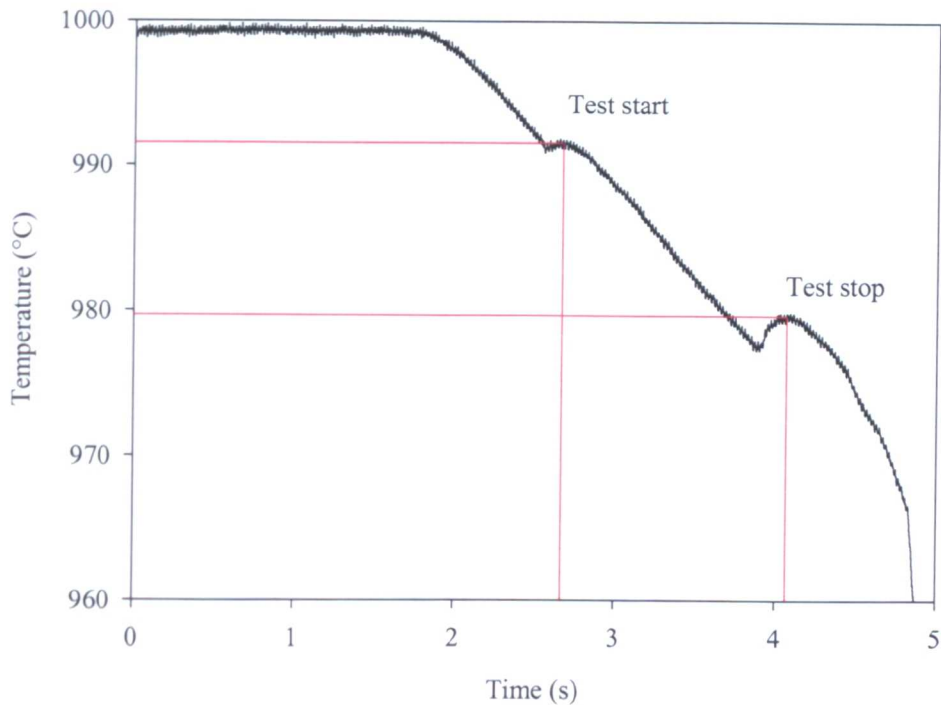
Figure 5.20 Temperature-time graph for forward-reverse torsion test

The problem was later solved by simply modifying the heater command to remain on during the deformation. Although a simple mistake, such a significant change in temperature could have a large bearing on any test data produced and so care should be taken when programming the ASPII machine to avoid such an issue.

To provide data for the FE models presented in Section 5.3.1 and 5.3.3 the temperature profile along the entire length of an ASP sample was measured. Figure 5.21 below shows the heat up of a Ti-6Al-4V sample at a rate of 3 °C s^{-1} to 900 °C, held for 200s and then cooled down. In the data presented here and in Figures 5.21 and 5.22, the thermocouple numbering has no relation to those displayed in Figure 5.17. Thermocouple number 3 is the control thermocouple (95mm from the end of the sample), number 4 is 76mm from the end of the sample (positioned at the first reducing radii), number 7 is 35mm from the end of the sample (half way along the largest diameter) and number 8 is 15mm from the end of the sample. Each thermocouple position in this plot is shown in Figure 5.22. Only thermocouples numbers 3 and 4 lie within the 'red hot' region of the heated sample and reach the test temperature for number 3 and 810 °C for number 4. Even after a 200 second hold thermocouple 4 has not reached an equilibrium temperature. By extrapolating the curve this equilibrium temperature is estimated at 825 °C. Two plots are present for thermocouple 3 due to failure (dashed line) approximately one minute into the cool down and so the solid line for the second thermocouple 3 plot does not start at the same temperature as the others. The test was repeated later with a new thermocouple and the two sets of results were

superimposed. Neither thermocouple 7 nor 8 reach an equilibrium temperature. These are estimated at 300 and 200 °C respectively and to reach these temperatures the sample would have to be held for approximately 15 minutes, an impractical amount of time. Two lines are present for thermocouple 3 as this failed during the test. The second line is data from a similar test at the same temperature, superimposed on the first set of data.
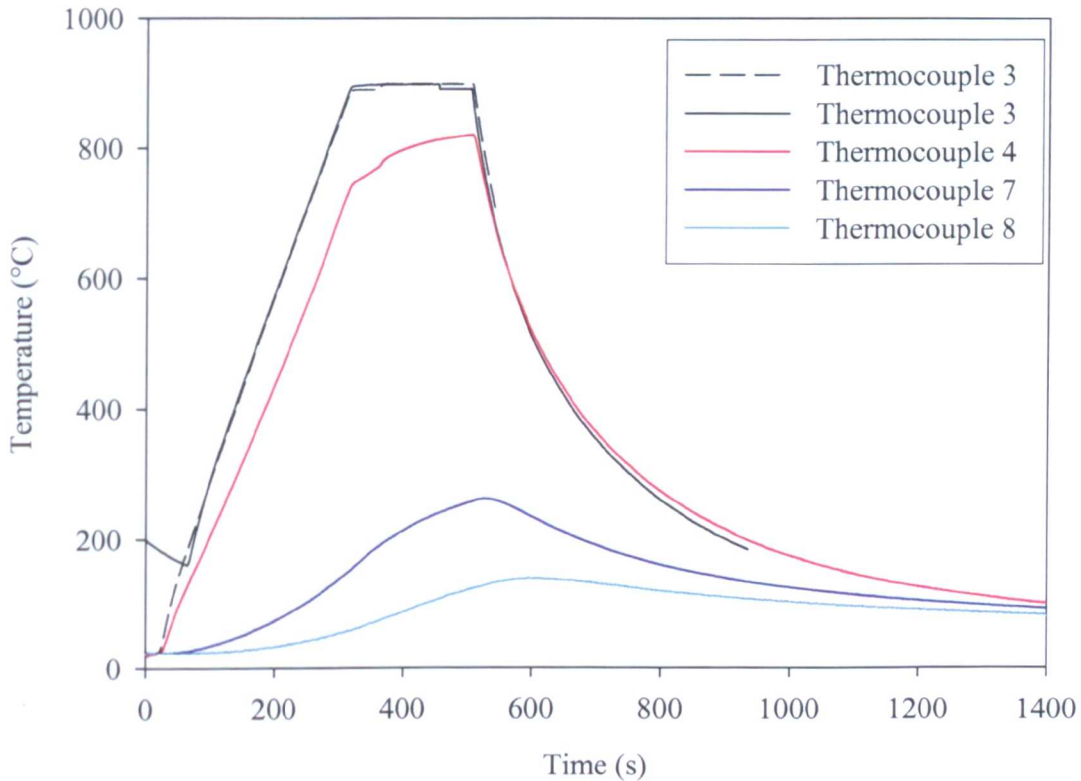
Figure 5.21 Heat up and cool down of a Ti 6Al-4V sample heated to 900°C

Interestingly both thermocouple 3 and 4 have exactly the same cooling rate for the first 100 seconds and a very similar rate for the remainder of the cooling down. This shows that the ratio of external area to temperature is the same for the gauge length and the narrower shoulder of the sample. The measured cooling curve for thermocouple 3 from this test is used in Section 5.3.3 to demonstrate the difference between laboratory and industrial air cooling.

All temperatures level out at 100 °C suggesting the clamping assembly of the machine have been heated by the coil and by direct conduction of heat from the sample, and as a result the final stages of cooling are very slow. For this reason it is also assumed that the very end of a sample is at 100 °C, the same as the clamping assembly. Figure 5.22 shows an ASP sample imposed on a plot of the temperature at each measured point if the same was held for sufficient time for all points to reach equilibrium temperatures during a test at 900 °C. This plot includes results from the above test and an additional three temperatures measured in later tests along the region where the radiating temperature falls away, out of the volume where the induction coil is directly heating.

At 60mm the temperature quickly begins to fall, as this material is no longer inside the induction coil and the dense electro-magnetic field intensity, and so the material quickly stops radiating heat in the visible spectrum. The rate at which the temperature falls slows down at 35mm and is due to an interaction between the clamping fixture and the sample both being heated by the coil and so there is a smaller difference in temperature between the two driving the heat loss mechanisms.
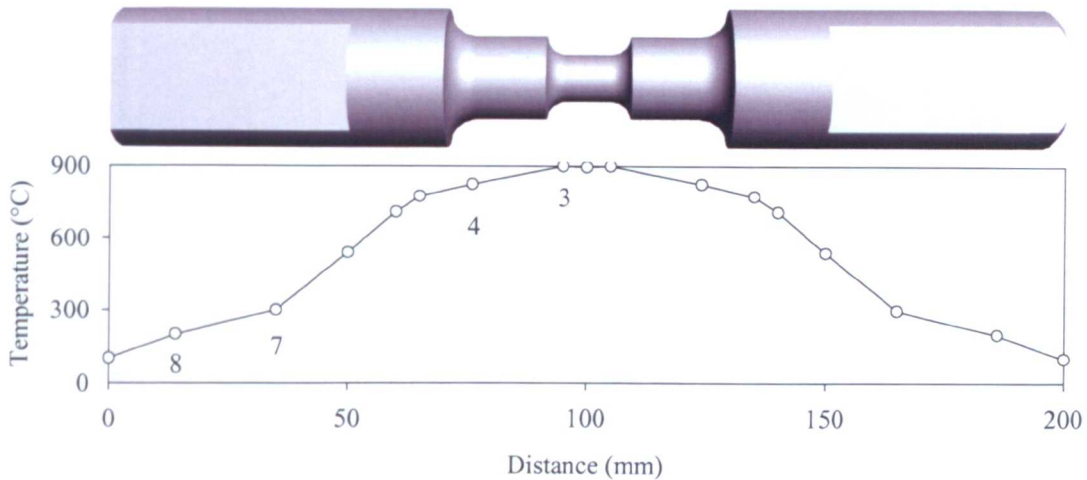
Figure 5.22 Temperature profile along an ASP sample. Numbers show where the thermocouples were positioned along the centre of the sample and relate to the test plotted in Figure 5.21

5.2.1.1. Machine noise

Early calibration tests were carried out on the ASPII machine under displacement control, i.e. the actuator would hold a set displacement, in this case zero. Such a case will impose a tensile strain on the material as the sample is heated within a fixed length. This may influence microstructural evolution during strain path testing and so tests are required to be carried out under load control (set to zero) and allow actuator displacement to compensate for any thermal and textural induced changes in axial dimension. Figure 5.23 demonstrates an early problem encountered when carrying out tests in load control, where the load cell would measure significant positive axial loads and attempt to alleviate these by moving the actuator down. However, these loads were not real and so were never compensated by the actuator displacement and the sample was destroyed. Such an effect is shown below in Figure 5.23 for temperatures up to 400 °C and plots the axial load measured by the load cell when a sample was heated up with manual control of the induction coil. When the power to the induction coil is suddenly increased and the temperature raises a large axial load of up to 1000 N is measured. This is shown four times and during the fourth a tensile and compressional force is measured. The peak axial loads tend to get larger as the temperature rises due to higher

135

induction coil power required as showed in Figure 5.23. At high temperatures, where more power is needed in the induction coil this false axial load reading reached values as high as 1.25kN, more than enough load to crush a sample.
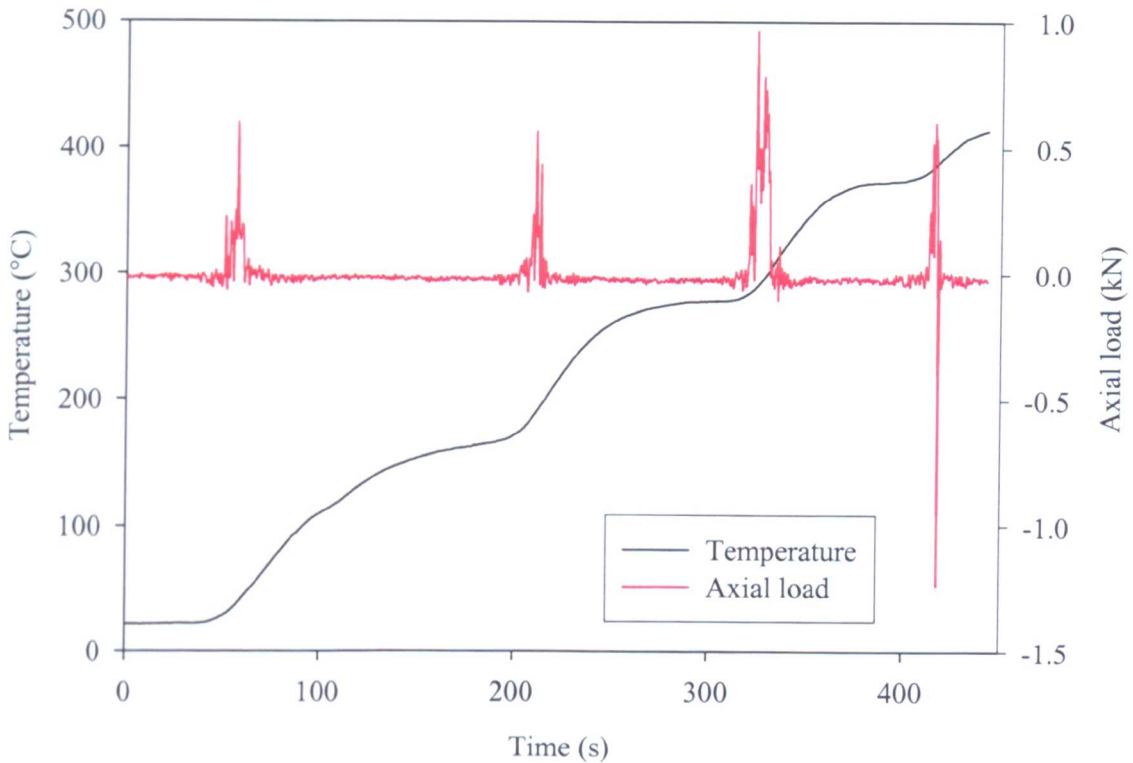
Figure 5.23 Temperature & Axial load readings verses time for a sample being heated up to 400 °C via manual control

To determine whether the load cell was operating correctly it was tested with a helical compression spring of know stiffness. The 275 lb/in spring was supplied by Dark Peak Engineering Ltd that manufacture springs to a tolerance of ± 10%. Figure 5.24 plots the measured compressional force against axial displacement is compressing the spring 21mm.
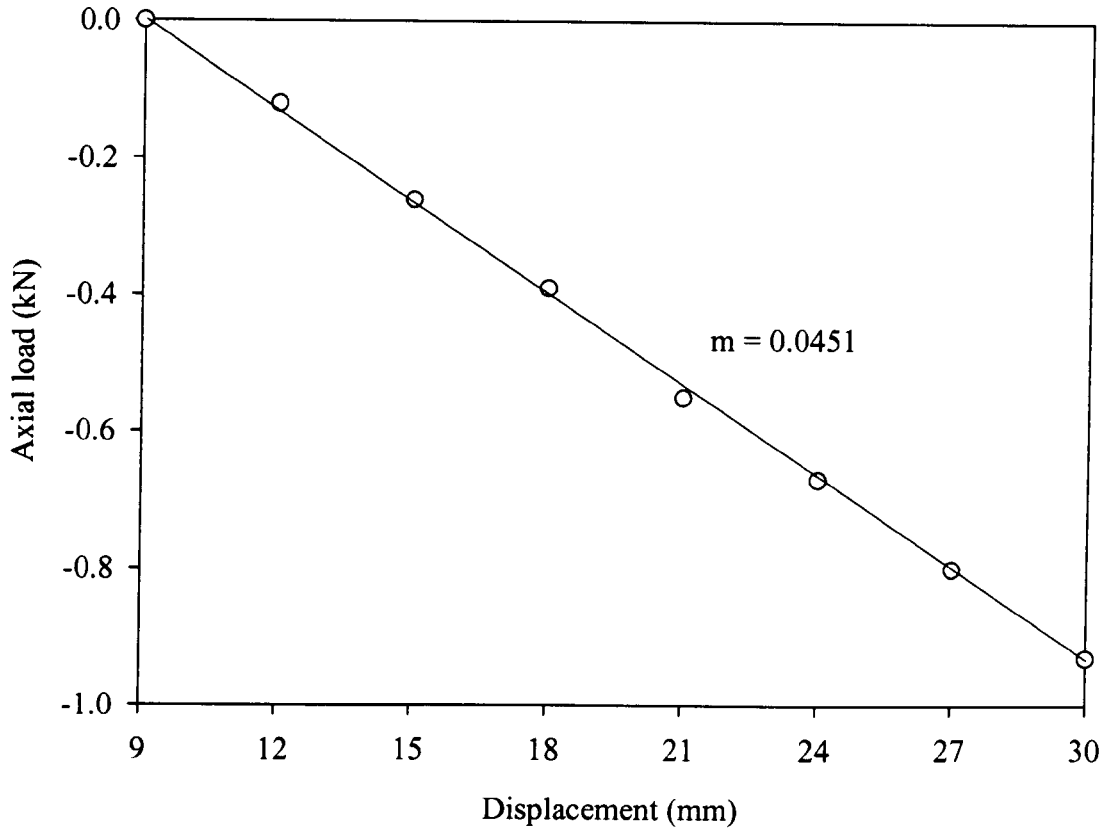
Figure 5.24 Load-displacement graph for a compression spring with a spring rate of 275lb/in (± 10%). Gradient from the best-fit line: - 0.0451 ≡ 256 lb/in.

The gradient of the above plot was calculated to be 256 lb/in, which is within the manufacturing tolerances and shows the load cell is measuring load correctly. Thus the noise producing the axial load error is electro-magnetic interference coming from the induction coil. The problem was overcome by introducing a negative differential feedback term into the actuators axial PID controller. Thus, the large axial load signal produced by the induction coil the less effect it had on the system and was rendered impotent.

5.2.2. Torsional calibration

Calibration of the ASPII machine to perform industrial strain rates initially proved difficult due to the complex nature of the forward-reverse deformation mode. This section introduces the initial machine response to fast rates of change and it will be seen that these were far from acceptable. A brief overview of the PID control scheme used to control this is then presented along with the results of tuning. Several errors in the

initial test can be seen in Figure 5.25 below. Although the machine does carry out the deformation at the correct strain rate the PID controller 'kicks in' too soon before the desired reverse angle of 137° is reached.
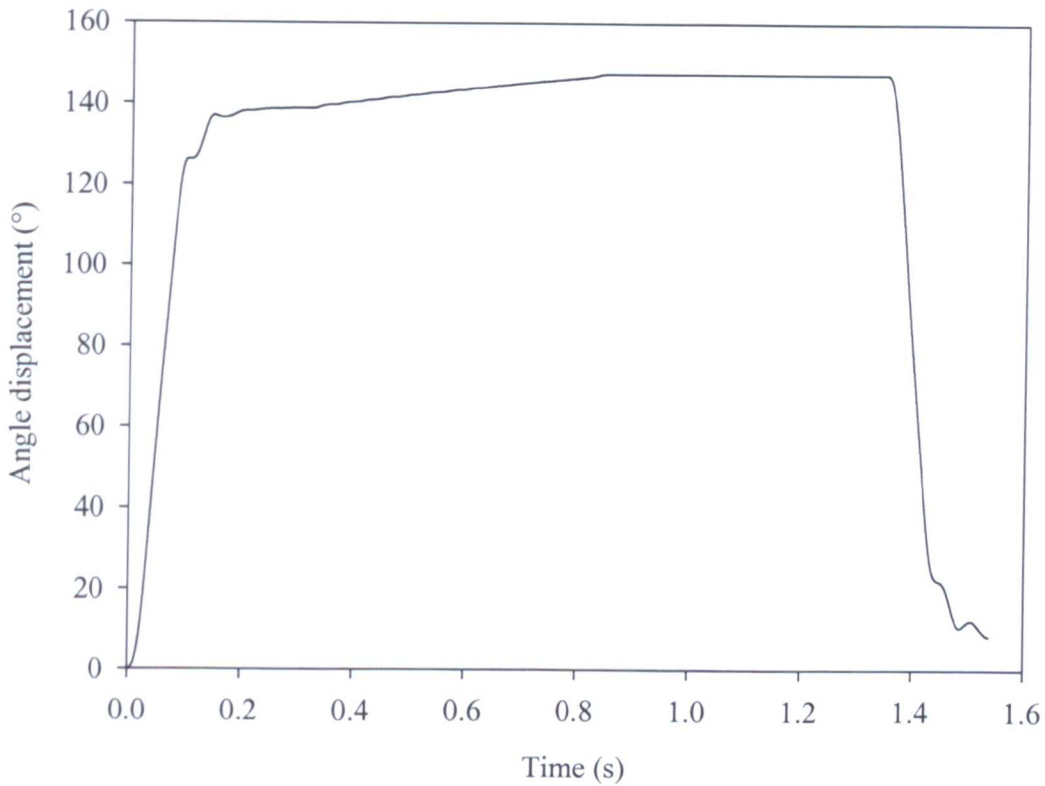
Figure 5.25 Angle-time graph showing a poorly tuned PID controller and it's effect on a forward-reverse torsion test conducted at 990 °C,

At approximately 125° the sample's rotation is stopped before being accelerated again to 137°. The machine then proceeds to drift for 1 second and deforms the sample for an additional 8°. After this time the reverse torsion produces the same effect, however the sample left with an 8° permanent twist due to the drift (Figure 5.26).

Figure 5.26 Sample after failed forward-reverse torsion showing ~8° permanent twist (table top used as datum reference)

The initial machine response under fast deformation rates is clearly unacceptable and tuning of the PID controller for the torsional and axial deformations was required. More than half of the industrial controllers in use today utilise PID control schemes as they are generally applicable to most control systems, particularly when a mathematical plant model is not known and therefore analytical methods cannot be used [127] and are cheap and robust [128]. Considering a simple control system as depicted in Figure 5.27, the controller compares a measured system output signal, $u(t)$, from the process to that of the desired set point value, producing an error signal, $e(t)$. This error signal is then processed to calculate a new value for a manipulated process input in order for the system output signal to be brought back to its desired set point.
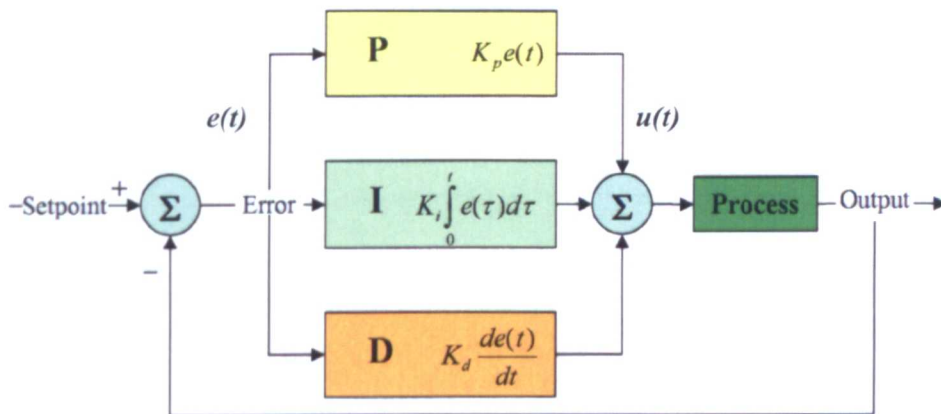
Figure 5.27 Schematic representation of a PID controller [129]

A PID controller can perform the control philosophy using three elements, proportional, integral and iterative control. In a proportional controller the output signal, $u(t)$ comprises of a single term, which is simply the error signal multiplied by the controller gain (K_p), as in:

$$u(t) = K_p\, e(t) \tag{5.1}$$

So a signal can be applied in an attempt to control the system such that the larger the output error, the larger the control signal. K_p however rarely provides adequate control to process an output signal equal to that of the input signal. As K_p is increased the frequency of oscillations in a response to a step signal (e.g. 180° torsion) will increase and there will be a decrease in the damping of these oscillations [128]. For most applications there is typically an upper limit on the proportion of gain necessary in order to achieve a well damped and stable response [130]. Figure 5.28 demonstrates this effect on a theoretical controller under proportional control. Considering the desired steady state output sign to be 8 units, then the system is over damped, slow to rise and fails to reach the desired output when too little ($P = 0.1$) proportional gain is applied. Conversely, when too much proportional gain ($P = 0.4$) is applied then the system

becomes possibly unstable, has a longer settling time and large transient error can be induced. Proportional feedback at the least increases the speed of driving the error to zero [130].
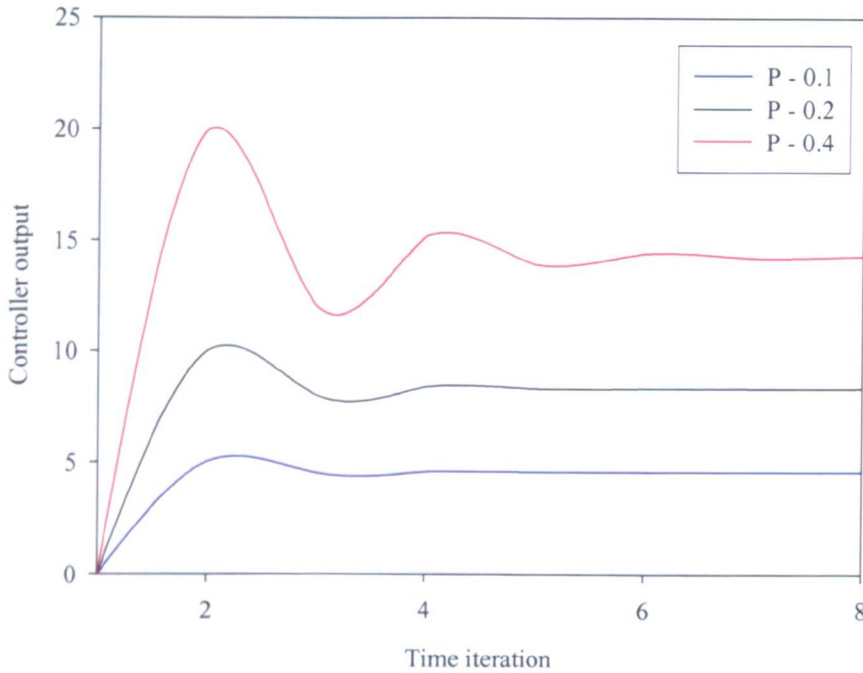
Figure 5.28 Graph showing the effect of proportional gain on the overshoot and settling time for a proportional controller

Thus, by employing only a proportional control scheme it becomes difficult to cater for both steady state and transient response and in the case of a torsion test this will result in desired strains not being reached, slow machine response (i.e. strain rates not reproduced) and possible multiple forward-reverse torsional deformation being induced by un-damped oscillations. The fundamental requirements of the ASPII closed loop control system include stability, steady state following and desirable transient response, thus the full PID control system must be utilised.

The integral action of the controller is to deal with the past, and once started at $t = 0$, holds a memory of all the error signals which occur up to and including that at time $t = t_i$. Hence, the steady state following of the desired output value is obtained by the employment of an integral controller. This feedback has the primary virtue that it can provide a finite value of $u(t)$ with no error signal input, $e(t)$, as $u(t)$ is a function of the previous values of $e(t)$ rather than the current value as in the proportional case [130]. The slope of the control input signal during an error period is dependent on the integrating gain K_i:

140

$$u(t) = K_i \int_{t_0}^{t_i} e(t)dt \qquad (5.6)$$

Selecting K_i to be positive and small to obtain a low frequency oscillation will result in a high damping factor [128]. However, if K_i is selected to be positive and large to obtain low damping, this will result in a high frequency oscillation. Thus, integral control alone results in good steady state following but leaves transient responses to be desired [128, 130].

The derivative function is to cope with the future error by assessing the rate of change of the error signal. The use of derivative control alone however, is generally not regarded as a sensible arrangement as the results are very system dependent.

$$u(t) = K_p \frac{de(t)}{dt} \qquad (5.7)$$

The effect of the derivative term is two fold, firstly to introduce a zero into the closed loop system and more importantly, allows for the selection of the closed-loop transient response as desired [128]. The derivative term is based on a multiple of the rate of change of error and therefore can have little effect on steady state values where as the integral term is based on the value of error over a relatively long period of time and therefore can have little effect on the transient values. The larger the derivative term, the more rapidly the controller responds to changes in the process's output. Practical controllers for slow processes can even do without K_d however in the case of the ASPII it is essential. Table 5.8 gives a summary of the effect of each controlling term has on the response of a typical system.

Table 5.8 Effects of the individual components of a PID controller

Parameter	Rise Time	Overshoot	Settling Time	S.S. Error
P	Decrease	Increase	Increase	Decrease
I	Decrease	Increase	Increase	Eliminate
D	Small Change	Decrease	Decrease	Small Change

Each control element has a purpose for which it is particularly suited and these cover the basic requirements for almost all linear control systems, (especially the ASPII machine) no matter how complicated the system. The overall PID control system maybe represented by Equation 5.8 and contains three coefficients, K_p, T_i, T_d that can be tuned by the operator to meet the desired system criterion.

$$u(t) = K_p \left[e(t) + \frac{1}{T_i} \int_0^T e(t)dt + T_d \frac{de(t)}{dt} \right]$$ (5.8)

The most widely used method for tuning PID controllers is that detailed by Ziegler-Nichols [128]. This method lacks background theoretical details as it is based on experimental evidence. The method requires that the gain K_p of the proportional control be increased until the system just begins to oscillate. The critical value of gain K_p at which oscillation just starts and stops is denoted K_c. The frequency of such oscillations is taken to be ω_c with a period of $T_c = 2\pi/\omega_c$. The 'best' values for proportional, integral and derivative terms are then calculated using Table 5.9.

Table 5.9 Ziegler-Nichols three term controller coefficient values [128]

	P	**P + I**	**P + I + D**
K_p	$0.5K_c$	$0.45K_c$	αK_c $(0.6 \leq \alpha \leq 1)$
T_i	-	$0.83T_c$	$0.5T_c$
T_d	-	-	$0.125T_c$

The Ziegler-Nichols tuning rules give an educated guess for the parameter values and provide a starting point for the fine tuning, rather than giving the final settings for K_p, T_i, and T_d in a single shot use [127].

The overall above control method was applied to the ASPII machine response although full Ziegler-Nichols tuning was not carried out. An advantage of the ASPII is its ability to run a desired step input in the actuator, be it torsional or axial, without the need for a sample to be loaded, thus the response can be fine tuned without the need to break many samples. Multiple experiments driving the machine calibrated in torsion at a strain rate of 10 s^{-1} gave the best results with PID setting of $4.5P$, $1I$, $0.01D$, $0.005T_d$ and $0.3VFF$, where T_d and VFF are the derivative time constant and velocity force feedback respectively. Although tests (at slightly lower hot working temperatures) showed that it was not possible to carry out some tests at this high strain rate, the machine was calibrated to successfully operate up to a strain rate of 10s^{-1}.

Figure 5.29 below shows the improvements in the machine response over that observed initially in Figure 5.25, where the black, blue and red lines represents the angle displacement (in degrees), the desired step input and temperature respectively.
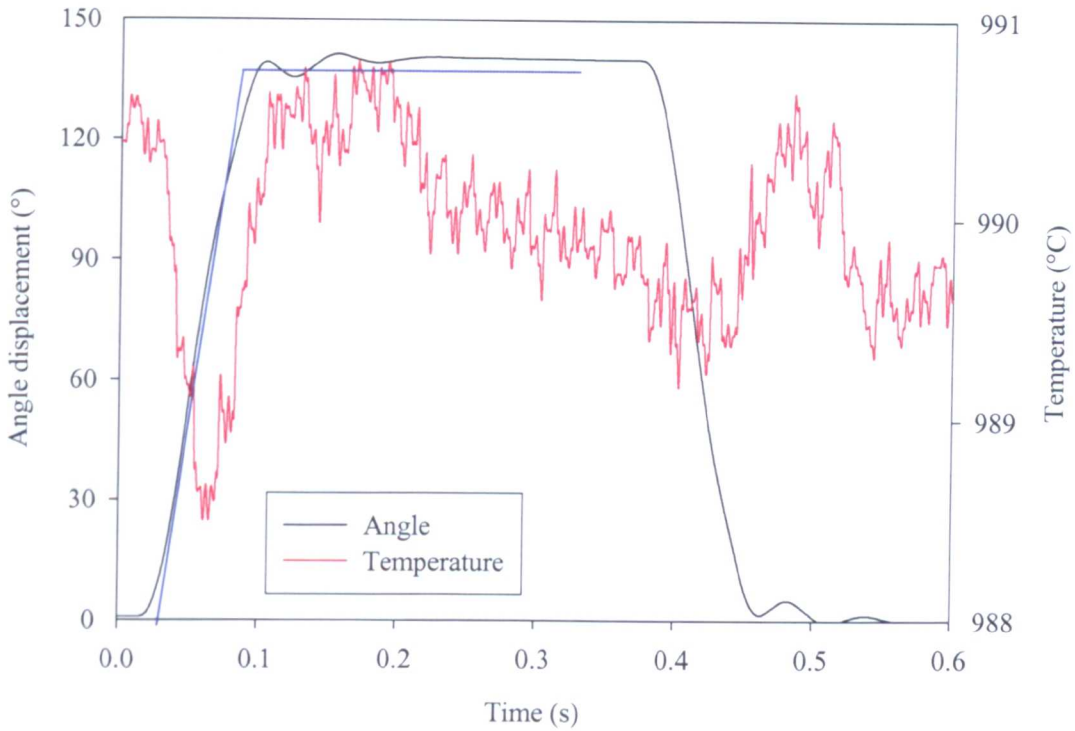
Figure 5.29 Angle-time graph (including the temperature) during forward-reverse torsion test at 990 °C, $\dot{\varepsilon} = 4s^{-1}$

Firstly, the drift of 8° was removed by eliminating a force torque to zero command in the test schedule after the forward torsion. This command was to remove any stress and thus deformation on the sample before the rotation direction was reversed. It seems the drift was produced by the machine being temporarily out of a control mode as it switched from angle control to torque control. Removing this reset should have no influence on a test as the elastic component of strain at these temperatures will be negligible.

The influence of too much derivative control prematurely slowing the actuator down, and essentially stopping it briefly, has been reduced immensely to just a small reduction in strain rate towards the end of the deformation and can be seen when comparing the angle displacement to the desired step input in Figure 5.29. The temperature drop of 8 °C at the start of the test has now been reduced to only 2 °C, as the machine response is now so rapid, although the control signal on the induction coil does seem to turn off very briefly during, and only during, the first twist.

Quantifying the machine response using the same denotation as [130] it can be seen there is very little overshoot, M_p, and only two oscillations as the machine stops the forward torsion. The overshoot equates to 2° at peak time, t_p, of 0.11 seconds and a settling time, t_s, of 0.1 seconds. The rise time, t_r, although not that relevant as this is not a true step input, rather a constant actuator displacement rate, is 0.05 seconds. The

amplitude of the largest oscillation is approximately 8° so there is only 4° torsional deflection in any given rotation direction and equates to an inconsequential shear strain of 0.035. There is also a very short hold time of 0.3 seconds before the torsion is reversed so no heat induced factors (e.g. static recovery or meta dynamic recrystallisation) will be imposed on a test due to a high temperature hold between deformations.

The improvements in actuator control in response to controller tuning is clear to see from the above results. Figure 5.30 plots the flow curve for Timetal®834 along with the angle displacement of the actuator during a 180° torsion at 990 °C and 2s^{-1}. From the torque and angle data gathered the torsional flow curves can be plotted in von Mises equivalent stress with the following equations as reported by [131-136]. The derivation of these equations can be found in the appendix and is based on work conducted by Barraclough *et al.* [111].

$$\tau_{eq} = \frac{3\sqrt{3}T}{2\pi R^3} \tag{5.9}$$

$$\varepsilon_{eq} = \frac{\gamma}{\sqrt{3}} \tag{5.10}$$
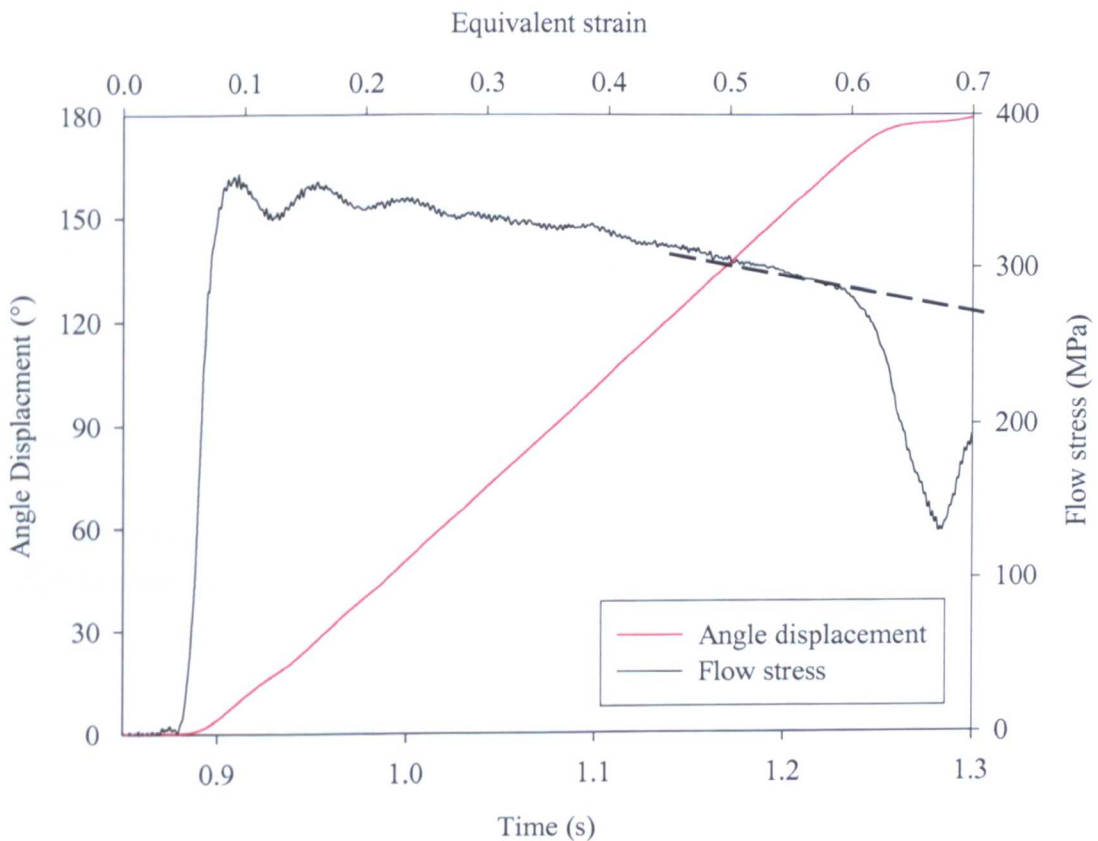
Figure 5.30 *PID control effects on the flow curve of the Timetal®834 deformed to 180°* *at 990 °C and 2 s^{-1}. Angle displaced is shown by the solid red line and the extrapolated* *flow curve towards the end of deformation is shown by the dashed black line*

When the material begins to yield there is an oscillation in the flow curve. Such oscillations in steady state flow stress have been shown to be the influence of dynamic recrystallisation where new grains nucleate preferentially on grain boundaries [92].

Another possibly cause of such oscillations could stem from "load cell ringing" as a result of mechanical deformation of the load cell due to abrupt load changes which is manifested by vibrations at its natural frequency. However, by referring to the angle displacement plot it is possible to see very small deviations, before 1 second, from the otherwise very constant rate of deformation. These coincide with the oscillations in the flow curve and so this feature is not a microstructural mechanism in operation but titanium demonstrating its extreme sensitivity to strain rate. Under these conditions the material does exhibit a slow rate of softening up to an equivalent strain of 0.6. After this the flow curve is dominated by the PID response in attempting to reach the desired actuator deflection and slowing down causing a large drop in flow stress of 70 MPa. The linear manner in which the flow stress steadily falls allows the flow stress up to an equivalent strain of 0.7 to be estimated at 275 MPa.

5.2.3.   Tension-compression calibration

The same theory of calibration applied to the torsional deformation was also applied to the axial deformation, as complex strain path deformation will require simultaneous displacements in both. Figure 5.31 below shows a positive (up) and negative (down) actuator displacement a strain of 0.5 at $10s^{-1}$.

During the positive displacement there is a small amount of deviation from the desired displacement rate. This is followed by a very efficient and rapid slow down and reverse in deformation direction with no visible effects of the PID causing premature retardation, overshoot or oscillations. The reverse of the deformation is not as good as the previous as the implement rate is slower and the PID causes a significant drop in the displacement rate towards the ends of the stroke. There is a small amount of overshoot, 0.1 mm that equates to an inconsequential strain of 0.01 with an equally small setting time. Considering the machine is operating at as strain rate of $10s^{-1}$ over a period of 0.0525 seconds the PID response is very effective.
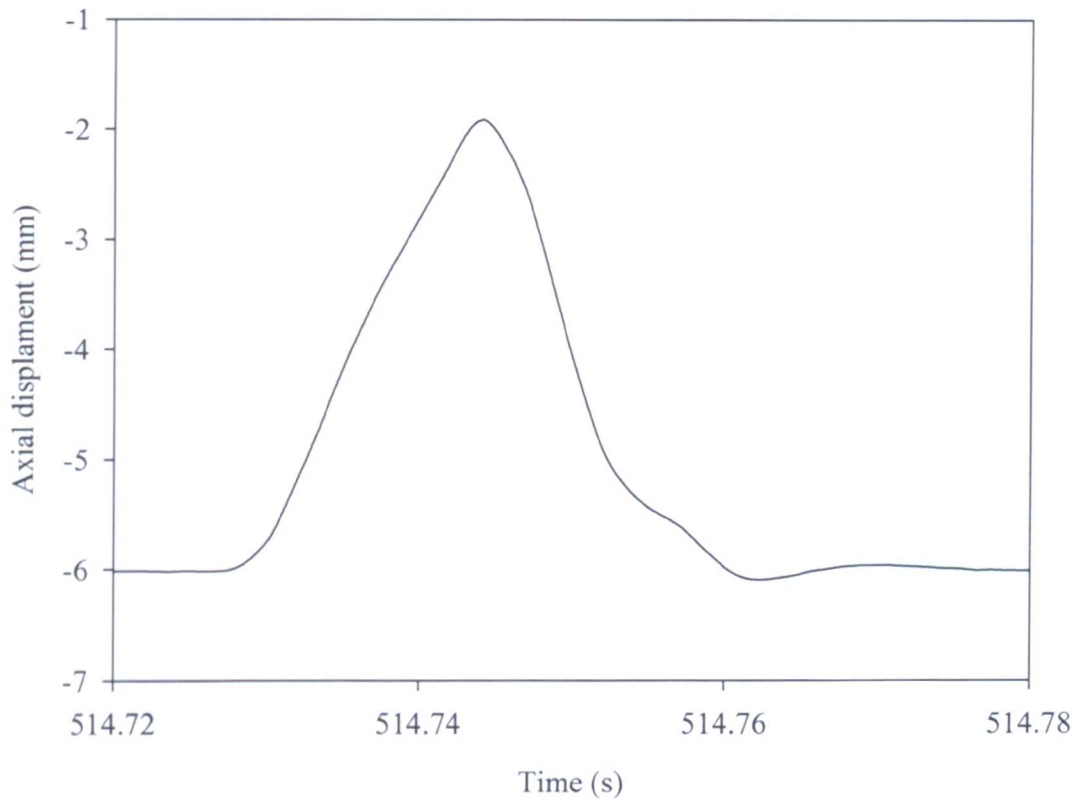
Figure 5.31 Axial displacement-time graph for a compression-tension test carried out at a strain rate of $10s^{-1}$ to a strain of 0.5

5.2.4. Reproducibility

With the tension and torsional PID controller tuned within acceptable levels the machines reproducibility was tested by compiling the data from two different tests (both containing a 180° rotation at the same strain rate) and is shown below in Figure 5.32. There is clearly a difference between both the curves however this can be explained by a slight temperature difference between the two tests. When the ASPII machine's computer is first switched on the heater command value, essentially an offsetting value can vary depending on the first temperature it measures and is caused by a small bug in the machine software. In this case it is the control thermocouple temperature, which measured two slightly different temperatures on different days. Thus, if this value is not checked before a test is performed there a small amount of error in the temperature generated by the induction coil will ensue.
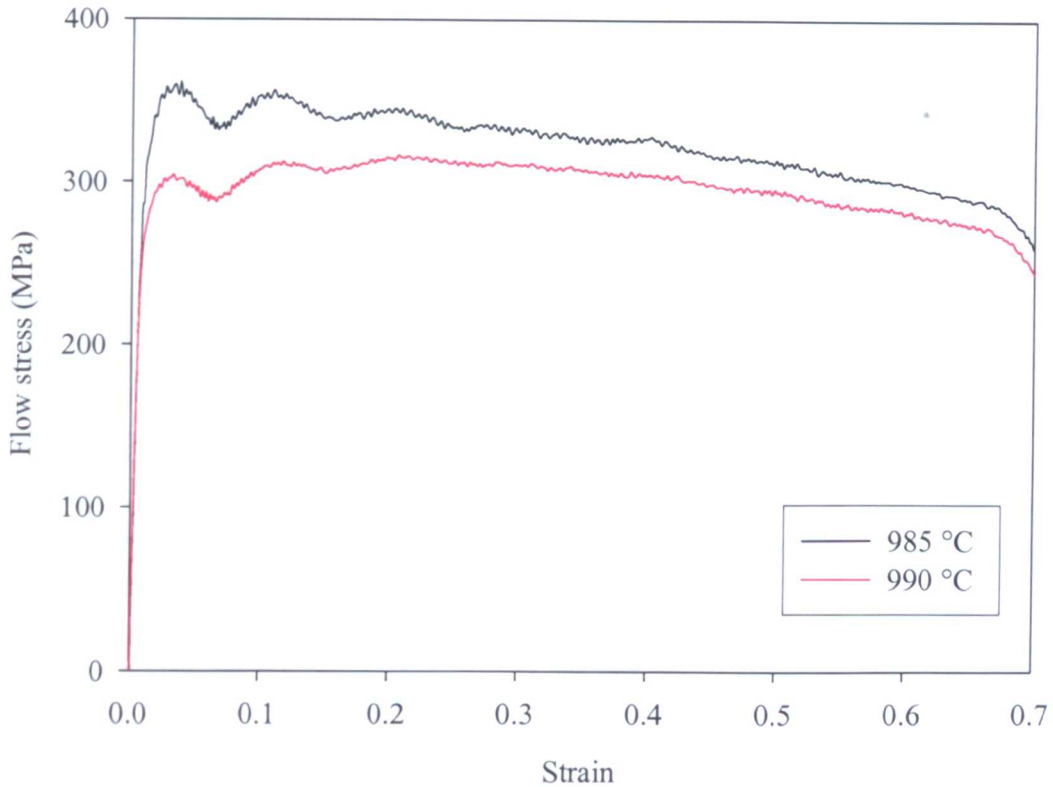
Figure 5.32 Torsion tests carried out at 990 °C and 2s⁻¹ on Timetal®834. At the instant of deformation there was a 5 °C temperature difference between the two samples

In the case of the above tests the heater command offset value was 5 °C different for each test resulting in one sample being slightly cooler then the other and demonstrating higher yield strength of 75MPa and a larger peaked flow stress at 350 and 310 MPa for the 985 and 990 °C tests respectively. Despite the small difference in the flow stress brought about by the temperature differences, both curves exhibit exactly the same oscillations and overall behaviour. Again the PID effects are seen at the start of the deformation as the actuator suddenly ramps up to speed and at the end when it slows down to stop at the desired set point. The rate at which they soften is the same and comparing this to the very linear actuator displace during the 'middle' period of deformation this can be attributed to material behaviour, either flow softening due to a small temperature rise or more likely material softening similar to that observed in previous tests (Figure 3.4-3.6). This error is user generated and not a direct effect of the machine and so shows how well, once programmed correctly, the servo-hydraulic system can consistently reproduce complex deformations. Ideally these tests would have been conducted again but this was not possible due to limited time and funding.

5.3. FE modelling results

The second section of modelling presents the data generated by the two stage forging model. This model forms the basis of the 'complex' strain path tests by predicting all the equivalent strain component histories required to calculate strain path changes. Such a model also reveals the large discrepancy between a so-called air cool (AC) from elevated temperature in the laboratory and in industry.

Initially, there was to be additional work carried out on the modelling of the ASP samples under testing in the ASPII machine. The work that has not been presented in this section, included FE modelling of the heating effects of the induction coil and ASP samples under complex deformations. Due to time constraints and inaccuracy of some of this work development was halted and so only the more relevant work is presented and concentrates on generating the correct temperature distribution within a sample.

The final section presents the as-received material from both billet sources in order to compare the strain path effects on the microstructural evolution. Two sets of strain path tests were conducted: 'simple' strain path changes which involved one single but extreme strain path change of 180° and the 'complex' strain path tests which replayed points of interest within the forging for the whole shaping operation.

5.3.1. Heat and cooling of an ASPII sample

During each temperature calibration the power required to hold the sample at a given temperature was recorded. Figure 5.33 shows the relationship between induction coil power and test sample control temperature and demonstrates that the power required to maintain a temperature increases exponentially with temperature, as radiation heat loss becomes the more dominant heat loss mechanisms at elevated temperatures. A best-fit line with the equation shown below gives an excellent fit to the data.
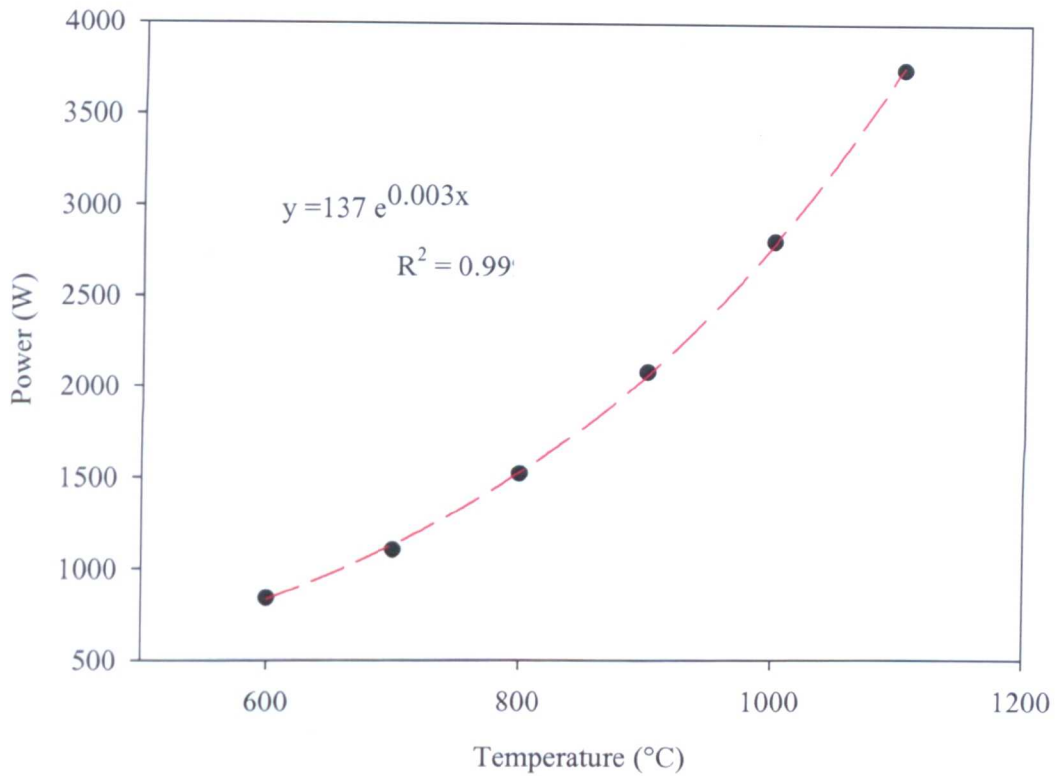
Figure 5.33 Measured power of the induction coil at various temperatures for a Ti 6Al-4V sample

As mentioned above, even though exact numerical modelling of the induction coil could not be produced by the induction theory some useful information was acquired. When an alternating current is induced within a conducting medium by the electro-magnetic fields of an induction coil the current distribution is non-uniform. The higher the frequency of this field, the more concentrated the current density is towards the surface of the material. For example, high frequency induction coils are utilised to case harden steel as the materials surface can be rapidly heated and then cooled by the atmosphere and the 'cold' bulk material. The frequency of the ASPII's induction coil is low at 180 Hz and as a result the depth of penetration is high and the coil will be assumed to produce a uniform heat distribution across the cross section of a sample. Due to the small diameter of the samples used the induction coil will not be very efficient in generating heat in the sample. As a result the heat energy input for the model will be a fraction of that measured in Figure 5.33.

Two different thermal cooling models are presented here. The first, the simpler model, assumes the whole of an ASP sample is the same temperature and is allowed to cool from

900 °C with a fixed heat transfer coefficient of 70 Wm⁻²K. Figure 5.34 shows the temperature distribution generated in the sample (half model) that has been cross-sectioned along the central axis for visualisation, after it has been allowed to cool for 1.6 minutes. The numbered points in this figure represent the node numbers at these points that correspond to where the temperature in a real sample has been measured, and node 23 is the control thermocouple position. In this model the heat is quickly lost in the thinner sections of the sample (i.e. gauge length) where as the more bulky sections retain the heat. Any corner cools slightly faster as the heat at that point has effectively two surfaces to be lost from.
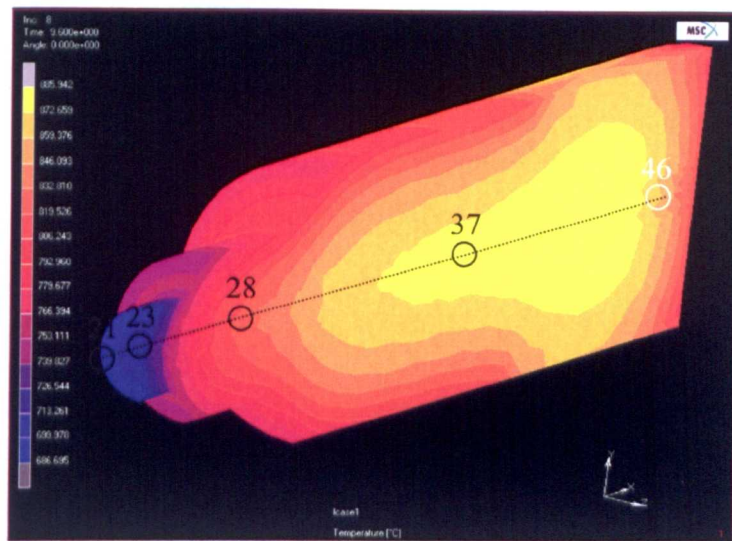
Figure 5.34 Section of an ASP sample FE model that has under gone cooling from 900 °C for 96 seconds. Numbers indicate the node numbers where temperature histories where recorded

Figure 5.36 shows the cooling curve (red line) for an ASP sample that has been heated to a temperature of 900 °C. Results from the above model are also shown plotted in black. This model would seem to accurately reproduce the cooling curve experienced by a sample, however, the plot only shows the first 100 seconds of the cool. After some time the single (initial) temperature model begins to deviate from that of the measured temperature. The second cooling model was developed using the temperature data presented in Section 5.2.1 where a samples temperature was measured at various points along its length. This data showed that the temperature generated in a sample is far from uniformly distributed. Figure 5.35 shows how the FE sample was divided into regions of known temperatures, high towards the centre, and relatively cold towards the ends.

150
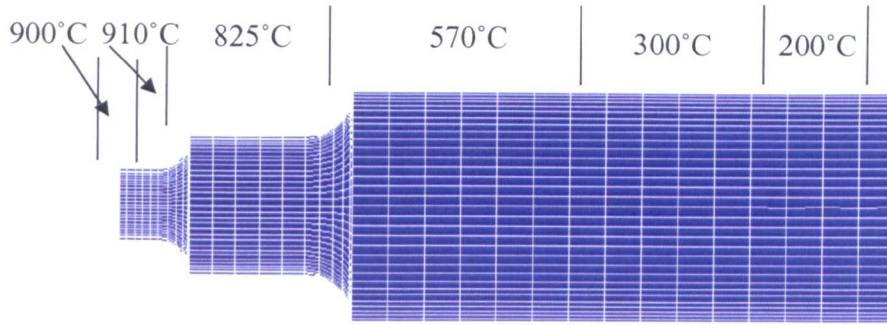
Figure 5.35 Position of different temperature regions in an FE model of ASP specimen

All the nodes within a region were set to the same temperature and the results for three different heat transfer coefficients are plotted in Figure 5.36. The coefficient of 80 Wm^2K^{-1} was derived mathematically as shown in Section 4.2.1.5.2, however this proved to be too high a value and cooled considerably quicker than the measured rate. Tuning of this value resulted in the value of 30 Wm^2K^{-1} being able to accurately reproduce the measured cooling rate down to below 100 °C within ± 10 °C.
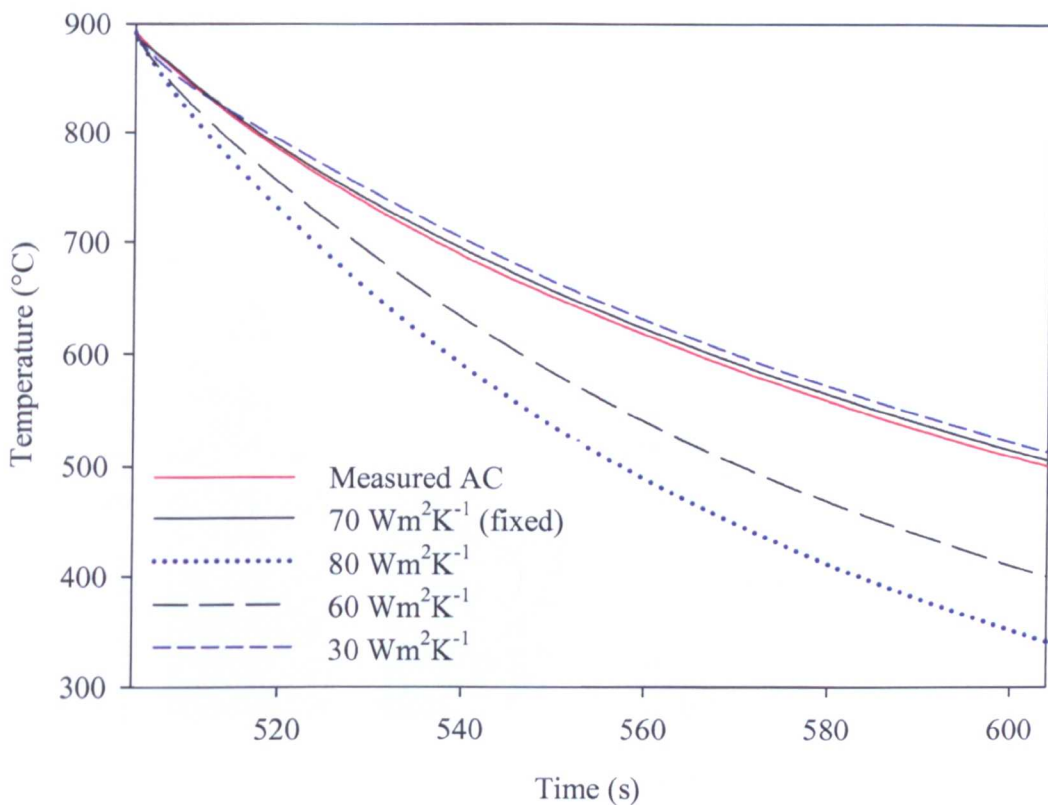
Figure 5.36 Measured and FE predicted air cool curves for a model with uniform
temperature distribution (70 Wm^2K^{-1} fixed) and one with multiple temperature regions

151

Error in the calculated heat transfer coefficient could have been introduced by many different sources including the values of emissivity used and assuming the wrong type of airflow over the sample. However, the calculated value does show that the analytical theory was correct and produced a good 'ball park' value to begin tuning the model to the exact value enabling very accurate temperature modelling of an ASP test.

5.3.2.   Closed die industrial forging model

The FE model presented in this section which is used to simulate the forging of a typical compressor disc utilises the knowledge and information generated by the early, simpler modelling of the axisymetric compression tests. Such components are manufactured at Firth-Rixson using a screw driven hammer press whose energy is delivered by a flywheel and is controlled via a clutch. Such a machine is not easy to model so the FE model utilises the time-velocity curves for the tools this process creates. Figure 5.37 shows the initial billet (a) and the final shapes (b & c) at the end of each forging stage. Figures 5.38 and 5.39 show the TEPS and temperature distribution at the end of each blow respectively. The original, distorted FE mesh is shown in Figure 5.37 (b) and (c) to illustrate how the material has flowed during the process. The numbers shown on all the plots shows the position of track points where material data is tracked and analysed.
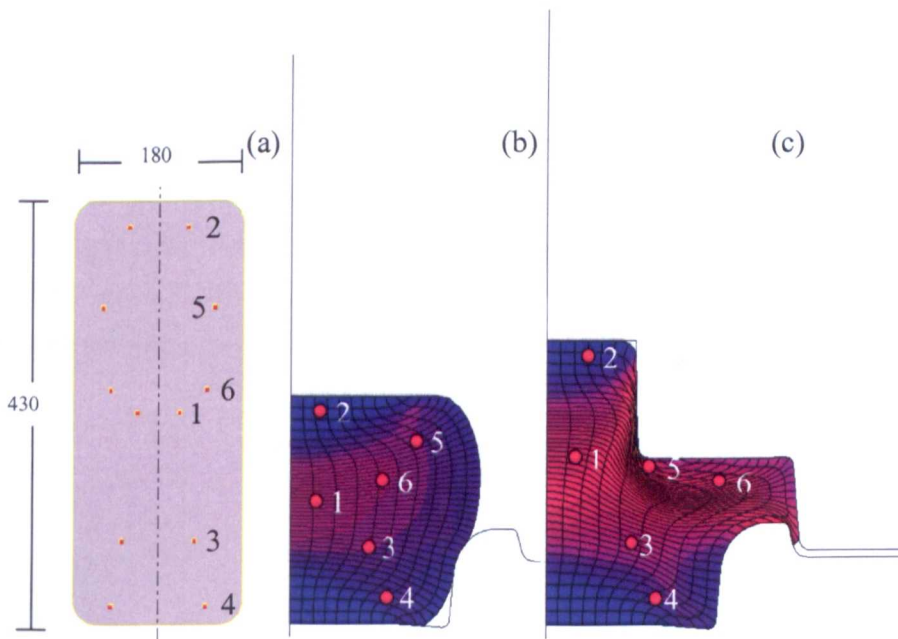
Figure 5.37 Total equivalent plastic strain distribution of the 1st (b) and 2nd (c) forged shape together with the initial billet (a)

152

The initial billet has a large aspect ratio that undergoes a large reduction of 251mm during the first forming stage. This is intended to generate a large amount of strain in the material and break up the coarse billet microstructure. The fast, high intensity blows generate large frictional forces at the workpiece-tool interface and as a result relatively large amounts of material are constrained within the top and bottom mid-section regions of the workpiece. Due to these large constraining forces the sliding of the top and bottom workpiece surfaces relative to the tools is limited and so 20mm radii on the edges of the cylinder are machined on. These facilitate smooth and easy folding of the corners, allowing the side surfaces of the billet to roll over to become the top surface as the material spreads laterally as axial compression progresses. This prevents a large scale circumferential groove being created in this region like those seen in the original failed billet forging from Firth-Rixson (Figure 5.45(a)) and in some axisymmetric tests (Figure 5.1(b)).

The deformation within the billet is very similar to that observed in earlier axisymmetric models (Section 5.1) where the majority of the deformation is accommodated by shearing along the slip line fields at roughly 45° and can clearly be seen in Figure 5.38. This differs from an axisymmetric model as there are two slip line fields generated at the start of the operation which merge to become one during the fourth blow. During the final blow of the first operation the upright, almost vertical shoulder of the lower die begins to form another slip line field as material begins to deform around it, however this deformation and it's effect is very small.

During the second operation, the second die firstly begins to extrude material outwards to from the horziontal flange of the disc as this is initially the largest opening between the dies and shearing of the material takes place in the previously deformed, and so significantly warmer (and softer), region of central material. Once this cavity is filled the pressure for material to flow into the upper, vertical channel of the die is less than than to fill the tight bottom and right hand corners. Only when the majority of the die is filled and material begins to flow into the flash line does the pressure on the workpiece become high enough to force the matieral into the corners and completely fill the die.
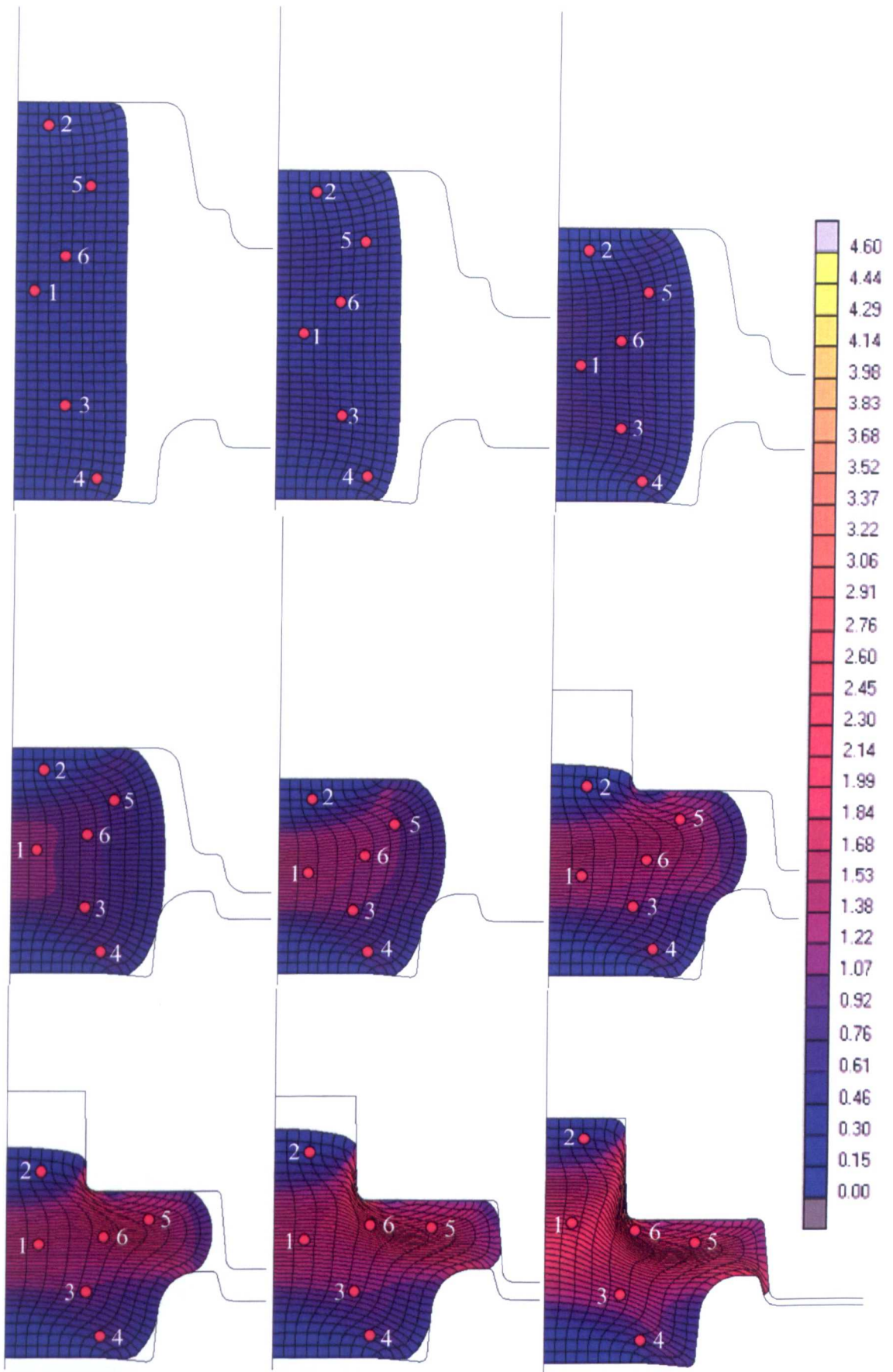
Figure 5.38 TEPS distribution within the workpiece after each subsequent blow of the die for all stages of the forging
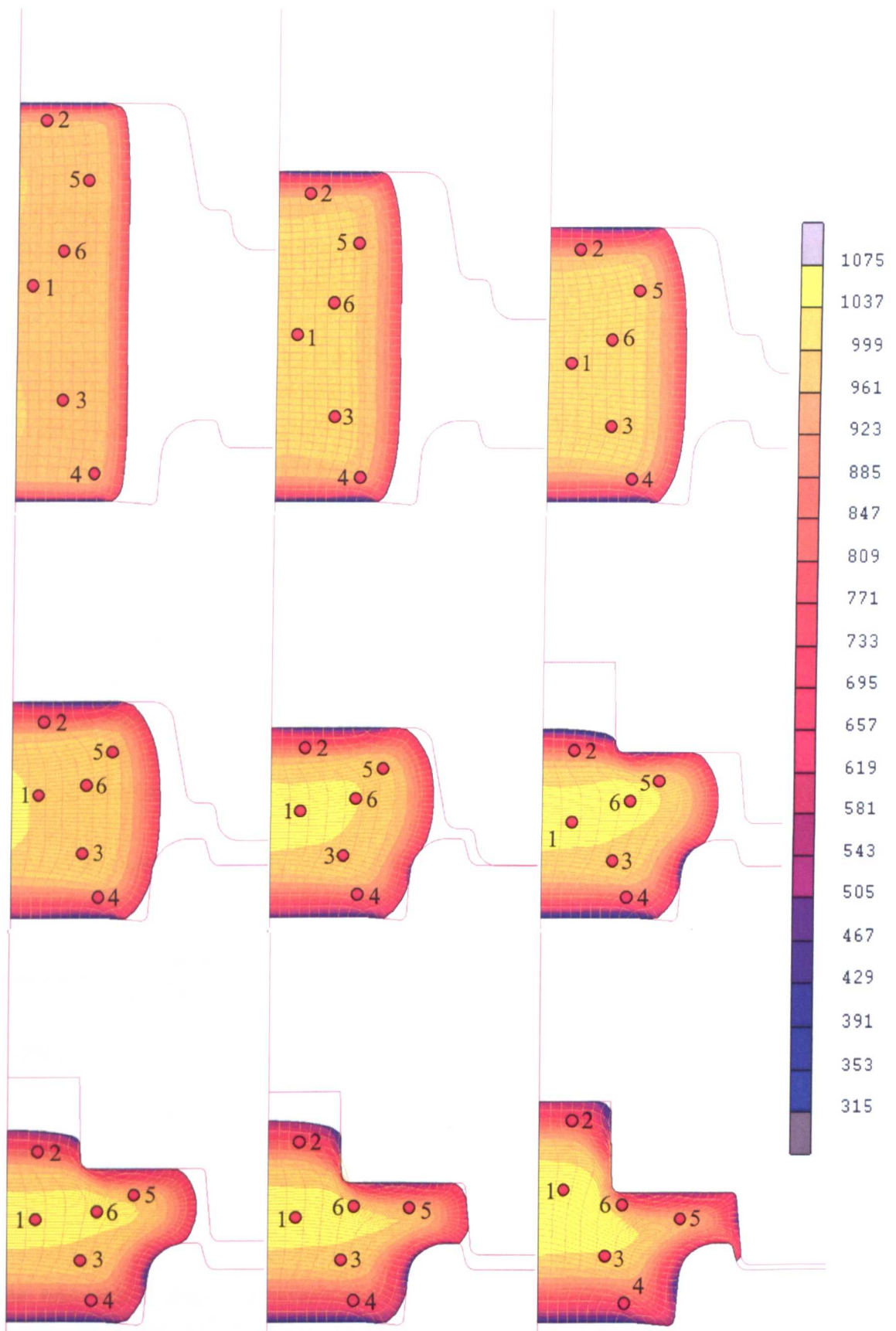
Figure 5.39 Temperature distribution (°C) of the initial billet and after each subsequent blow of the die for all stages of the forging

Considering the track points during this operation points 2 and 4 sit in regions of material that experiences little deformation, commonly known as dead zones, in this case caused by frictional constraint at the tool-workpiece interface. This is shown in Figure 5.37 and in Table 5.10 where these two points only receive a maximum TEPS of 0.3 compared to that of approximately 1 for all the other points in the material for the first operation. These two points are also reasonably close to the top and bottom tools and so as suggested by the lack of plastic deformation (deformation heating) and die chill the temperature rapidly falls. Such a temperature drop is very noticeable (in Figure 5.39) during the first operation for point 4, which does not have intermittent contact with the tool like point 2, and where its temperature drops from 960 to 925 °C.

All six points experience low to intermittent strain rates of between 0.25 and 3s^{-1}. Points 1, 3, 5 and 6 are situated in regions of large strain (all approximately 1) and subsequently experience large amounts of deformation heating, 55 °C in the case of point 1, which lies in the centre of the billet. During the second operation, points 2 and 4 receive very little deformation of 0.05 and 0.09 respectively. Their temperatures are maintained by a balance of heat generated by deformation heating and heat loss to the upper and lower tools. Interestingly point 2 does experience a very high strain rate of 25 s^{-1} and is caused by the extrusion up into the top channel of the die. In practice it would not be possible to reproduce such a high strain rate upon the ASPII, such a result can be ignored as only a strain of 0.05 is produced during the whole second operation (all four blows) and so the affect on microstructural evolution will be negligible.

Table 5.10 Deformation parameter (strain, strain rate and temperature) range during each forging operation

Operation	Deformation parameter	Point 1	Point 2	Point 3	Point 4	Point 5	Point 6
OP1 (b)	ε	0 - 1.2	0 - 0.3	0 - 1	0 - 0.3	0 - 1	0 - 1
	T	985 - 1040	980 - 974	985 - 1020	960 - 925	980 - 1015	984 - 1024
	$\dot{\varepsilon}$	0.25 - 3	1 - 1.6	1.3 - 1.6	0 - 2	0.75 - 2.75	0.5 - 2.4
OP2 (c)	ε	1.2 - 1.6	0.3 - 0.35	1 - 1.25	0.3 - 0.39	1 - 1.9	1 - 1.95
	T	985 - 1013	976 - 974	990 - 1006	975 - 975	987 - 987	990 - 988
	$\dot{\varepsilon}$	0 - 22	0 - 25	0 - 12	0 - 4	5 - 8	3 - 9

The high strain rates experienced by point 1 and 2 are caused by the material being constrained at the corner/vertical edge of the upper channel, when the material is rapidly extruded upwards in the final blow. This regions produces the largest strains and strain

rates in the whole forging but the effects are very constrained to the material in contact with the vertical surface of the upper die. Points 5 and 6 experienced strains of ~0.9 during this stage although the heat produced by deformation heating is more rapidly drawn out of the material as it is compressed thinner on the horizontal extrusion and so these points become much close to the relatively cold tools. On the whole the temperature distribution is quite even throughout the workpiece. The skin of the material is chilled by the tools to a minimum of 315 °C, with a very steep temperature gradient over the first 15 mm into the material.

In terms of the strain paths imposed on the material, point 1, 5 and 6 undergo the most complex deformation histories. Point 1 during the first stages simply receives a lot of deformation and is pushed down and outwards. When the second die set begins to extrude both the horizontal and vertical channels point 1 will be influenced by both of these as it is positioned close to the corner of both channels. However, as the horizontal channel is filled point 1 is drawn up into the vertical channel, reversing the direction it was deformed in by the previous die set. Points 5 and 6 are brought reasonably close together at the end of the process even though they did not start off so. They also seem to experience similar deformation paths, both being squashed down and out by the first operation and then extruded into the horizontal channel by the second. Point 5 however is in one of the slip line fields during the large upset forging and so should experience a sizeable amount of shear strain.

The final forged component has two large and one reasonably small areas where the material has received no or little deformation and as a result the billet microstructure is these regions will have not been broken up nor will complex strain paths have been generated. As a result, only points 1, 5 and 6 are considered in later sections when analysing the strain paths produced during the operations. In addition to this, the model provides average strain rates of 10 s^{-1} and a strain of 1.2 to act as the conditions to calibrate the ASPII machine with, the results of this work can be found in Section 5.2.2.

5.3.3. Cooling rate of industrial forging

Figure 5.40 below shows the completed (three stage) forging air cooling from the solution heat treatment temperature of 1025 °C. This thermal model has been run with the final forged geometry, even though only the first two forging stages are being thermomechanically modelled as the CAD data was reliably available. To form the second extruded channel the forging has the flash trimmed and is flipped 180° and as a result only points 3 and 4 would be significantly affected by the forming of the top extrusion. In

157

addition to this, photocopies of micrographs taken at each of the six points were kindly supplied by Firth-Rixson and show a direct relationship between the cooling rate and the (diffusionally controlled) Widmanstätten lathe width, with the faster the cooling rate the smaller the lathe width. Unfortunately their quality was not good enough to be reproduced in this report. A paper by Hall [137] presents an almost identical forged component in cross-section as that of the one examined in this report and can be seen below in Figure 5.41 along with micrographs of two points in the forging. Point 2 and 6 in Halls work are in very similar locations as depicted by points 3 and 5 of this study and shows the effects of cooling rates on lath size as point 6 that is close to the outer skin of the component is cooled more rapidly than point 2. In addition to this these micrographs highlight the heterogeneous microstructure generated throughout such a forging with large discrepancies in primary alpha content (52 and 27% for point 2, 6 respectively) brought about by differences in strain and thus deformation heating.
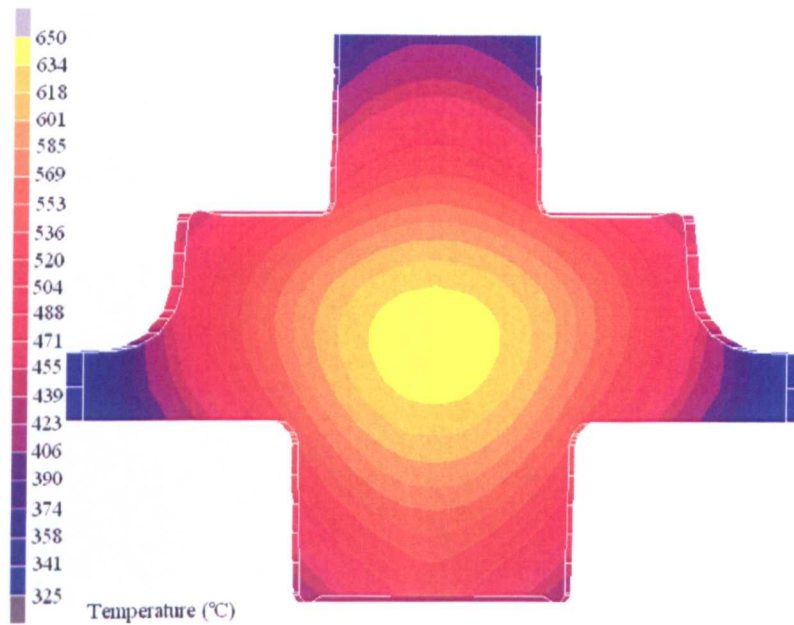
Figure 5.40 Cross section from a FE model of a finished forging that has undergone solution heat treatment (1025 °C) and has been cooling in air for 180 seconds

As points 3 and 4 will receive no further investigation and assuming the final geometry does not have a major effect on the cooling of the part then the calculated cooling rates can be taken as accurate for the already modelled two stage forging.

158

This result shows that heat is retained within the bulky centre of the material, due to titanium's low thermal conductively. The very base of the forging also remains relatively hot, as there is poor conduction between the forging and the floor. The thinnest parts of the horizontal extrusion cools the fastest due to the thin section losing heat rapidly on two surfaces. A similar mechanism operates at all the corners of the component. Figure 5.42 shows a graphical representation of the cooling from 900 °C for two hours until the component reaches room temperature. 900 °C was chosen as air cooling data from an ASP sample was available for the same temperature. All six of the cooling curves are relatively similar in magnitude with 3 pairs of points having almost identical cooling curves.
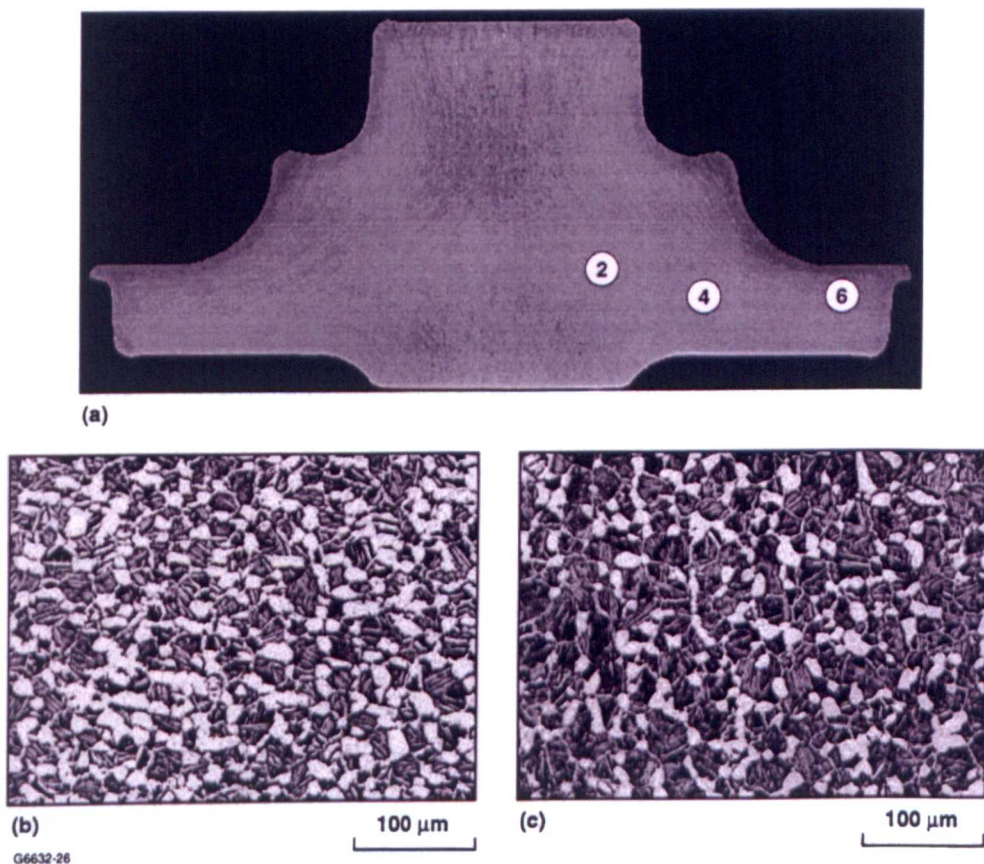
Figure 5.41 (a) Cross-section of a rotor forging of Ti 6-2-4-2 together with micrographs (b) and (c) of locations 2 and 6, respectively [137]

The curve is an exponential decay, rapid at the begining and becoming increasingly slower as heat loss at high temperature is very efficient due to combined high temperature differentials and radiational heat loss. However as the temperature drops so do the differential and the radiational heat losses and the temperature is only further reduced by the slower conduction and convectional loss mechanisms. The slowest cooling parts of the forging are points 1 and 3, which lie towards the very centre of the component and are so in

effect insulated by a thick section of poor heat conducting titanium. Next points 2 and 6 display an intermediate cooling rate, followed by that of points 4 and 5 that lie very close to the outer surface of the forging. Although the forging takes two hours to cool to room temperature it still takes 1800 seconds (30 minutes) for the temperature to drop below 400 °C, the point where it is assumed no thermally induced microstructural mechanisms will operate.
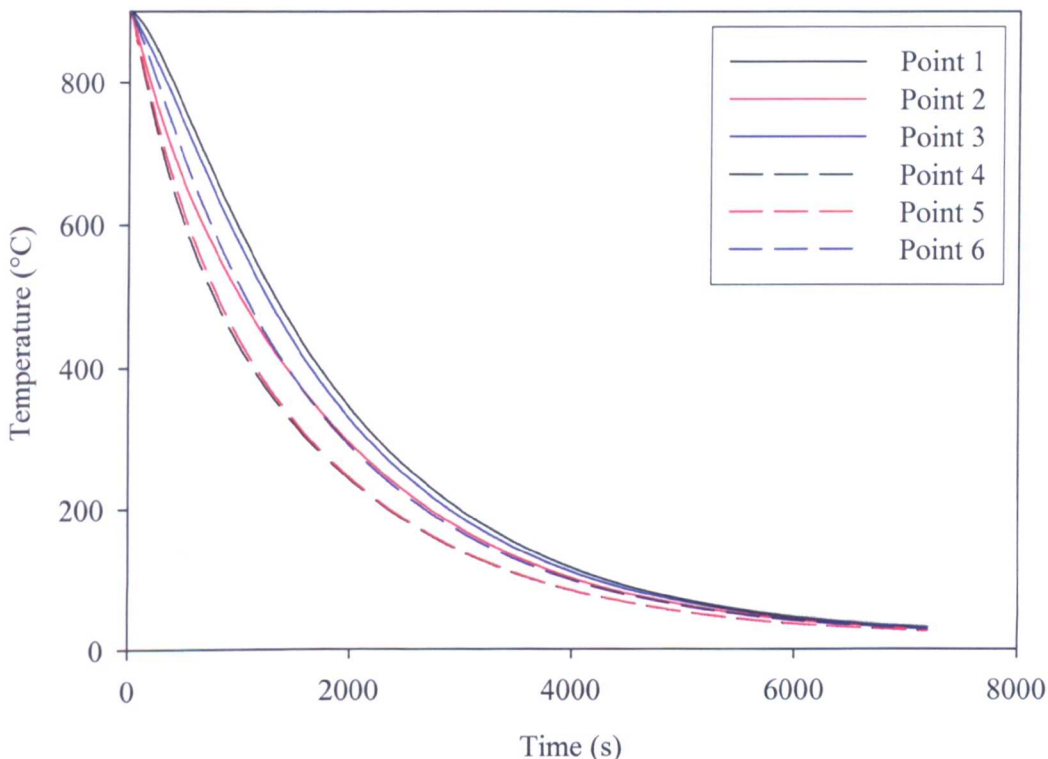
Figure5.42 Cooling curves for each point in a forged component from 900 °C

By comparing this to the cooling data from an ASP sample at the sample temperature in Figure 5.43 below it is clear to see that the smaller ASP sample undergoes a considerably faster air cool than that of the industrial forging that is being modelled. Comparing the two, the ASP samples temperature falls below 400 °C in approximately one tenth of the time and reaches ambient temps in 15 minutes. Measuring the cooling rates at a 650 °C, halfway between 400 and 900 °C, it can be seen that the cooling rate for an air cool of an ASP sample is 3 °Cs^{-1} and for the 50 kg forging it is 0.4 °Cs^{-1}.
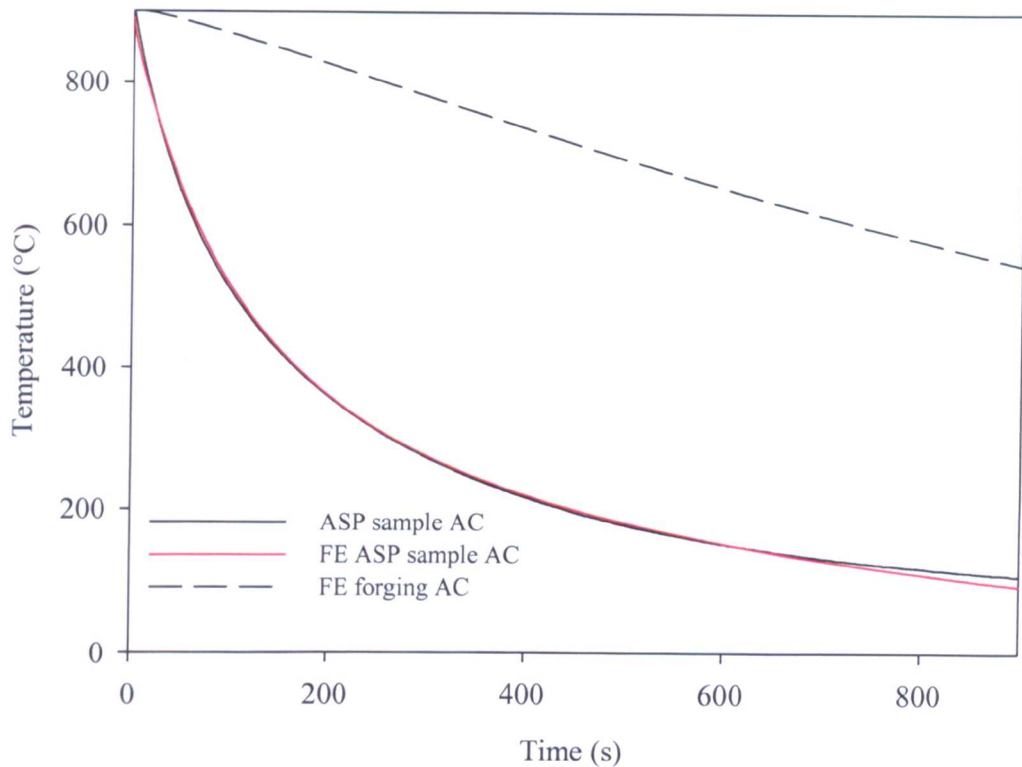
Figure 5.43 Air cooling curve for an ASP sample together with a corresponding FE model and an addition FE model of the compressor forging

As a result of such discrepancies between the two perceived air cools the ASP tests carried out were followed by a controlled air cool to reproduce an industrial air cool. This entailed using the PID control on the ASPII's induction coil to maintain coil power after a test had finished and attempt to slowly cool the sample and reproduce the air cooling rate experienced by the industrial forging. The results of this test can be found in Section 5.4.4.

5.3.4. Strain path analysis

The methodology to extract strain component history was first investigated on the similar axisymetric compression model. This revealed an inconvenient problem with regards to using the MSC Superform software to automatically extract time dependent data. Figure 5.44 shows a strain history plot for a quarter axisymmetric model where the node being analysed is highlighted by the red circle. The $\varepsilon_{11}, \varepsilon_{12}$ and ε_{33} components of strain were measured throughout the deformation with reference to a fixed axis. One model was run

161

with no remesher active (black lines) and another with the remesher active (red and blue lines). The history plot for both black and red lines is gathered simply by selecting the node of interest in the undeformed mesh and then using the MSC software to plot the component of strain at each time interval.
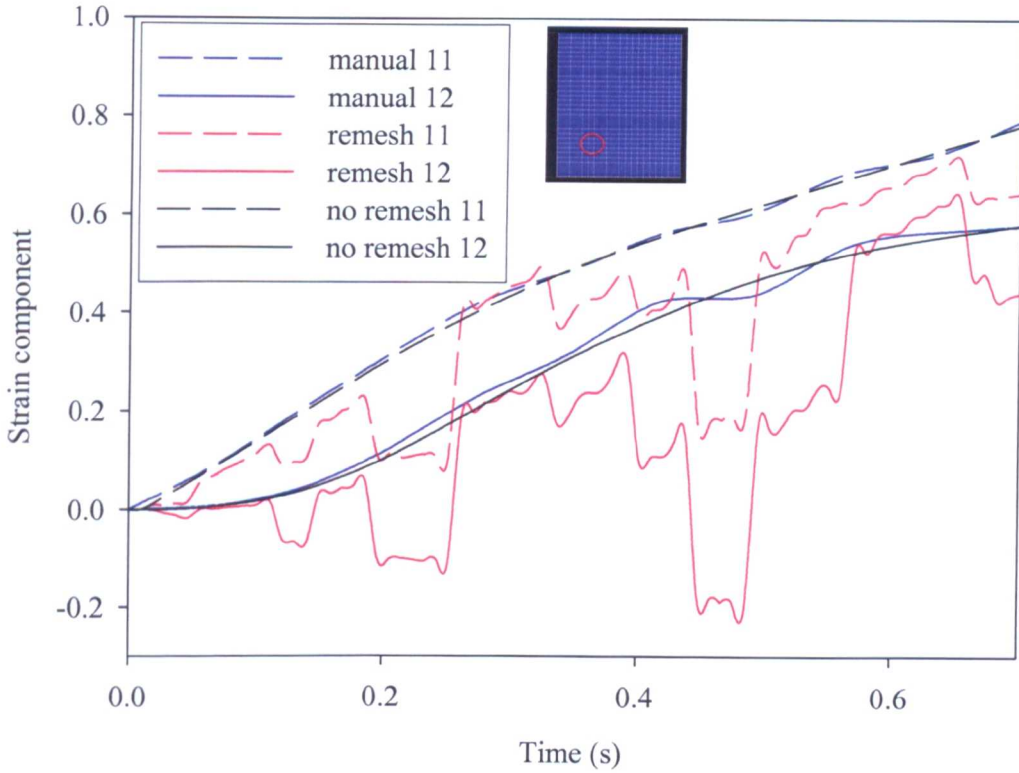
Figure 5.44 Affects of the remesher on strain history plots for a node (see undeformed quarter model) within an axisymetric compression sample deformed to a strain of 0.7 at 990 °C, $\dot{\varepsilon} = 20s^{-1}$

Considering the model with the remesher on (red lines), one might assume that a very complex strain path is being generated at this point in the material as the ε_{12}, shear strain component fluctuates between positive and negative values throughout. This however, is not the case and highlights the problem of directly using the software to plot strain histories for a model that remeshes. Each time the model remeshes a new mesh is created with new elements and node numbers that do not have the same numbers or positions as their predecessors. For example, after a remesh node 105 from the previous iteration may now be somewhere else in the component as part of the new mesh, and so the indicated strain for that node jumps to a new value of strain in a different point within the material every time there is a remesh. Thus, in order to track a point (or node) through out a deformation in this present software the user must track that node manually (blue lines) and when a remesh

162

occurs then decide which of the new nodes generated most accurately represents the position the original node was in. This typically means moving several millimetres in x or y to locate this node, and explains the slight oscillations in strain values in the manually selected nodes compared to the model that did not remesh. These deviations are small (~0.04) and will be assumed to have no measurable affect on the overall strain path calculation when analysis is carried out of the forging model.

By manually tracking each point (1, 5 and 6) in the forging model using the method described above the $\varepsilon_{11}, \varepsilon_{22}, \varepsilon_{12}, \varepsilon_{33}, \dot{\varepsilon}$ and temperature for each blow of the tool was extracted and plotted in Tables 5.11-5.13. The blue highlighted section represents the first forging die and the green the second die. By using all four components of strain the strain path angle compared to that of the previous deformation is calculated using Equation 2.12 derived in Section 2.3.6. By assuming an isotropic material and applying Equation 4.54 to Equation 2.12 it can be shown that the strain path angle change is related to a ratio of $\varepsilon_{12}/\varepsilon_{33}$. For the purposes of ASP testing ε_{12} is taken to been the torsional component on the machine and ε_{33} the axial component of strain. Table 5.14-5.16 gives the calculated $\varepsilon_{12}/\varepsilon_{33}$ values, and the corresponding angle and axial deformations and rates to impose the calculated values that have been derived using the equations in Section 4.4. For the purposes of this work strain path angles less than 10 degrees are assumed to be negligible and so ignored and taken to be linear strain deformations, i.e. purely torsion, tension or compression and are highlighted in red.

Table 5.11 Strain components and strain path angle calculations for point 1. Blue and green sections relate to the 1ˢᵗ and 2ⁿᵈ forging dies and the number of blows with each

Blow	ε_{11}	ε_{22}	ε_{12}	ε_{33}	ε_{eq}	Strain path angle (cosα)	Angle (α)
1	-0.18	0.09	0.00	0.09	0.18	0	0
2	-0.24	0.12	0.01	0.12	0.24	1.00	1
3	-0.29	0.14	0.01	0.15	0.29	1.00	1
4	-0.34	0.16	0.02	0.18	0.34	1.00	1
5	-0.22	0.11	-0.08	0.13	0.25	0.95	19
1	-0.01	0.01	0.14	0.02	0.17	-0.12	97
2	0.01	0.00	0.01	0.00	0.01	0.61	52
3	0.08	-0.01	0.41	-0.08	0.49	0.84	33
4	0.45	-0.33	0.31	0.00	0.58	0.61	52

Table 5.12 Strain components and strain path angle calculations for point 5. Blue and green sections relate to the 1ˢᵗ and 2ⁿᵈ forging dies and the number of blows with each

Blow	ε_{11}	ε_{22}	ε_{12}	ε_{33}	ε_{eq}	Strain path angle ($\cos\alpha$)	Angle ($\alpha°$)
1	-0.20	0.09	-0.05	0.11	0.21	0	0
2	-0.20	0.08	-0.10	0.12	0.23	0.98	11
3	-0.18	0.07	-0.17	0.11	0.27	0.96	16
4	-0.16	0.04	-0.34	0.12	0.42	0.93	21
5	-0.13	0.01	-0.34	0.12	0.42	1.00	6
1	-0.27	0.21	0.09	0.13	0.32	0.15	81
2	-0.02	0.09	0.30	0.02	0.35	0.47	62
3	-0.04	0.10	0.51	0.07	0.59	0.99	7
4	-0.16	-0.09	-0.91	-0.38	1.10	-0.93	159

Table 5.13 Strain components and strain path angle calculations for point 6. Blue and green sections relate to the 1ˢᵗ and 2ⁿᵈ forging dies and the number of blows with each

Blow	ε_{11}	ε_{22}	ε_{12}	ε_{33}	ε_{eq}	Strain path angle ($\cos\alpha$)	Angle ($\alpha°$)
1	-0.19	0.09	-0.01	0.09	0.19	0	0
2	-0.22	0.10	-0.02	0.12	0.22	1.00	3
3	-0.23	0.10	-0.05	0.13	0.24	0.99	7
4	-0.26	0.10	-0.12	0.16	0.29	0.98	11
5	-0.23	0.11	-0.14	0.13	0.28	0.99	7
1	-0.23	0.17	0.31	0.06	0.42	0.27	74
2	-0.29	0.22	0.16	0.07	0.35	0.92	23
3	-0.11	0.11	0.00	0.02	0.13	0.91	25
4	0.13	-0.03	0.57	0.00	0.67	-0.18	101

Considering point 1, it can be seen that there are insignificant changes in strain path angle for the first four blows. Only when the side of the forging comes into contact with the side of the lower die in the final blow does this have (a small) effect on the strain path angle. In the second operation there are considerable strain path angle changes as point 1 is extruded upwards into the top channel of the upper die. Point 5 and 6 both exhibit similar results although point 5 does show small changes in strain path angle change for blow 2, 3 and 4 in the first operation however point 6 only shows a small change in blow 4. This is most likely caused by the two slip line fields intersecting this point as they become established during the second blow and then dominate the deformation for these two points. Much larger strain path changes are observed in the second operation due to the extruding channels of the die. A very large, almost full reversal (159°) is created on the final blow for point 5 as material is forced to fill the entire mould and the flash skirt is created just below

point 5 that generates a large shear component of strain. Again, a similar affect is observed for point 6 although the angle change is less, as it is further away from the flash skirt.

Table 5.14-5.16 below show the values of angle and axial deformations converted from the FE data in order for the ASPII to generate the calculated strain paths. Figures highlighted in red represent when the deformation, be it axial or torsional, was reversed so as not to cause sufficient deformation to induce fracture in a sample. For example, comparing Table 5.14 and 5.11 for point 1 there are no appreciable strain path angle changes during the first 4 blows of the die so all the deformation on the ASPII is generated by a purely torsional deformation. The first two deformations require a twist of 45 and 60° respectively. The third twist of 72° is then applied in opposite direction to the previous two deformations to minimise the net deformation imposed on the sample.

Table 5.14 Calculated torsional and axial deformation together with derived angle and axial values to produce such strains and generate strain path changes for point 1

ε_{12}	ε_{33}	ε_{eq}	θ (°)	l (mm)	total θ	total l	$\dot{\varepsilon}$ (s^{-1})	$\dot{\theta}$ (° s^{-1})	dl/dt
0.00	0.00	0	0	0.00	0	0.00	0.00	0	0.00
0.16	0.00	0.18	45	0.00	45	0.00	0.76	189	0.00
0.21	0.00	0.24	60	0.00	105	0.00	1.05	261	0.00
0.25	0.00	0.29	72	0.00	34	0.00	1.53	380	0.00
0.30	0.00	0.34	86	0.00	119	0.00	2.18	541	0.00
0.20	0.06	0.25	57	0.58	176	0.58	2.18	510	5.12
0.04	-0.16	0.17	13	-1.50	189	-0.93	0.77	59	-7.02
0.01	0.00	0.01	3	0.03	192	-0.90	0.17	34	0.35
0.42	0.06	0.49	121	0.62	71	-1.52	3.52	871	-4.47
0.30	0.46	0.58	87	5.90	157	4.38	0.20	30	2.04

Table 5.15 Calculated torsional and axial deformation together with derived angle and axial values to produce such strains and generate strain path changes for point 5

ε_{12}	ε_{33}	ε_{eq}	θ (°)	l (mm)	total θ	total l	$\dot{\varepsilon}$ (s^{-1})	$\dot{\theta}$ (° s^{-1})	dl/dt
0.00	0.00	0	0	0.00	0	0.00	0.00	0	0.00
0.18	0.00	0.21	52	0.00	52	0.00	0.84	209	0.00
0.20	0.03	0.23	56	0.34	-4	-0.34	1.11	268	-1.59
0.22	0.10	0.27	63	1.01	59	0.67	1.22	282	4.51
0.28	0.27	0.42	81	3.07	-22	-2.40	1.41	268	-10.22
0.36	0.00	0.42	104	0.00	82	-2.40	2.16	536	0.00
0.02	0.13	0.32	7	1.39	88	-1.01	3.11	65	13.66
0.29	0.09	0.35	84	0.90	4	-1.91	4.49	1081	-11.53
0.52	0.00	0.59	148	0.00	-143	-1.91	3.67	911	0.00
0.92	0.31	1.10	264	3.63	120	1.72	1.34	321	4.42

Table 5.16 Calculated torsional and axial deformation together with derived angle and axial values to produce such strains and generate strain path changes for point 6

ε_{12}	ε_{33}	ε_{eq}	θ (°)	l (mm)	total θ	total l	$\dot{\varepsilon}$ (s⁻¹)	$\dot{\theta}$ (° s⁻¹)	dl/dt
0.00	0.00	0	0	0.00	0	0.00	0.00	0	0
0.16	0.00	0.19	46	0.00	46	0.00	0.77	191	0.00
0.19	0.00	0.22	56	0.00	102	0.00	1.10	273	0.00
0.20	0.00	0.24	59	0.00	160	0.00	1.34	333	0.00
0.25	0.04	0.29	72	0.42	89	-0.42	1.81	439	-2.57
0.25	0.00	0.28	71	0.00	159	-0.42	2.16	536	0.00
0.35	0.10	0.42	100	1.05	59	-1.47	2.78	656	-6.88
0.30	0.00	0.35	86	0.00	-27	-1.47	4.91	1189	-0.03
0.11	0.04	0.13	31	0.41	4	-1.06	6.01	1436	19.12
0.41	-0.48	0.67	117	-3.81	121	-4.88	0.60	105	-3.41

This section has shown how Timetal®834 deforms under a typical industrial forging operation. During the first upsetting stage the deformation is very similar to that of an axisymmetric compression test, though be it on a much larger scale. The strain path angle changes here are minimal and only really become significant when the die set begins to extrude the material into channels and form the complex shape of a compressor disc. For three points of interest in the material the deformation parameters have been recorded with respect to time. The strain path angles have then been calculated using the mathematical derivations presented earlier in this manuscript. These angle changes have then been converted into representative torsional and axial deformation to be replayed on the ASPII machine with corresponding strain rates and temperatures (also calculated from the FE model). The results of the machine performance based on the above inputs and combined with the thermal modelling data of Section 5.1.4.1 can be found in Section 5.4.4.

5.4. Strain path testing

5.4.1. As-received material

Test material came from two different sources; Firth-Rixson Ltd. and Timet UK Ltd. The first billet was a failed forging billet courtesy of Firth-Rixson Ltd, Darley Dale, UK. The second batch of test material was a cylindrical quartile of a billet, which came from Timet UK. The Timet material was classic billet material however the Darley Dale material had undergone unknown thermomechanical processing. A combination of high friction and rapid cooling between the forging tools and workpiece caused the top of the material to harden and stick to the tools. As the material spread out laterally under the compressive strain the sides of the cylindrical material began to fold over becoming the top surface of the workpiece in the same fashion as observed during axisymetric tests and modelling shown in Section 5.1.1. This is evident due to a v-shaped ridge on the top on the material and is visible in the computer aided design (CAD) drawing in Figure 5.45(a). Assuming the top ridge is the original corner of the billet and has a diameter of Ø190mm and the estimated weight of the (non-sectioned) billet to be 32 kg then the original height of the cylindrical billet was approximately 250mm. To compress to a final height of 102mm requires a strain of approximately 0.9. Figure 5.45(a) shows a semi-transparent CAD model of the forged billet and demonstrates where the samples were machined. Dimensions of the samples can be found in Section 4.3.1. These samples were used in some calibration tests and the 'simple' strain path tests which are discussed in Section 4.4.7. Figure 5.45(b) shows the quartile of billet material from Timet UK where samples for the complex strain path tests were machined parallel to the longitudinal axis of the billet as illustrated by the black arrow.

(a)   (b)
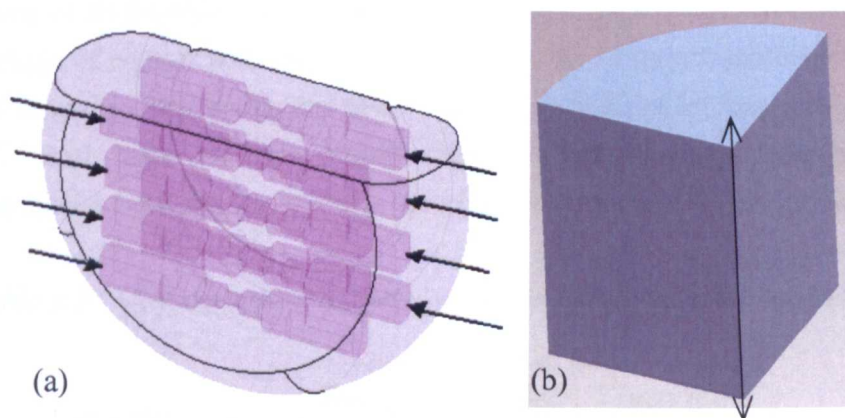
Figure 5.45 Billet material showing where test specimens were machined from (a) Darley Dale and (b) Timet material

Micrographs of both Darley Dale and Timet billet materials are shown below in Figure 5.46(a) and (b) respectively. Both of these optical samples were taken from the centre of each billet. The deformation temperature at which the Darley Dale billet was processed is estimated at approximately 960 °C. This was established by volume fraction analysis of the primary alpha (α_P) grains present in material taken from near the top surface of the billet. This is slightly different than the centre material as it has experienced a faster cooling rate due to die chill and so the alpha-beta hot deformation microstructure is better preserved when compared to that of the very slowly cooled (coarsened) centre region which made distinguishing between α_P and secondary alpha (α_S) grains easier.
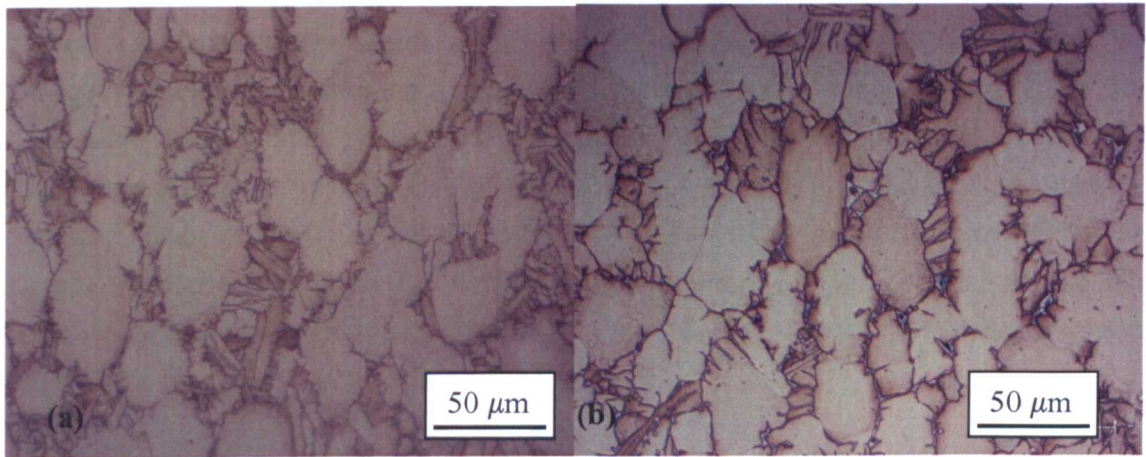
Figure 5.46 Optical images of (a) Darley Dale and (b) Timet billet

The large lath size in both materials indicates a slow cooling rate and also makes it difficult to distinguish between the primary alpha grains and the secondary alpha grains (transformed β grains) and so the percentage of α_P grains present in billet material can only be taken as an estimate. Both materials display typical billet microstructures of a high percentage of equiaxed α_P grains in a matrix of very coarse transformed beta laths. The size of α_P grains, lath width and α_P percentage for both billet materials is shown in Table 5.17. Both materials have almost identical microstructural features with only small discrepancies between the two that are easily within experimental error.

Table 5.17 Microstructural differences between the two billet materials

	Darley Dale billet	Timet billet
Percentage α_P	70%	75%
α_P grain size	$32 \pm 10\ \mu m$	$36 \pm 12\ \mu m$
Lath width	$5 \pm 3\ \mu m$	$4 \pm 3\ \mu m$

168

The chemical analysis of Timetal®834 used in this work was measured using LECO inductively coupled plasma ion source mass spectrometry and is shown in Table 5.18. The chemical analysis is very close to the desired alloy content for all elements as this is a highly process controlled aerospace alloy.

Table 5.18 Chemical composition of as-received Timetal®834 (wt%)

Al	Sn	Zr	Nb	Mo	Si	C	Fe	O	N	H
5.64	3.95	2.72	0.45	0.50	<0.05	0.12	<0.02	0.144	0.004	213 ppm

The orientation image map for the Darley Dale and Timet material are shown in Figure. 5.47(a & b) respectively together with Pole Figures in Figure 5.48 and 5.49. The Darley Dale material shows the typical clustering observed by other authors [22-25,90] of similarly orientated α_p grains with cluster sizes up to 0.5mm, though on a bulk scale the texture is relatively weak. The same effect is present in the Timet material where a distinct cluster, primarily of (0001) orientation, can be seen in the bottom left of the figure. Although the Darley Dale billet is not identical to original billet material that has slightly more α_p with no substructure, though for the purposes of this investigation they can be considered to be sufficiently similar.
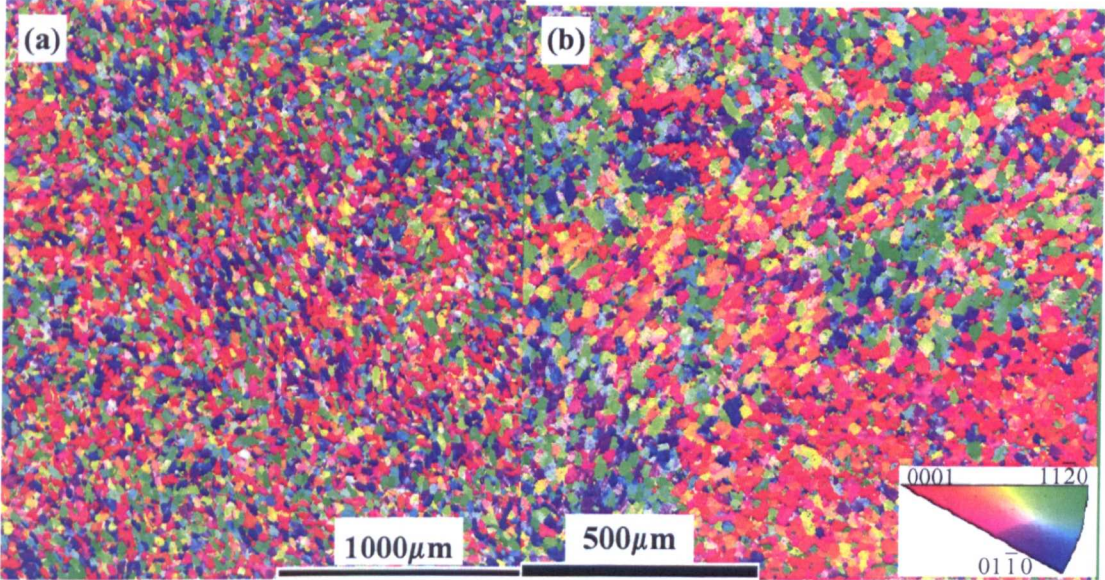
Figure 5.47(a) Texture scale orientation image maps using inverse pole Figure (IPF) colouring for Darley Dale material and (b) Timet material in the radial direction
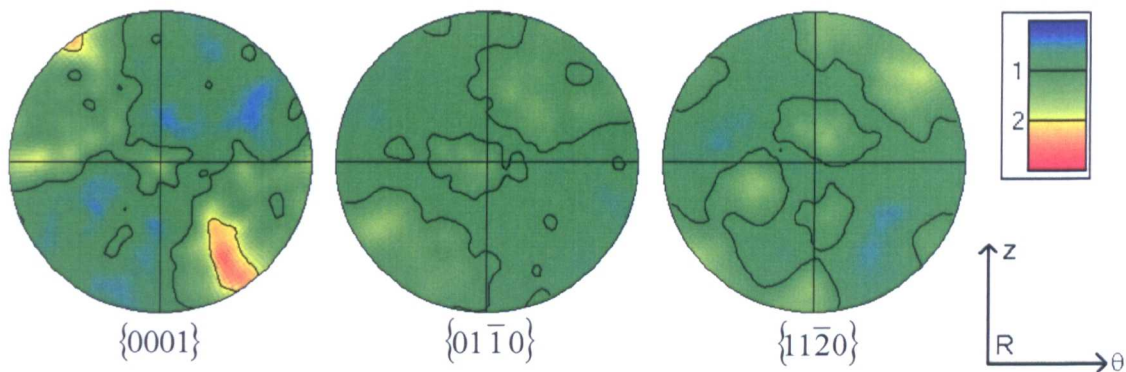
Figure 5.48 Pole Figures for Firth-Rixson supplied billet perpendicular to compression axis
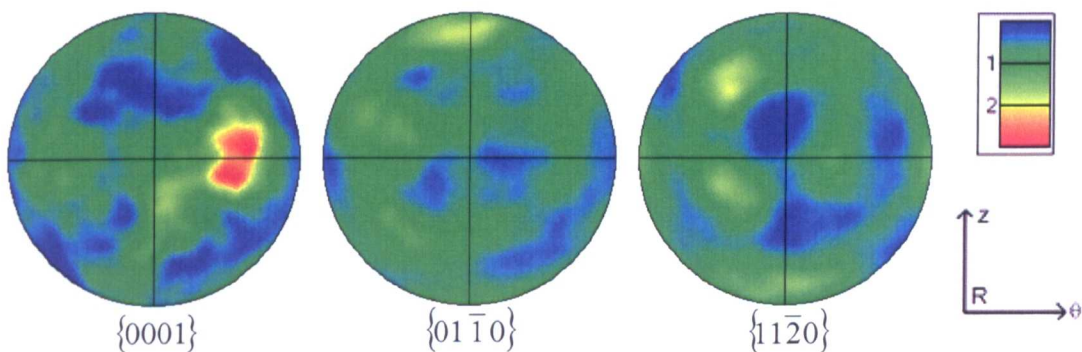
Figure 5.49 Pole Figures for Timet supplied billet perpendicular to compression axis

5.4.2. Alpha case

Due to titanium's high affinity with small interstitial solutes such as oxygen, nitrogen and hydrogen, all of which are alpha stabilising elements, a brittle highly alloyed alpha case is produced on titanium surfaces held at high temperature for sufficient time in atmospheric conditions. The micrographs below in Figure 5.50 reveal that a solid, thin alpha case is produced on the surface of a Timetal®834 sample and penetrates approximately 2-3 grains in depth that is equivalent to approximately $60\mu m$. There is an increase in the percentage of alpha grains near to a depth of $150\mu m$ before the normal volume fraction is observed throughout the bulk of the material. It can be concluded the interstitial pick up is limited to the very surface of the material and only influences the microstructure to a total depth of $150\mu m$. All analysis of ASP samples is carried out at r_m as outlined in Section 4.4.6 which is 1mm below the surface of the sample and so the absorption of interstitial elements will have no bearing on the observed results.
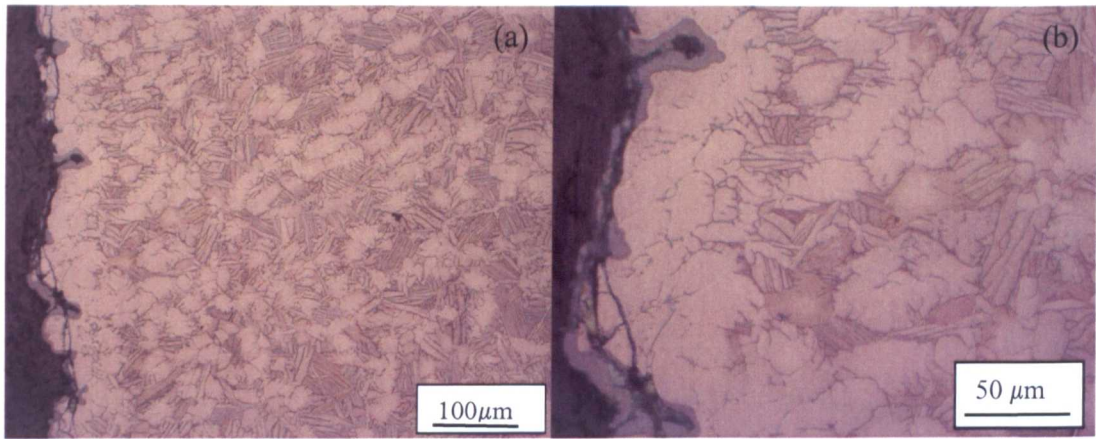
Figure 5.50 Optical micrographs at magnifications of (a) 20 and (b) 50 times, showing the alpha case formed during an ASP test (longitudinal axis aligned with page) of point 6 (followed by an AC) from the forging

Some cracking of the hard alpha case during testing can be seen in the above micrographs. Under tests conditions where strains and strain rates are sufficiently low, such an alpha case causes no adverse problems. However, more substantial surface initiated cracks were observed in torsion tests conducted at strains rates of 10 s^{-1} to strains of 1.8 (360° torsion). The cracks occurred at either end of the gauge length where the reducing radii of the sample shoulder blends into the gauge length. It is believed this is attributed to a combination of reduced ductility due to the alpha case and a machining induced stress concentration in the form of a very slight undercut of the radii, the effects of which can be seen in Figure 5.52 in Section 5.3.3.

5.4.3.   'Simple' strain paths

The matrix of 'simple' strain path tests (Table 4.4 in Section 4.4.7) was undertaken although not all of the tests were successful. During tests 1 and 2 the samples cracked at the radius where the gauge length ended and blended into the first larger shoulder of the sample, demonstrating strain rates of 10 and 4s^{-1} is too rapid to deform Timetal®834 to 180° at 990 °C. The strain rate was again reduced to that of 2s^{-1} and it was possible to impose large, 360° rotations of the samples at this temperature. This test along with a forward and reverse 180° torsion are shown below in Figure 5.51 and represent tests 5 and 6 in Table 4.4. The thinner line represents the temperature in the gauge length and the thicker lines are the flow stress of the material with each deformation, 360°, +180° and -180° plotted in black, blue and red respectively.
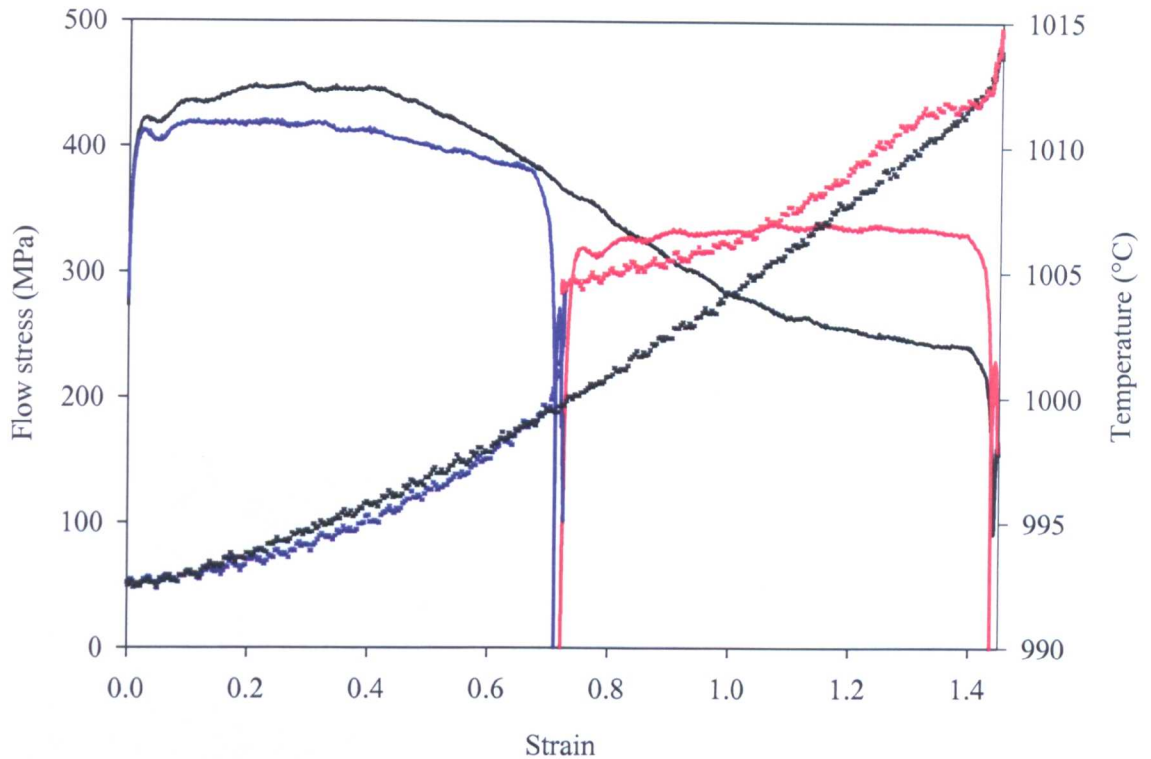
Figure 5.51 Stress-strain curve for 360° and 180°/-180° torsion at 990 °C, 2s⁻¹. Thick and thin lines represent flow stress and temperature respectively

For the forward 180° and the 360° torsion there is almost exactly the same deformation heating, as to be expected. The 360° torsion temperature gradually increases through out the whole deformation and a total of 23 °C of deformation heating is measured. When the 180° ends and the rotation is reversed, during the very short pause the temperature increases from 1000 °C to 1005 °C and shows there is thermocouple lag even though the thermocouple is only 5mm from the centre of the gauge length. This is a common phenomenon in thermomechanical processing at high strain rates [94] however titanium's low thermal conductively again plays a negative roll in delaying the heat flow from the gauge length. The (deformation) heating rate for the reverse 180° is considerably lower compared to that of the forward and slowly increases throughout the deformation, but not before a levelling off at a strain of 1.3 followed by another increase to equal that of the 360° torsion. There is no change in the flow behaviour at this point, nor was any localised shearing observed. Additionally if the curve is extrapolated from the point at which it drops to the ends where it equals the 360° temperature then this is not likely to be a material effect and more so the thermocouple being effected by the deformation e.g. losing contact with the material for a brief moment as the thermocouple hole is deformed.

Examining the flow stress of the two tests, the 360° and forward 180° torsion yield at 280 MPa and have a σ_{peak} of 450 and 410 MPa respectively. Both the curves exhibit rapid rate work hardening. The 180° curve displays steady state flow up to a strain of

0.27 before beginning to soften slowly. The 360° curve continues to work harden to the same strain however its flow softening is considerably greater than that of the 180° and can be attributed to flow localisation in the same region were tests 1 and 2 broke. This caused cracks to form in the sample but it did not fail like the previous tests. This sample is shown in Figure 5.52(a) and a cross section of the crack in 5.52(b) demonstrating the flow localisation at this point. The issue of so many samples failing in the same place raises the question of whether the samples were machined to specification or is there another issue with regard to testing titanium at high strain rates with this sample geometry?
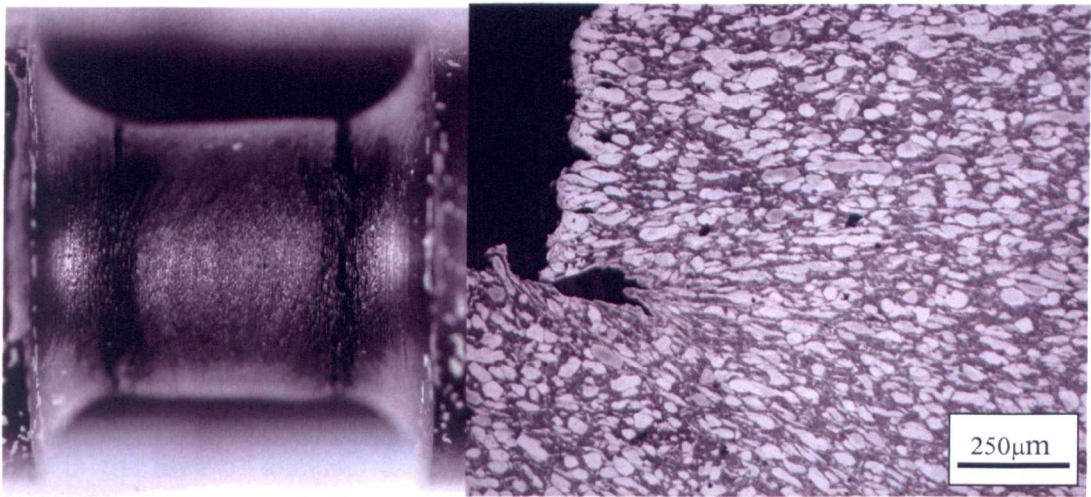
Figure 5.52(a) Test 6, 360° torsion sample showing cracking at either end of the gauge length and (b) cross section of the crack in the bottom left corner

Before testing the samples were not checked to see if there was any under cutting at the gauge length radius. It was not however stated on the samples machining drawings that no undercut could be tolerated. It could be that although this geometry (2:1 radii to length ratio) is well suited to carry out high strain rates as discussed previously [111], the two step down radii maybe too great a change in cross section (i.e. stress concentration) and that larger radii should be employed to give a more gradual change in cross section. To overcome this problem the same samples could be turned by a precision workshop with express instructions not to undercut the gauge length radius. The tests could then be repeated to prove whether it was a machining deviation of sample geometry that was causing the failure of the samples.

In both tests the PID response of the actuator can be seen in the flow curves at the start of the deformation as oscillations. An oscillation is also observed further into the deformation and is due to the nature of the raw data presented rather than a smoothed curve and is not believed to be a major machine or microstructural effect.

When the torsion direction is reversed in the 180°/-180° test the material yields at the lower value of 175 MPa and this is followed by a region of rapid work hardening, but

lower than that observed in the forward torsion until a steady state flow is reached at 310 MPa. The flow stress remains at this plateau stress until the end of the deformation and does not soften in the same fashion as the forward 180° even though the temperature is 15° higher, and so suggests that a regime of more rapid work hardening encountered.

Figure 5.53 shows texture scale orientation image maps (OIM) using inverse pole figure (IPF) colouring for (a) billet material (Darley Dale), (c) 360° rotated material and (e) 180°/-180° rotated material together with high resolution maps using Euler contrast for (b) billet material, (d) 360° rotated material and (f) 180°/-180° rotated material. All EBSD scans are measures in the radial direction of the billet and ASPII sample. Due to the flow localisation experienced in the 360° forward torsion test sample the area analysed for texture and microstructure investigation did not receive the total applied strain. By considering the orientation of torsional deformed grains is defined with respect to both the macroscopic maximum principle stress and strain directions then the maximum principle stress or tensile stress axis in torsion lie at 45° to the applied forward shear stress. However, the principle strain direction which gives the principle axes of elongation in a torsional deformed grain is rotated during deformation [138]. A relationship between this rotation angle and the applied shear strain is given by Canova et al. [139] and from the shape change of the α_p grains in Fig. 5.53(d) the equivalent strain in the area of analysis is estimated to be 0.7. Many of the α_p grains contain deformation induced twins and deformation substructure which appears to also align itself parallel to the direction of tensile strain. Misorientation analysis of the α_p grains shows misorientation accumulations of up to 20° in individual grains, indicating that a significant amount of the applied macroscopic strain was accommodated by the α_p grains and that at this temperature the α_p grains do not act like hard inclusions in a softer matrix of β grains as described by other authors [140,141] as the proportion of the β phase (at this working temperature) is insufficient for it to be a continuous matrix encircling the α_p grains.
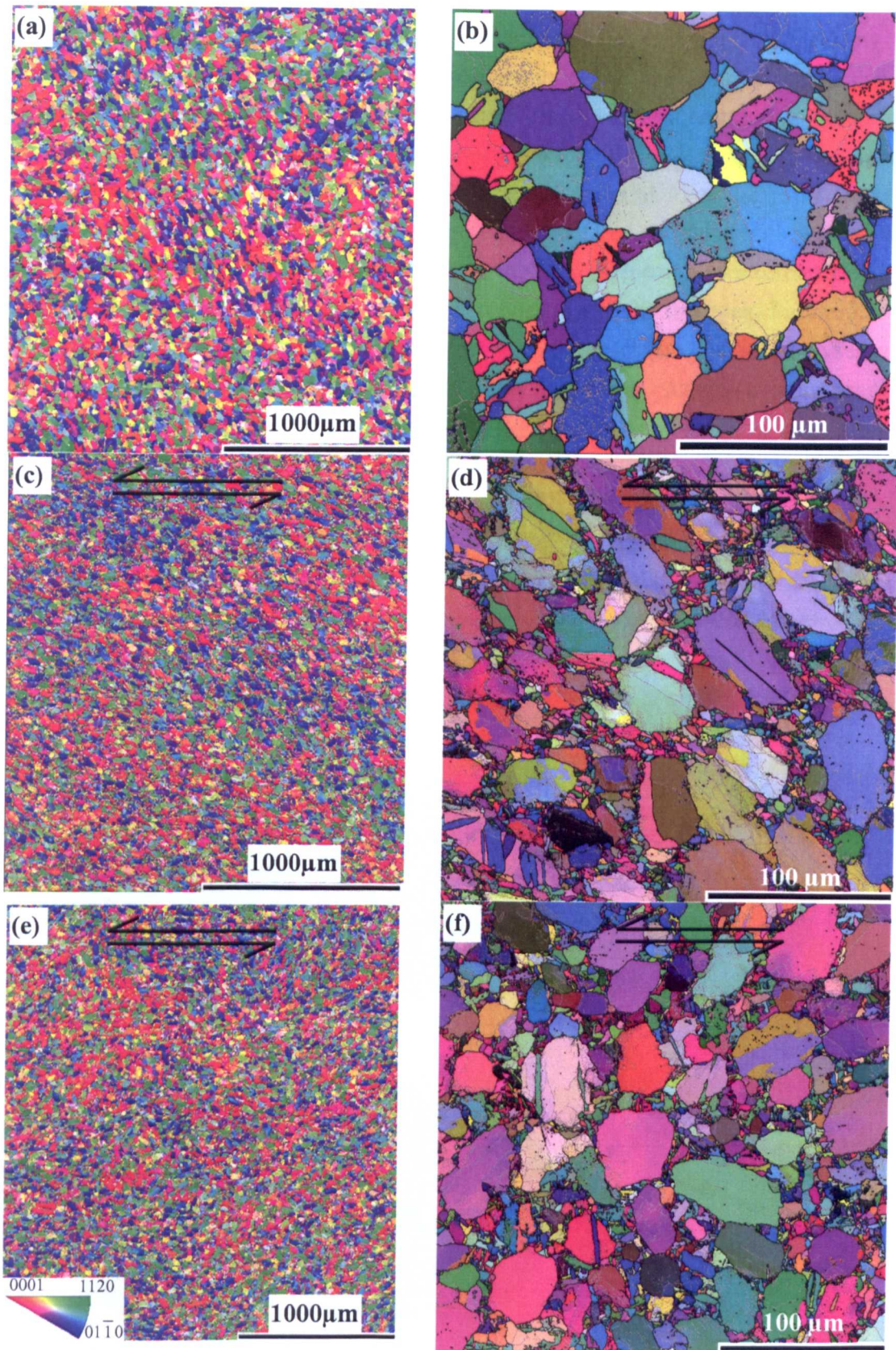
*Figure 5.53 Texture scale orientation image maps using inverse pole figure colouring
for (a) billet, (c) 360° and (e) 180°/-180° rotated material together with high resolution
maps using Euler contrast for (b) billet, (d) 360° and (f) 180°/-180°rotated material.
Black lines represent misorientation of >10° and grey >2°*

175

Further analysis of the twins showed that many had serrated edges, suggesting that many were formed early in the deformation sequence. There is no evidence that the large torsional strain broke up the clustering of the similarly orientated α_p grains with clusters visible on the same scale as the billet material. The pole figures in Figure 5.54 also show similar levels of intensity as the original material. For the 180°/-180° test, Figure 5.53(e) shows the clustering of similarly orientated α_p grains still remains after the severe change in strain path. This change in strain path has also returned elongated α_p grains back to an equiaxed structure. The pole figure for this area, Figure 5.54(b), also shows there is no significant change in the global texture for the analysed area. Accumulated misorientation analysis of the α_p grains shows a heterogeneous distribution in deformation substructure with some α_p grains containing large amounts of deformation substructure with accumulated misorientations of 10-20° whilst others contain virtually no accumulated misorientation.

This observation may explain the significant drop in σ_{ss} on strain reversal as grains of favourable orientation have reduced their dislocation density, reducing the effective number of barriers to further dislocation movement. Twins are also observed in the reversed material and again many have serrated boundaries. It is unclear, however, whether these twins were formed during the forward or reverse torsional deformation.
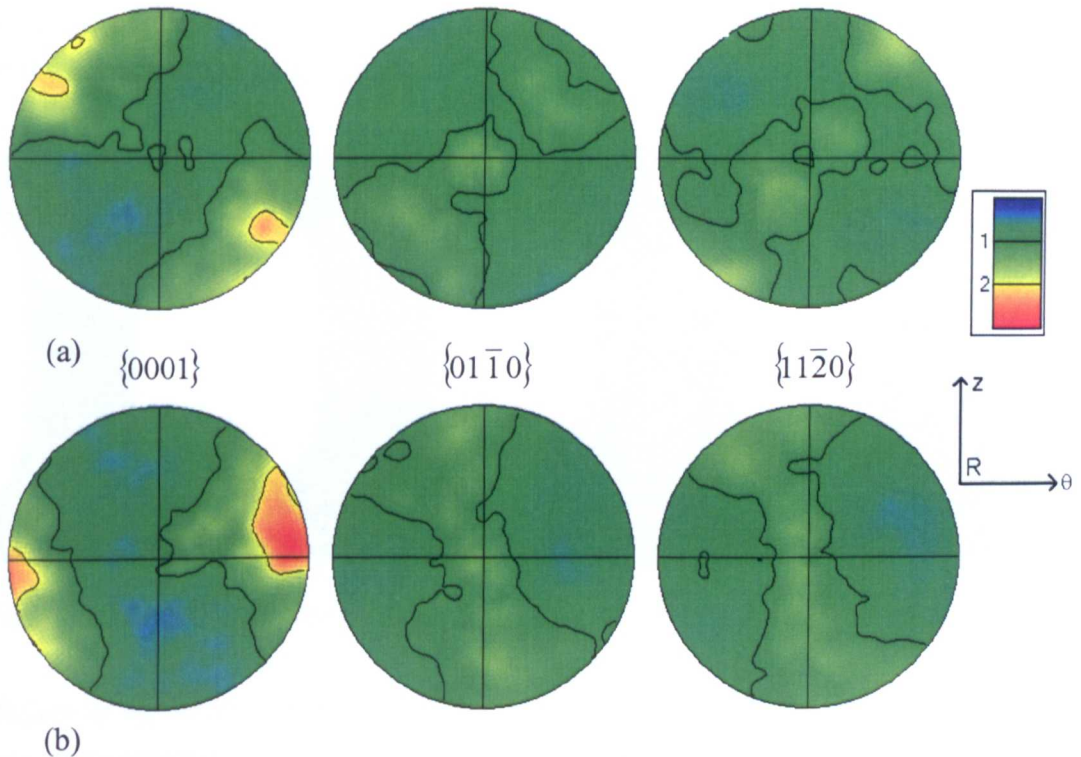
Figure 5.54 Pole figures for (a) 360° torsion and (b) 180°/-180° torsion. Arrows represent shearing direction relative to the pole figures

This analysis of the results suggests that neither larger strain deformation nor severe changes in strain path is capable of breaking up the clusters of similarly orientated α_p grains. This would suggest that during a typical forging operation the clustering of similarly orientated α_p grains inherited from the as-received billet will not be reduced. This suggests that improved in-service fatigue performance of this alloy, as reported in previous studies [19-21,26], can only be achieved by reducing the clustering upstream in the manufacture of the billet.

5.4.4. Industrial strain paths

Of the three points in the forging selected for analysis in Section 5.3.2 point 1's equivalent strain was also carried out in pure (free end) torsion. All four samples, point 1, 5, 6 and point 1 torsion from each test are shown respectively in Figure 5.55. It can be seen in the shape of the samples after deformation that point 1 and 5 result in an overall tensile and torsional strain, where point 6 results in a compressional and torsional strain. All the samples are perfectly uniform in their deformation demonstrating that the machined chamfer and precise fit at the end of a sample ensures that it is aligned perfectly with the rotational axis of the machine. No cracking or flow localisation of the samples was observed although a small amount of oxide did spall from the surface of the gauge length.

(a)   (b)   (c)   (d)
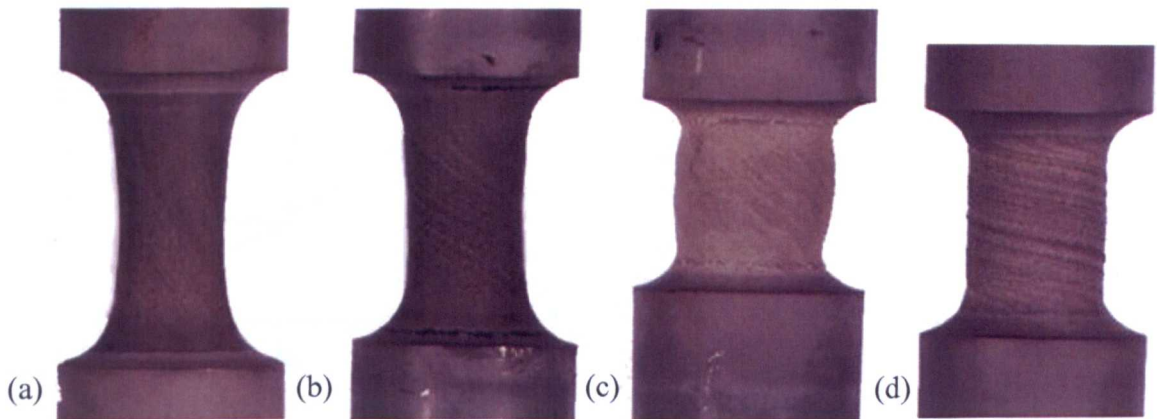
Figure 5.55 ASPII samples for point 1(a), 5(b), 6(c) and point 1 (d) in pure torsion

No failure of any of the complex strain path test samples was observed unlike the earlier simple strain path tests. Although the complex strain path samples were machined from the Timet supplied billet by a different workshop than the previous set of samples it is not possible to conclude whether the breakage of the first set of tests was a result of machining induced stress risers, harsher testing conditions or material effects. It is the author's opinion that there is insignificant difference between the microstructures of the two billets from which samples were harvested from and that the early breaks were most

177

likely caused by the high strain and strain rates used to test such a temperature and strain rate sensitive material. Machining induced effects however cannot be fully ruled out and so it is suggested that a small set of experiments be conducted to prove whether this is the case. Another reason as to why the complex test samples did not fail is the fact that although they are deformed to higher strains at similar strain rates as previous tests they experience this in short bursts, simulating the forging blows, and are held at high temperature between these blows. As a result several recovery mechanisms may be in operation allowing the material to accommodate such large strains.

Results from reproducing point 6 deformation are given in Figure 5.56 which plots the rotational displacement, desired temperature and measured temperature of the test. The desired temperature, derived from the FE model, predicts a temperature rise with each blow and is caused by deformation heating. Due to the high strain rates being imposed during the deformation the heating rates are equally large ranging from 14-58 $°Cs^{-1}$.
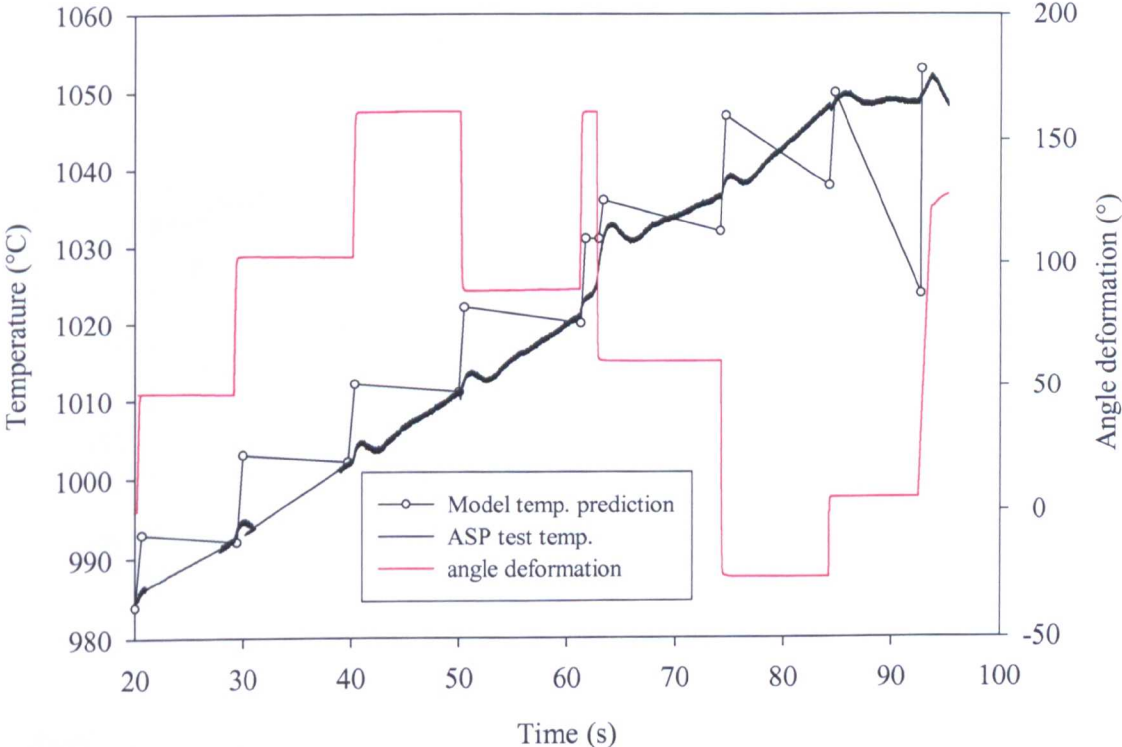
Figure 5.56 ASP reproduction of point 6 from forging model

Between each forging blow the material cools, slowly at first, but then gradually increases as this region of material flows closer to the surface of the component in the horizontal channel. The actual temperature during the test is always slightly behind that of the desired temperature as the response of the induction coil is insufficiently quick to respond to the high heating rates experienced at each blow. In calibrating the coil (before forging FE models were developed) only heating rates of up to 6 $°Cs^{-1}$

178

where employed and the rates calculated by the FE model predict rates of ten times this value. It is possible, with tuning of the coil's PID controller that such high heating rates could be reproducible in a controlled manner. The induction heater response does lag behind the desired temperature however it does always attempt to reach the target temperature and carries on heating when the model should be cooling. This response is always approximately 2 seconds late for each blow and results in an accumulated error of ~ 20 seconds which subsequently makes the whole test 20 seconds longer than it should be as the control system waits for all inputs parameters to reach their desired values. This would suggest that somewhere in the software the system will only wait for a short period of time to allow the response time to converge however it will move on through the programmed flow chart if this time period is up.
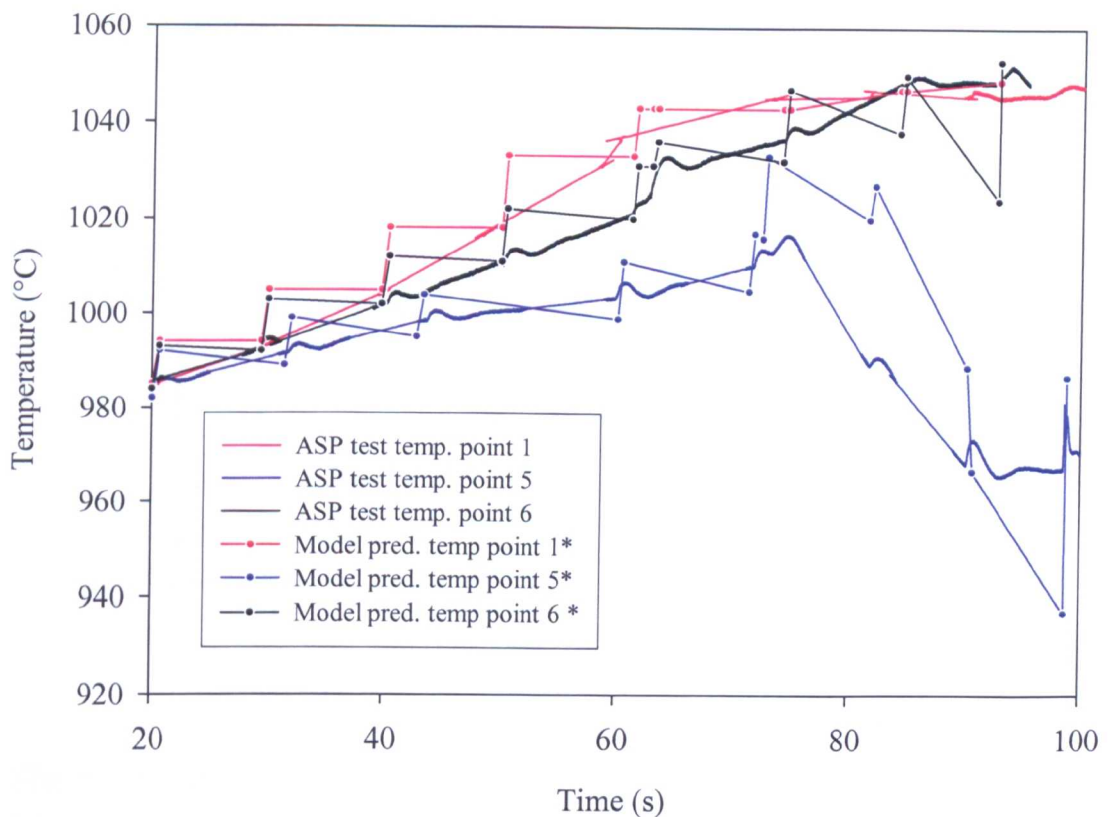
Figure 5.57 Desired temperature history as predicted by FE models (*corrected to coincide with the deformation) together with actual measured temperature during an ASP test for points 1, 5 and 6 in the forging

Figure 5.57 plots the desired temperatures predicted by the FE model together with the temperature of each ASP test corrected to coincide with each deformation. The net result is although the exact calculated temperature histories for all three points are not imposed, the overall trend in temperature change is successfully reproduced with a maximum discrepancy of 40 °C and with only +0, -5 °C error in final temperature. It is unlikely that faster response from the induction coil to accurately reproduce the

179

temperature history will have any significant affect on the microstructural evolution as temperature induced mechanisms (e.g. phase transformation) will simply not response quick enough.

The flow behaviour along with the temperature for point 1 tested in pure torsion is plotted below in Figure 5.58. The graph is divided with blue lines to represent the start and end of each forging blow. The numbers within these blue lines represents the strain rates experienced during each blow and are taken from the FE calculated values in Table 5.5.
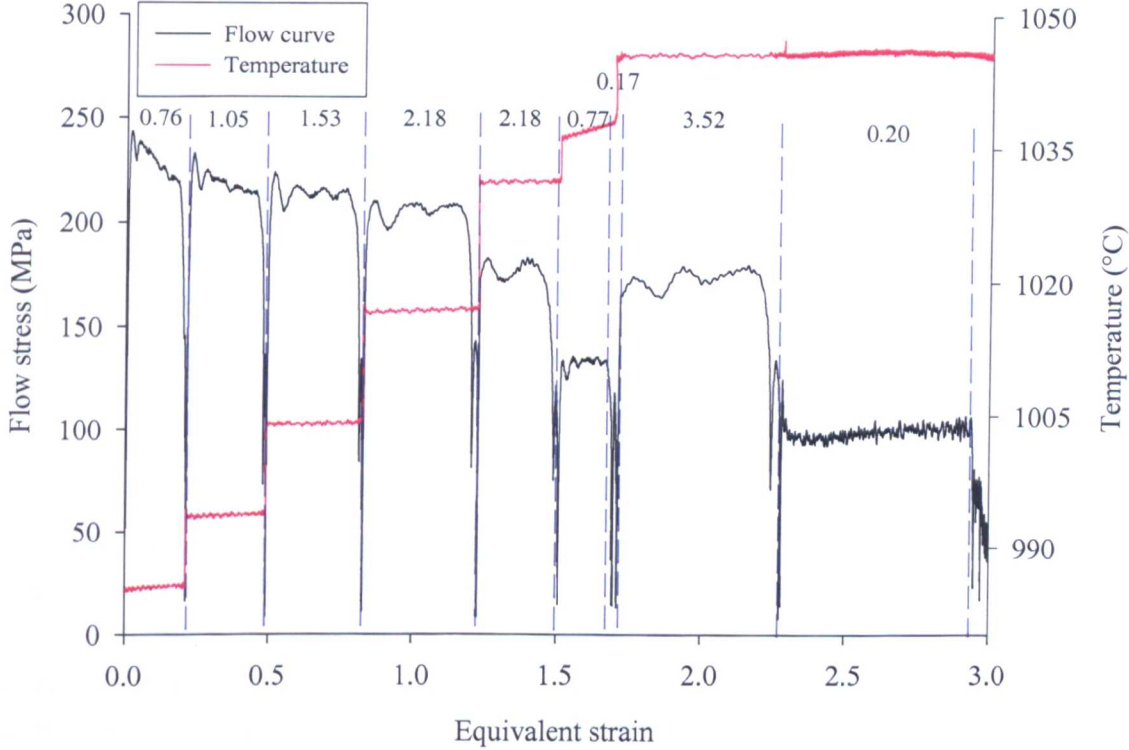
Figure 5.58 Flow curve and temperature for ASP test of point 1 in pure torsion. Blue dashed lines indicate each forging blow and the corresponding numbers represent the strain rate of the deformation

180

As observed in previous tests the material slowly flow softens during deformation. As the operation progresses the temperature increases and subsequently the flow stress slowly decreases. For the first four blows when the strain rates are of similar values then a single flow curve line could be plotted throughout suggesting that any microstructural mechanism (e.g. recovery, recrystallisation or phase transformation) has too low a rate or has insufficient driving force to evoke any measurable microstructural changes even at such a sizable equivalent strain. Even though the rate of heating is essentially linear, the flow softening rate decreases to zero by the end of the 4th blow. On the 5th blow the strain rate is the same as the previous and the heating rate remains unchanged, however the flow stress drops by 25 MPa and suggests that some form of recovery mechanism is active at this large torsional strain. On the 6th blow there is another drop in flow stress of 50 MPa as the material is quickly heated by 9 °C and deformed at a lower strain rate of 0.77 s^{-1}. The 8th blow is delivered at the highest strain rate of 3.52 and so the flow stress increases by 55 MPa however the material can now been seen to work-harden. This effect, although small, is also observed in the final 9th blow which is delivered with the lowest strain rate of 0.20 s^{-1} and results in no PID controller effects being imposed on the flow curve, only signal noise. It is impossible to say what is causing the drops in flow stress and the change in work hardening rates from these tests, however it is very likely that different microstructural mechanisms are in operation at high strains (blow 5) and at high temperatures & strains (blow 8). Further tests stopped at various intervals of the full test could be carried out to capture possible changes in the microstructure and possibly like the changes in flow behaviour due to the dissolution of alpha to beta grains.

Figures 5.59- 5.61 below plot the stress-strain curves for the complex strain path tests of points 1, 5 and 6 respectively using Equations 4.16 and 4.18. From Figure 5.59 for point 1 the peak flow stress of forging blows 1-3 drops as the temperature increases due to deformation heating. Over blows 1-4 it is not possible to superimpose a monotonic flow curve as is possible for point 1 tested in pure torsion (Figure 5.58) due to blow 3 exhibiting a lower peak flow stress due to a reverse in torsion direction. Comparing blows 4 and 5 which share the same strain rate of 2.18 s^{-1}, blow 5 exhibits a lower flow stress but is delivered at a temperature ~10 °C hotter that the previous blow. Both blows 6 and 7 impose very small strains and so can not be distinguished in this plot. For both blows 3 and 8 the torsion direction is reversed. As mentioned blow 3 only exhibits a drop in flow stress, unlike blow 8 that shows a reduction in work hardening rate at the start of the deformation. Overall the purely torsional and complex strain path flow curves are very similar in terms of the flow stress pattern. However, values of stress differ due to fact they are calculated acting over difference cross sectional areas if the cylindrical gauge length is tested in torsion or axial displacements.
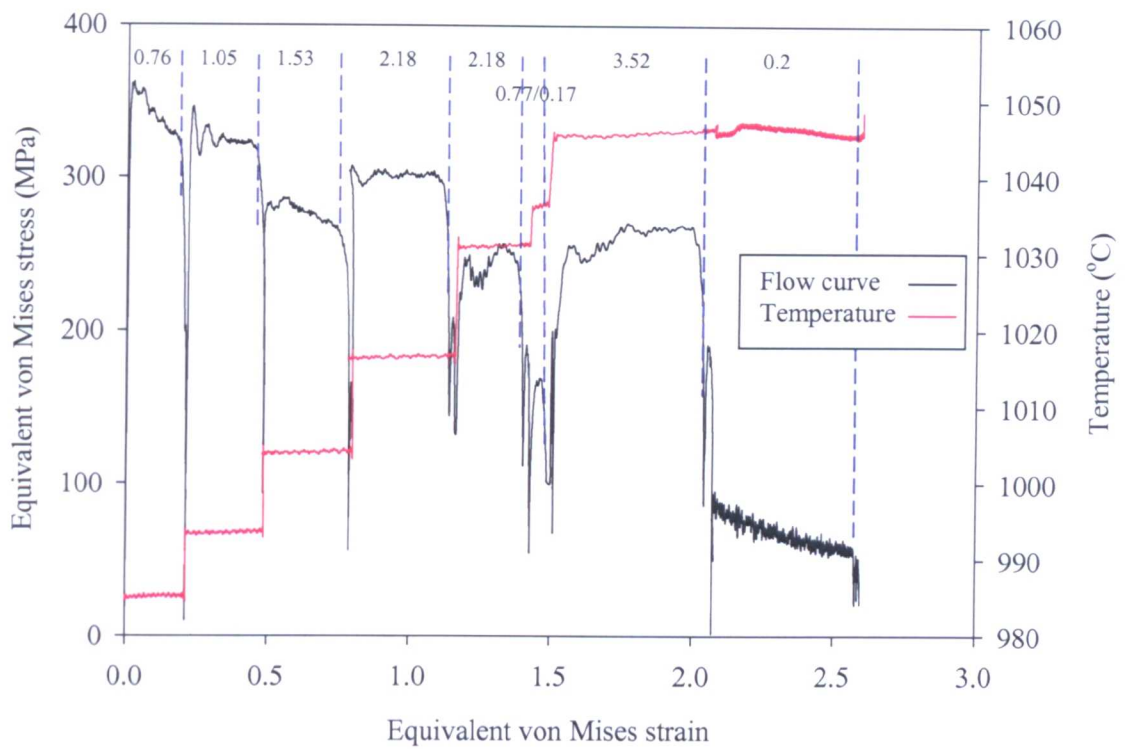
Figure 5.59 Equivalent von Mises stress-strain flow curve for strain path reproduction of point 1. Displayed numbers indicate the strain rate for each forging blow
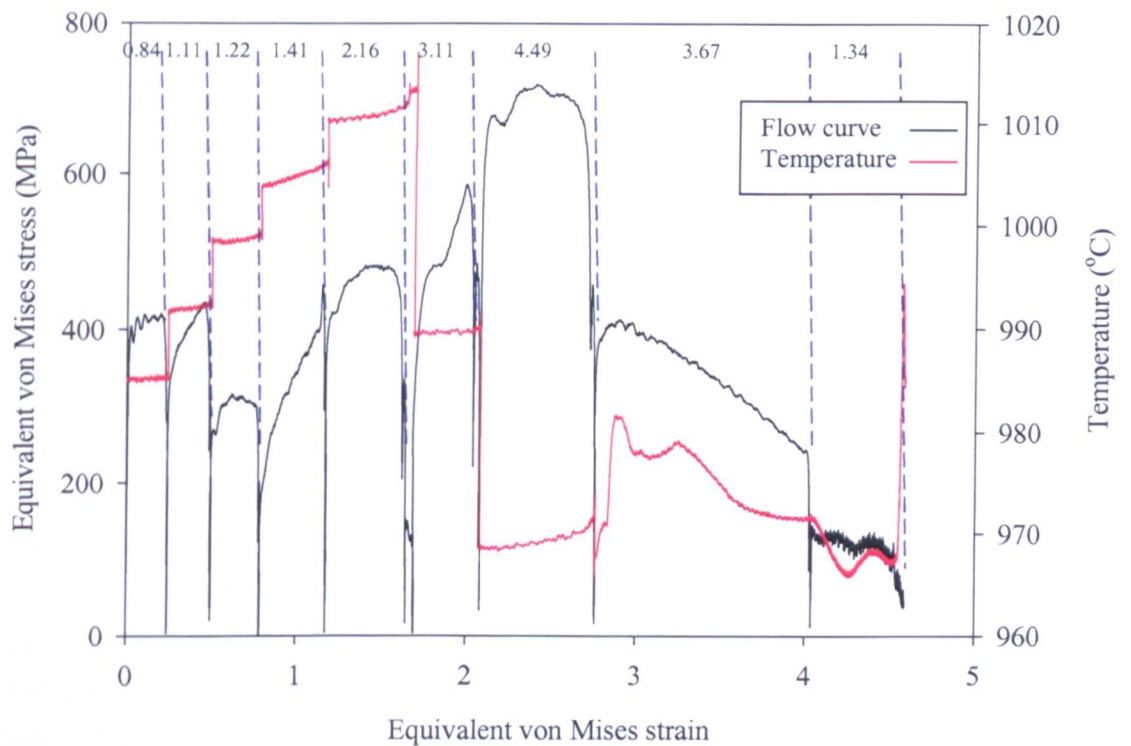
Figure 5.60 Equivalent von Mises stress-strain flow curve for strain path reproduction of point 5. Displayed numbers indicate the strain rate for each forging blow
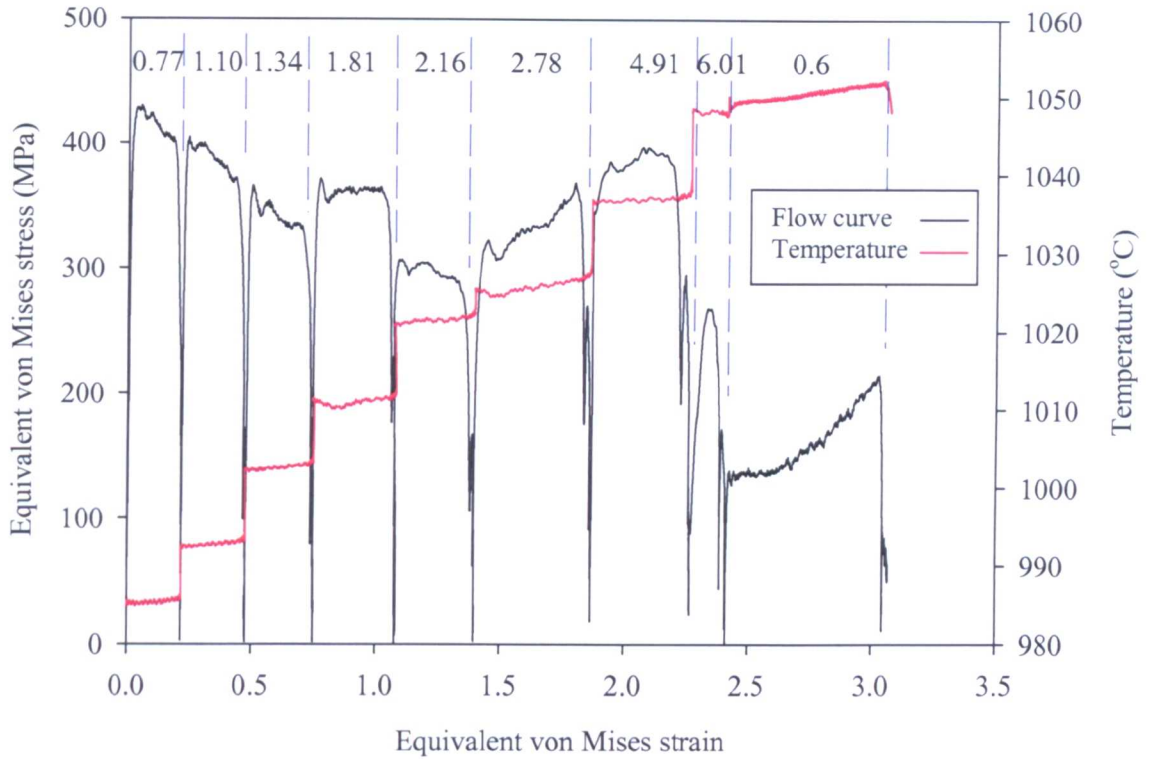
Figure 5.61 Equivalent von Mises stress-strain flow curve for strain path reproduction of point 6. Displayed numbers indicate the strain rate for each forging blow

Considering point 5 stain path deformation by combing data from Table 5.15 and Figure 5.60 it can be seen that after blow 1 the direction of torsional strain is reversed and a slow rate of work hardening follows. This same slow rate of work hardening is observed through all blows 2-6. The flow stress displayed during blow 6 is lower than excepted as it is accompanied by and increase in strain rate and a simultaneous drop in temperature of approximately 27 °C and so would suggest a mechanism has caused the material to soften. Blow 7 exhibits the highest flow stress of point 5's deformation history and that o fall points analysed. This is due to the high strain rate of 4.5 s⁻¹ and the lowest temperature of 970 °C brought about by die chilling and the point being force out and away from the centre of the billet where the majority of the deformation is accommodated (and deformation heating generated) as can be seen is Figure 5.38. Another possible recovery mechanism is highlighted during blow 8, where another high strain rate deformation (3.7 s⁻¹) is applied at a similar temperature as the previous blow. However, the peak flow stress observed for this blow is approximately 400MPa lower than that of the previous blow. More evidence of an activated recovery mechanism is shown in the final blow where the strain rate is similar to that experienced in blow 3 but the flow stress is lower, as is the deformation temperature.

Analysing point 6's flow curve in Figure 5.61, for blows 1-3 the flow stress gradually decreases as the temperature increases due to deformation heating even though strain

rate is increasing. Again, these first three deformations could have a monotonic flow curve imposed on them showing no recovery mechanism is active at these low strains. During blow 4 there is an increase in strain rate and a small concurrent axial strain applied (see Table 5.16), resulting in a small increase in flow stress. The direction of the torsional component of strain is also reversed (compared to the first 3 blows) however a decrease in the work hardening rate is not observed. The fifth blow does not induce any significant stain path change and the deformation is applied in pure torsion and combined with an increase in temperature causes the flow stress to drop with respect to blow 4. For blows 6&7 both axial and torsional strain components are reversed and the strain rate increases to 2.78 and 4.91 respectively. This causes the flow stress to increase and the rate of work hardening at the beginning of the each deformation is reduced. Despite blow 8 possessing the highest strain rate of the entire deformation its peak flow stress is 125 MPa lower than that of blow 7 and suggests a critical strain has been reached to instigate a recovery mechanism in the material.

During torsion testing the strain and strain rate vary along the radius of the cylindrical sample, with the outside of the material experiencing gradually increasing values of strain compare with material near the samples centre. Thus, material long the radius will have varying amounts of work imposed on it. When subsequent (or concurrent) strains are then applied in the axial direction, strain is applied uniformly over the cross sectional area of previously non-uniformly strained material. Thus, the complexity of strain path research and the difficultly in quantifying the flow behaviour of such a behaving alloy under equally complex dual component strain path changes is highlighted and that extensive additional testing is required to provide insight to the microstructural evolution and mechanisms.

Previously it has been shown (Figure 5.45) that the induction coil does not react quickly enough during the high heating rates experienced by the material during the forming operation. Figure 5.62 shows the experimental reproduction of the cooling rates predicted by the FE model of the air cooling of the forging after the final shaping operation as seen in Figure 5.41. After the final deformation was applied to the sample a final command in the programme was given to the induction coil in the form of a look up table of desired temperature-time response. Initially the heat command PID successfully matches the desired temperature for the first 75 seconds with a $\pm 3°C$ error. After which, the temperature then falls linearly at a faster rate than the desired value. The difference in the two temperatures when the material should be cooled from the α/β to the α phase field (as highlighted in Figure 5.62) is 18°C resulting in the sample leaving the α/β phase field 25 seconds too soon. Although the exact cooling rate is not accurately reproduced after the first minute and a quarter the cooling rate imposed on the material is considerably slower than that of a natural (non-induction heater assisted)

air cool and provides an suitable approximation of the industrial cooling process to be viable for microstructural evolution investigation.
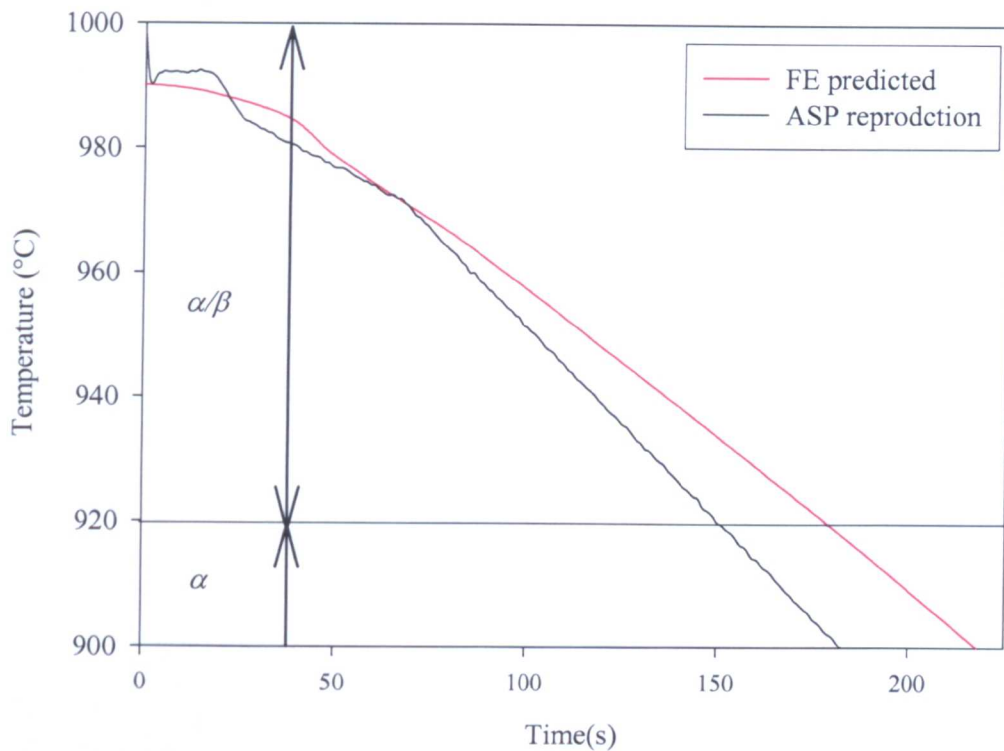
Figure 5.62 Desired forging cooling rate and the reproduced cooling rate for point 1 carried out on a Ti-6Al-4V sample

This result highlights another incident where a process controller simply failed to respond to the changes in the system quickly enough and error is introduced into the test. It seems that in terms of temperature, torsional and axial displacements the ASPII machine will produce desired test results once each of the corresponding controllers have been tuned. However, under high rate dynamic changes or multiple command input signals the machine simply becomes overwhelmed in processing such signals. The result is control lag on some or all PID controllers and the machine begins to drift away from the desired response and steady state errors are introduced. This is observed in many of the results shown in this report whose affects range from 2-4 seconds in delays in torsional or axial actuator displacements (Figure 5.55) or similar lags in heating (Figure 5.56). A possible cause of the error could be insufficient CPU processing power which is unable to cope in real-time with the shear volume of information, or the control input signal cards sampling frequency for the control actuators is too low. Both of which imply that the machine hardware does not receive control information at a sufficient rate to carry out the desired machine response. It is proposed that before any subsequent high rate, multiple control command tests are carried out that a series of experiments are run to finely tune all PID controllers to a greater level and presented here.

185
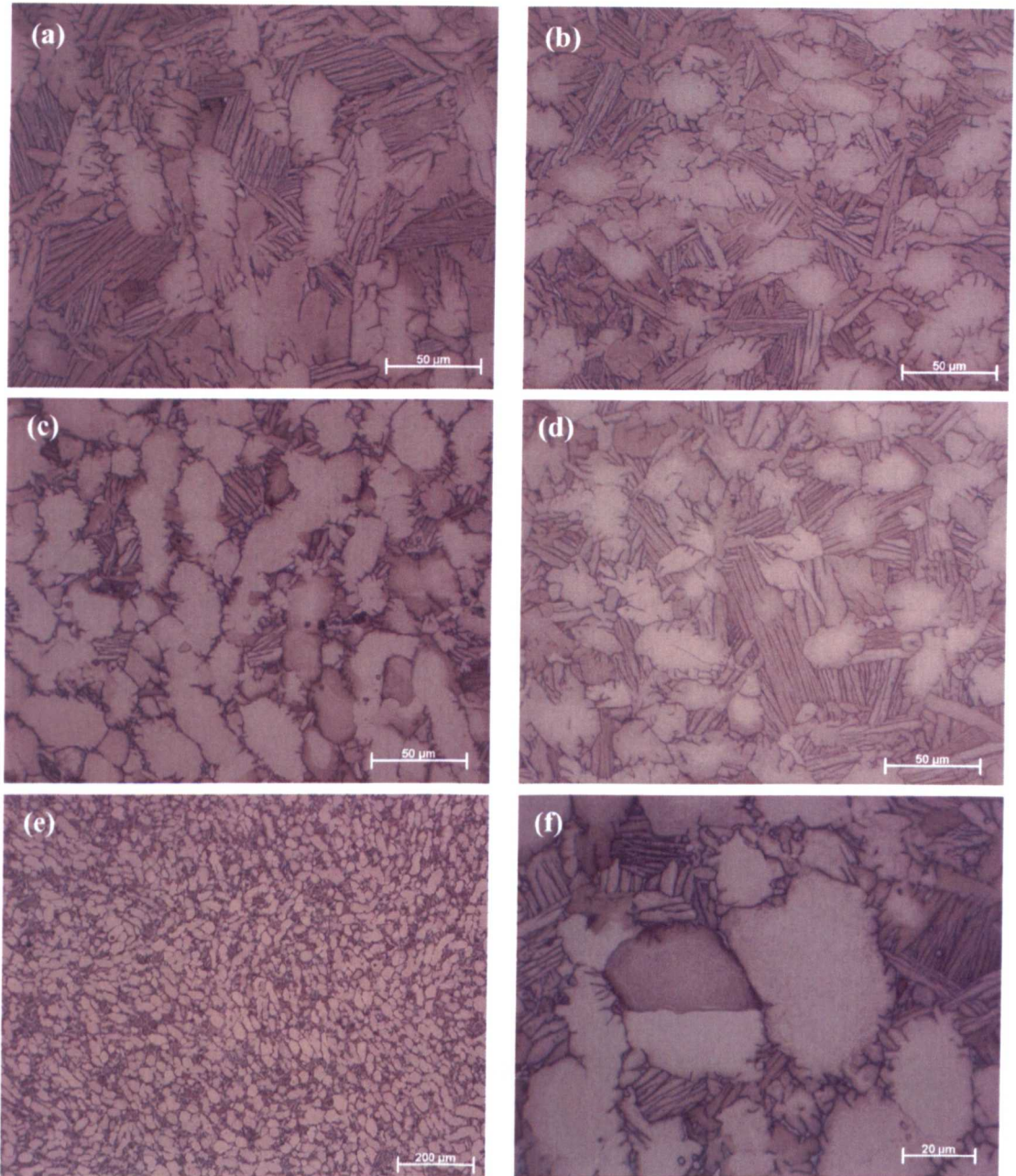
*Figure 5.63 Optical micrographs showing strain path tests of (a) point 1, (b) point 1
pure torsion, (c) point 5 and (d) point 6, together with lower (e) and higher (f)
magnification images of point 5. All tests followed by a simulated industrial air cool*

Once each controller is optimised to the highest degree and all high rate demands can be
precisely met then a second design of experiments of increasing complexity (and thus
demand on the CPU) can be implemented to determine whether the drifting from
desired control response seen in this work is due to insufficiently tuned controllers or
the machine hardware itself. Optical micrographs for strain path tests of point 1, 5 and
6 together with point 1 tested in pure (equivalent) torsion and followed by a simulated
industrial air cool are shown in Figure 5.63.

Comparing all the three points the resultant microstructures and morphologies differ, however this is not purely a result of differing strain path histories but also process temperatures. For example, Figure 5.57 shows that point 1 and point 6 exhibit similar thermal histories and the same final temperature of 1050 °C thus resulting in the same phase volume fractions. Point 5's final temperature however is only 990 °C due to die chill, thus demonstrates a higher proportion of α_P. The morphology of point 1 and 6 is very alike, both displaying feathery alpha morphology (together with coarse lathed (7µm) transformed beta), some equiaxed, some elongated combined with a heterogeneous orientation. Similarly, this is highlighted by the lower magnification in Figure 5.63(e) for point 5. The feathery alpha grain morphology is documented by other authors [90,26] and is cited as a possible mechanism in dwell fatigue, however due to the long high temperature hold times the serrated grain boundary is more prominent when, for example, compared to other work [90] in which a dedicated EBSD technique is developed to distinguish the feathery alpha. EBSD analysis (Figure 5.64) of point 1 fails to relieve the feathery alpha morphology, agreeing with Thomas [90] it exhibits the same orientation as it's parental α_P grain. In Figure 5.64 it is also possible to see there is very little misorientation within some grains where as others are entirely free of dislocation networks. This suggests a recrystallisation mechanism is active in reducing the stored dislocation energy during the prolonged hold at high temperature. The fact that some grains contain small amounts of misorientation may suggest that the recrystallisation mechanism was also active before the final deformation.

It can also be observed that individual laths within transformed beta grains all have the same orientation and from Euler contrast alone it is impossible to distinguish primary from secondary alpha.
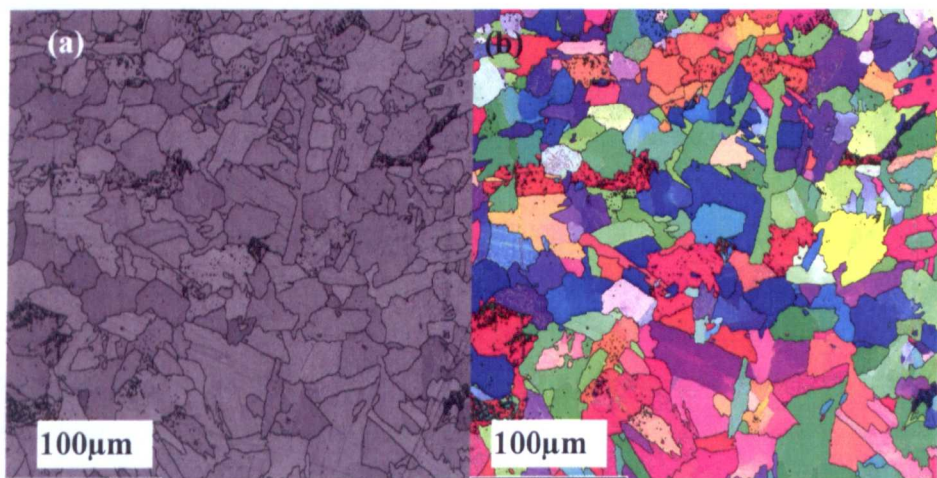
Figure 5.64 High-resolution EBSD texture scale orientation image maps using (a) band contrast and (b) Euler contrast for point 1. Black lines represent misorientation of >10° and grey >2°

From these results it is not possible to determine whether the heterogeneous orientation of the α_p grains is a result of regions of 'hard' and 'soft' orientations of similarly orientated grains giving rise to the differences in deformation and primary alpha grain orientation or whether it is a result of the changes in strain path direction that is causing a similar effect.

Although air cooling after strain path testing produces the microstructure of the forged component prior to heat treatment, recovery mechanisms mask the as-produced microstructure after the final deformation stage and as a result subsequent test specimens were water quenched. During microscope set up for EBSD analyses of the water quenched strain path samples an interesting feature was observed surrounding the α_p grains, which are shown below in Figure 5.65. Figure 5.65(a) shows a low magnification optical image demonstrating that all the α_p grains display the same phenomena. Figure 5.65(b) shows a high magnification SEM image revealing a 'beach' like structure with a rippled, speckled appearance and extends up to 5µm from the edge of the grain.
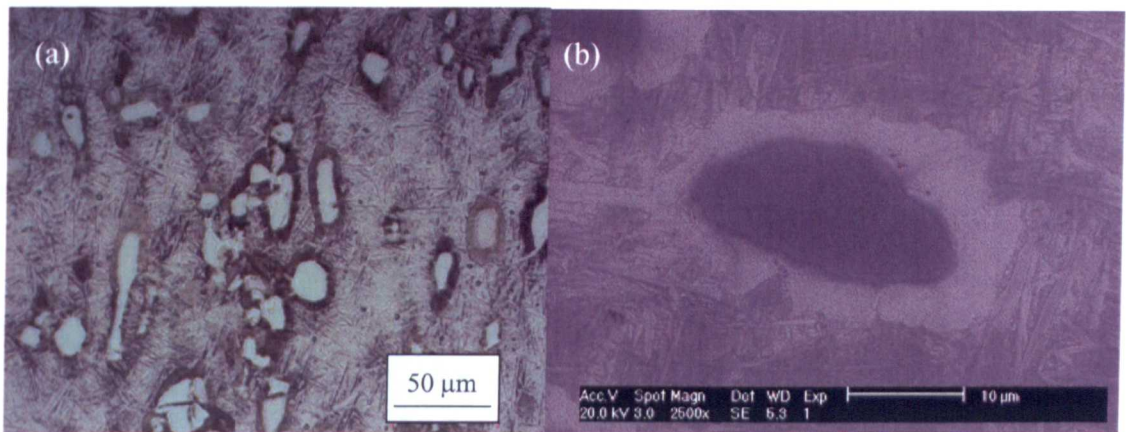
Figure 5.65 Optical (a) and (b) SEM micrographs of 'beach' structures surrounding primary alpha grains in strain path test of point 1 followed by a water quench

The structure is not visible when analysing EBSD data (Figure 5.67) suggesting that it has the same crystallographic orientation as the primary α_p grain it seems to originate from or that of the surrounding β grain. EDX analyses for the α_p grain pictured in Figure 5.65 are shown below in Figure 5.66. The alloying elements of titanium, zirconium, tin and aluminium were analysed and showed a uniform distribution with no element segregation in the α_p grain, the transformed β matrix or the 'beach' like structure surrounding the α_p grain. Even though the EDX analysis in Figure 5.66 does not identify element segregation of the main alloying elements within this region, the etch effect to highlight the 'beach' structure is most likely caused but small enough (undetectable) chemical differences or additional alloying elements than were not scanned for. The thermal history for this material begins at 990 °C (after a hold time of

5 minutes) and rises during the forming operation steadily to 1045 °C in just over 73 seconds. Referring to the beta approach curve for this alloy the percentage of α_P present at 990 and 1045 °C is 50% and 0% respectively. Thus, at the end of the test if the microstructure had time to reach equilibrium then there would be no α_P grains as the beta transus temperature had been exceeded. In fact Thomas [90], and other authors [4,140,141] all of who carried out beta approach curve work held samples at temperature for times in the region of 30 minutes to allow all α_P grains to transform to β grains. It is likely that the structure is a result of the α_P grains diffusing as the test temperature rises to form beta grains, however the sluggish nature of the $\alpha \rightarrow \beta$ transformation kinetics (when compared to titanium alloys such as grade 5 [142]) has not permitted full transformation before the material is quenched.

Whether the orientation of the 'beach' structure is inherited from the transformed β matrix or the parent α_P grain is unknown at this present time, however by employing the same technique devised in work done by Thomas [90] where an EBSD scanned area is revealed by subsequent etching, re-polishing and etching again the 'beach' structure could be revealed and compared to a corresponding EBSD map and thus reveal whether the 'beach' has a common orientation with the α_P or transformed β grain. In addition to this an interesting piece of work could be carried out to investigate such kinetics of transformation.
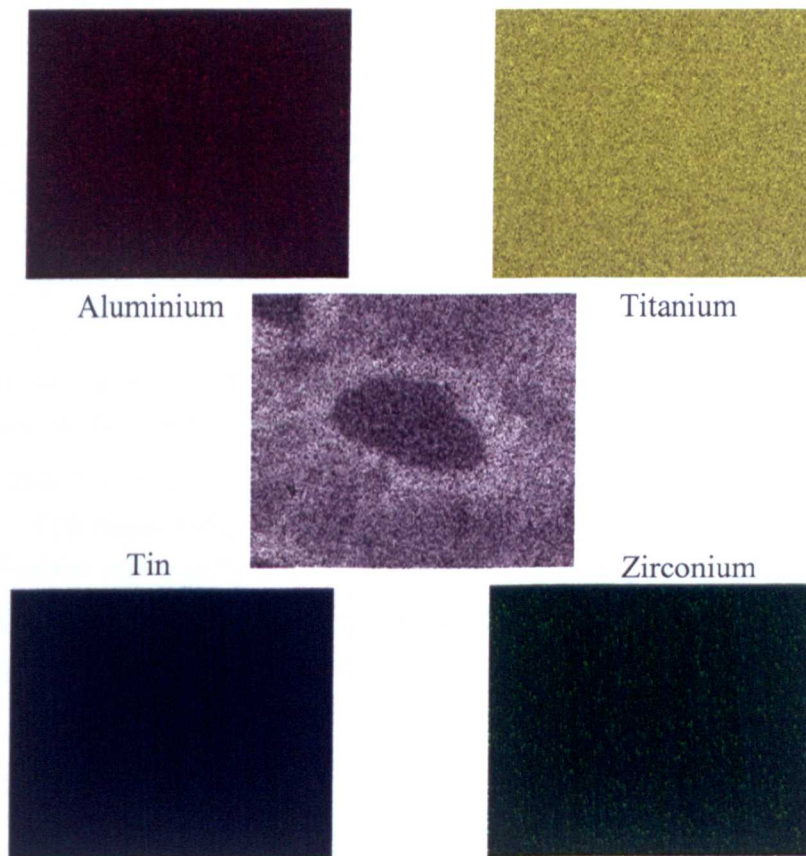
Figure 5.66 EDS maps of primary alpha grain (centre map) surrounded by 'beach' structure and the corresponding element maps

189

Strain path tests of point 1 and point 1 in pure equivalent torsion were carried out again but cooled by water quenching to capture the final 'forged' microstructure. Figure 5.67 presents band contrast maps for material deformed in simulating point 1's industrial strain path (a) and the same point deformed in equivalent pure torsion (b). Figure 5.68 presents the same data as shown in Figure 5.67 as OIM (Euler contrast) maps. In both the strain path and torsional tested material significant amounts of deformation is accommodated by α_p grains. For the torsional tested material it is clear to see elongation of the α_p grains parallel with the direction of principle strain. This is also true for the strain path tested material where the final deformation is a combined large positive axial and torsional deformation as shown in Table 5.14 and Figure 5.55. Even though the temperatures are higher towards the final stages of the two tests presented here, such results are in agreement with earlier work [143] conducted on simple strain path changes which can be seen in Section 5.3.3. This is in direct contrast to the AC material (Figure 5.63) where very little misorientation and subgrain formation within the primary alpha grains is observed. The substantial hold at high temperature due to slow cooling rate enables restoration and coarsening mechanisms to mask the direction of principle strain indicated by orientation α_p grains.

In the torsion tested material all primary alpha grains have sufficient dislocation networks to form extensive subgrains and this substructure and subgrains are quite homogeneous. In the strain path tested material the misorientation within the primary alpha grains is heterogeneous with some grains containing no dislocation substructure, some display regions of subgrains while others are fully fragmented into subgrains as in the torsion tested material. No twinning is observed in any of the tests unlike the forward-reverse strain path tests done previously (Section 5.3.3). this may be attributed to an increasing number of active slip systems as the test temperature gradually increases or that each blow did not impart sufficient strain to cause a grain to twin and recovery during the delay time before each blow was sufficient to reduce stored dislocation energy so that the accumulating strain for subsequent blows also did not generate any twins. Mean misorientations angles of $3°\pm_2^5$ are observed in the torsional tested material with significant numbers of subgrains with high angle grain boundaries of 15-85°. The mean subgrain size in the torsion material (measured in grain A) is $3\pm_2^9\,\mu m$. For the strain path test mean misorientation angles of $3°\pm_2^8$ are measured in grain F. High angle grain boundaries of 45 and 25° are measured within grain E, and a mean sub grain size of $6\pm_3^7\,\mu m$ was measured in grain G for torsion tested material.
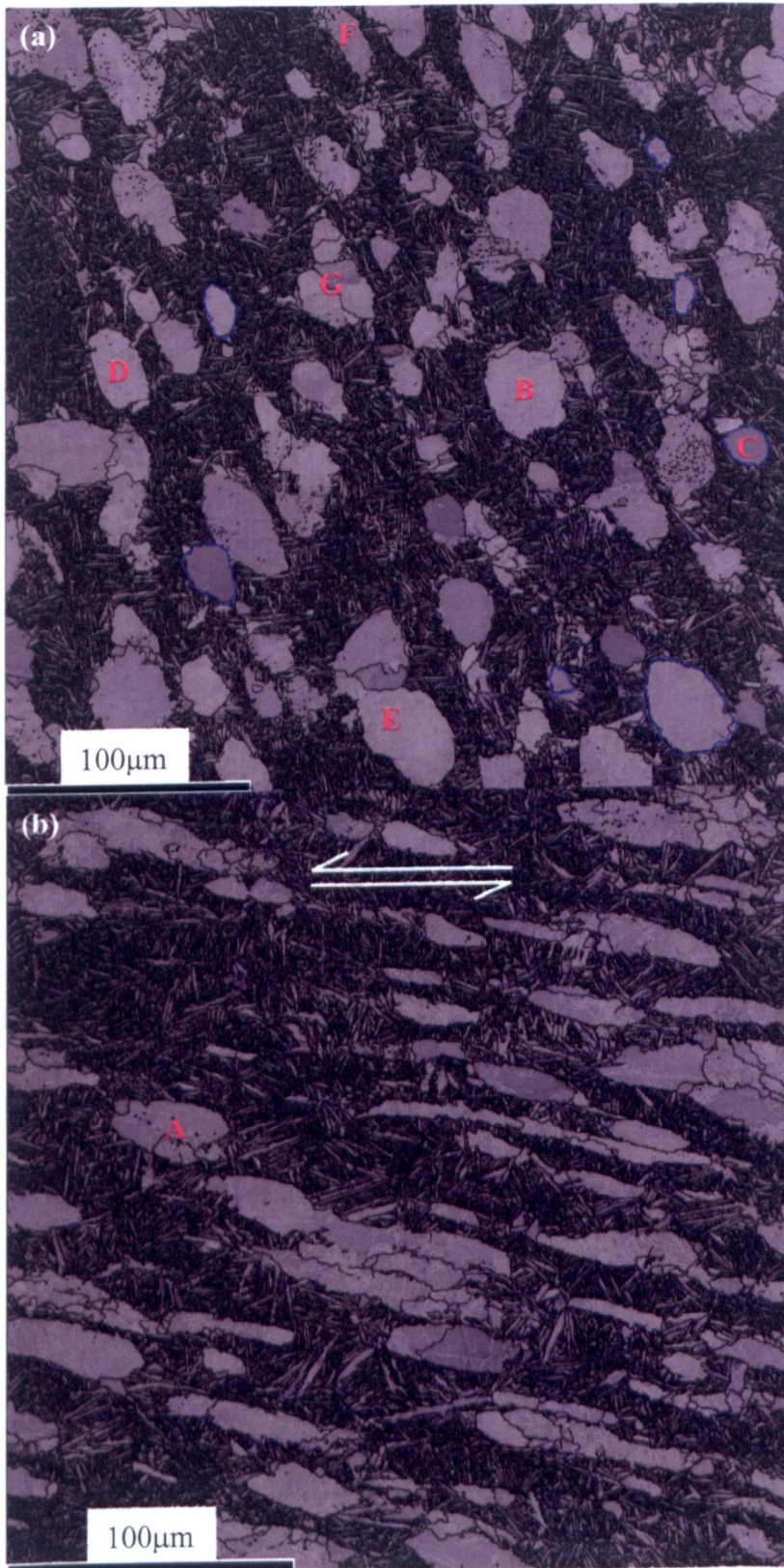
Figure 5.67 Band contrast of point 1 industrial strain path (a) and point 1 pure torsional deformation (b). Blue contours indicate substructure free grains, and lettering, individually analysed grains. Black lines represent misorientation of >10° and grey >2°

The smaller subgrain size in the torsional tested material would seem to suggest that more dislocation networks and thus energy is stored within the α_p grains when compared to the strain path test and show that dislocation density is reduced in the strain path material most likely by dislocation annihilation as observed in previous tests (Section 5.3.3). This would lead to a reduced driving force for the grains to reduce their energy states via a recovery/recrystallisation mechanism and behave in a similar fashion to work conducted by McLaren and Sellars [81], where rolled feedstock does not recrystallise as predicted at the surface due to changes in strain path angles as thus some dislocation annihilation.

In the industrial strain path tested material α_p grain deformation and substructure are heterogeneous with some equiaxed grains containing zero (or minimal) misorientation and some completely free of substructure. Mean misorientation angles of $0.5° \pm_{0.5}^{0.5}$ are measured in grains B and C. Figure 5.67(a) highlights such grains with a blue contour. Despite some elongation parallel to the direction of maximum deformation these seemingly strain free grains are very round and equiaxed. This is not present in the torsional tested material, with all the primary alpha grains containing significant misorientation. By observing the substructure in the reconstructed prior β grains (Figure 5.69) it is possible that more subgrain boundaries are present around these strain free α_p grains which could indicate that these grains have been of hard deformation orientations throughout the deformation and forced the softer β phase to accommodate the strain imposed on the material. This seems a more realistic explanation to these particular α_p grains reducing the stored dislocation energy within them by a form of recovery or recrystallisation as the same mechanism should also operate in the torsional tested material as this is subjected to a greater amount of net strain. However, it is recognised that this is a small subset of data and additional investigation should be carried out to confirm or disprove this theory.

Figure 5.69(a & b) show beta reconstructed OIM maps for the strain path and torsional tested material respectively. The method utilised for such maps has been developed by Davies et al [144] who devised a method to automatically reconstruct the parent beta microstructure from the inherited secondary alpha phase microtexture obtained by EBSD analysis. This is carried out in four steps, firstly, separation of the primary and secondary alpha phases by applying average band contrast to both phases where the lightly coloured α_p grains are distinguished from the darker transformed beta grains. Additional steps are employed for the user to separate any variants on their size and resolve any discrepancies. Secondly, a grain reconstruction procedure is used to determine the extent of each parent beta grain. Each grain is reconstructed by examining misorientations between neighbouring secondary alpha pixels to determine whether they belong to the same variant or different variants inherited from the same

Figure 5.68 Texture scale orientation image maps using inverse pole figure colouring of point 1 industrial strain path (a) and point 1 pure torsional deformation (b). Black lines represent misorientation of >10° and grey >2°

193

grain. Pixels are deemed to form the same variant if the misorientation is less than 3°. Pixels from different variants are deemed to be inherited from the same parent grain if both the angle and the axis of the misorientations are close to the 5 specific misorientations that occur between secondary alpha variants inherited from the same parent grain [145]. To determine the beta orientations for each secondary alpha variant all misorientations along the boundary between it and neighbouring variants in the same parent grain are calculated. Each of these experimental misorientations will be close to 1 of 11 remarkable identities [146]. The closet remarkable identity is assigned to each misorientation. A more detailed description of the technique is given by Davies *et al.* [144] who's work draws on earlier work conducted in the field by Gey and Humbert [145,146].

Comparing both tests in Figure 5.69(a & b) there are considerable differences between the two reconstructed beta grain structures. Of the subgrain boundaries formed in the beta phase few are greater than 10°, with most less than 2°. The neighbouring grains which have formed distinct high angle grain boundaries display two very different orientations rather than a small rotation of the crystal orientation as observed in the lower angle grain boundaries. However, this is also true of the strain path tested material. In the equivalent torsion material the large deformed β grains containing substructure can be seen to be pancaked across the torsional axis inline with the maximum principle strain and contain very little low angle grain boundaries and misorientation within the grains, especially when compared to that seen in the harder, lower stacking fault energy primary alpha grains. Even though the primary alpha grains accommodate a sizable proportion of the strain the majority of the plastic deformation takes place within the softer BCC β phase. Thus the lack of dislocation networks and subgrains within these parent β grains combined with the large amounts of plastic strain would suggest a recrystallisation mechanism is in operation, producing the larger dislocation free grains. Dynamic recrystallisation is observed for the same alloy by other authors [144,147]. Vo *et al.* [147] observes no recrystallisation below 1000°C and is very limited below the beta transus (1040°C) but does observe that the percentage of recrystallised material is increases with strain rate. Vo *et al.* [147] go on to mention that other authors have reported Timetal®834 displaying β recrystallisation during forging at temperatures near the β transus, at intermediate temperatures (950–1020°C) and at higher strain rates ($\geq 3 \times 10^{-3}$ s^{-1}) while others observed β grain size refinement through dynamic recrystallisation under all test conditions (900–1100°C and 10^{-4} to 10^{2} s^{-1}). Ding *et al.* [148], working on grade 5 titanium show that dynamic recrystallisation of the β phase and/or metadynamic recrystallisation did not occur in the (α+β) phase field under the experimental conditions (850-1050°C, 0.05-1 s^{-1}), but occurred in the β phase field; the degree of (meta)dynamic recrystallisation increased with strain rate.
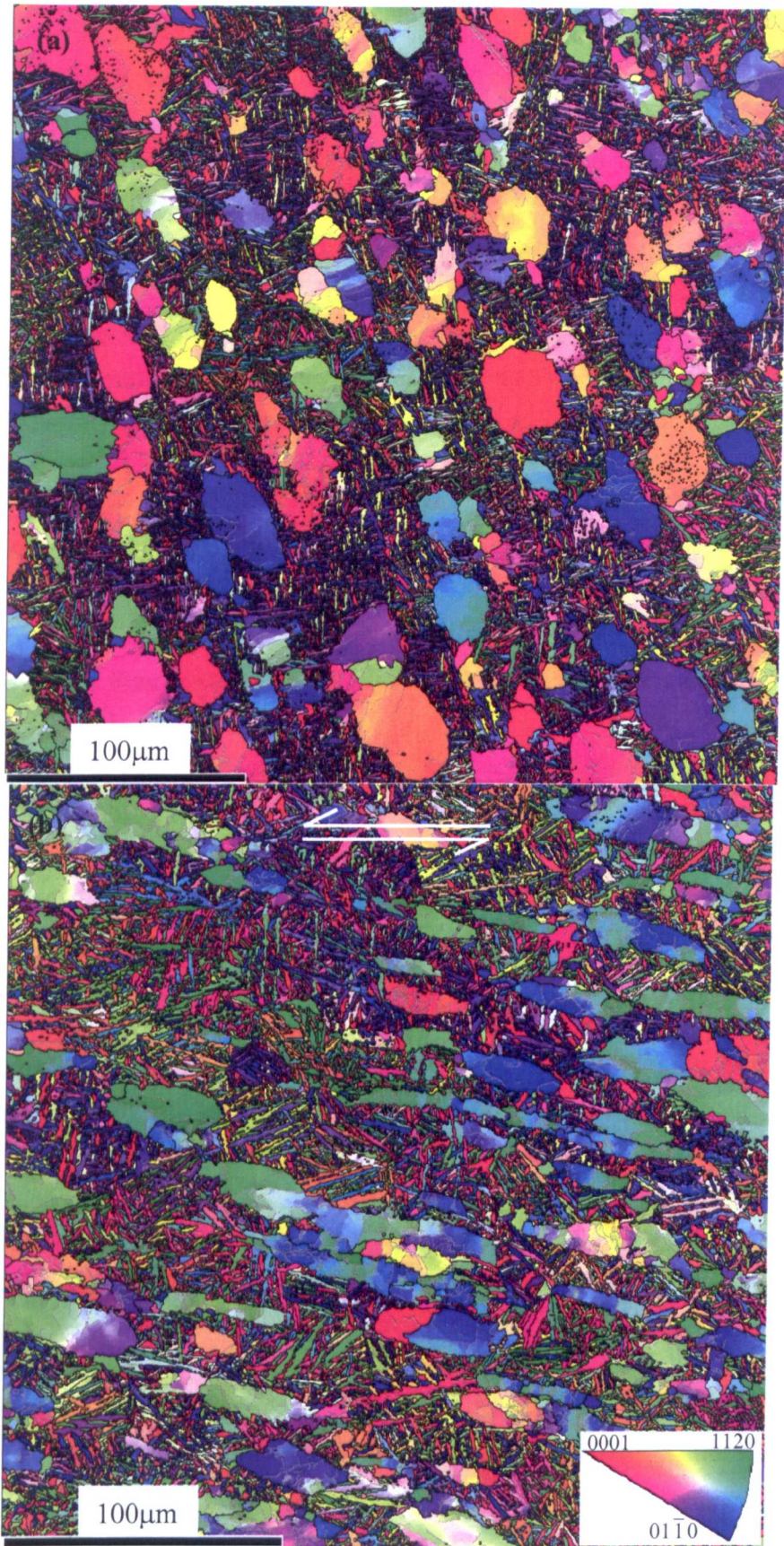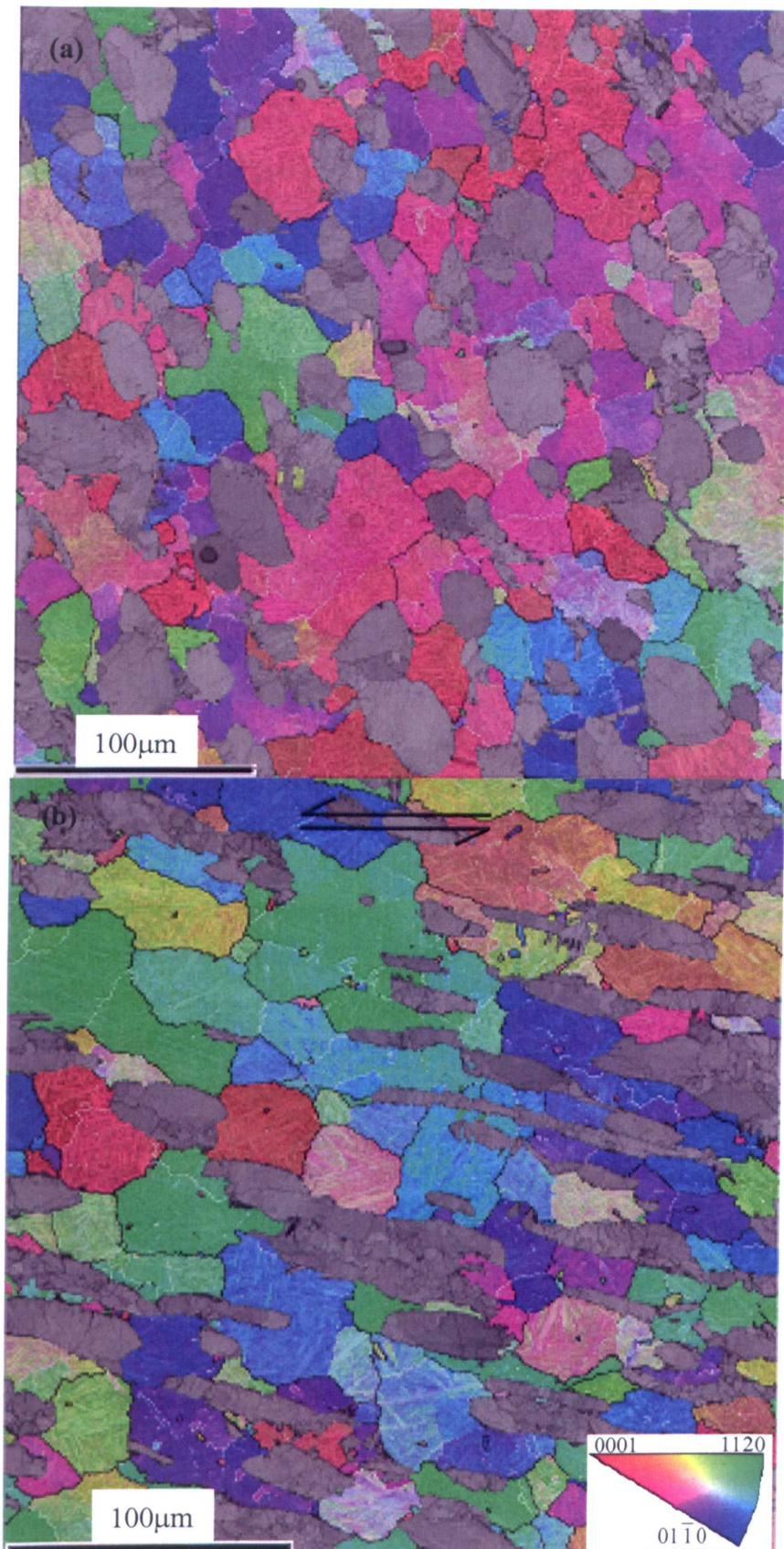
Figure 5.69 Texture scale orientation image maps using inverse pole figure colouring of point 1 industrial strain path (a) and point 1 pure torsional deformation (b). Black lines represent misorientation of >10° and grey >2°

Davies *et al.* [144] deform Timetal®834 at 1010°C and 2s^{-1}, and observe approximately 20 and 45% recrystallised β grains for 0.64 and 1.23 equivalent strains respectively. These recrystallised grains have a grain size of 10-20 μm and can be seen in Figure 5.70 where the α$_p$ grains are coloured grey and high and low angle grain boundaries are highlighted by grey and black lines which corresponded to misorientations of >5° and >15° respectively.
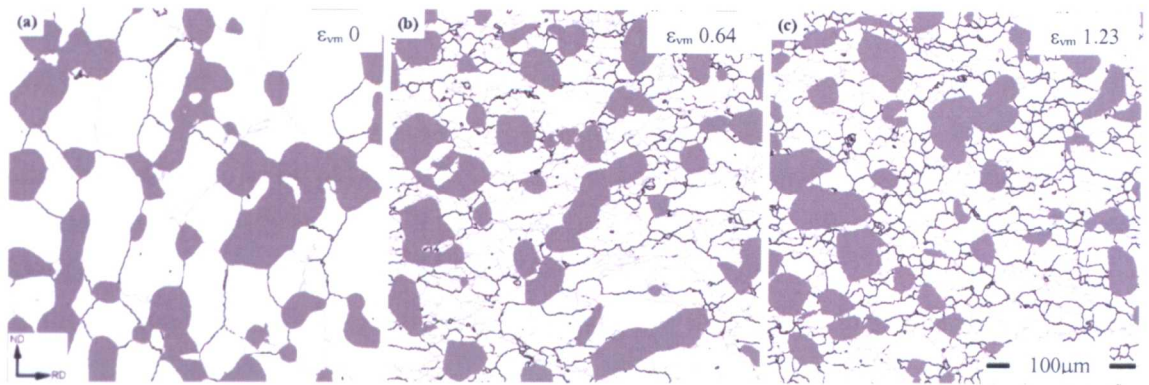
Figure 5.70 EBSD maps of reconstructed β phase (coloured white) with increasing (von Mises) strain levels, showing high and low angle grain boundaries [144]. Grey and black lines represent grain boundary of >5° and >15° respectively

From the Davies *et al.* [144] work it can be observed that the strain free recrystallised grains nucleate in a necklace like fashion typical of a microstructure that has undergone dynamic recrystallisation. This recrystallisation is heterogeneous which is indicative of the inhomogeneous nature of the β phase deformation due to the complex flow behaviour imposed by the harder α$_p$ grains. In this study of strain path effects, the β phase still acts as a continuous matrix at the tested temperatures, but it is difficult to directly compare this work (~50%α$_p$) to Davies (~25%α$_p$) where the β phase is a distinct continuous matrix. Thus, taking meaningful grain size measurements of the transformed β phase is not possible. One conclusion can be drawn from the grain size of both the strain path and torsion tested point 1 when comparing to Davies *et al.* [144] is the substantially larger grain size of the transformed β phase with some grains 80-100 μm in diameter, but again this is highly heterogeneous with smaller recrystallised grains (~20 μm) also present. Thus, there is evidence showing that there is significant β grain growth due to the longer deformation times when compared fast plane strain compression tests.

It seems likely that the test conditions (temperature, strain and strain rate) applied in conducting the complex strain path tests would be appropriate in activating both recovery and recrystallisation mechanisms in Timetal®834 and this is concurred by the level and sometimes falling steady state flow stress of the stress-strain curves. For example, Vo *et al.* [147] observe recrystallisation taking place at temperatures near to

the β transus and increasing with strain rate are the same conditions of the final forging blows for both points 1 and 6 which have final test temps of 1045-1050°C respectively. In addition to this, the pure torsion test of point 1 applies equivalent strains of 3, almost twice that of Davies *et al.* [144] and so substantial recrystallisation must take place during the presented complex strain path tests, especially with high temperature hold times in between forging blows.

The degree to which the torsional PID controller has been tuned may not be high enough and as a result maybe masking the oscillations in the flow curve that dynamic recrystallisation produces. For example thermal activation of slip systems induced by deformation heating may not be the only attributing factor to the flow stress drops observed in the stress-strain curve for the torsional tested material (Figure 5.58) especially for the flow stress drop between blow 4 and 5 where the strain rates are identical and there is only a small difference in temperature.

In the torsion material there are well developed high angle grain boundaries dividing the larger transformed β grains, some of which also contain well defined subgrain boundaries. In contrast, the strain path tested material exhibits substantially less high angle grain boundaries >10° but does contain more misorientation and subgrains boundaries >2°. This would seem to suggest that dynamic recrystallisation is less prevalent in the strain path tested material compared to the torsional tested. It seems plausible that reduced total net strain as well as enhanced recovery due to full reversals in dislocation motion (i.e. annihilation) during the complex strain path deformation results in a microstructure of lower accumulated dislocation energy and thus driving force for subsequent recrystallisation.

5.5 Conclusions

FE models of axisymmetric compression tests demonstrate excellent agreement with measured temperature changes and reproduced the deformed shape of the samples, thus demonstrating accurate calculation of the strain distribution within. Combined with good agreement between the measured and modelled tool force, this signifies the constitutive model is representative of Timetal®834 under the analysed test conditions. Analysis of input parameter sensitivity shows that the models are largely unaffected by the remesher angle and both tool and environmental heat transfer coefficients chosen. The heat transfer coefficients effects are only prominent at the very surface of the material and do not largely affect the main deformation zones with the workpiece. The mesh density and friction coefficient have been shown to have the largest influence on FE model output.

Thermal modelling of an ASPII sample based on both analytical analysis of heat transfer coefficients and experimental data has produced very accurate air cooling curve predictions. The information gathered from parameter analysis of simple axisymmetric compression tests has been successfully applied to model the first two stages of a three stage industrial aerospace titanium forging. Three key points of interest within the forged component were highlighted and their deformation history throughout the entire forming process was recorded. Comparing the calculated cooling rates for an industrial sized forging air cool and a laboratory air cool there is a sizable difference between the two definitions resulting in very different microstructures. From the deformation data derived by the FE models equivalent axial and torsional strains and strain rates have been calculated to reproduce the forging process within the laboratory using the ASPII machine.

During thermal calibration the ASPII machine has demonstrated its ability to accuracy heat at desired rates up to 6 °Cs^{-1}. The temperature gradient over the entire length of an ASPII sample has been measured and a relationship derived to calculate the centre gauge length (test) temperature from the value of the control temperature over the range of 400-1100 °C. Heater control issues when operating under load control have been solved. The torsional and axial PID controller values have been successfully tuned to enable high strain rate deformations and direction reversals up to rates of 10s^{-1}. Under certain high rate/demanding testing conditions the ASPII machine introduces some experimental error in the form of lag. The overall response of the ASPII machine demonstrates it is capable of reproducing very complex thermomechanical processes to enable meaningful microstructural evolution investigations.

Timetal®834 when subjected to a full strain reversal under industrial hot working conditions undergoes the typical Bauschinger effect with a significant drop in flow stress, however there is no significant increase in work hardening rate following the reversal. α_p grains when subjected to torsion elongate in the direction of principal tensile strain and are returned to their equiaxed structure on full strain reversal. Upon reversal there is significant reduction in the accumulated misorientation within the α_p grains. However, both large strains and severe changes in strain path do not break down the inherited clustering of similarly orientated α_p grains.

The laboratory simulation of strain path changes at three points within an industrial hot closed die forging of an advanced titanium alloy has been successfully undertaken. In simulating these complex strain path changes the stress-strain curves for tests of point 1, 5 and 6 exhibit erratic fluctuations in the flow curve and present a wider range of values for peak stress (325-700MPa) and total accumulated strain (2.6-4.5) when compared to that of point 1 tested in pure equivalent torsion. This highlights the complexity of strain

198

path research and the difficultly in quantifying the flow behaviour of such a complex alloy under equally complex dual component strain path changes. The simulated industrial air cool of the work piece contained a sizable error of 18°C difference in the desired response when cooling the material through the α/β phase field however such an error is not deemed to be significantly detrimental to the experiment. After strain path testing, cooling test samples under industrial air cool rates produces a fully recovered microstructure which exhibits feathery α_p grains and coarse transformed β laths typically of $7\mu m$ width. The three difference strain paths create differences in the deformation and orientation of α_p grains which is also heterogeneous throughout the material. EBSD data however, reveals fully recovered α_p and transformed β grains with no preferential orientation of α_p grains to the principle strain axis.

Water quenching of an industrial strain path sample yields a presently undocumented α_p grain morphology of a α_p grain surrounded by a 'beach' like structure which is believed though to originate from interrupted $\alpha \rightarrow \beta$ transformation. EBSD analysis does not reveal the 'beach' structure and thus suggests this it is of the same orientation of either the parent α_p grain and the β matrix.

In industrial strain path tested material α_p grain deformation and substructure are heterogeneous with some equiaxed grains containing zero (or minimal) misorientation and are completely free of substructure. This is not present in equivalently tested material where the α_p grain deformation and substructure are homogeneous. There is substantially more high angle grain boundaries $>10°$ observed in the transformed β phase of torsional tested material when compared to an equivalent industrial strain path test. This suggests that significant levels of recovery, by mechanisms such as dislocation annihilation, are in operation when the material is subjected to large angle strain path changes and as a result the driving force for recrystallisation of the β phase is reduced.

6. Conclusions

Due to the broad investigative natural of this study the following chapter is broken down in to six individual sub sections. Firstly, the conclusions that can be drawn from Chapters 2-4 are summarised. These are followed by conclusions derived from experimental results of FE modelling (both model validation and forging simulation), the ASPII machine and strain paths effects.

6.1   Literature review

- Titanium has proved to be a highly versatile, lightweight material and as a result is extensively utilised throughout aircraft structures. However it considered difficult to TMP when compared to more common engineering alloys and the unpinning science of such processes is relatively young.

- The issue of dwell fatigue is a very concerning matter and studies have shown that the near alpha alloys are particularly prone to such a phenomena due to damage accumulation on the basal planes within clusters of similarly orientated primary alpha grains [22-25]. Bache [19] showed that the issue is aggravated further by forging, a common processing route for such materials, by aligning preferential crystallographic planes (basal) that are susceptible to LCF damage. Thus, it is concluded that further work should be carried out to examine the effects of TMP on the LCF properties of near alpha alloys. Some of the work presented in this report aims at investigating the effects of strain path on the clustering of primary alpha grains and whether they can be used to break up such clusters.

- The directions for easy crystallographic slip in HCP single crystals are the three $\langle 11\bar{2}0 \rangle$ or $\langle a \rangle$ closed packed directions [27,34,35]. Prismatic slip $(10\bar{1}0)[11\bar{2}0]$ is always the easiest slip mode at low temperatures in α titanium containing small amounts of alloying elements [47].The three dominant sets of planes that contain this slip direction are the $\{0001\}$ basal, $\{10\bar{1}0\}$ prismatic and the $\{10\bar{1}1\}$ pyramidal planes. Crystallographic slip in titanium single crystals is commonly observed to occur on the prismatic $\langle a \rangle$ or basal $\langle a \rangle$ systems [36]. All of the easy $\langle 11\bar{2}0 \rangle$ slip directions are perpendicular to the c-axis and therefore do not produce any elongation or shortening parallel to c-axis. It is concluded that in order for a HCP crystal to fulfil the von Mises criteria straining in the c-direction is accommodated by slip or twin systems with $\langle c+a \rangle$ slip/twin directions [14,36,39] and the presence of oxygen and/or aluminium is effective in suppressing twining: thus, in the absence of twinning, $\langle c+a \rangle$ slip is required to

allow grains in a polycrystalline specimen to undergo an arbitrary shape change during plastic deformation [14].

- The CRSS for twinning to occur in titanium is magnitudes higher than that of slip and subsequently is not a very common deformation mechanism. Mechanical twinning typically occurs at lower temperatures, under 'hard orientation' loading or in high strain rate deformation (e.g. explosive forming).

- The EBSD technique is now sufficiently mature that it is able to generate very accurate and statistically meaningful texture data over reasonably short time periods.

- The principle of strain path and its definition has been introduced. Significant strain path angle changes can be observed in many different industrial TMP and many authors have shown this to have significant effects on the microstructural evolution of the processed material. The majority of the strain path work carried out has provide valuable insight to the deformation mechanisms in operation however these tests do not address:
  - Real strain paths
  - Engineering metals
  - Industrial process parameters
  - Sequential testing
  - Higher temperatures

6.2   Material Properties

- The data shows that many of the parameters to be used in FE modelling do not need to be defined as a function of temperature as variations are small over the processing temperature range.

- Many of the properties of titanium are not well established in the literature and so the information has been extrapolated based either upon available data or theoretical considerations. Examples of this are the specific heat capacity, which shows large amounts of scatter in the data, and the emissivity which is always notoriously difficult to predict. When extrapolations have been employed, the reasoning has been explained.

- Overall, the necessary information for modelling has been described. However, a model is only a reflection of reality and is only as good as the information provided to it. As a result any input parameter demonstrating uncertainty in its exact value will be evaluated with FE modelling; this will include effects of k and c_p.

- The flow curves of Timetal®834 have been calculated and show the typical behaviour of the material under various strain rates and temperatures. For the

purpose of FE modelling a mathematical empirical model has been developed based on the activation energy and method applied by Wanjara *et al* [95]. This model takes into account the initial model has significant error due to the lack of isothermal correction. A modified value of Q_{def} is therefore used which, with a degree of experimental error, is similar to that measured by this report and additional authors [90,96].

6.3   Experimental

- Three experimental methods have been successfully applied in this project: FE modelling, mechanical testing and electron microscopy.
- The FE modelling can be subdivided into axisymmetric validation experiments and industrial (forging) processing of titanium.
- Extensive work has been conducted on validation tests to ensure the validity of the complex forging models including checking the deformation behaviour, frictional affects and the heat loss from the workpiece. Results provided by this work have been compared with that measured during mechanical testing.
- FE modelling of the forging will yield the range of strain paths imposed during an industrial process with complex material flow.   The method of their extraction from the model and their conversion to a laboratory test is also shown.
- The mechanical testing can be subdivided into 'simple' strain path testing to investigate whether extreme changes in strain path (180° forward-reverse torsion) could be exploited to break up the clustering of similarly oriented primary alpha grains. The second 'complex' strain paths focused on replaying the of strain path angle changes that are induced in forging complex components.
- Initial work with the ASPII machine has aimed to produce parameters that enable precise control at high strain rates and temperatures together reproducibility.   The mathematical derivation behind all test definitions and material flow behaviour were also presented in this chapter.
- The preparation of optical and EBSD samples has been shown to be very rapid and reproducible when using automatic grinding and polishing machines. With respect to the best etchant, although the Krolls reagent produced superior contrast between the two different morphologies it is very dependant on chemical cleanliness and age and the working conditions. Etching times may vary widely when using ammonium hydrogen di-fluoride but as soon as bubbles are seen on the samples surface then the material is etched sufficiently.

6.4   FE Analysis

- Axisymetric FE models utilising equation 3.12 are shown to be in excellent agreement with axisymetric compression tests, provided a fine enough mesh ($\geq$200 elements) and a remeshing strategy is employed.

- Such models are able to reproduce measured deformation heating that is directly related to the plastic deformation imposed on the material. In addition to this the model highlights where and when the side surface of a sample folds over and become the top surfaces. This is seen on the small laboratory scale and the large industrial scale.

- Parameter sensitively analysis has shown that models are largely unaffected by the remesher angle and both tool and environmental heat transfer coefficients chosen. The heat transfer coefficients effects are only prominent at the very surface of the material and although can cause processing problems do not largely affect the main deformation zones with the workpiece with respect to strain distribution.

- The mesh density and friction coefficient have been shown to have the largest influence on FE model output. It has been demonstrated that the axisymetric models become mesh insensitive when an element density of 4.4 mm^{-2} or greater is used. The friction coefficient has a significant effect on the TEPS distribution not only at the surface of sample but also throughout the whole sample.

- Thermal modelling of an ASPII sample has been very successful and a very accurate air cooling curve prediction has been made based on combined analytical analysis and experimental data.

- The information gathered from parameter analysis of simple axisymetric compression tests was successfully applied to model the first two stages of a three stage industrial aerospace titanium forging.

- Three key points of interest within the forged component were highlighted and their deformation history throughout the entire forming process was recorded.

- In the software utilised in this work, it is not possible to simply track the deformation history of a desired node in a model when the remesher is active. Instead the user must manually track each point, which proves to be a laborious and time consuming task.

- The ranges of strains paths imposed on material during (complex geometry) closed die forging are varied throughout the multistage process and various points in the workstock.

- Of all the three points selected to be analysed very small strain path changes are imposed during the first stage of the billet breakdown forging.

- Points 1 and 6 essentially exhibit insignificant strain path changes during the first stage of the forging. Only when the work piece comes into contact with

203

corner sections of the lower die, which in turn imposes addition shear components of stain on the material, are significant strain path changes are generated.

- Slightly larger changes in strain paths are observed at point 5 as this lies in the shear band at accommodates large deformation strains in the same manor observed in axisymmetric compression tests in Section 5.1.1.

- For all three points strain path angle changes of 0-21° are calculated for the first stage of the forging.

- During the second stage of forging where the die geometry is considerably more complex than the first, the levels of strain path changes for each forging blow are very sizable. Here the changes in strain path angle typically range from a small 23° to the very large 159°.

- Comparing the calculated cooling rates for an industrial sized forging air cool and a laboratory air cool there is a sizable difference between the two definitions.

- From the deformation data derived by the FE models equivalent axial and torsional strains and strain rates have been calculated to reproduce these deformations within the laboratory.

6.5 Summary of the ASPII Machine

- The ASPII machine has demonstrated its ability to accuracy heat at desired rates up to 6 °Cs^{-1}. It is likely the machine can heat in a controlled manner at higher rates however this has not been tested in this work.

- The temperature gradient over the entire length of an ASPII sample has been measured and a relationship derived to calculate the centre gauge length (test) temperature from the value of the control temperature over the range of 400-1100 °C. It has been proved that this temperature profile is symmetrical over the gauge length (and the whole of the sample) and that any uneven heating of a sample with respect to vertical height can been observed and corrected by eye.

- The heater control issues of the induction coil shut off during testing and load cell interference causing samples to be crushed when operating under load control have been solved by changing the test control procedure and by introducing a negative feedback signal respectively.

- The torsional and axial PID controller values have been successfully tuned to enable high strain rate deformations and direction reversals up to rates of 10s^{-1}. The PID values to produce such results are given in section 5.2.2. Typical control response values for high strain rate torsional and axial displacements respectively are given below:

o	t_p	0.11s,	0.03s
o	t_r	0.05s,	0.01s
o	t_s	0.10s,	0.02s
o	M_p	2°,	0.1mm
o	e_{ss}	3%,	0.2%

- Under certain high rate/demanding testing conditions the ASPII machine does introduce some experimental error in the form of lag and in some cases (for example in temperature) these are quite substantial. However, the overall response of the ASPII machine demonstrates it is capable of reproducing very complex thermomechanical processes to enable meaningful microstructural evolution investigations.

6.6   Strain path effects

- Timetal®834 when subjected to a full strain reversal under industrial hot working conditions undergoes the typical Bauschinger effect with a significant drop in flow stress, however there is no significant increase in work hardening rate following the reversal.

- α_P grains when subjected to torsion elongate in the direction of principal tensile strain and are returned to their equiaxed structure on full strain reversal. Upon reversal there is significant reduction in the accumulated misorientation within the α_P grains.

- Both large strains and severe changes in strain path do not break down the inherited clustering of similarly orientated α_P grains. Thus, in order to eliminate this clustering effect, improvements in the upstream processing are required to refine the α_P clustering.

- The very complex nature of the calculated forging strain path changes yields equally complex flow curves for all three analysed points, to the point where no evidence for microstructural changes and mechanisms can be detected or interpreted.

- Cooling test samples under industrial air cool rates produces a fully recovered microstructure which exhibits feathery α_P grains and coarse transformed β laths (7μm). The three differenct strain paths create differences in the deformation and orientation of α_P grains which is also heterogeneous throughout the material. EBSD data however, reveals fully recovered α_P and transformed β grains with no preferential orientation of α_P grains to the principle strain axis.

- Water quenching of an industrial strain path sample yields a previously undocumented α_P grain morphology of a α_P grain surrounded by a 'beach' like

structure which is believed though to originate from interrupted $\alpha \rightarrow \beta$ transformation. EBSD analysis does not reveal the 'beach' structure and thus suggests this it is of the same orientation of either the parent α_P grain and the β matrix.

- In industrial strain path tested material α_P grain deformation and substructure are heterogeneous with some equiaxed grains containing zero (or minimal) misorientation and are completely free of substructure. This is not present in equivalently tested material where the α_P grain deformation and substructure are homogeneous.

- There are substantially more high angle grain boundaries >10° observed in the transformed β phase of torsional tested material when compared to an equivalent industrial strain path test, suggesting that significant amounts of recovery by mechanisms such as dislocation annihilation are in operation when the material is subjected to large strain path angle change and as a result the driving force for recrystallisation of the β phase is reduced.

- Large angle strain path changes may instigate recrystallisation of α_P grains by attempting to 'force' slip with multiple stress fields on energetically unfavourable 'hard' slip planes of the anisotropic HCP crystal when compared to equivalently tested monotonic deformed material. A similar mechanism is not observed in the transformed β phase due to its great number of favourable slip planes and high stacking fault energy. Thus, the β phase is able to easily accommodate the large strain path angle changes when compared to the α_P phase.

7. Future Work

This chapter considers the conclusions and overall findings of this study and suggests additional work to be carried out to fully explore any remaining unknowns unearthed during investigations. The further work is divided into high strain rate sample manufacture, additional PID controller tuning and microstructural analysis

7.1. High strain rate sample manufacture

Due to the high number of high strain rate sample failures by cracking at the gauge length – radii interface it is proposed that a series of experiments are carried out to determine whether the sample geometry, material or machining/manufacturing technique effects caused the failures of so many samples. Machining/manufacturing effects can be investigated but carrying out two sets of high strain rate tests on samples that had been conventionally turned (as presented in this study) and samples that have been ground to shape on the gauge length. It is envisaged that the ground samples will not cause any undercutting of the length and thus yield a smoother transition between the shoulder radius and the gauge length reducing the stress concentration and minimising the chances of failure. Before testing samples could also be checked for undercuts by using a dial gauge (before they are removed from the lath) or by CMM (Coordinate Measuring Machine).

Alternative sample geometries should also be investigated however they should still ensure the 2:1 radii to length ratio currently employed as discussed previously in Section 5.3.1. The transition between the shoulder radius and gauge length could be made more gradual with a larger radius.

7.2. Addition PID controller tuning

The PID tuning conducted in this study could be carried out in a more vigorously scientific manor with the use of a devised control theory (e.g. Ziegler–Nichols method), and attempt to more accurately control axial and torsional displacements at high rates. This tuning should include the heater command PID controller to enable faster response in order to eliminate the heating delay observed in the complex strain path tests and in the simulated industrial air cool, thus yielding more accurate representations of thermal histories and ensuring the correct microstructures are generated, (for example in the case of Timetal®834 the correct percentage of phases are present).

It is proposed that before any more high rate, multiple control command tests are carried out that a series of experiments are run to finely tune all PID controllers to a greater level currently presented here. Once each controller is optimised to the highest degree and all high rate demands can be precisely meet then a second design of experiments of increasing complexity (and thus demand on the CPU) can be implemented to determine whether the drifting from desired control response seen in this work is due to insufficiently tuned controllers or the machine hardware itself.

7.3. Microstructural analysis

The combined time limit and broad scope of work presented in this thesis did not allow for the investigation of microstructural evolution throughout each step of the modelled forging operation. It is proposed that by utilising the same experimental procedure as presented in this study that one of the same strain path histories is replayed again and quenched after each successive forging blow to enable the investigation of microstructural evolution and related this to the strain path and previous deformation history applied. This could also include additional work to investigate the effects and types of recovery mechanisms in operation during dwell times (brought about by forging hammer rise times) and long period (industrial) air cooling.

The 'beach' type structures surrounding primary alpha grains as discovered in Section 5.3.4 suggests incomplete transformation of the primary alpha grains to beta phase as the temperature of the test gradually increased. It would be of interest to investigate the kinetics of the alpha → beta transformation when heating in the alpha/beta phase field and could be carried out with simple tests. Material samples could be placed in an induction coil to ensure rapid and accurate temperature changes and control. Here the effects of the hold time to water quench at various temperatures within the alpha-beta phase field could yield the rate at which elemental diffusion controls the transformation between the two phases.

EBSD showed the 'beach' structure to be of the same orientation as either the parent α_P grain or transformed β matrix as it was undetectable. The orientation relationship of this structure can be investigated by employing the same technique devised by Thomas [90] where an EBSD scanned area is revealed by subsequent etching. By re-polishing with colloidal silica and etching again the 'beach' structure could be revealed and compared to a corresponding EBSD map and thus reveal whether the 'beach' has a common orientation with the α_P or transformed β grain.

8. References

1. M.A. Daeubler, D. Helm and D.F. Neal "*Applications of IMI 834 in aeroengines-a collaborative IMI/MTU programme*", Titanium 1990: Products and Applications, USA, 78-87.

2. R. R. Boyer "*An overview on the use of titanium in the aerospace industry*", Materials Science and Engineering, 1996, p.103-114.

3. J. C. Williams and E.A. Starke "*Progress in structural materials for aerospace systems*", Acta Materialia, 2003, 51, 5775-5799.

4. D.F. Neal "*Development of Timetal®834*", Materials Design Approaches and Experiences, Indianapolis, edited by Minerals and Materials Society/AIME, 2001, 78-87.

5. D. R. Askeland "*The science and engineering of materials*", 3rd edition, Stanley Thornes Ltd, Cheltenham, 1996.

6. J. Esslinger "*Titanium in Aero Engines*",
   www.mtu.de/channel/files/pdf/33386Esslinger.pdf, viewed on 16/08/05.

7. J.A. Hooker and P.J. Dorbar "*Metal matrix composites for aeroengines*", Materials Science and Technology, 2000, 16, 725-731.

8. Joachim Kurzke "*Achieving maximum thermal efficiency with the simple gas turbine cycle*",
   http://www.mtu.de/channel/files/pdf/34127Kurzke_AchievingMaximumThermalE
   fficiencyFinal.pdf, viewed on 18/04/06.

9. H. Jahed, B. Farshi and J. Bidabadi "*Minimum weight design of inhomogeneous rotating discs*", International Journal of Pressure Vessels and Piping, 2005, 82, 35-41.

10. Y.Q. Zhao, L. Zhou and J. Deng "*The role of interface in the burning of titanium alloys*", Materials Science and Engineering, 1999, A267, 167-170.

11. Y. Honnorat "*Issues and breakthrough in the manufacture of turboengine titanium parts*", Materials Science and Engineering, 1996, A213, 115-123.

12. I.J. Polmear "*Light alloys-metallurgy of the lights metals*" in Metallurgy & Materials Science, ed. by R. Honeycombe, Arnold, London, 1995, 248-315.

13. C. Leyens & M. Peters "*Titanium and titanium alloys, fundamentals and applications*" ed. by M. Peters, Wiley-VCH, 2003, 1-366.

14. J.C. Williams, R.G. Baggerly and N.E. Paton "*Deformation behaviour of HCP Ti-Al alloy single crystals*", Metallurgical and Materials Transactions, 2002, 33A, 837-850.

15. G. Lutjering and J.C. Williams "*Titanium*", 1st edition, Berlin, 2003.

16. H. Kestler, H. Mughrabi and H.Renner "*Optimisation of microstructure and mechanical properties of the hot-forged titanium alloy IMI 834 by heat -*"

treatment", Titanium '95, Birmingham, UK, ed. by Institute of Materials, 1 Carlton House Terrace, London, SW1Y 5DB, UK, 22-26 Oct. 1995, 1171-1186.

17. Titanium Metals Corporation, *"Timetal®834 data sheet"*, http://www.timet.com/pdfs/834.pdf, viewed on 06/06/08.

18. P. Ruffles *"Aerospace structural materials: present and future"*, Materials World, 1995, 3, 469-470.

19. M.R. Bache *"A review of dwell sensitive fatigue in titanium alloys: the role of microstructure, texture and operating conditions"*, International Journal of Fatigue, 2003, 25, 1097-1087.

20. A. N. Stroh *"The formation of cracks as a result of plastic flow"*, Proceedings of the Royal Society, 1954, 223, 404-414.

21. M.R. Bache *"Processing titanium alloys for optimum fatigue performance"*, International Journal of Fatigue, 1999, 21, S105-S111.

22. L. Germain, N. Gey, M. Humbert, P. Bocher, M. Jahazi *"Analysis of sharp microtexture heterogeneities in a bimodal IMI 834 billet"*, Acta Materialia, 2005, 53, 3535-3543.

23. L. Germain, N. Gey, M.Humbert, A. Hazotte, P. Bocher, M. Jahazi *"An automated method to analyze separately the microtextures of primary alpha grains and the secondary alpha inherited colonies in bimodal titanium alloys"*, Materials Characterisation, 2005, 54, 216-222.

24. M.J. Thomas, B.P. Wynne, W.M. Rainforth *"An alternative method to separate and analyse the microtextures and microstructures of primary alpha grains and transformed beta grains in near alpha titanium alloy Timetal®834"*, Materials Characterisation, 2005, 55, 388-394.

25. M.J. Thomas, B.P.Wynne, W.M. Rainforth *"Texture evaluation of titanium aerospace alloy Ti 834 using hot axisymmetric compression tests"*, Materials Science Forum, 2005, 495-497, 693-698.

26. M.R. Bache, M. Cope, H.M. Davies, W.J. Evans and G. Harrison *"Dwell sensitive fatigue in a nears alpha titanium alloy at ambient temperature"*, International Journal of Fatigue, 1997, 19, 83-88.

27. R.W. Cahn *"Physical metallurgy"*, 1st edition, North-Holland Company, 1965.

28. S. Nemat-Nasser, W.G. Guo and J.Y. CHeng *"Mechanical properties and deformation mechanisms of a commercially pure titanium"*, Acta Materialia, 1999, 47, 3705-3720.

29. G.E. Dieter *"Mechanical metallurgy"*, 2nd edition, McGraw-Hill, New York, 1976.

30. E.A. Ewing and W. Rosenhain *"On the Crystalline Structure of Metals"*, Philosophical Transactions of the Royal Society, 1900, A195, p279.

31. E.A. Ewing and W. Rosenhain *"On the Crystalline Structure of Metals"*, Philosophical Transactions of the Royal Society, 1899, A193, p353.

32. G. E. Dieter *"Mechanical metallurgy"*, SI metric edition, McGraw-Hill, 1988.

33. R.W.K. Honeycombe *"The plastic deformation of metals"*, 4th edition, Edward Arnold, London, 1975.

34. R.E. Smallman and R.J. Bishop *"Modern physical metallurgy and materials engineering"*, 6th ed, Butterworth-Heinemann, 1999

35. M.A.W. Lowden *"Textures and texture strengthening in Ti 6Al 4V"*, University of Aston, 1973.

36. A. T. Churchman *"The slip modes of titanium and the effect of purity on their occurrence during tensile deformation of single crystals"*, Proceedings of the Royal Society, 1954, A226, 216-226.

37. S. Balasubramanian and L. Anand *"Plasticity of initially textured hexagonal polycrystals at high homologous temperatures: application to titanium"*, Acta Materialia, 2002, 50, 133-148.

38. R. von Mises and Z. Angrew *"Mechanik der plastichen. Formanolerungen von kristallen"*, Mathematics and Mechanics, 1928, 3, 161-185.

39. P.G. Partridge *"The crystallographic and deformation modes of hexagonal close-packed metals"*, Metallurgical Reviews, 1967, 169-194.

40. M.H. Yoo, S.R. Agnew, J.R. Morris and K.M.Ho *"Non-basal slip in HCP metals and alloys: source mechanisms"*, Materials Science and Engineering, 2001, A319, 87-92.

41. G.W. Groves and A. Kelly *"Independent slip systems in crystals"*, Philosophical Magazine, 1963, 8, 877.

42. H.G van Bueren *"Imperfections in crystals"*, 1st edition, North-Holland, 1960.

43. C.S. Roberts *"Magnesium and its alloys"*, 1st edition, John Wiley, 1960.

44. W. J.McG. Tegart *"Independent slip systems and ductility of hexagonal polycrystals"*, Philosophical Magazine, 1963, 9, 339-341.

45. H. Numakura, Y. Minonishi and M. Koiwa *"<-1-123>{10-11} slip in titanium polycrystals at room temperature"*, Scripta Materialia, 1986, 20, 1581-1586.

46. M.H. Yoo, S.R. Agnew, J.R. Morris and K.M.Ho *"Non-basal deformation modes of HCP metals and alloys: Role of dislocation source and mobility"*, Metallurgical and Materials Transactions, 2002, 33A, 813-822.

47. M.H. Yoo *"Slip, twin and fracture in hexagonal close-packed metals"*, Metallurgical and Materials Transactions, 1981, 12A, 409-418.

48. S. Naka and A. Lasalmonie *"Prismatic slip in the plastic deformation of alpha titanium crystals below 700 K"*, Materials Science and Engineering, 1982, 56, 19-24.

49. M.J. Blackburn and J.C. Williams *"Strength, deformation modes and fracture in titanium-aluminium alloys"*, Transactions of the ASME, 1969, 62, 398-409.

50. R.W. Hertzberg *"Deformation and fracture mechanisms of engineering materials"*, 1st edition, John Wiley & Sons, 1976.

51. F. J. Humphreys and M. Hatherly *"Recrystallization and related annealing phenomena"*, 2nd edition, Elsevier Science Ltd, Oxford, 2002.

52. S.B. Davenport and R.L. Higginson *"Strain path effects under hot working: an introduction"*, Journal of Materials Processing Technology, 2000, 98, 267-291.

53. H.R. Wenk and P. Van Houtte *"Texture and anisotropy"*, Reports on Process in Physics, 2004, 67, 1367-1428.

54. U.F. Kocks, C.N. Tome and H.R Wenk *"Texture and anisotropy"*, 2nd edition, Cambridge press, Cambridge, 2000.

55. F.J. Humphreys *"Review-Grain and subgrain characterisation by electron back scatter diffraction"*, Journal of Materials Science, 2001, 36, 3833-3854.

56. D.J. Dingley and V. Randle *"Review - Microtexture determination by electron back scatter diffraction"*, Journal of Materials Science, 1992, 27, 4545-4566.

57. M. Hathreley and W.B. Hutchinson *"An introduction to textures in metals"*, Chameleon Press Ltd., London, 1979.

58. F. Bridier, P. Villechaise and J. Mendez *"Analysis of the different slip systems activated by tension in a α/β titanium alloy in relation with local crystallographic orientation"*, Acta Materialia, 2005, 53, 555-567.

59. V. Randle and O. Engler *"An introduction to texture analysis"*, 1st edition, Gordon and Breach, Amsterdam, 2000.

60. H.J. Bunge *"Texture analysis in materials science"*, 1st edition, Butterworth, London, 1992.

61. F.C. Frank *"Orientation mapping"*, Metallurgical and Materials Transactions A, 1988, 19, 403.

62. http://www.krist.uni-freiburg.de/studium/Praktikum/Praktikum_Manuskripte/EBSD/EBSD.pdf, view on 11/10/06.

63. F.J. Humphreys *"Quantitative metallography by electron backscattered diffraction"*, Journal of Microscopy, 1999, 195, 170-186.

64. F.J. Humphreys, Y. Huang, I. Brough and C. Harris *"Electron backscatter diffraction of grain and subgrain structures - resolution considerations"*, Journal of Microscopy, 1999, 195, 212-216.

65. C.M. Sellars and B.P. Wynne, *"Microstructural evolution - effects of microstructural and hot processing variables (invited paper)"*, Proceedings of 25th Risø International Symposium on Materials Science: Evolution of Deformation Microstructures in 3D, Denmark, ed. by C. Gunglach *et al.*, Risø National Laboratory, 2004,117-136.

66. J.H. Schmitt, E. Aernoudt and B. Baudelet *"Yield loci for polycrystalline metals without texture"*, Materials Science and Engineering, 1984, 75, 13-20.

67. J.L. Raphanel, E. Rauch, E.L. Shen and J.-H. Schmitt *"Shear of prestrained steel specimens"*, Scripta Metallurgica, 1987, 21, 1087-1090.

68. J.H. Beynon and B.P. Wynne *"Understanding and exploiting strain paths"*, Engineering Materials 2001, Melbourne, ed. by E. Pereloma, The Institute of Materials and Engineering, 2001, 1-10.

69. S.B. Davenport, R.L. Higginson and C.M. Sellars *"The effect of strain path on the material behaviour during hot rolling of FCC metals"*, The Royal Society, 1999, 357, 1645-1661.

70. B.L. Hutchinson and T. Davis *"The effects of strain path on the plastic flow properties of steel"*, 4th Inter. Conf. On Mechanical Behaviour of Materials, Stockholm, ed. by J.C. Olsson and N.G. Carlsson, 1983, 1227-1236.

71. M.G. Stout and A.D. Rollett *"Large-strain Bauschinger effects in FCC metals and alloys"*, Metallurgical and Materials Transactions, 1990, 21A, 3201-3213.

72. B. Peeters, M. Seefeldt, C. Teodosiu, S.R. Kalidindi, P. Van Houtte and E. Aernoudt *"Work-hardening/softening behaviour of B.C.C polycrystals during changing strain paths: I. An integrated model based on substructure and texture evolution, and its prediction of the stress-strain behaviour of an IF steel during two-stage strain paths."* Acta Materialia, 2001, 49, 1607-1619.

73. B. Peeters, B. Baroix, C. Teodosiu, P. Van Houtte and E. Aernoudt *"Work-hardening/softening behaviour of B.C.C polycrystals during changing strain paths: II.TEM observations of dislocation sheets in an IF steel during two stage strain path and their representation in terms of dislocation densities"*, Acta Materialia, 2001, 49, 1621-1632.

74. B. Peeters, S.R. Kalidindi, P. Van Houtte, E. Aernoudt *"A crystal plasticity based work-hardening/softening model for B.C.C. metals under changing strain paths"*, Acta Materialia, 2000, 48, 2123-2133.

75. P. Pinheiro, W.A. Monteiro, R. Barbosa and P.R. Cetlin *"The effects of strain path on the mechanical behaviour and dislocation arrangements in the hot working of copper"*, Materials Chemistry and Engineering, 2004, A368, 280-285.

76. M. Lewandowska *"Dependence of the deformed microstructure of aluminium alloys on the strain path"*, Materials Chemistry and Physics, 2003, 81, 555-557.

77. M. Zandrahimi, S. Platias, D. Price, D. Barrett, P.S. Bate, W.T. Roberts and D. V. Wilson *"Effects of changes in strain path on work hardening in cubic metals"*, Metallurgical and Materials Transactions, 1989, 20A, 2471-2482.

78. P.S. Bate *"The effects of combined strain-path and strain-rate changes in aluminium"*, Metallurgical and Materials Transactions, 1993, 24A, 2679-2689.

79. R.L. Higginson and C.M. Sellars *"The effect of strain path reversal during hot rolling on austenitic stainless steel"*, Materials Science and Engineering, 2002, A338, 232-330.

80. A.J. McLaren and C.M. Sellars *"The effect of transients in the conditions of hot deformation on the kinetics of static recrystallisation"*, Met. Soc. CIM, ed. N.D. Ryan *et al*, Montreal, 1993, 107-115.

81. A.J. McLaren and C.M. Sellars "*Modelling distribution of microstructure during hot rolling of stainless steel*", Materials science and technology, <u>8</u>, 1992, 1090-1094.

82. M.P. Black, R.L. Higginson and C.M. Sellars "*Effect of strain path on recrystallisation kinetics during hot rolling of Al-Mn*", Materials Science and Technology, <u>17</u>, 2001, 1055-1060.

83. F. P. E. Dunne and I. Katramados "*Large deformation compression-torsion behaviour of a titanium alloy and its modelling*", International Journal of Mechanical Sciences, 1997, <u>40</u>, 901-912.

84. R.B. Figueiredo, I.P. Pinheiro, M.T.P. Aguilar, P,.J. Modenesi and P.R. Cetlin "*The finite element analysis of equal channel angular pressing (ECAP) considering the strain path dependence of the work hardening of metals*", Journal of Materials Processing and Technology, 2006, <u>180</u>, 30-36.

85. E.F. Rauch and J.-H. Schmitt "*Dislocation substructures in mild steel deformation in simple shear*", Materials Science and Engineering, 1989, <u>A113</u>, 441-448.

86. S.L. Semiatin, J.O. Brown, T.M. Brown, D.P. DeLo, T.R. Bieler, J.H. Beynon "*Strain-path effects during hot working of Ti-6Al-4V with a colony-alpha microstructure*", Metallurgical and Materials Transactions, 2001, <u>A32</u>, 1556-1559.

87. E.C.S. Correa, M.T.P. Aguilar, P.R. Cetlin "*The effect of tension/torsion strain path changes on the work hardening of Cu-Zn brass*", Journal of Materials Processing Technology, 2002, <u>124</u>, 384-388.

88. A. Gholinia, P.B. Prangnell, M.V. Markushev "*The effect of strain path on the development of deformation structures in severely deformed aluminium alloys processed by ECAE*", Acta Materialia, 2000, <u>48</u>, 1115-1130.

89. R.H. Wagoner and J.V. Laukonis "*Plastic behaviour of aluminium-killed steel following plane-strain deformation*", Metallurgical and Materials Transactions, 1983, <u>14A</u>, 1487-1495.

90. M. J. Thomas "*The effects of thermomechanical processing parameters on the microstructure and crystallographic textural evolution of Timetal®834*", PhD thesis, The University of Sheffield, 2007.

91. B. Roebuck, J.D. Lords, M. Brooks, S.M Loveday, C.M. Sellars, R.W. Evans, "*Measurement of flow stress in hot axisymmetric compression tests*", Materials at High Temperature, <u>23</u>, 2006, 59-83.

92. G.J. Richardson, D.N. Hawkins and C.M. Sellars "*Worked examples in metalworking*", 1st ed, Institute of Metals, London, 1985.

93. S.B. Davenport, N.J. Silk, C.N. Sparks and C.M. Sellars "*Development of constitutive equations for modelling of hot rolling*", Materials Science and Technology, 2000, <u>16</u>, 539-546.

94. S.P. Jupp "*Fundamental modelling of friction during the hot rolling of steel*", University of Sheffield, 2005.

95. P. Wanjara, M. Jahazi, H. Monajati, S. Yue, J.-P. Immarigeon *"Hot working behaviour of near alpha alloy IMI834"*, Materials Science and Engineering, 2005, A396, 50-60.

96. P. S. Bate, P.L. Blackwell and J.W. Brooks *"Thermomechanical processing of titanium IMI 834"*, Sixth World Conference on Titanium, Cannes, ed. by L.E. Physique, 1988, 287-292.

97. Y.S. Touloukian *"Thermal conductivity-metallic elements and alloys"* in Thermophysical properties of matter, ed. by Y.S. Touloukian, New York, 1970, 102-1504.

98. MSC Software, *"MSC.Superform command reference"*, Santa Ana, 2004.

99. N.T. Rudkins, P. Hartley, I. Pillinger and D. Petty *"Friction modelling and experimental observations in hot ring compression tests"*, Journal of Materials Processing Technology, 1996, 60, 349-353.

100. L.X. Li, D.S. Peng, J.A. Liu and Y. Jiang *"An experimental study of the lubrication behaviour of A5 glass lubricant by means of the ring compression test"*, Journal of Materials Processing Technology, 2000, 102, 138-142.

101. Z.M. Hu, J.W. Brookes, T.A. Dean *"The interfacial heat transfer coefficient in hot die forging of titanium alloy"*, Proceedings of the Institute of Mechanical Engineers, 1998, 212, 485-496.

102. I.Y. Liu and T.N. Baker *"A comparison of experimental and computer-simulated isothermal upset forging of IMI685 titanium alloy"*, Materials Science and Engineering, 1996, A205, 117-126.

103. J.W. Brookes, T.A. Dean, Z. M. Hu, E. Wey *"Three-dimensional finite modelling of a titanium aluminide aerofoil forging"*, Journal of Materials Processing Technology, 1998, 80-81, 149-155.

104. N. Srinivasan, N. Ramakrishan, A. Venugopal Rao, N. Swamy *"CAE for forging of titanium alloy aero-engine disc and integration with CAD-CAM for fabrication of the dies"*, Journal of Materials Processing Technology, 2002, 124, 353-359.

105. M. Zhan, Y. Liu, H. Yang *"A 3D rigid-viscoplastic FEM simulation of compressor blade isothermal forging"*, Journal of Materials Processing Technology, 2001, 117, 56-61.

106. F. P. Incropera and D. P. DeWitt *"Introduction to heat transfer"*, ed. by John Wiley & Sons, New York, 1996, 373-575.

107. A.C. Metaxas *"Foundations of electroheat-A unified approach"*, ed. by John Wiley & Sons, Chichester, 1996, 65-69.

108. R.J. Hand, S.R. Foster, and C.M. Sellars *"Temperature changes during hot plane strain compression testing"*, Materials Science and Technology, 2000, 16, 442-450.

109. Z. Malinowski, J.G. Lenard and M.E. Davies "*A study of the heat-transfer coefficient as a function of temperature and pressure*", Journal of Materials Processing Technology, 1994, 41, 125-142.

110. P. R. Burte, Y-T. Im, T. Altan and S.L. Semiatin "*Measurement and analysis of heat transfer coefficient and friction during hot forging*", Transactions of the ASME, 1990, 112, 332-338.

111. D.R. Barraclough, H.J. Whittaker, K.D.Nair and C.M. Sellars "*Effect of specimen geometry on hot torsion test results and tubular specimens*", Journal of Testing and Evaluation, 1, No. 3, 1973, 220-226.

112. J. Chakrabarty "*Applied plasticity*", 1st edition, Springer-Verlang, 2000.

113. R. Hill "*The mathematical theory of plasticity*", 1st edition, Claredon Press, Oxford, 1950.

114. S. C. Shrivastava, J.J. Jonas and G. Canova "*Equivalent strain in large deformation torsion testing: Theoretical and practical considerations*", J. Mech. Phys. Solids, 1981, 30, 75-90.

115. G.R. Canova, U.F. Kocks and J.J. Jonas "*Theory of texture development*", Acta Metallurgia, 1983, 32, 211-226.

116. Z. Gronostajski "*The effect of cyclic strain path on the properties and structure of CuA110 aluminium bronze*", Journal of Materials Processing Technology, 2004, 155-156, 1138-1143.

117. B. Burton "*Theoretical assessment of influence of deformation inducted heating on mechanical behaviour at elevated temperatures*", Materials Science and Technology, 2000, 16, 175-186.

118. W. Nshama, J. Jeswiet and P.H. Oosthuizen "*Evaluation of temperature and heat transfer conditions at the metal forming interface*", Journal of Materials Processing Technology, 1994, 45, 637-642.

119. K. Andersson, S. Kivivuori and A.S. Korhonen "*Effect of the heat transfer coefficient in ring compression test*", Journal of Materials Processing Technology, 1996, 62, 10-13.

120. A. Behrens and H. Schafstall "2D and 3D simulation of complex multistage forging processes by use of adaptive friction coefficient", Journal of Materials Processing Technology, 1998, 80-81, 298-303.

121. R.G. Snape, S.E. Clift and A.N. Bramley "*Sensitivity of finite element analysis of forging to input parameters*", Journal of Materials Processing Technology, 1998, 82, 21-26.

122. Guy Snape, Sally Clift and Alan Bramley "*Parametric sensitivity analyses for FEA of hot steel forging*", Journal of Materials Processing Technology, 2002, 125-126, 353-360.

123. Y.V.R.K. Prasad and T. Seshacharyulu "*Processing maps for hot working of titanium alloys*", Materials Science and Engineering, A243, 1998 82–88.

124. Woei-Shyan Lee and Chi-Feng Lin "*Plastic deformation and fracture behaviour of Ti–6Al–4V alloy loaded with high strain rate under various temperatures*", Materials Science and Engineering, A241, 1998, 48–59.

125. Woei-Shyan Lee and Chi-Feng Lin "*High temperature deformation behaviour of Ti6Al4V alloy evaluated by high strain rate compression tests*", Journal of Materials Processing Technology, 75, 1998, 127–136.

126. V. Gopala Krishna, Y. V. R. K. Prasad, N. C. Birla and G. Sambasiva Rao "*Processing map for the hot working of near alpha titanium alloy 685*" Journal of Materials Processing Technology, 71, 1997, 377-383.

127. R.C. Dorf and R.H. Bishop "*Modern control systems*", Addison-Wesley, Reading, 1994, 662-666.

128. K. Warwick "*Control systems: an introduction*", Prentice-Hall International, London, 1989, 306-327.

129. http://en.wikipedia.org/wiki/PID_controller, viewed on 21/12/07.

130. G.E. Franklin "*Feedback control of dynamic systems*", Addison-Wesley, Wokingham, 1994, 179-194.

131. G. Angella, B.P. Wynne, W.M. Rainforth and J.H. Beynon "*Microstructure evolution of AISI 316L in torsion at high temperature*", Acta Materialia, 53, 2005, 1263-1275.

132. G. Angella, "*Strain path, flow stress and microstructure evolution of an austenitic stainless steel at high temperature*", University of Sheffield, 2002.

133. M. Zhou and M.P. Clode "*Effects of specimen geometry on temperature rise and flow behaviour of aluminium alloys in hot torsion testing*", Materials & Design, 17, 1997, 275-281.

134. M. Zhou and M.P. Clode "*Thermal analysis of the torsion test under hot-working conditions*", Computational Materials Science, 9, 1998, 411-419.

135. S. Khoddam & P.D. Hodgson "*Conversion of the hot torsion test results into flow curve with multiple regimes of hardening*", Journal of Materials Processing Technology, 153-154, 2004, 839-845.

136. G. R. Canova, S. Shrivastava, J.J. Jonas and C. G'Sell "*The use of torsion testing to assess material formability*", Formability of Metallic Materials-2000 A.D., Philadelphia, American society for testing, 1982, 189-210.

137. J.A. Hall "*Fatigue crack initiation in alpha-beta titanium alloys*", International Journal of Fatigue, 19, 1997, 23–37.

138. M. López-Pedrosa "*An analysis of microstructure evolution in hot worked aluminium subjected to non-linear deformation*", PhD thesis, The University of Sheffield, 2007.

139. G. Canova, S. Shrivastava, J. Jonas, C. G'Sell "*The Use of Torsion Testing to Assess Material Formability*", eds. ASTM STP 753, edited by J.R. Newby and B.A. Niemeier, 1982, 189-240.

140. H.M. Flower "*Microstructural development in relation to hot working of titanium alloys*", Materials Science and Technology, <u>6</u>, 1990, 1082-1092.

141. D.F. Neal "*Development and evaluation of high temperature titanium alloy IMI 834*", Proceedings of the Sixth World Conference on Titanium, Cannes, France, 1988, 253-258.

142. Private communication with Dr A. Wilson of Timet UK, April 2006.

143. M.L. Blackmore, B.P. Wynne, J.H. Beynon and P.S. Davies "*Strain path effects on titanium alloy-834 under hot working conditions*", Advanced Materials Research, <u>15-17</u>, 2006, 959-964.

144. P. Davies, B. Wynne and W.M. Rainforth "*Investigating microstructural evolution in near alpha alloy Timetap®834 using electron back scatter diffraction (EBSD)*", Ti-2007 Science and Technology, Kyoto, edited by M. Ninomi, 2007, 949-952.

145. N. Gey and M. Humbert "*Specific analysis of EBSD data to study the texture inheritance due to the $\beta \rightarrow \alpha$ phase transformation*", Journal of Materials Science, <u>38</u>, 2003, 1289-1294.

146. M. Humbert, F. Wagner, H. Moustahfid, and C. Esling "*Determination of the orientation of a parent β grain from the orientations of the inherited α plates in the phase transformation from body centred cubic to hexagonal close packed*", Journal of Applied Crystallography, <u>28</u>, 1995, 571-576.

147. P. Vo, M. Jahazi, S. Yue and P. Bocher "*Flow stress prediction during hot working of near-α titanium alloys*", Materials Science and Engineering, <u>A447</u>, 2007, 99–110.

148. R. Ding, Z.X. Guo, A. Wilson "*Microstructure of a Ti-6Al-4V alloy during thermomechanical processing*", Materials Science and Engineering, <u>A327</u>, 2002, 233–245.

149. R.J. Crawford, C.G. Armstrong and P.P. Benham "*Mechanics of Engineering Materials*", 2nd edition, Longman, 1996.

150. D. Loveless, V. Rudnev, R. Cook and M. Black "*Handbook of induction heating*", Marcel Dekker Inc, New York, 2003, 99-113.

151. J.P. Holman "*Heat Transfer*", 9th edition, McGraw-Hill, New York, 2002.

9. Appendix

9.1. Yield criterion

The state of stress in a material element can be expressed by a point in nine dimensional space. This takes into account the one normal (e.g. σ_{xx}) and two shear stresses (e.g. σ_{xy}, σ_{xz}) which may be imposed on the element in each of the x, y and z-directions.

Around the origin of the stress state, there exists a domain in the elastic range representing the totality of elastic states of stress. The external boundary of this elastic domain defines the yield surface. By assuming an initially isotropic material then the plastic yielding depends only on the magnitudes of the three principle stresses and not the direction in which they act [149].

There are two yield criteria based on concepts of shear which are commonly used to describe yielding in ductile materials. Both the criteria are expressed in the principle stresses. These are the Tresca criterion which is based upon maximum shear-stress and the Von Mises criterion which is based on the shear-strain energy.

The Tresca theory assumes that yield will occur when the maximum shear stress (τ_{max}) in the body reaches a critical value regardless of the stress state. For a 3D stress system it can be seen that;

$$\tau_{max} = \frac{\sigma_x - \sigma_z}{2} \tag{9.1}$$

Under uniaxial loading conditions, i.e. a tensile test Equation 9.1 becomes (and at yield $\tau_{max} = \tau_{yd}$);

$$\tau_{max} = \tau_{yd} = \frac{\sigma_{yd}}{2} \tag{9.2}$$

Therefore;

$$\frac{\sigma_{yd}}{2} = \frac{\sigma_x - \sigma_z}{2} \tag{9.3}$$

$$\sigma_{yd} = \sigma_x - \sigma_z \tag{9.4}$$

The von Mises shear strain criterion considers the energy stored within an element of material due to the change in volume and shape distortion.
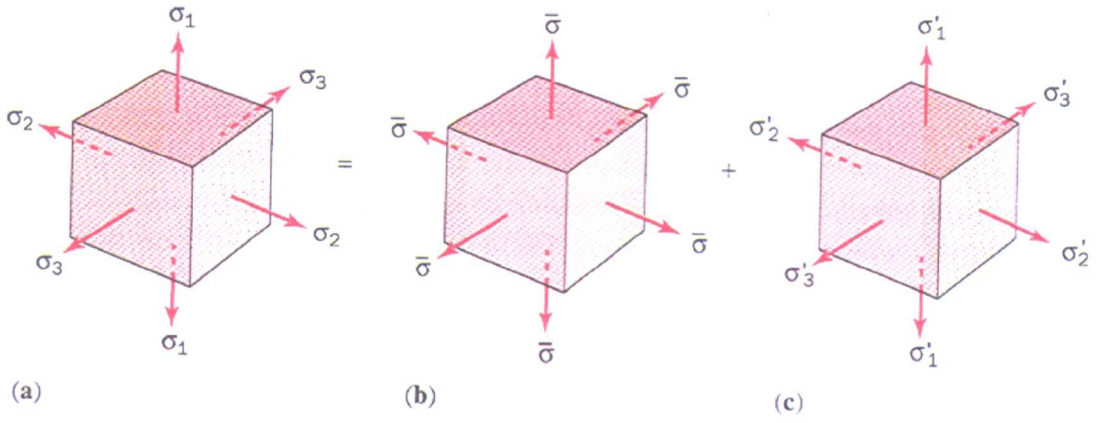
Figure 9.1 Deformation upon an element of material separated into volume and shape change [149]

To show that the deformation of an element of material can be separated into volume and shape change, consider the element in Figure 9.1 subjected to three principle stresses. These principle stresses can be written in terms of 'average' stresses in the element (note that in Figure 9.1 $\sigma_1 = \sigma_x$, $\sigma_2 = \sigma_y$, $\sigma_3 = \sigma_z$);

$$\sigma_x = \overline{\sigma} + \sigma'_x$$
$$\sigma_y = \overline{\sigma} + \sigma'_y$$
$$\sigma_z = \overline{\sigma} + \sigma'_z$$

Where $\overline{\sigma}$ is the mean stress and σ' is the deviatoric stress. $\overline{\sigma}$ is defined as:

$$\overline{\sigma} = \left(\sigma_x + \sigma_y + \sigma_z\right)/3 \tag{9.5}$$

If the element to subjected to $\overline{\sigma}$ in all directions, this hydrostatic stress will produce a volume change with no distortion. By collecting the terms in above equations;

$$\sigma_x + \sigma_y + \sigma_z = 3\overline{\sigma} + \sigma'_x + \sigma'_y + \sigma'_z$$

But as $\overline{\sigma} = \left(\sigma_x + \sigma_y + \sigma_z\right)/3$, then;

$$\sigma'_x + \sigma'_y + \sigma'_z = 0 \tag{9.6}$$

But from the stress strain relationship for elastic deformation;

$$\varepsilon'_x = \frac{1}{E}\left(\sigma'_x - \upsilon_p\left(\sigma'_y + \sigma'_z\right)\right)$$

220

$$\varepsilon_y^{'} = \frac{1}{E}\left(\sigma_y^{'} - \upsilon_p\left(\sigma_z^{'} + \sigma_x^{'}\right)\right)$$

$$\varepsilon_z^{'} = \frac{1}{E}\left(\sigma_z^{'} - \upsilon\left(\sigma_x^{'} + \sigma_y^{'}\right)\right)$$

Hence

$$\varepsilon_x^{'} + \varepsilon_y^{'} + \varepsilon_z^{'} = e^{'} = \frac{\left(1 - 2\upsilon_p\right)}{E}\left(\sigma_x^{'} + \sigma_y^{'} + \sigma_z^{'}\right) \qquad (9.7)$$

But as the sum of these stresses is zero;

$$\varepsilon_x^{'} + \varepsilon_y^{'} + \varepsilon_z^{'} = e^{'} = 0 \qquad (9.8)$$

Therefore the deviatoric stress components cause no change in the volume but only shape change.

This criterion considers the total strain energy as two components;
- A component due to volume change (U_V).
- A component due to shape change (U_D).

$$U_T = U_V + U_D \qquad (9.9)$$

By considering the strain energy associated with a load F in one dimension (δ is the deflection caused by the force F);

$$\text{Strain energy} = \frac{1}{2}F\delta \qquad (9.10)$$

Considering a small element of material the above equation becomes;

$$\frac{1}{2}F\delta = \frac{1}{2}\left(\sigma_x dydz\right)\left(\varepsilon dx\right) \qquad (9.11)$$

This can also be written as the strain energy per unit volume;

$$U = \frac{1}{2}\sigma\varepsilon \qquad (9.12)$$

The same equation can now be applied to 3D space to encompass the total strain per unit volume;

$$U_T = \frac{1}{2}\left(\sigma_x \varepsilon_x + \sigma_y \varepsilon_y + \sigma_z \varepsilon_z\right) \qquad (9.13)$$

By substituting for Poisson strains as shown previously $\left(\varepsilon_x = \frac{1}{E}\left(\sigma_x - \upsilon_p\left(\sigma_y + \sigma_z\right)\right)\right)$, and rearranging gives;

$$U_T = \frac{1}{2E}\left(\left(\sigma_x^2 + \sigma_y^2 + \sigma_z^2\right) - 2\upsilon_p\left(\sigma_x \sigma_y + \sigma_y \sigma_z + \sigma_z \sigma_x\right)\right) \qquad (9.14)$$

The volumetric strain energy can be determined from the hydrostatic component of stress, $\bar{\sigma}$;

$$U_V = \frac{1}{2}\bar{\sigma}e = \frac{1}{2}\bar{\sigma}\frac{3\bar{\sigma}}{E}\left(1 - 2\upsilon_p\right) \qquad (9.15)$$

Substituting the average stress, volumetric strain energy per unit volume is;

$$U_V = \frac{1 - 2\upsilon_p}{6E}\left(\sigma_x + \sigma_y + \sigma_z\right)^2 \qquad (9.16)$$

As $U_D = U_T - U_V$ this yields;

$$U_D = \frac{1}{2E}\left(\left(\sigma_x^2 + \sigma_y^2 + \sigma_z^2\right) - 2\upsilon_p\left(\sigma_x \sigma_y + \sigma_y \sigma_z + \sigma_z \sigma_x\right)\right) - \frac{1 - 2\upsilon_p}{6E}\left(\sigma_x + \sigma_y + \sigma_z\right)^2$$

Which reduces to;

$$U_D = \frac{1 + \upsilon_p}{6E}\left[\left(\sigma_x - \sigma_y\right)^2 + \left(\sigma_y - \sigma_z\right)^2 + \left(\sigma_z - \sigma_x\right)^2\right] \qquad (9.17)$$

Alternatively this can be written as;

$$U_D = \frac{1}{12G}\left[\left(\sigma_x - \sigma_y\right)^2 + \left(\sigma_y - \sigma_z\right)^2 + \left(\sigma_z - \sigma_x\right)^2\right] \qquad (9.18)$$

The yield criterion proposes that yielding will occur when U_D reaches the equivalent value at yielding in tension and so $\sigma_y = \sigma_z = 0$ and $\sigma_x = \sigma_{yd}$, and so;

$$U_D = \frac{\sigma_y^2}{6G} \text{ per unit volume}$$

Also;

222

$$\frac{1}{12G}\left[\left(\sigma_x - \sigma_y\right)^2 + \left(\sigma_y - \sigma_z\right)^2 + \left(\sigma_z - \sigma_x\right)^2\right] = \frac{\sigma_{yd}^2}{6G}$$

or;

$$2\sigma_{yd}^2 = \left[\left(\sigma_x - \sigma_y\right)^2 + \left(\sigma_y - \sigma_z\right)^2 + \left(\sigma_z - \sigma_x\right)^2\right] \qquad (9.19)$$

or;

$$\bar{\sigma}_u = \frac{1}{\sqrt{2}}\left[\left(\sigma_x - \sigma_y\right)^2 + \left(\sigma_y - \sigma_z\right)^2 + \left(\sigma_z - \sigma_x\right)^2\right]^{1/2} \qquad (9.20)$$

Where $\bar{\sigma}_u$ is equal to the von Mises equivalent stress. It can be shown that Equation 9.20 is also equivalent to;

$$2\sigma_{yd}^2 = \left[\left(\sigma_x - \sigma_y\right)^2 + \left(\sigma_y - \sigma_z\right)^2 + \left(\sigma_z - \sigma_x\right)^2 + 6\left(\tau_{xy}^2 + \tau_{yz}^2 + \tau_{xz}^2\right)\right] \qquad (9.21)$$

In the case of plane stress, $\sigma_z = 0$;

$$\sigma_{yd}^2 = \sigma_x^2 - \sigma_x\sigma_y + \sigma_y^2 \qquad (9.22)$$
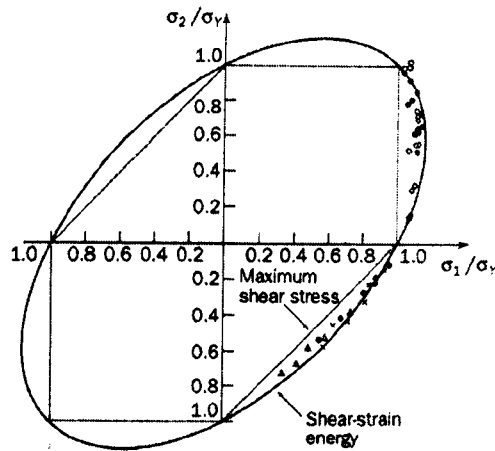
Figure 9.2 Yield loci for a ductile material, demonstrating both von Mises and Tresca yield criteria [149]

Several experimental studies have been carried out [149] to establish the appropriate yield criterion under various combinations of principle stresses. Thus when the equivalent applied von Mises stresses reach that of the materials yield strength in tension the material is considered to have yielded. From Figure 9.2 the von Mises shear-strain energy criterion seams to be the more accurate, although both are

acceptable criteria. The Tresca criterion is more often used when designing components as this offers a more conservative solution with a greater safety factor. However for this for the purpose of this work the more accurate von Mises yield criterion will be utilised.

9.2. Induction heating

Due to several electromagnetic phenomena, the current and thus power distribution generated within a workpiece is not uniform. This nonuniformity causes a nonuniform temperature profile within the material in the magnetic field.

The ability of a material to conduct electrical current is specified by electrical conductivity σ_{cond}. The inverse of this is electrical resistivity ρ_{res}. The units of ρ_{res} and σ_{cond} are $\Omega.m$ and $S.m^{-1}$ respectively. The electrical resistivity of titanium is modelled using the expression below, which is obtained from [150]. This assumes that there is no change in the lattice structure of the material.

$$\rho_{Ti} = 0.42[1 + 0.0035(T - 20)] \tag{9.23}$$

Electrical conductivity (σ_{cond});

$$\sigma_{cond} = \frac{1}{\rho_{res}} \tag{9.24}$$

For most binary alloy systems, the concentration of alloying elements can have a dramatic effect on the ρ_{res} of the material. By plotting alloy concentration against ρ_{res}, it can be seen that a bell shaped curved is produced which peaks at a maximum value at approximately 50% weight percent alloying element. In other cases alloying elements can continuously increase or decrease the electrical resistivity. The value of electrical resistivity is also affected by the grain size, plastic deformation, heat treatment, and some other factors[150].

9.3. Skin effects

When a current flows through a conducting material the current distribution across the cross section is uniform. In contrast to this, when an alternating current is applied to a conductor, the distribution is non-uniform. The maximum value of current density will

always be concentrated towards the surface of the conductor and decrease towards the centre. Such effects are known as the skin effect. It is caused by the circumferential nature of the induced eddy currents within the material, are as thus more dominate towards the surface rather than the centre of the conductor. Because of this effect, approximately 86% of the power generated will be concentrated at the surface of the conductor. This layer is called the depth of penetration (δ_d) and can be calculated using Equation 9.25 below. Mathematically speaking δ_d is the distance from the surface of the conductor towards its core at which the current decreases exponentially to $(\exp)^{-1}$.

Depth of penetration is given by;

$$\delta_d = 503\sqrt{\frac{\rho_{res}}{\mu_r f}} \qquad (9.25)$$

Where μ_r is the relative magnetic permeability and indicates how efficiently a material conducts magnetic flux better than a vacuum or air environment. From Equation 9.25 it can be seen that magnetic permeability will have a clear effect on the skin depth.

9.4. Thermophysical properties of air

The following temperature dependent data is used in calculations shown in Section 4.2.1.5

Table 9.1 Temperature dependant properties for air at atmospheric pressure. Note, the values of dynamic viscosity, thermal conductivity, specific heat, and Pr are not strongly pressure dependant and may be used over a fairly wide range of pressures [151]

Temperature (K)	Density (kg/m³)	Specific heat (kJ/kg°C)	Dynamic vis (10⁻⁵kg/ms)	Kinematic vis. (m²/s)	Thermal conductivity (W/mK)	Thermal diffusivity(m²/s)	Prandtl No.	Reynolds No.
100	3.6010	1.0266	0.6924	1.923	0.0092	0.0250	0.770	1872.3
150	2.3675	1.0091	1.0283	4.343	0.0137	0.0575	0.753	828.8
200	1.7684	1.0061	1.3289	7.490	0.0181	0.1017	0.739	479.1
250	1.4128	1.0053	1.5990	11.310	0.0223	0.1568	0.722	318.1
300	1.1774	1.0057	1.8462	15.590	0.0262	0.2216	0.708	229.6
350	0.9980	1.0090	2.0750	20.760	0.0300	0.2983	0.697	173.1
400	0.8826	1.0140	2.2860	25.900	0.0337	0.3760	0.689	139.0
450	0.7833	1.0207	2.4840	31.710	0.0371	0.4222	0.683	113.5
500	0.7048	1.0295	2.6710	37.900	0.0404	0.5564	0.680	95.0
550	0.6423	1.0392	2.8480	44.340	0.0436	0.6532	0.680	81.2
600	0.5879	1.0551	3.0180	51.340	0.0466	0.7512	0.680	70.1
650	0.5430	1.0635	3.1770	58.510	0.0495	0.8578	0.682	61.5
700	0.5030	1.0752	3.3320	66.250	0.0523	0.9672	0.684	54.3
750	0.4709	1.0856	3.4810	73.910	0.0551	1.0774	0.686	48.7
800	0.4405	1.0978	3.6250	82.290	0.0578	1.1951	0.689	43.7
850	0.4149	1.1095	3.7650	90.750	0.0603	1.3097	0.692	39.7
900	0.3925	1.1212	3.8990	99.300	0.0628	1.4271	0.696	36.2
950	0.3716	1.1321	4.0230	108.200	0.0653	1.5510	0.699	33.3
1000	0.3524	1.1417	4.1520	117.800	0.0675	1.6779	0.702	30.6

1100	0.3204	1.1600	4.4400	138.600	0.0732	1.9690	0.704	26.0
1200	0.2947	1.1790	4.6900	159.100	0.0782	2.2510	0.707	22.6
1300	0.2707	1.1970	4.9300	182.100	0.0837	2.5830	0.705	19.8
1400	0.2515	1.2140	5.1700	205.500	0.0891	2.9200	0.705	17.5
1500	0.2355	1.2300	5.4000	229.100	0.0946	3.2620	0.705	15.7
1600	0.2211	1.2480	5.6300	254.500	0.1000	3.6090	0.705	14.1
1700	0.2082	1.2670	5.8500	280.500	0.1050	3.9770	0.705	12.8
1800	0.1970	1.2870	6.0700	308.100	0.1110	4.3790	0.704	11.7
1900	0.1858	1.3090	6.2900	338.500	0.1170	4.8110	0.704	10.6
2000	0.1762	1.3380	6.5000	369.000	0.1240	5.2600	0.702	9.8
2100	0.1682	1.3720	6.7200	399.600	0.1310	5.7150	0.700	9.0
2200	0.1602	1.4190	6.9300	4332.600	0.1390	6.1200	0.707	8.3
2300	0.1538	1.4820	7.1400	464.000	0.1490	6.5400	0.710	7.8